

Université du Québec
Institut national de la recherche scientifique
Centre Énergie, Matériaux et Télécommunications

**ADDITIVE-ENHANCED BIOPOLYMER SCAFFOLDS
FOR BONE REPAIR**

By
Imran Deen

A thesis submitted in partial fulfillment of the requirements for the degree
Doctor of Philosophy, (Ph.D.)
in Energy and Material Sciences

Jury of Evaluation

President of the Jury and Internal Examiner	Dr. Fiorenzo Vetrone INRS-EMT (Varennes, QC, Canada)
External Examiner	Dr. Muthukumaran Packirisamy Concordia University (Montreal, QC, Canada)
External Examiner	Dr. Fabio Variola University of Ottawa (Ottawa, ON, Canada)
Supervisor	Dr. Federico Rosei INRS-EMT (Varennes, QC, Canada)

Université du Québec
Institut national de la recherche scientifique
Centre Énergie, Matériaux et Télécommunications

Échafaudages de biopolymère avec additifs pour la réparation des os

Par
Imran Deen

Thèse présentée pour l'obtention du grade de
Philosophiae Doctor, (Ph.D.)
en sciences de l'énergie et des matériaux

Jury d'évaluation

Président du Jury et examiner interne

Dr. Fiorenzo Vetrone
INRS-EMT (Varennes, QC, Canada)

Examinateur externe

Dr. Muthukumaran Packirisamy
Concordia University (Montreal, QC, Canada)

Examinateur externe

Dr. Fabio Variola
University of Ottawa (Ottawa, ON, Canada)

Directeur de recherche

Dr. Federico Rosei
INRS-EMT (Varennes, QC, Canada)

For my mother and father

Abstract

The current approach for harvesting bone tissue for bone grafts is well established, yet has a host of complications associated with it. Biomaterials are viewed as the next step in regenerative medicine that can replace the need to either have an invasive surgery to harvest bone, or harvest bone from an external source that elicits an antigenic response. Creating biomaterials that can incorporate bioactive elements and have significantly higher healing properties than traditional materials is thus extremely desirable.

The aim of this project is to incorporate bioactive elements, such as silk fibroin derived polypeptides (FDP) and bioactive glasses (e.g. phosphate glass, PG), into hydrogel scaffolds based on collagen and/or chitosan (CTS). The end goal is to create a dense, biocompatible scaffold with suitable biological properties that can be used for bone repair. Furthermore, the use of these materials to create bioactive coatings for biomedical implants is also being investigated.

The bioactive additives were incorporated into the hydrogels with the expectation that they would improve the biological properties of the gel and biocompatibility of the scaffold, making it more suitable for clinical applications. The composition, morphology and structure of these gels and scaffolds with and without bioactive additives incorporated were analyzed and compared. Then end goal was to characterize the effect of incorporating additives into hydrogels and scaffolds in terms of their material and biological properties.

CTS, a natural cationic polysaccharide, is derived from chitin, a naturally available marine polymer, and Type I collagen, the organic component of bone, were used for scaffold creation. CTS is a non-toxic, biocompatible and biodegradable polymer and has attracted considerable interest in a wide range of biomedical and pharmaceutical applications including drug delivery and tissue engineering. The use of silk FDPs and CuO-doped PG to improve hydroxyapatite (HA) nucleation was investigated in the following work, which shows that the anionic phosphate groups and calcium ions released from dissolved phosphate glasses can be used to generate HA *in vitro*. To this end, blended CTS-collagen hydrogels (at a 1:1 and 1:2 ratio by mass) incorporating 50 wt% glass phosphate were fabricated, as well as CTS-collagen-PG coatings manufactured via Electrophoretic Deposition (EPD) using similar ratios.

Experimental results including particle size analysis (PSA), scanning electron microscopy (SEM) imaging, attenuated total reflectance-Fourier transform infrared (ATR FT-IR) spectroscopy, Thermogravimetric Analysis (TGA), Electron Diffraction Spectroscopy (EDS), Electro Impedance

Spectroscopy (EIS), Liquid Chromatography–Mass Spectrometry (LCMS), X-ray Diffraction (XRD), Quartz Crystal Microbalance (QCM) and weight analysis were used to characterize the resulting hydrogels and coatings and investigate their composition and structure.

The characterization of the bioadditives via ATR FT-IR and XRD showed that silk FDPs immersed in Simulated Body Fluid (SBF) did nucleate HA *in vitro*, but when incorporated into a hydrogel did not show a significant different compared to the control. Furthermore, LCMS results showed that the FDPs were composed of largely neutral amino acids (~97% of the total), which provides an explanation for its inability to attract the necessary anions and cation to nucleate HA. Conversely, PG showed potential to mineralize HA, as it retained ~20% of its initial mass when immersed in SBF (compared to total dissolution in H₂O), and increased in mass when placed in a hydrogel *in vitro*. SEM of the PG immersed in SBF showed the formation of new particles after three days. Similar results were seen observed in DC gels, and after seven days the mass of the PG hydrogel was significantly higher than that of pure DC gels. ATR FT-IR spectra showed bands associated with the presence of calcium phosphates, and elemental characterization via EDS showed 30-40% phosphorus when CuO-doped PG was incorporated into the dense hydrogels. XRD confirmed the formation of a new particle that matches the profile of amorphous calcium phosphate (ACP).

EPD showed the co-deposition of PG particles within collagen/CTS coatings at standard ambient temperature and pressure (1 kPa, 25 °C) was possible, and the addition of collagen led to the steric stabilization of PG in solution. PSA showed that the a colloidal suspension of PG sediment with time, with average particle size decreasing from 11.8 µm to 5.6 µm after being left to sit for 15 minutes. However, the deposition yield at different time points showed a profile typical of constant voltage deposition. Increasing the concentration of collagen in the PG solution allows for a higher deposition yield, while pure collagen solutions resulted in hydrogen gas evolution at the cathode. SEM images showed larger PG particles deposited with collagen than chitosan, and ATR FT-IR showed a significant phosphate presence that increased with collagen concentration, and TGA showed that the mass of PG particles deposited increases from 5-15 wt% with only chitosan to 62-68 wt% with collagen.

This work provides a foundation to further optimize the properties of hydrogels incorporating phosphate glasses for bone tissue engineering. The results obtained show that PG has the ability to nucleate into a bone-analogous material within a hydrogel *in vitro*, as well as co-deposit with biopolymers and form coatings that can mimic native bone tissue. The use of PG allows for the potential to fabricate replacement bone tissue or orthopaedic implants with tailored biological properties with

lower risk of rejection from the host and exhibit increased bioactivity.

Keywords: biomaterials; tissue engineering; collagen; chitosan; hydrogel; scaffold; electrophoretic deposition; mineralization; hydroxyapatite; phosphate glass

Résumé

Présentement, la technique de prélever du tissu osseux d'un site donneur pour une greffe osseuse est bien établie, mais entraîne toutes sortes de complications. Les biomatériaux sont considérés comme la prochaine itération pour avancer la médecine régénératrice, et qui peut remplacer la nécessité d'une opération chirurgicale pour prélever l'os, ou d'utiliser l'os d'une source externe, ce qui produit dans une réponse antigénique. La création des biomatériaux qui peuvent incorporer des éléments bioactifs et qui ont des propriétés de guérison significativement plus élevées que les matériaux traditionnels est donc extrêmement désirable.

Le but de ce projet est d'incorporer des éléments bioactifs, tels que des polypeptides dérivés de la fibroïne (FDP) de soie et des verres bioactifs (spécifiquement du verre de phosphate, PG), dans des échafaudages de collagène et de chitosan. L'objectif est de créer un échafaud biocompatible avec des propriétés mécaniques et biologiques comparables au tissu osseux et qui peuvent être utilisés pour la réparation des os. En outre, l'utilisation de ces éléments peuvent également être utilisés pour créer des couches bioactives pour les implants biomédicaux (prothèses métalliques).

Les éléments bioactifs seront incorporés dans les hydrogels dans le but d'améliorer les propriétés biologiques et mécaniques du gel et la biocompatibilité de l'échafaudage, le rendant plus attractif pour des applications cliniques. La composition, la morphologie et la structure de ces gels et échafaudages, avec et sans additifs bioactifs incorporés, seront analysées. L'objectif final est de caractériser l'effet des additifs dans les hydrogels et les échafaudages en termes de propriétés de matériaux et biologiques.

Le chitosan (CTS) est un polymère non toxique, biocompatible et biodégradable qui a suscité un intérêt considérable dans un large éventail d'applications biomédicales et pharmaceutiques, y compris l'administration de médicaments et l'ingénierie des tissus osseux. L'utilisation des verres de phosphates dopés avec CuO pour améliorer la nucléation de l'hydroxyapatite (HA) a été étudiée au cours de ce projet/recherche, qui montre que les groupes phosphate anioniques et les ions calcium libérés des verres phosphatés dissous peuvent être utilisés pour générer HA *in vitro*. À cette fin, on a fabriqué des hydrogels de CTS-collagène mélangés (à un rapport de 1:1 et 1:2 par poids) incorporant 50 wt% de PG, ainsi que des revêtements de CTS-collagène PG fabriqués par dépôt électrophorétique (EPD).

Les résultats expérimentaux comprennent l'analyse de la taille des particules (PSA), l'imagerie par microscopie électronique à balayage (SEM), la spectroscopie par réflectance totale atténuee et

infrarouge à transformée de Fourier (ATR FT-IR), l'analyse thermogravimétrique (TGA), la spectroscopie par diffraction des électrons (EDS), la spectroscopie de diffraction des électrons (EDS), la spectroscopie d'électro-impédance (EIS), la chromatographie liquide-spectrométrie de masse (LCMS), la diffraction des rayons X (XRD), la microbalance à cristaux de quartz (QCM) et l'analyse pondérale ont été utilisées pour caractériser les hydrogels et les revêtements obtenus et étudier leur composition et leur structure.

La caractérisation des bioadditifs par ATR FT-IR et XRD a montré que les FDP immergés dans du fluide corporel simulé (SBF) ont nucléé HA *in vitro*, mais lorsqu'ils ont été incorporés dans un hydrogel, ils n'ont pas montré de différence significative par rapport au contrôle. En outre, les résultats du LCMS ont montré que les FDP étaient composés d'acides aminés largement neutres (~97% du total), ce qui explique leur incapacité à attirer les anions et les cations nécessaires à la nucléation de HA. D'autre part, le PG ont montré un potentiel de minéralisation de HA, car il a conservé ~20% de son masse initiale lorsqu'il a été immergé dans le SBF (par rapport à une dissolution totale dans H₂O), et a augmenté en masse lorsqu'il a été placé dans un hydrogel *in vitro*. De plus, les images SEM du PG immergé dans le SBF a montré la formation de nouvelles particules après trois jours. Des résultats similaires ont été observés dans les hydrogels, et après sept jours la masse de l'hydrogel de PG était significativement plus élevée que la masse des hydrogels sans PG. Les spectres ATR FT-IR ont montré des bandes associées à la présence de phosphates, et la caractérisation élémentaire par EDS a montré 30-40% de phosphore lorsque le PG dopé avec CuO était incorporé dans les hydrogels. Les profils XRD ont confirmé la formation d'une nouvelle particule qui correspond au profil du phosphate de calcium amorphe (ACP).

L'EPD a montré que le co-déposition de particules de PG dans les revêtements de collagène/CTS à température et pression ambiantes standard (1 kPa, 25 °C) était possible, et que l'ajout de collagène conduisait à la stabilisation stérique du PG en solution. PSA a montré que la suspension colloïdale de PG sédimentait avec le temps, et la taille moyenne des particules diminuant de 11,8 µm à 5,6 µm après avoir été laissée au repos pendant 15 minutes. Cependant, le rendement du dépôt à différents points de temps a montré un profil typique du dépôt à tension constante. L'augmentation de la concentration de collagène dans la solution de PG permettait d'obtenir un rendement de dépôt plus élevé, tandis que les solutions de collagène pur ont entraîné la formation des bulles d'hydrogène gazeux à la cathode. Les images SEM ont montré des particules de PG plus grandes déposées avec le collagène qu'avec le chitosan, et l'ATR FT-IR a montré une présence significative de phosphate qui augmente avec la

concentration de collagène. Le TGA a montré que la masse des particules de PG déposées augmente de 5-15% en poids avec le seul chitosan à 62-68% en poids avec le collagène.

Ce travail fournit une base pour optimiser davantage les propriétés des hydrogels incorporant des verres de phosphate pour l'ingénierie du tissu osseux. Les résultats obtenus montrent que le PG a la capacité de se former un matériau analogue à l'os dans un hydrogel *in vitro*, ainsi que de se co-déposer avec des biopolymères et de former des revêtements qui peuvent imiter le tissu osseux natif. L'utilisation du PG offre la possibilité de fabriquer des tissus osseux de remplacement ou des implants orthopédiques aux propriétés biologiques adaptées, et avec une bioactivité accrue, tout en minimisant le risque de rejet de la part de l'hôte.

Mots clés : biomatériaux; ingénierie tissulaire; collagène; chitosan; hydrogel; échafaudage; dépôt électrophorétique; minéralisation; hydroxyapatite; verre phosphate

Acknowledgements

I would like to acknowledge, first and foremost, my supervisor, Prof Federico Rosei. His support and supervision was invaluable to the work I was able to complete, without which I would not have been able to undertake this PhD. His professionalism, experience, and guidance were both critical in getting me to this point, and I could not have gotten here without him.

I am grateful for the help and support my NanoFemto LAB group members have given me. In particular, I would like to thank Dr. Gurpreet Singh Selopal for all his help. His expertise and guidance in crafting and carrying out experiments was invaluable. I consider myself lucky to have found myself among such a supportive and hardworking group of peers, who provide motivation and support to each other as we each work towards completing our studies.

I also am grateful for the support the institute staff has provided me during my work at INRS. Among the institute's staff, I would like to thank in particular Catalin Harnagea, Julie Gaudet, and Christophe Chabanier for the training they provided on various scientific equipment, and Hélène Sabourin, Tatiana Brahmi, Michelle Marcotte, and Sylvain Gingras for the administrative support they have provided while at INRS. The support they have shown me was critical in my being able to accomplish work.

I would like to express my deepest gratitude to Professor Fiorenzo Vetrone and Professor Jinyang Liang from INRS-EMT, Varennes. I am very grateful that, as the members of my PhD committee, they spent their time and effort reviewing my work in order to provide me with their valuable insight on how I might advance my PhD project. I am also grateful to the external examiners, Dr. Muthukumaran Packirisamy and Dr. Fabio Variola for their valuable comments and suggestions.

Last but not least, I would like to express my heartfelt gratitude to my family for their unending support and encouragement as I worked my way towards achieving my doctorate. My parents, for their unconditional love, were the foundation that I have built all my success upon. For everything they have sacrificed for me, they will always have my love and gratitude.

Table of Contents

Abstract	vii
Résumé.....	xi
Acknowledgements.....	xv
Table of Contents	xvii
List of Figures	xxi
List of Tables	xxvii
List of Abbreviations	xxix
1. Introduction	2
2. Background and motivation	4
2.1. The Skeletal system.....	4
2.1.1. Collagen	5
2.1.2. Non-collagenous proteins.....	7
2.1.3. Hydroxyapatite	8
2.2. Bone development.....	9
2.2.1. Mineralization in bone development.....	10
2.2.2. Mineralized bone nanostructure	10
2.3. Conventional bone grafting techniques	11
2.3.1. Advantages and disadvantages of conventional bone grafts	12
2.4. Orthopaedic implants.....	12
2.5. Bone tissue engineering	13
2.5.1. Requirements for biomaterials in tissue engineering	14

2.6. Materials for scaffold construction	14
2.6.1. Biocompatibility of collagen	14
2.6.2. Biocompatibility of chitosan	16
2.6.3. CTS-collagen hydrogels	19
2.6.4. Bioactive additives	19
2.7. Scaffold construction.....	26
2.7.1. Sol-gel method	26
2.7.2. Electrophoretic deposition.....	27
2.7.3. Bioglass fabrication.....	37
3. Research outline and organisation.....	38
3.1. Research outline.....	38
3.2. Aim and research hypothesis	38
3.3. Research objectives.....	39
3.4. Thesis organization.....	39
4. Methodology.....	42
4.1. Sample preparation	42
4.1.1. Silk fibroin polypeptides preparation	42
4.1.2. Fabrication of CuO-doped phosphate glass.....	42
4.1.3. Preparation of simulated body fluid	43
4.1.4. Plastically compressed dense collagen hydrogels	43
4.1.5. Coatings preparation.....	44
4.1.6. Electrophoretic deposition.....	45
4.2. Mineralization of hydroxyapatite within additive-incorporated hydrogels	45
4.3. Liquid chromatography–mass spectrometry	46
4.4. Particle size analysis	46

4.5.	Fourier transform infrared spectroscopy	46
4.6.	X-Ray diffraction	47
4.7.	Scanning electron microscopy	48
4.7.1.	Backscattered Electrons and Electron Diffraction Spectroscopy	48
4.8.	Quartz Crystal Microbalance	48
4.9.	Electrophoretic mobility and zeta potential	49
4.10.	Electrical Impedance Spectroscopy	49
4.11.	Thermogravimetric Analysis	50
4.12.	Statistical analysis.....	50
5.	Materials characterization.....	52
5.1.	Silk Fibroin-derive polypeptides	52
5.2.	Collagen and CTS	55
5.2.1.	Electrophoretic mobility and zeta potential measurements.....	55
5.2.2.	ATR-FTIR Spectroscopy of collagen-CTS Hydrogels.....	56
5.3.	Copper-doped phosphate glasses.....	57
5.3.1.	Scanning Electron Microscopy of phosphate glasses.....	57
5.3.2.	XRD of phosphate glasses.....	58
5.3.3.	ATR-FTIR of phosphate glasses.....	59
5.3.4.	Particle Size Analysis before and after sedimentation	60
6.	Silk Fibroin-enhanced hydroxyapatite mineralization <i>in vitro</i>	61
6.1.	XRD analysis of silk fibroin-derived polypeptides <i>in vitro</i>	61
6.2.	Scanning electron images of DC hydrogels post-immersion in SBF	62
6.3.	ATR-FTIR and XRD analysis of DC/FDPs hydrogels.....	63

6.4. Mass analysis of DC/FDPs hydrogels.....	67
7. Copper-doped Phosphate glass additives for hydroxyapatite mineralization	70
7.1. Analysis of PG and DC hydrogels in SBF.....	70
7.2. Scanning Electron Microscopy and Electron Diffraction Spectroscopy.....	71
7.3. Elemental Analysis of Hydrogels Over Time.....	76
7.4. ATR-FTIR Spectroscopy copper-doped PG.....	83
8. Electrophoretic deposition of composited glass-polymers coatings.....	88
8.1. Electrical characterizations of co-polymer films	88
8.2. Structural characterizations of EPD deposited CuO-doped PG film	89
8.3. Adhesion tests of co-polymer films.....	93
8.4. Chemical characterization of EPD deposited CuO-doped PG films.....	94
8.5. Deposition yield of EPD composite films	95
9. Conclusions and future perspectives	100
9.1. Conclusions.....	100
9.2. Future perspectives.....	101
References	102
Appendix I: Sommaire récapitulatif.....	126
Appendix II: Supporting figures.....	146

List of Figures

Figure 1.1: Estimated incidence of fracture as a function of A) bone mass and B) age [5].	2
Figure 1.2: A) Population of Canada by age group, 2001-2016 and B) Number of persons aged 80 and over, observed (1923 to 2013) and projected (2023 to 2063) according to the low-growth (L), medium-growth (M1) and high-growth (H) scenario.....	3
Figure 2.1: The cellular, organic, and inorganic components of bone [21]	5
Figure 2.2: Schematic of a) collagen-composed triple helix, and b) collagen-forming microfibrils composed of 200 nm segments with 67 nm gaps and overlaps [19].....	7
Figure 2.3: A) Interaction between proteoglycans (pg) and collagen fibrils (F) and B) collagen molecules (M) forming a staggered structure within a fibril. [36].....	8
Figure 2.4: Bone-remodelling cycle [48]	9
Figure 2.5: A) Hierarchical schematic of collagen [60] (Copyright (2006) National Academy of Sciences, U.S.A.), B) mineralization of HA within collagen fibrils at gaps [58] and C) Transmission Electron Microscopy (TEM) of a mineralized collagen fibril [59]	11
Figure 2.6: X-ray microtomography images of (a) bioactive glass foam scaffold and (b) trabecular bone from a human femur proximal to the knee [73].	13
Figure 2.7: Layout of processing steps for various forms of extracellular matrix scaffolds [78]..	15
Figure 2.8: Schematic of a plastically compressing a collagen gel [83].....	16
Figure 2.9: Chemical structures of the repeating units of idealised chitin and CTS [98]	17
Figure 2.10: FT-IR spectra of collagen, CTS and collagen- CTS scaffolds [100].....	18
Figure 2.11: a,b) Images of the domestic <i>Bombyx mori</i> silkworm and the nonmulberry <i>Antheraea pernyi</i> silkworm, and their cocoons. c,d) SEM images of the natural <i>B. mori</i> silk fibers and <i>A. pernyi</i> silk fibers (Insets show the corresponding degummed silk fibers). e) Schematic illustration of the structure of a silk fiber. [111]	20
Figure 2.12: a) SF extracted from <i>Bombyx mori</i> cocoons and b) analyzed through optical microscopy; c) SF fiber is composed of hydrophobic crystalline polypeptides linked by hydrophilic amorphous amino-acidic sequences; d) α -chymotrypsin can be used to selectively separate C _p and C _s ; e) SEM images of C _p and C _s fragments [80]......	20
Figure 2.13: DC-C _p and DC-C _s hydrogels immersed in SBF analysed via a) ATR-FTIR, b) TGA and c) XRD [80].....	21
Figure 2.14: Structure of a glass network [128].....	22

Figure 2.15: Weight loss vs time for different CaO mol% [138].....	24
Figure 2.16: Confocal Laser Scanning Microscopy images showing cells assemble into a capillary-like network over 5 days of culture in collagen gels [147].....	24
Figure 2.17: The possible tetrahedral sites that occur in phosphate glasses [150].....	25
Figure 2.18: Structure of phosphate anions a) PO_4^{3-} , b) $\text{P}_2\text{O}_7^{4-}$, c) $\text{P}_3\text{O}_9^{3-}$ and d) $\text{P}_3\text{O}_{10}^{5-}$. Adapted from [138]	25
Figure 2.19: Release rate of a) PO_4^{3-} , b) $\text{P}_2\text{O}_7^{4-}$, c) $\text{P}_3\text{O}_9^{3-}$ and d) $\text{P}_3\text{O}_{10}^{5-}$ anions. [138].....	26
Figure 2.20: Schematic illustration of (a) cathodic and (b) anodic electrophoretic deposition process [157]	28
Figure 2.21: Weight of deposited HA2 versus applied voltage for different deposition durations: (a) 30 s; and (b) 120 s [164].	28
Figure 2.22: Weight of deposited HA2 versus deposition time at different applied voltages: (a) 10 V; (b) 50 V; (c) 100 V; (d) 200 V [164].....	29
Figure 2.23: Evolution of the potential in an electrophoretic deposition cell.	30
Figure 2.24: Electrical circuit of an EPD cell [165].....	31
Figure 2.25: Equivalent circuit of electrophoretic deposition [168]	32
Figure 2.26: Suspension conductivity as a function of (a) remaining powder concentration in suspension during EPD and (b) deposition time for different powders in acetone/n-butylamine [165].	33
Figure 2.27: Representation of the electrostatic, steric and electrosteric stabilizing mechanisms of aqueous alumina suspension. (EDL = electric double layer) [176]	36
Figure 4.1: Schematic of method used for plastic compression.....	44
Figure 5.1: A) ATR-FTIR spectra showing secondary structures and B) XRD patterns showing amorphous/crystalline structure for as-made i) C_s and ii) C_p . Arrows in the XRD patterns indicate crystalline regions and amorphous regions	52
Figure 5.2: SEM images of A) C_s and B) C_p particles	53
Figure 5.3: Size distribution of i) C_p and ii) C_s particles.....	53
Figure 5.4: Zeta potential measurements of collagen, CTS, and collagen:CTS particles with different relative ratio of collagen and CTS in solution (SD for n=10, p<0.05).....	56
Figure 5.5: ATR-FTIR spectra for collagen a) collagen b) 1:1 collagen-CTS, c) 1:2 collagen-CTS and d) CTS	57

Figure 5.6: SEM images of CuO-doped phosphate glass particles with different doping of CuO: 0% (left); 5% (middle); 10% (right).....	58
Figure 5.7: XRD patterns for a) 0 mol% b) 5 mol% and c) 10 mol% CuO-doped PG.....	58
Figure 5.8: ATR-FTIR spectra for PG incorporating a) 0 mol% b) 5 mol% and c) 10 mol% CuO	59
Figure 5.9: Particle size analysis of CuO-doped PG immediately after (black color line/circle) and 15 minutes after ultrasonication (red color line/circle): A) 0 mol% B) 5 mol% and C) 10 mol%; D) Variation of Diameter with CuO doping (mol%).....	60
Figure 6.1: XRD patterns of i) HA (ICDD file 00-009-0432) and polypeptides ii) C _s and iii) C _p immersed in SBF	62
Figure 6.2: SEM of Plastically compressed A) DC, B) 1:10 DC-C _s and C) 1:10 DC-C _p hydrogels immersed in SBF for 7 days (scale bar is 10 μ m, arrows indicate particles)	63
Figure 6.3: ATR-FTIR Spectra for A) DC, B) 1:10 DC-C _s and C) 1:10 DC-C _p , gels immersed in SBF at day i) 0, ii) 3, c) 7, iii) 10 and iv) 14.	63
Figure 6.4: Ratio of A) v3 PO ₄ ³⁻ and B) v3 CO ₃ ²⁻ bands to amide I bands from ATR-FTIR spectra of DC gels containing no additives, C _s and C _p (at a 1:10 ratio to collagen) immersed in SBF (SD, n=4, p<0.05).....	65
Figure 6.5. XRD pattern for A) DC, B) 1:10 DC-C _s and C) 1:10 DC-C _p hydrogels immersed in SBF at days i) 3, ii) 7, iii) 14 (● – HA corresponding to ICDD file 00-009-0432, ■ – PE corresponding to ICDD file 00-060-1505).....	66
Figure 6.6: ATR-FTIR for A) 1:1 DC-C _s , B) 1:1 DC-C _p , C) 1:2 DC-C _s and D) 1:2 DC-C _p , i) as-made and immersed in SBF for ii) 3 and iii) 7 days	67
Figure 6.7: Mass of DC, DC-C _s and DC-C _p hydrogels immersed in SBF for A) 0 (as-made), B) 3 and C) 7 days (* - statistically significant, one-way ANOVA, SD, n=4, p < 0.05).....	69
Figure 7.1: Mass of A) PG immersed in SBF for 1, 3 and 5 days and B) collagen gels with 50 wt% PG, immersed in SBF for 3 and 7 days (n = 3, p < 0.05)	70
Figure 7.2: XRD for a) 0 mol% b) 5 mol% and c) 10 mol% CuO PG immersed in SBF.....	71
Figure 7.3: SEM images of 0, 5 and 10 mol% CuO-doped PG immersed in SBF 5 days	72
Figure 7.4: SEM images of 0, 5 and 10 mol% CuO-doped PG immersed in SBF 1 day.....	72

Figure 7.5: SEM of as-made hydrogels with a 1:1 collagen-CTS ratio containing 50 wt% A) 0, B) 5 and C) 10% CuO-doped PG particles, as made and immersed in H ₂ O for 1 and 3 days (scale bars are 100 μm)	73
Figure 7.6: SEM-BSE of as-made hydrogels with a 1:1 collagen-CTS ratio containing 50 wt% A) 0, B) 5 and C) 10% CuO-doped PG particles, as made and immersed in H ₂ O for 1 and 3 days (scale bars are 100 μm)	74
Figure 7.7: SEM of as-made hydrogels with a 1:2 collagen-CTS ratio containing 50 wt% A) 0, B) 5 and C) 10% CuO-doped PG particles, as-made and immersed in H ₂ O for 1 and 3 days (scale bars are 100 μm)	75
Figure 7.8: SEM-BSE of hydrogels with a 1:2 collagen-CTS ratio containing 50 wt% A) 0, B) 5 and C) 10% CuO-doped PG particles, as-made and immersed in H ₂ O for 1 and 3 days (scale bars are 100 μm).....	76
Figure 7.9: EDS of 1:1 collagen-CTS gels containing 50 wt% 0, 5 and 10 mol% CuO-doped PG particles, immersed in H ₂ O for 0, 1 and 3 days.....	77
Figure 7.10: Elemental composition of 1:1 collagen-CTS gels containing 50 wt% A) 0, B) 5 and C) 10% CuO-doped PG particles, immersed in H ₂ O for 0, 1 and 3 days	78
Figure 7.11: EDS of 1:2 collagen-CTS gels containing 50 wt% 0, 5 and 10 mol% CuO-doped PG particles, immersed in H ₂ O for 0, 1 and 3 days.....	79
Figure 7.12: Elemental composition of 1:2 collagen-CTS gels containing 50 wt% A) 0, B) 5 and C) 10% CuO-doped PG particles, immersed in H ₂ O for 0, 1 and 3 days	80
Figure 7.13: SEM images A) 0% B) 5% and C) 10% CuO-doped PG DC hydrogels immersed in SBF for 7 days.....	81
Figure 7.14: Elemental analysis of particles in collagen gels with A) 0 mol%, B) 5 mol% and C) 10 mol% CuO-doped PG immersed in SBF for 7 days.....	82
Figure 7.15: ATR-FTIR for 0%, 5% and 10% CuO-doped PG, as-made (D0) and immersed in SBF 1, 3 and 5 days (D1, D3 and D5, respectively)	83
Figure 7.16: Hydrogels with a 1:1 collagen-CTS ratio containing 50 wt% CuO-doped PG particles (0, 5 and 10 mol%), immersed in H ₂ O for A) 0, B) 1 and C) 3 days	84
Figure 7.17: Hydrogels with a 1:2 collagen-CTS ratio containing 50 wt% CuO-doped PG particles (0, 5 and 10 mol%), immersed in H ₂ O for A) 0, B) 1 and C) 3 days	85

Figure 7.18: ATR-FTIR for A) DC and B) 0% C) 5% and D) 10% CuO-PG DC hydrogels a) as-made (black) and 3 (red) and 7 days (blue) immersed in SBF.....	86
Figure 8.1: EIS measurements of Current produced at 5-30V for EPD of collagen/CTS solutions containing collagen: A) 0 wt.%; B) 33 wt.%; C) 50 wt.%; D) 66 wt.%; E) 100 wt.% F) shows the calculated resistance of films for various collagen (wt.%) contents G) Schematic of EPD cell (SD for n=4, p<0.05)	89
Figure 8.2: Images for EPD of A) 0.5 g/L CTS B) 0.33 g/L CTS, 0.17 g/L collagen, C) 0.25 g/L CTS, 0.25 g/L collagen, E) 0.17 g/L CTS, 0.33 g/L collagen and F) 0.5 g/L collagen films co-deposited with 0.5 g/L 0% CuO-doped phosphate glass (arrows: white = bubbles, grey = spalling, black = crack)	90
Figure 8.3: SEM images of EPD of 1 g/L (a) 0% (b) 5% and (c) 10% CuO-doped PG and 0.5 g/L CTS co-deposited with 0.5 g/L (d) 0% (e) 5% and (f) 10% CuO-doped PG. Inset of each figure shows the high resolution SEM images of the corresponding samples.....	91
Figure 8.4: EDS map of CTS-PG films of 0, 5 and 10% CuO-doped PG (scale bars are 100 μ m)	92
Figure 8.5: SEM images for EPD of A) 0.5 g/L CTS B) 0.33 g/L CTS, 0.17 g/L collagen and C) 0.25 CTS, 0.25 g/L collagen, D) 0.17 g/L col. 0.33 g/L CTS, E) 0.5 g/L collagen co-deposited with 0.5 g/L 0, 5 and 10 mol% CuO-doped phosphate glass.....	93
Figure 8.6: Adhesion test carried out to ASTM D3359 protocol for A) blended polymer layer, B) pure CTS layer+blended polymer layer and c) pure col layer+blended polymer layer (Note: pure col film was completely removed).	94
Figure 8.7: ATR-FTIR spectra of collagen, CTS and collagen/CTS films incorporating A) no PG and B) 0% c) 5% and D) 10% CuO-doped PG in (a) 0.5 g/L collagen, (b) 0.17 g/L CTS, 0.33 g/L collagen (c) 0.25 g/L CTS, 0.25 g/L collagen, (e) 0.33 g/L CTS, 0.17 g/L collagen and (e) 0.5 g/L CTS solutions	95
Figure 8.8: Mass deposited for EPD of collagen, collagen/CTS and CTS solutions compared to polymer co-deposited with PG (n=3, p< 0.05).....	96
Figure 8.9: TGA for films fabricated by EPD of collagen, collagen/CTS and CTS solutions co-deposited with CuO-doped PG: (a) 0 mol%; (b) 5 mol%; (c) 10 mol% and (d) their weight percent.	97

Figure 8.10: QCM measurements of mass deposited vs time for the EPD in A) collagen and B)
CTS co-deposited with phosphate glass.....98

List of Tables

Table 2.1: Classes of collagen and different types [22]	5
Table 2.2: Types of fibrillar collagen and their locations in the body [22], [24], [25]	6
Table 2.3: Amino Acid Composition of Silk Fibroin Derived Polypeptides [118]	21
Table 2.4: Composition of different bioglasses (mol%)	23
Table 2.5: Classification of Hydrogels [152]	26
Table 4.1: CuO-doped phosphate glass compositions (mol%)	42
Table 4.2: Collagen/CTS-PG solutions used for EPD	45
Table 5.1. Comparison of Amino Acid Composition for Fibroin-derived Polypeptides, C _p and C _s , obtained from LCMS (Right – from literature, left – as-made)	54
Table 5.2. Comparison of charged amino acids (as percentage of total) within FDPs (Right – from literature, left – as-made).....	55
Table 5.3: Diameter of particles before and after sedimentation	61
Table 6.1. Mass of as-made hydrogels at compared to the theoretical values	68
Table 8.1: Adhesion rating of EPD collagen/CTS and multilayer collagen/CTS films to SS substrate according to ASTM D3359 standards (0B – lowest, 5B – highest).....	94

List of Abbreviations

<i>3D</i>	Three Dimensional
<i>ANOVA</i>	Analysis of Variance
<i>ATR-FTIR</i>	Attenuated Total Reflectance Fourier Transform Infrared
<i>BD</i>	Bovine Dermis
<i>BMU</i>	Basic Multicellular Unit
<i>BO</i>	Binding Oxygen
<i>BSE</i>	Backscattered Electrons
<i>BSP</i>	Bone Sialoprotein
<i>BTE</i>	Bone Tissue Engineering
<i>CFD</i>	Collagen Fibril Density
<i>CIHR</i>	Canadian Institutes of Health Research
<i>col</i>	Collagen
<i>C_p</i>	hydrophobic/non-soluble polypeptides of silk fibroin
<i>C_s</i>	hydrophilic/soluble polypeptides of silk fibroin
<i>CTS</i>	Chitosan
<i>DC</i>	Dense Collagen
<i>DC-C_p</i>	Dense Collagen hydrogels containing C _p
<i>DC-C_s</i>	Dense Collagen hydrogels containing C _s
<i>DMEM</i>	Dulbecco's Modified Eagle Medium

<i>ECM</i>	Extracellular Matrix
<i>EDL</i>	Electric Double Layer
<i>EDS</i>	Electron Diffraction Spectroscopy
<i>EIS</i>	Electro Impedance Spectroscopy
<i>EM</i>	Electron Microscopy
<i>EPD</i>	Electrophoretic Deposition
<i>FDP</i>	Silk Fibroin-derived Polypeptide
<i>GAG</i>	Glycosaminoglycan
<i>HA</i>	Hydroxyapatite
<i>HHC</i>	Highly Hydrated Collagen
<i>HMDS</i>	1,1,1,3,3,3-hexamethyldisilazane
<i>IC</i>	Ion Chromatography
<i>LC-MS</i>	Liquid Chromatography–Mass Spectrometry
<i>NBO</i>	Non-Binding Oxygen
<i>NCP</i>	Non-Collagenous Protein
<i>OC</i>	Osteocalcin
<i>ON</i>	Osteonectin
<i>OPN</i>	Osteopontin
<i>PC</i>	Plastic Compression
<i>PG</i>	Phosphate-based glasses
<i>PSA</i>	Particle Size Analysis

<i>QCM</i>	Quartz Crystal Microbalance
<i>SBF</i>	Simulated Body Fluid
<i>SE</i>	Secondary Electrons
<i>SEM</i>	Scanning Electron Microscopy
<i>SF</i>	Silk Fibroin
T_G	Glass Transition Temperature
<i>TGA</i>	Thermogravimetric Analysis
<i>XRD</i>	X-Ray Diffraction

1. Introduction

Musculoskeletal diseases (e.g. osteoporosis) are a frequently occurring problem that impacts the health and quality of life of many people as they age. In recent years, more and more people suffer from bone-related diseases [1] such as bone fractures, osteoporosis, scoliosis and other musculoskeletal problems [2] as a result of an increasingly elderly population suffering from age-related bone mass loss, which leads to higher incidences of bone fracture [3], [4] (see Figure 1.1). Often, this requires invasive surgery to correct, which can lead the patient with residual trauma and affect their quality of life.

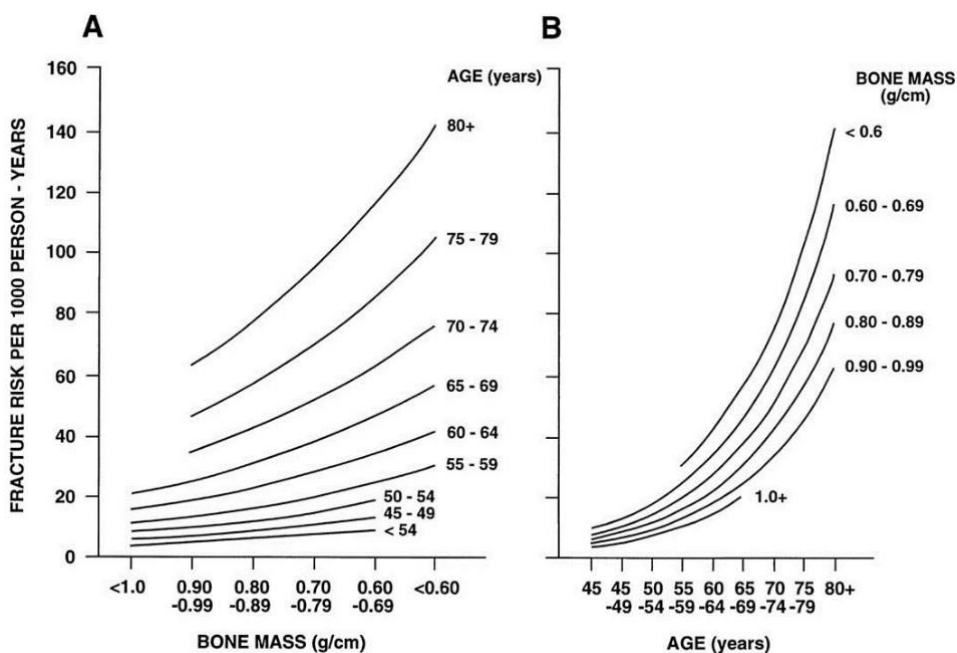


Figure 1.1: Estimated incidence of fracture as a function of A) bone mass and B) age [5].

In 2017, Statistics Canada released a *Census in Brief* based on the 2016 census data. It was found that while life expectancy in Canada is about 80 and 84 years among men and women, respectively, more and more Canadians are living beyond 85 years [6]. The report stated that:

Given the reality of population aging in Canada, knowing more about the older population is important, notably because of increased needs for health care and other services. The population aged 85 and older contribute in many ways to society — for example, by sharing their wisdom, acting as role models and fostering family relationships across generations. At the same time, a significant share of the population aged 85 and older lives with activity limitations and has particular needs related to health and community care, housing, income security, and transportation [6].

With the increasingly ageing population who are susceptible to bone loss [3], [4], bone diseases such

as osteoporosis will cause an increase in surgeries to replace damaged bone, from simple fractures to bone grafts to total hip and joint replacements. As a result, excessive bone loss is a major public health concern among the elderly [7]. An analysis of the population of Canada based on past census (2001–2016) [8]–[11] shows that the population of Canada increasingly elderly (see Figure 1.2A), with current projections indicating that the elderly population (people 80 years or older) will continue to rise in the coming years [12] (see Figure 1.2B).

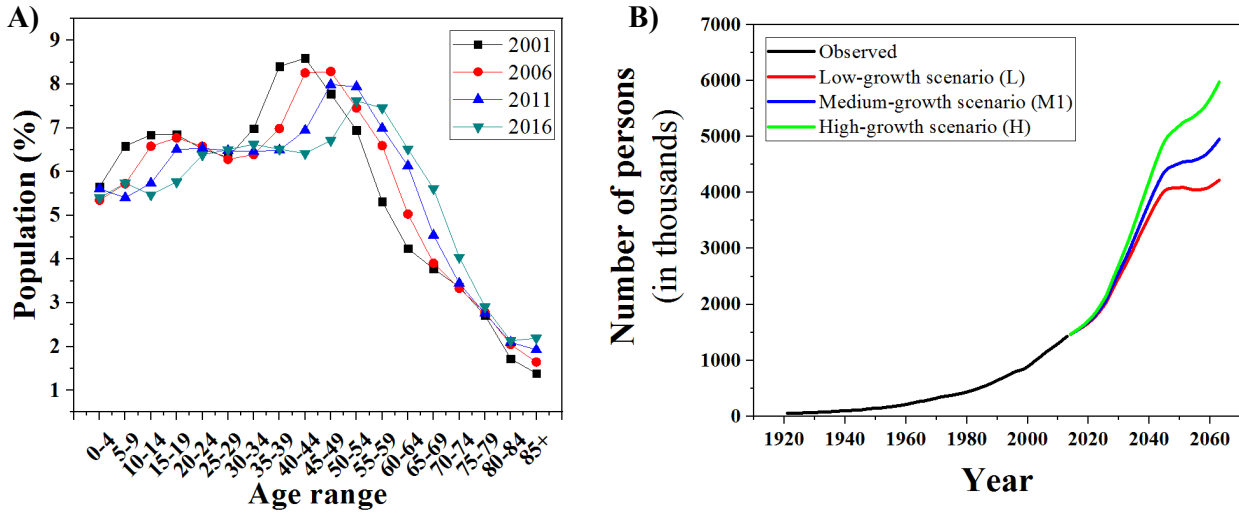


Figure 1.2: A) Population of Canada by age group, 2001-2016 and **B)** Number of persons aged 80 and over, observed (1923 to 2013) and projected (2023 to 2063) according to the low-growth (L), medium-growth (M1) and high-growth (H) scenario.

With disability due to musculoskeletal disorders estimated to have increased on average by 45% between 1990 to 2010, compared to 33% for all other diseases [13], a more robust solution to traditional surgery is sorely needed. For example, in Canada, a 2005 study found that 30,000 hip fractures occur yearly [14]; by 2041 it is expected to reach 88,124 cases [15]. This increase has economic effects as well; the current \$650 million annual cost of hip fracture in Canada is expected to rise to \$2.4 billion by 2041 [16]. Biodegradable devices, both temporary and permanent, are needed to address musculoskeletal diseases as occurrences of these grow more frequent [2]. Solutions, both in terms of new techniques and novel materials, are needed, both to meet an increasing demand for treating musculoskeletal disorders and to contain the resulting increasing cost, and to improve the quality of life of the patients.

2. Background and motivation

2.1. The Skeletal system

Bone is an organic/inorganic composite that forms a hard, dense tissue that makes up the skeletal system. The skeletal system, essentially the frame of the body, provides support and protection for the internal organs from outside forces [17], [18]. As such, it performs the following critical functions [17]:

- Supports the body.
- Facilitates movement by serving as sites for muscle attachment and acting (mechanically) as levers and fulcrums.
- Protects internal organs (e.g. the brain, heart, lungs, etc.) by covering or surrounding them.
- Produces blood cells within the bone marrow.
- Stores minerals (e.g. calcium ions) into bone tissue, which can be released to maintain normal physiological levels.

To meet these functions, it is important that the skeleton does not fracture or otherwise fail when repeatedly exposed to strain during everyday activities; cyclic loading can lead to fatigue in bone, causing microscopic damage that accumulates over time [18]. For structural purposes, it is the interaction of the inorganic (mineral) phase and organic phase at the nano- or micro-level that provides the inherent properties of the system. The inorganic phase provides stiffness or strength whereas the organic phase is responsible for the ductility of the material, and the combination of the two provides a high energy absorption prior to prevent failure [19].

Bone can be broadly divided into two categories; the Extracellular Matrix (ECM), within which are the organic (the osteoid tissue) and inorganic (HA) components of bone, and the Basic Multicellular Unit (BMU), the cells responsible for the dissolution and rebuilding of damaged bone tissue to maintain bone structural integrity [20], [21] (see Figure 2.1). The ECM can be further divided into a network of proteins and carbohydrates that provides structural and biological support for cells. The osteoid tissue of the ECM is composed of four major components [21]:

- collagen
- non-collagenous proteins (NCPs)
- hyaluronan
- proteoglycans

Among these components, collagen is particularly important in the osteoid structure of the ECM itself

as it provides the majority of the “scaffold” of the ECM.

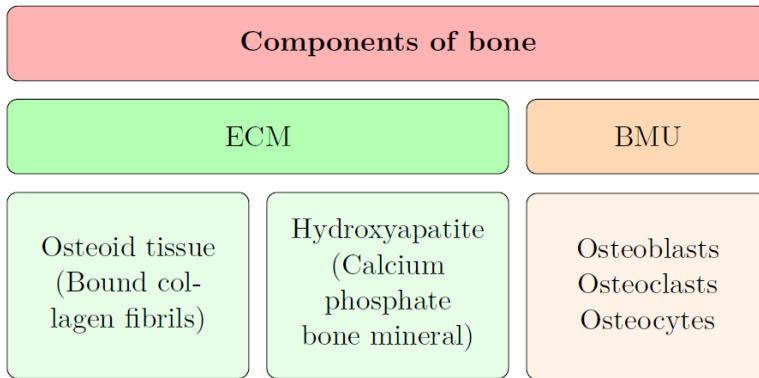


Figure 2.1: The cellular, organic, and inorganic components of bone [21]

2.1.1. Collagen

The collagen molecule is the primary structural element of tissues such as bone, skin and tendon [22], [23]. It is the basic structural material for both soft and hard tissues, and is present in many different organs where it provides structural integrity. Collagen fibers serve as ideal scaffolds, forming the ECM for many structures throughout the body. As a result, many disabling conditions result from disruptions in the nature and organization of collagen (e.g. heart-valve lesions, osteoarthritis, rheumatoid arthritis, osteogenesis imperfecta, etc.) [23], [24]. Collagen fibers are responsible for the functional integrity of bone, tendon and skin, as well as blood vessels and many other organs, and in order to fulfill a wide range of roles within the body come in many different classes and types (see Table 2.1) [22], [23].

Table 2.1: Classes of collagen and different types [22]

Class	Types of collagen
Fibrillar collagens	I, II, III, V, XI, XXIV and XXVII
Basement membrane collagens	IV, IX, XII, XIV, XVI, XIX, XX and XXI
FACIT	IX, XII, XIV, XVI, XIX, XX and XXI,
Short chain collagens	VIII and X
Anchoring fibril collagen	VII
Multiplexins	XV and XVIII
MACIT	XIII, XVIII, XXIII and XXV
Other	VI

Among these different types of collagen, fibrillar collagens are the most abundant and are found in a wide variety of sites in the body (see Table 2.2) [22], [24], [25], as they provide tensile strength to

connective tissues [26], [27].

Table 2.2: Types of fibrillar collagen and their locations in the body [22], [24], [25]

Types	Locations
Type I	Bone, skin, dentin, cornea, blood vessels, fibrocartilage and tendon
Type II	Cartilaginous tissues
Type III	Skin, ligaments, blood vessels and internal organs s (lungs, liver, spleen, etc.)
Type IV	Basement membrane in various tissues
Type V	Blood vessel wall, synovium, corneal stoma, tendon, lung, bone, cartilage and skeletal muscle
Type XI	Cartilage and vitreous body
Type XIII	Epidermis, hair follicle, endomysium, intestine, chondrocytes, lungs and liver

The common feature of all different type of collagen is the high content of glycine, proline, and hydroxyproline amino acids, which create the triple helical domain with the repeating amino acid sequence Gly-Pro-X (X can be any amino acid) in the primary structure [22], [28]. All collagen molecules take the form of a triple-helix 300 nm in length, and form fibrils with other collagen molecules, creating a structure that has “gaps” that are spaced approximately 67 nm apart due to the staggering of individual collagen molecules (see Figure 2.2) [19].

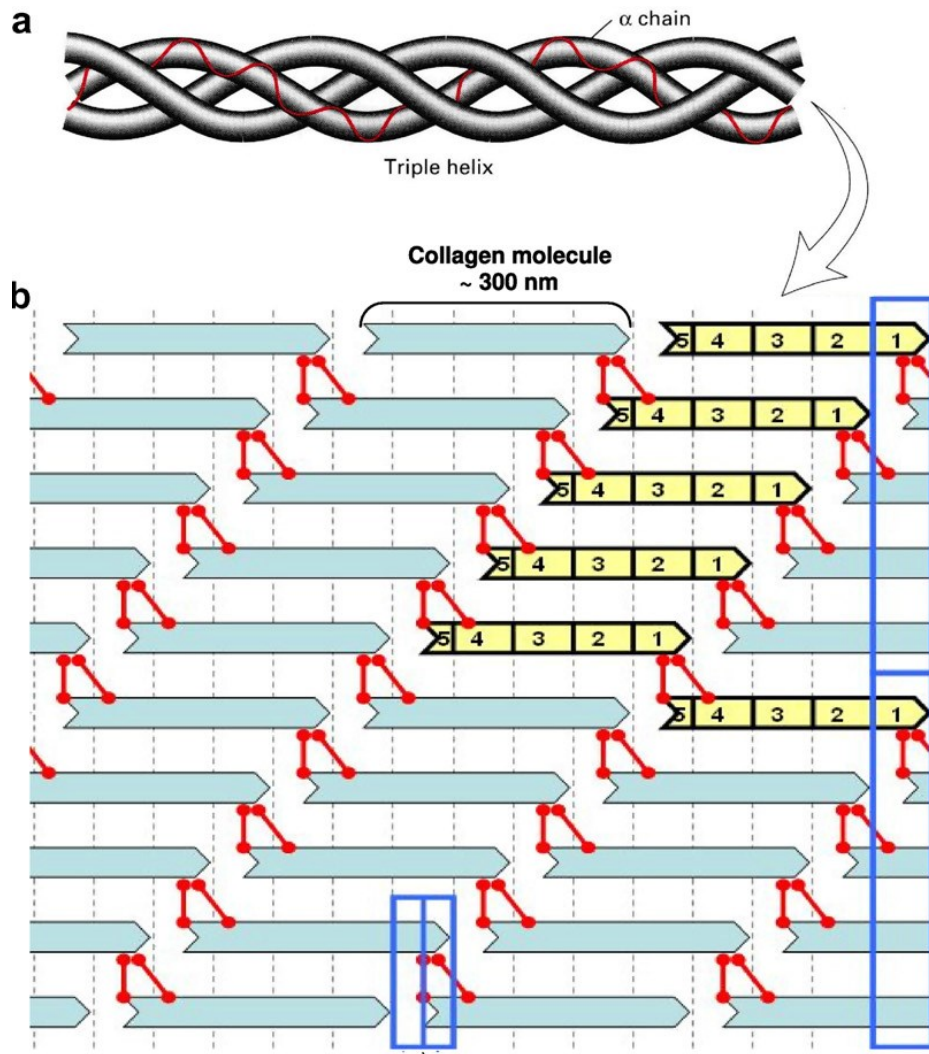


Figure 2.2: Schematic of a) collagen-composed triple helix, and b) collagen-forming microfibrils composed of 200 nm segments with 67 nm gaps and overlaps [19]

2.1.2. Non-collagenous proteins

Other than collagen, non-collagenous proteins (NCP), which account for 10% of the organic matrix, play important roles in bone formation due to their affinity to collagen and HA [29]. For example, osteopontin, regulate the presence of Ca^{2+} , and thus the formation of mineralized tissue [30], [31], while osteonectin helps bind HA crystals to collagen [32].

Proteoglycan is a NCP in the body that is not specific to bone and carries a sulfated carbohydrate component, glycosaminoglycan (GAG). While there are many different forms of proteoglycans, there are only four main types of GAGs: heparin/heparin sulfate, chondroitin sulfate/dermatan sulfate,

keratan sulfate, and hyaluronan/hyaluronic acid. Each GAG is a polymer composed of a disaccharide, typically N-acetylglucosamine [33]–[35].

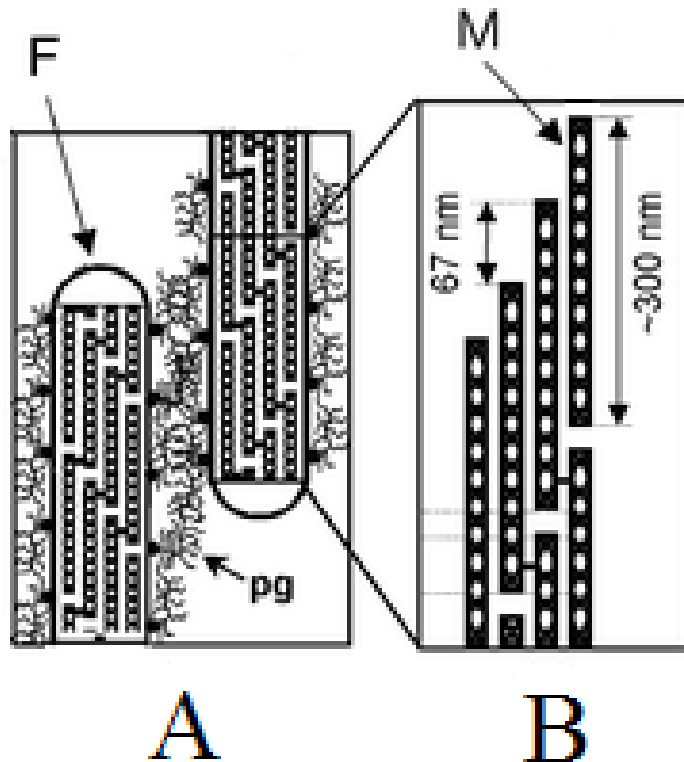


Figure 2.3: A) Interaction between proteoglycans (pg) and collagen fibrils (F) and B) collagen molecules (M) forming a staggered structure within a fibril. [36]

GAGs have a large hydrodynamic volume, and thus bind a large amount of water and occupy a large volume of space relative to their mass. Additionally, the high charge density of sulfated GAGs allows them to bind strongly to ligands of proteins such as collagen (see Figure 2.3). As proteoglycans contain a large amount of GAGs, they can act like glue, connecting collagen molecules to form larger structures [34], [35]. Additionally, proteoglycans serve as excellent lubricants and shock absorbers due to the water retention, great volume, and strength of GAGs [37].

2.1.3. Hydroxyapatite

The mineral phase of bone is a nanocrystalline ceramic, HA is a calcium apatite (a group of phosphate minerals) with the formula $\text{Ca}_{10}(\text{PO}_4)_6(\text{OH})_2$, and with a Ca/P ratio of 10:6 (1.67) [38]–[41]. As the major component of bone, HA is responsible for 70% of the weight of bone in the form of nano-sized (200 Å) crystals, and provides mechanical rigidity and load-bearing strength [42].

Due to the nature of HA, substitution often occurs, leading to non-stoichiometric apatites. The most common substitutions involve carbonate, fluoride and chloride substitutions for hydroxyl groups [43] or phosphate groups [44]. In bone, carbonated HA (CHA) is formed by CO_2^{3-} replacing PO_3^{4-} groups, creating an apatite with chemical formula $\text{Ca}_{10-x}[(\text{PO}_4)_{6-2x}(\text{CO}_3)_{2x}](\text{OH})_2$ [45].

2.2. Bone development

To prevent this damage from accumulating, the skeletal system requires a certain amount of “turnover” or renewal through the activity of osteoclasts (cells that resorb, or remove, bone tissue) and osteoblasts (cells that deposit, or form, new bone) – if renewal cannot repair damage faster than it occurs, damage accumulates in the bone, leading to fatigue induced fractures [18], [46]. This process is known as “remodeling,” and results in a significant change of bone shape, size and microstructure [18]. The entire process of remodeling can be expressed according to the following steps [18], [46], [47] (see Figure 2.4):

- 1) Activation (initiation of osteoclast formation, osteoclast-mediated resorption)
- 2) Reversal (osteoclast self-destruct)
- 3) Formation (osteoblast help lay down collagen and HA)
- 4) Resting (new bone and osteocytes formed)

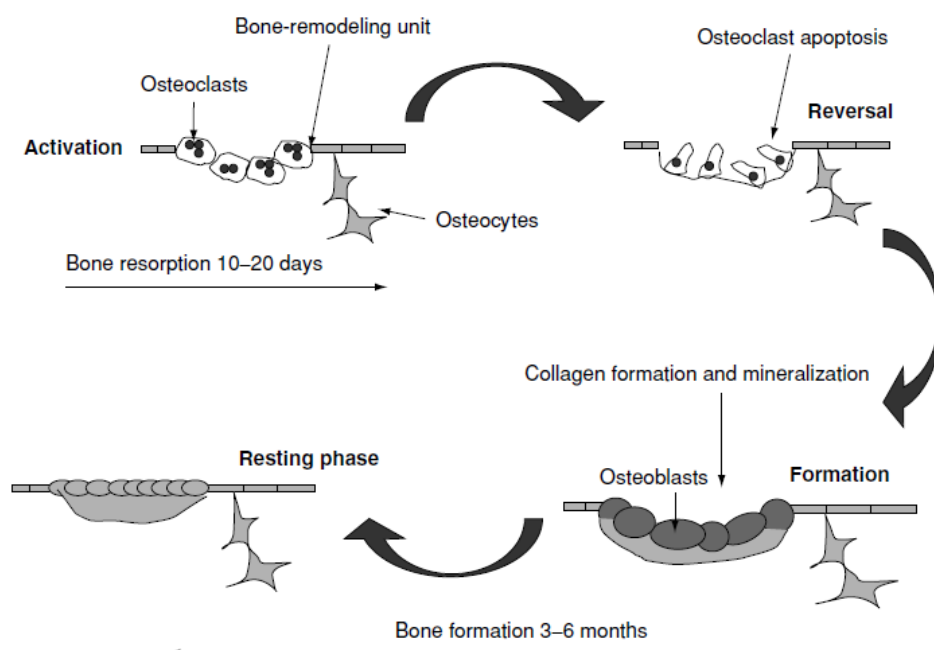


Figure 2.4: Bone-remodelling cycle [48]

2.2.1. Mineralization in bone development

The mineralization of bone due to the nucleation of HA crystals in the organic matrix of type I collagen has long been a subject of debate. While the nucleation of HA has long been associated with collagen fibrils, it is now generally accepted that collagen itself does not play a role in promoting or inhibiting nucleation. Instead, focus has shifted onto the role played by NCPs in HA formation [49].

Among the NCPs bone cells secrete, osteonectin (ON), osteopontin (OPN), osteocalcin (OC) and bone sialoprotein (BSP), all of which are acidic, have Ca- and HA-binding properties. In particular, these NCPs contain glutamic and aspartic amino acids, the former being found in NCPs that are specific to mineralized tissues [50]–[52].

The key to HA nucleation appears to lie in the ability to bind Ca^{2+} ions to negatively charged carboxylate. Clusters of Ca^{2+} and PO_4^{3-} ions can then be formed, reach a critical size, and act as nuclei for HA growth [50], [53], [54].

2.2.2. Mineralized bone nanostructure

As with all tissues in the body, bone is composed of a hierarchical structure that determines its properties. As mentioned above, bone is composed of an organic phase of collagen, an inorganic mineral phase of plate-like HA, and water. This composite structure of fibrillar collagen and HA is what gives bone its requisite strength, stiffness and high fracture toughness. [55]–[57].

The collagen fibers have gaps within the fiber (see Figure 2.5A), that allow for calcium phosphates to penetrate the fiber and allow for the nucleation of HA. As mineralization proceeds from interfibrillar to extrafibrillar and the collagen becomes mineralized (see Figure 2.5B,C) [58], [59]. The HA crystals continue to grow, eventually forming sheets, while the collagen framework maintains a specific orientation for their growth, leading to a stronger and stiffer composite structure [57], [59].

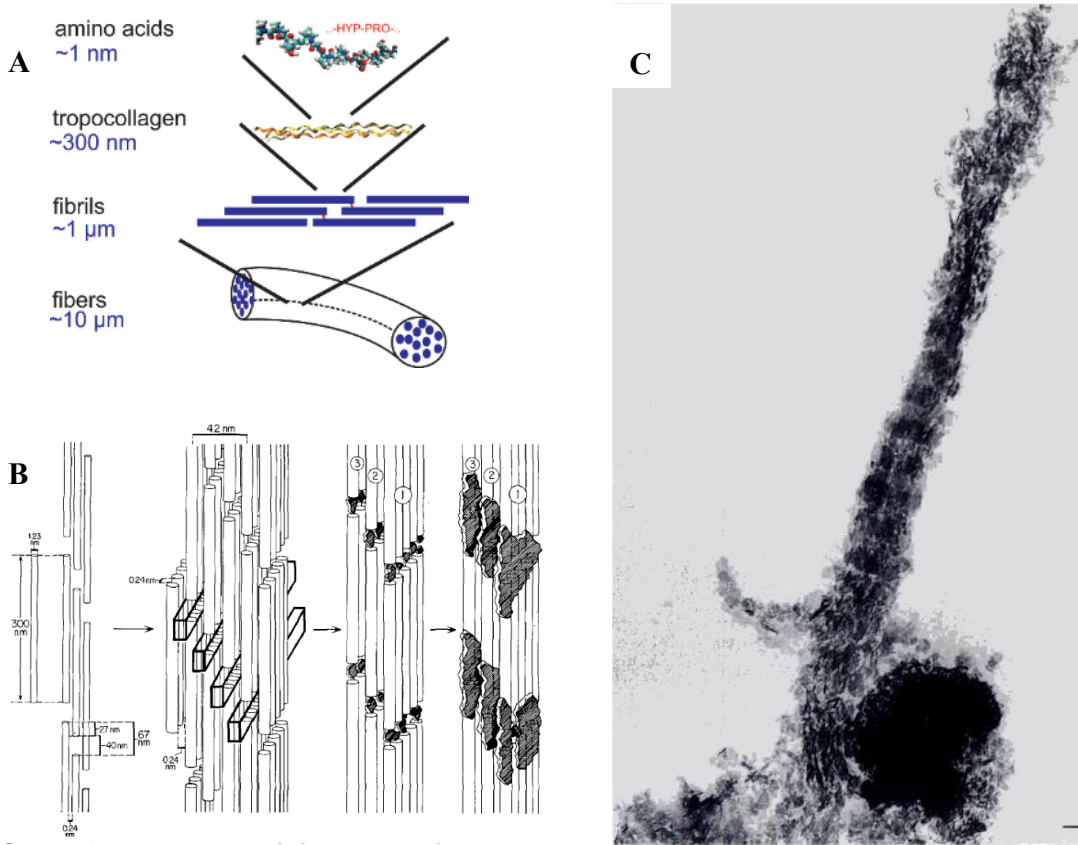


Figure 2.5: A) Hierarchical schematic of collagen [60] (Copyright (2006) National Academy of Sciences, U.S.A.), B) mineralization of HA within collagen fibrils at gaps [58] and C) Transmission Electron Microscopy (TEM) of a mineralized collagen fibril [59]

2.3. Conventional bone grafting techniques

In most instances, bone diseases are treated by a technique called “bone grafting,” which requires removing healthy bone from one part of the body and placing it elsewhere to help regenerate unhealthy bone [61]. Bone grafting is widely practiced; while the materials used may vary depending on what is required, in general the graft must include one or more of the following elements [62]:

- 1) An osteoconductive matrix/scaffold that supports bone regeneration,
- 2) Osteoinductive proteins that can stimulate the formation of osteoprogenitor cells,
- 3) Osteogenic cells (osteoblasts or osteoblast precursors) capable of forming bone.

Currently, there are three established methods that require harvesting bone tissue for implantation: autografts, allografts, and xenografts. An autograft is a transplant of bone tissue from one part of the

body to another within the same patient. An allograft is when bone tissue is transferred from two genetically different individuals of the same species, while a xenograft is a transplant between different species [62], [63].

2.3.1. Advantages and disadvantages of conventional bone grafts

Different bone grafting techniques offer their own advantages and disadvantages. Autografts, since they are taken from the body, are not viewed as a foreign substance by the immune system and are readily accepted by the body [63]–[65]. While this is the gold standard technique, certain problems are associated with it; they include donor site morbidity, limited donor bone supply, and inadequate resorption during healing [1], [56], [61], [66]. Furthermore, collecting bone tissue requires surgery and is only feasible if the patient has a large enough supply of bone [63]–[65], [67].

The use of allogeneic bone came into practice to avoid the problems associated with the use of autogenous bone [64]. The primary advantage is that it can be harvested from an external source, in different shapes and sizes, and does not create a bone defect or lead to donor-site morbidity [63], [65]. The problems associated with allografts include a lower osteogenic capacity (new bone formation occurs at a slower rate), a higher resorption rate, and a larger immunogenic response [63], [64].

Xenogeneic bone is rarely used as it is often rejected by the body. It is possible to reduce the body's antigenic response by deproteinization and defatting the xenograft, though this also removes the osteoinductive proteins that would normally elicit an osteogenic response [64].

2.4. Orthopaedic implants

Traditionally, implants for repairing damaged bone were made out of metals, ceramics or polymers. While these materials met the mechanical requirements for replacing bone, they lacked bioactive properties that were necessary to aid in the growth of new bone tissue [2], [68], [69]. Consequently, implants for the repair and regeneration of bone defects have continuously evolved: 1st generation bone implants were made of bioinert materials (stainless steel, Vanadium-Iron, or Cobalt-Chromium were initially used), second generation implants were made using bioactive and biodegradable materials, and 3rd generations implants were made with materials to elicit specific biological responses at the molecular level [2], [70].

2.5. Bone tissue engineering

Bone tissue engineering (BTE), which researches methods and materials of regenerating damaged bone, may provide alternatives to bone grafts and the problems associated with them [61], [66].

Though in the past "biointer" (i.e., they had no effect on the body but were not rejected as a foreign substance) materials were chosen for implantation, materials engineers are now investigating systems that can play a more active role in healing the body. Thus, materials are chosen because they are "bioactive," in that they can interact with the body to promote regeneration. In the case of bone, materials are chosen based on whether they are osteoinductive (promote differentiation of progenitor cells into osteoblasts), osteoconductive (support the formation of new bone tissue), and capable of osseointegration (integrate into surrounding bone). The ideal material is then one that will promote bone growth then eventually resorb or naturally degrade over time, leaving behind newly regenerated bone tissue [55].

Three dimensional (3D) scaffolds created from biomaterials that can incorporate bioactive elements (see Figure 2.6) are currently being explored. It is expected that these would have more desirable properties, such as the mineralization of hydroxyapatite (HA), increased cell proliferation and adhesion, biocompatibility with the surrounding tissue, reduced inflammatory response, and increased bone regeneration [66], [71], [72].

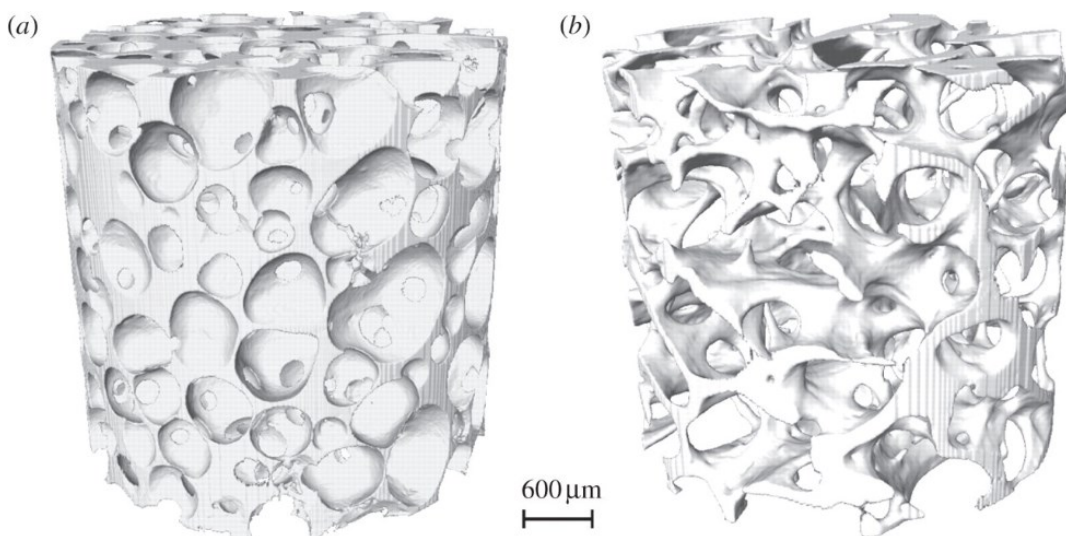


Figure 2.6: X-ray microtomography images of (a) bioactive glass foam scaffold and (b) trabecular bone from a human femur proximal to the knee [73].

2.5.1. Requirements for biomaterials in tissue engineering

The core concept behind tissue engineering is to control, promote and accelerate the body's natural biological response to damaged tissue using engineering principles. To achieve this, engineers are developing scaffolds with bioactive materials that would ideally mimic the native tissue environment and degrade with tissue growth. The criteria for an ideal scaffold for bone regeneration are that it [73], [74]:

- 1) has mechanical properties that provide required support to the host bone,
- 2) acts as a substrate for three-dimensional bone growth,
- 3) has a porous network (pore diameter > 100 μm) to allow cell migration and vascularization, cell penetration and bone growth
- 4) has a surface suitable for osteogenic cell attachment,
- 5) encourages bone cell migration, stimulates Basic Multicellular Unit (BMU) to produce new bone, enhance osseointegration
- 6) resorbs at the same rate as that at which the new bone remodels, with dissolution products that are non-toxic and easy to excrete from the body,
- 7) avoids production of toxic by-products during degradation
- 8) prevents inflammatory response
- 9) can be produced and sterilized for clinical use, without loss of bioactive properties.
- 10) releases drugs in a controlled manner
- 11) is of suitable shape for the site
- 12) is biocompatible (not cytotoxic),
- 13) bonds and creates a stable interface with existing bone/tissue

2.6. Materials for scaffold construction

2.6.1. Biocompatibility of collagen

The term “collagen” refers to an entire family of proteins that share common traits but are used for different purposes in the body [75]. It is one of the most prevalent materials being used in tissue engineering. As stated above, it is a major constituent of the body, making up nearly 90% of tendon and the organic component of bone, and 50% of skin [76].

Types I, II and III are the major sources of collagen in the body. Of these three, type I collagen, which is found in skin, tendon and bone [76], [77], is used as a biomaterial to create scaffolds for tissue engineering. Applications include wound dressing and tissue replacement for heart valves, blood vessels, skin, and skeletal muscle, among many others. The function and properties of the collagen scaffold is directly linked to the manner in which it is processed; depending on what is desired, collagen can be processed into sheets, powder or gels (see Figure 2.7) [78]. Collagen gels are of particular interest, as they can be injected directly into the affected site of the patient, requiring minimally invasive surgery yet still retaining their biological and mechanical properties [78], [79].

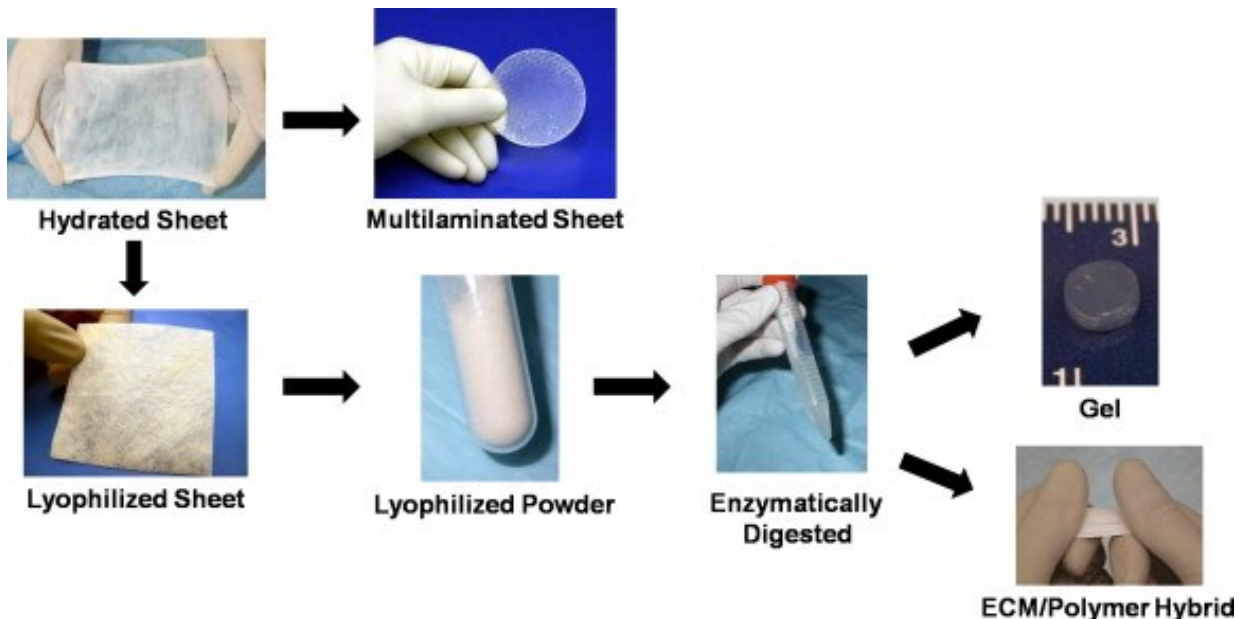


Figure 2.7: Layout of processing steps for various forms of extracellular matrix scaffolds [78]

Type I collagen is of particular interest for creating scaffolds for bone and dental repair. Research has shown that it is possible for collagen to mineralize and form HA [80], [81], and the mineralized collagen will closely match the composition of bone [81].

However, collagen gels alone are unsuitable for replacing bone tissue; as-made, Highly Hydrated Collagen (HHC) gels are approximately 99% excess fluid, which contributes to an extremely low collagen fibril density (CFD, <0.5 wt%), as well as poor mechanical properties [82].

To improve the mechanical properties of collagen gels, a method of removing excess water from the gel was developed called plastic compression (PC). By plastically compressing HHC gels (see Figure 2.8) and removing the excess water, a dense collagen (DC) hydrogel is formed, in which the Collagen

Fibril Density (CFD) increases to approximately 8% [82] along with an increased mechanical performance of the hydrogel, without affecting its biocompatibility [83]–[85].

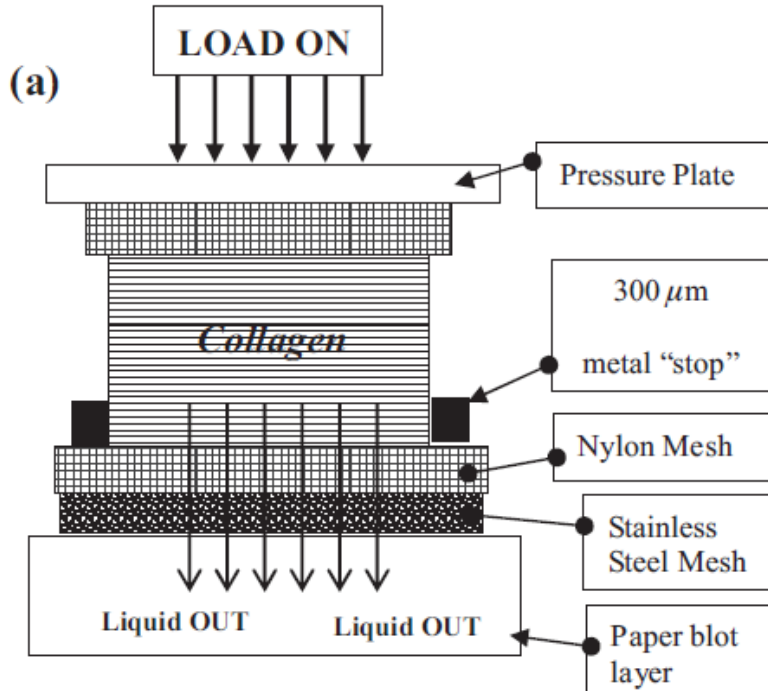


Figure 2.8: Schematic of a plastically compressing a collagen gel [83]

In addition to its good biocompatibility, collagen scaffolds also has the advantage of acting as a site for biomineralization. Collagen scaffolds seeded with MSCs show good mineralization properties; this is likely due to the fact that 3D collagen scaffolds mimic the natural matrix found in bone, where mineralization occurs between the gaps of collagen fibrils (see Figure 2.5B,C) [84], [86].

2.6.2. Biocompatibility of chitosan

Produced from chitin, the structure component of shells for crustaceans such as shrimp and crab, and which is insoluble in most solvents, chitosan (CTS) can be dissolved in acidic solutions, making it suitable for a wide range of applications [87] due to its biocompatibility, biodegradability, mucoadhesive, and antimicrobial properties, among others [88]. A polyelectrolyte produced by the deacetylation of chitin, CTS is composed of glucosamine and N-acetyl-glucosamine monomers linked by glycosidic bonds [89]. The deacetylation of CTS provides amino groups (see Figure 2.9) that can be protonated, a necessary step for the creation of ionic complexes [90], and can form hydrogels [91]–[93] or coatings [94]–[97].

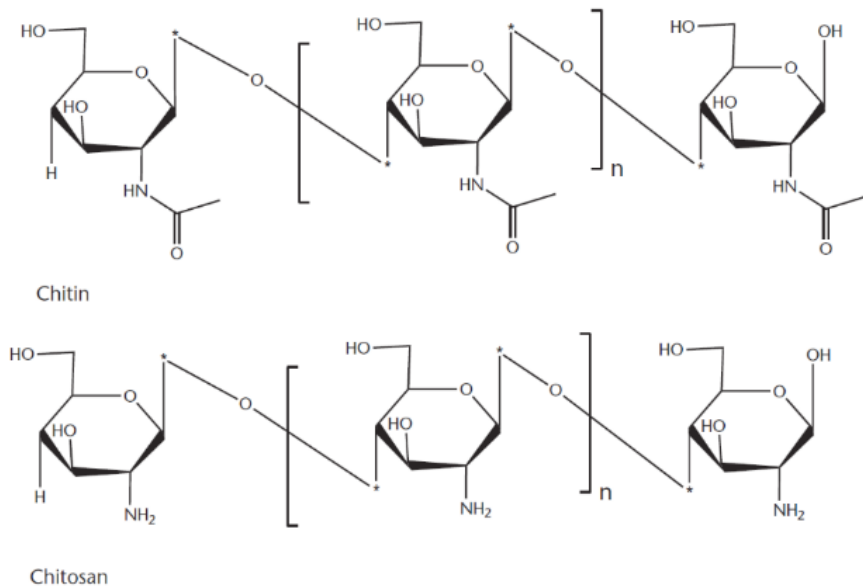


Figure 2.9: Chemical structures of the repeating units of idealised chitin and CTS [98]

Solutions of CTS can be obtained by protonating the amine groups (obtained from deacetyling chitin) in an acidic environment. Once dissolved, CTS remains in solution with a pH of approximately 6.2. When neutralized, CTS will form a gel-like precipitate that is both biocompatible and biodegradable, and can even be combined with other polymers of biological molecules (e.g. collagen [99], [100], see Figure 2.10) making it extremely attractive for biomedical applications [101].

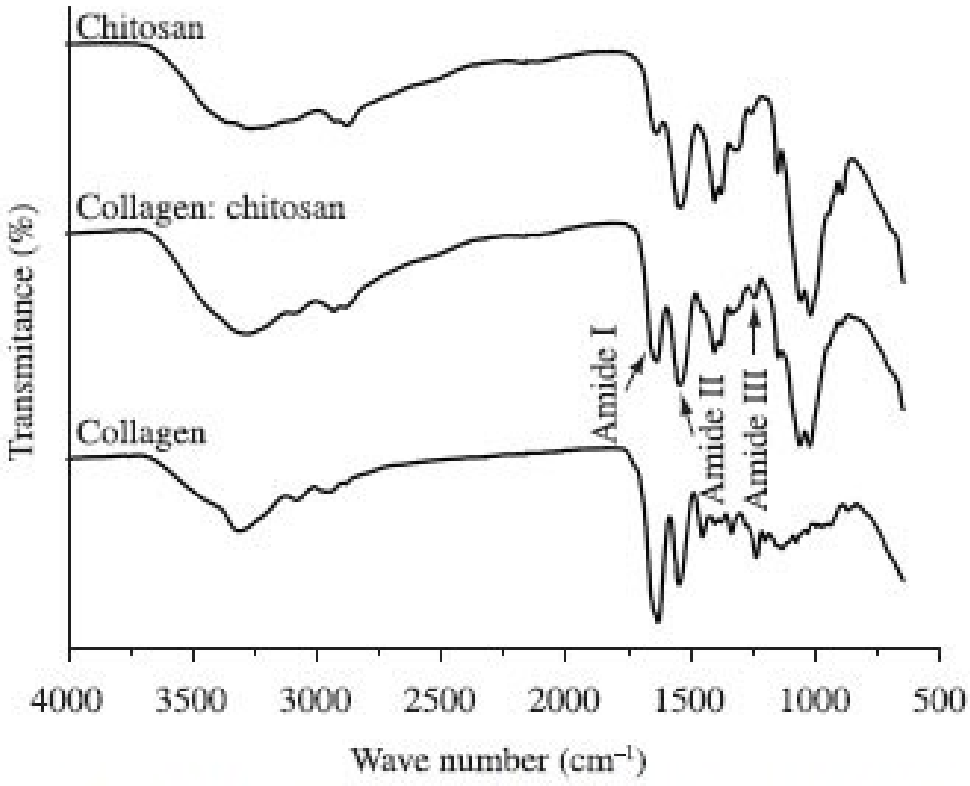
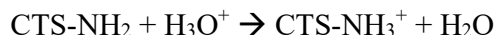
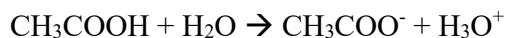


Figure 2.10: FT-IR spectra of collagen, CTS and collagen- CTS scaffolds [100].

CTS is a nontoxic polysaccharide composed of a repeating disaccharide unit. The result of the deacetylation of chitin, a naturally occurring polysaccharide found in the shells of crustaceans such as shrimps and crabs [101]–[103], chitin is the second largest biopolymer in the world after cellulose [102].

Using CTS powder, CTS molecules can be dissolved in an acidic medium with a pH<5.5-6 [103], [104]. This is due to the fact that in acidic media the –NH₂ groups are protonated, resulting in CTS becoming a polyelectrolyte [102], [104]. Traditionally, a 0.1 M solution of acetic acid is used to dissolve CTS, as it is protonated in the following reactions [102].



Using this method, complete protonation can be achieved, and the resulting pH dependent solution can be used to form a gel, without chemical modification or the use of cross-linkers [101].

Using the above method, hydrogels of CTS were made and demonstrated to be biocompatible. For example, the use of CTS gels for clinical applications such as subcutaneous and oral drug delivery is

possible, as CTS hydrogels can absorb drugs, be implanted in the body, and gradually release the drugs, which will then diffuse into the neighbouring tissue [105].

2.6.3. CTS-collagen hydrogels

The addition of CTS to collagen was shown to greatly influence the structure of the hydrogel. A natural biopolymer that resembles the structure, composition and biological activity of GAGs [84], CTS interacts with collagen and forms ionic bonds in solution when mixing, resulting in CTS tightly tethered to a collagen backbone. From previous research, it was shown that CTS incorporated into collagen hydrogels has a similar effect as GAGs, allowing for greater stability of the hydrogel and mimicking the structure of the osteoid found in bone [84].

CTS bonds to several collagen fibers, inducing collagen fiber crosslinking, which in turn reinforces the collagen matrix by anchoring the collagen fibers in place [106]. The end result is a reinforced structure and increased pore size. Furthermore, the adherence and growth of ligament cells improved thanks to the increased pore size, compared to hydrogels composed solely of CTS or collagen [107].

Furthermore, adding CTS to collagen effects the degradation of the scaffold. Increasing the biodegradation time corresponds to resistance to collagen degradation, indicating improved biological stability of the hydrogels, which will directly affect the scaffold behaviour during mineralization [84], [108].

2.6.4. Bioactive additives

2.6.4.1. Silk Fibroin derived polypeptides

Silk, a material that is extruded from the glands of various insects, is formed of protein polymers that are spun into fibers as it is extruded from insects. It consists primarily of fibroin and sericin proteins [109]–[111]. The silk fibroin (SF) is the core structural component of silk, and contributes to its toughness. Due to its ease of processing, biodegradability and high tensile strength, silk fibroin is especially attractive for biomedical applications [109], [111]–[113].

Like, bone, silk is a hierarchical material, with its properties being influenced by the arrangement of materials from the microscale to the macroscale [114]–[117]. While, like most organic tissue, SF is made up of protein molecules made up of a sequence of amino acids, it is in fact a composite material, with nanocrystalline β -sheet regions spread throughout an amorphous matrix (see Figure 2.11). The crystalline regions connected by amorphous structures form a silk fibril, and several of these fibrils interlink to create a silk fiber, or thread [116], [117], with diameters of 1 – 20 μm [117]. These

crystalline regions have a serve as multifunctional cross-links and impart great strength to the silk fibers, while the amorphous regions are responsible for its elasticity [114], [116].

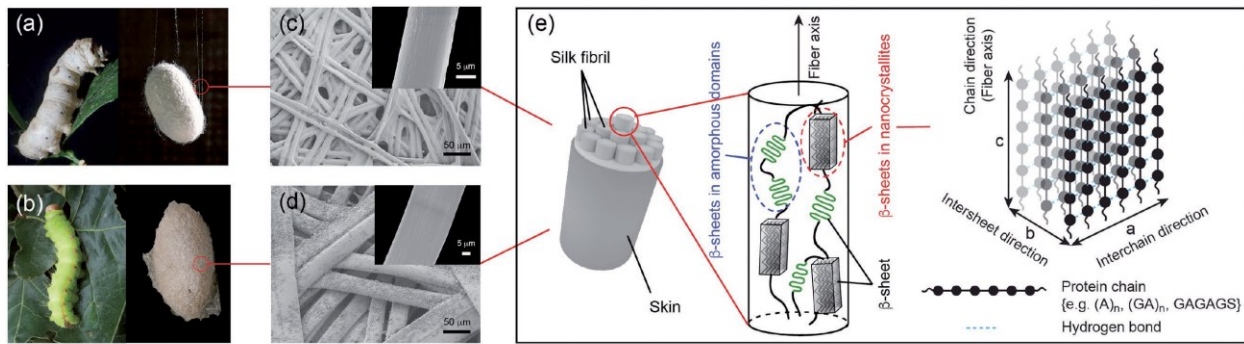


Figure 2.11: a,b) Images of the domestic *Bombyx mori* silkworm and the nonmulberry *Antheraea pernyi* silkworm, and their cocoons. c,d) SEM images of the natural *B. mori* silk fibers and *A. pernyi* silk fibers (Insets show the corresponding degummed silk fibers). e) Schematic illustration of the structure of a silk fiber. [111]

An interesting property of SF is that its amorphous component (C_s) is hydrophilic, while the crystalline component (C_p) is hydrophobic [118] (see Figure 2.12a). Due to their unique properties, it is fairly straightforward of separating SF into its constituent components (see Figure 2.12e) by degumming the silk source to remove the sericin covering the fibroin, dissolving the SF with α -chymotrypsin (see Figure 2.12d) (a digestive enzyme that breaks down proteins into polypeptides), and centrifuging the result to separate the C_s and C_p phases [80], [118].

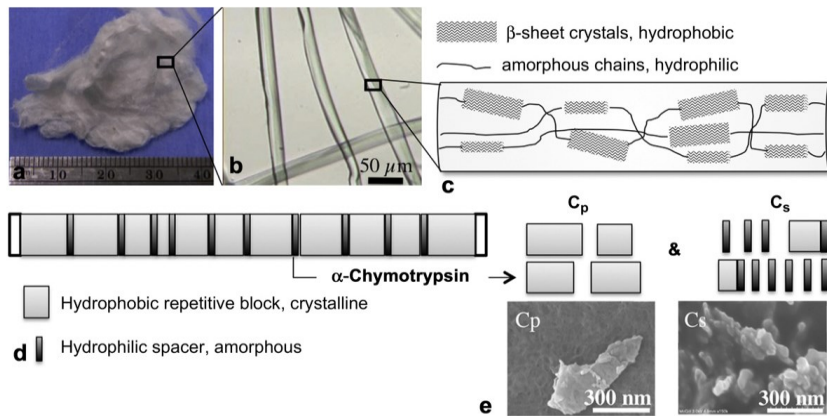


Figure 2.12: a) SF extracted from *Bombyx mori* cocoons and b) analyzed through optical microscopy; c) SF fiber is composed of hydrophobic crystalline polypeptides linked by hydrophilic amorphous amino-acidic sequences; d) α -chymotrypsin can be used to selectively separate C_p and C_s ; e) SEM images of C_p and C_s fragments [80].

Once separated, it was shown that the C_s and C_p have a very different composition, with C_s having more anionic amino acids than C_p (see Table 2.3) [118]. Furthermore, C_s component of SF has excellent biominerization properties; Attenuated Total Reflectance Fourier Transform Infrared (ATR FT-IR) Spectroscopy, thermogravimetric analysis (TGA), and X-Ray Diffraction (XRD) performed on DC

hydrogels that incorporated C_s (DC-C_s) and C_p (DC-C_p) and were immersed in simulated body fluid (SBF) have shown that the C_s fragments led to the formation of HA (see Figure 2.13a,b). The characterization of DC-C_s and DC-C_p via ATR FT-IR showed increased phosphate and carbonate groups at 1015 cm⁻¹ and 783 cm⁻¹ respectively, TGA showed an increased inorganic phase and XRD showed the peak for HA, while XRD of C_s showed mineral formation while C_p showed a lack of mineralization (see Figure 2.13c) [80].

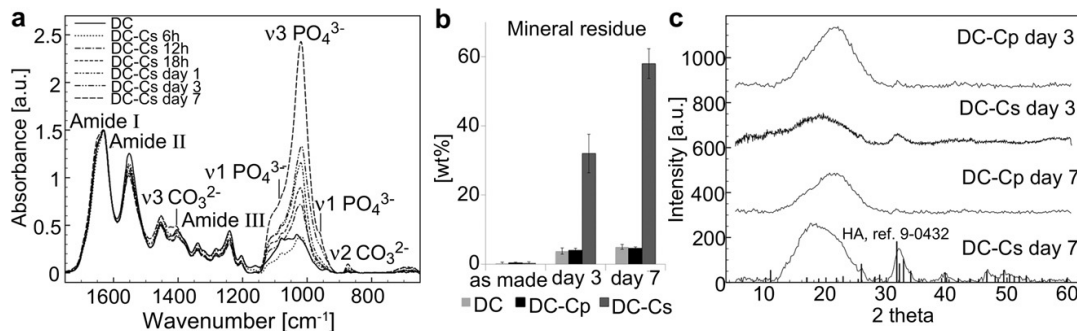


Figure 2.13: DC-C_p and DC-C_s hydrogels immersed in SBF analysed via a) ATR-FTIR, b) TGA and c) XRD [80].

Table 2.3: Amino Acid Composition of Silk Fibroin Derived Polypeptides [118]

Amino acids	Silk fibroin	C _p	C _s
Aspartic acid	1.63	0.42	4.50
Threonine	0.88	0.47	1.90
Serine	11.27	11.79	9.15
Glutamic acid	1.19	0.34	3.10
Glycine	0.46	0.13	0.95
Proline	45.24	49.13	36.28
Alanine	29.18	32.03	23.98
Cysteine	-	-	-
Valine	2.16	1.11	4.19
Methionine	0.08	0.03	0.31
Isoleucine	0.60	0.19	1.60
Leucine	0.51	0.10	1.70
Tyrosine	5.14	3.66	7.51
Phenylalanine	0.66	0.34	1.46
Lysine	0.32	0.12	0.94
Histidine	0.20	0.04	0.54
Arginine	0.47	0.10	1.30
Polar:non-polar amino acids	0.27	0.20	0.41

2.6.4.2. Bioglasses

One of the most commonly researched additives are bioactive glasses, or “bioglasses,” which were first made to aid in bone remineralization and repair [119]. Bioglass acts as a synthetic filler, replacing and integrating with damaged bone tissue by promoting HA nucleation [119]–[123]. Within a hydrogel, bioglass would be implanted into the hydrogel network, where it would stay bonded and act as sites for HA nucleation [124]–[126].

Glass is an inorganic amorphous compound that is created by rapidly cooling a melt below its glass transition temperature (T_g) to avoid crystallization. The oxides present in the glass can form either network formers or network modifiers; atoms that have a high affinity towards oxygen, such as phosphorus, make stable glass network formers in their oxide form, while oxides such as Na_2O , CaO and CuO , are network modifiers, and can influence the degradation rate, biological properties and network connectivity of the glass. The oxygen atoms can be either binding oxygen (BO) or non-binding oxygen (NBO), the latter of which form ionic bonds with between modifiers (see Figure 2.14) [127], [128].

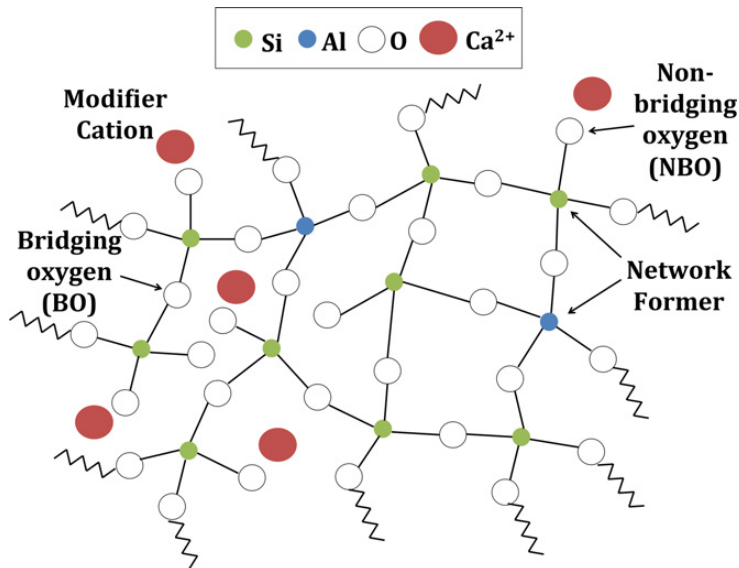


Figure 2.14: Structure of a glass network [128]

Initially, bioglasses were made using $\text{SiO}_2\text{-P}_2\text{O}_5\text{-CaO-Na}_2\text{O}$ [119], and are now being expanded with different compositions (see

Table 2.4), including the addition of metallic dopants to improve their bioactive properties. Metal oxides such as CuO [129], [130], Ag_2O [131], SrO [131]–[133], Nb_2O_5 [134] and Fe_2O_3 [135] were used for various purposes, including but not limited to bone rehabilitation.

Table 2.4: Composition of different bioglasses (mol%)

SiO₂	B₂O₃	P₂O₅	CaO	Na₂O	CuO	SrO	Ag₂O	Nb₂O₅	Fe₂O₃	V₂O₅	Ref
46.1		2.6	26.9	24.3							[119]
46.1		2.5	26.9 20.2 13.5 6.7 0.0	24.4		0.0 6.7 13.5 20.2 26.9					[133]
55			40			5 3 1	0 2 4				[131]
49.5		1.1	23.1 22.5 20.8 11.5 0.0	26.4		0.0 0.6 2.3 11.5 23.1					[132]
52 50 48 46 44 42		4	41	3					0 2 4 6 8 10		[135]
			95 90 85 80 75							5 10 15 20 25	[136]
		50	30	20 19 15 10	0 1 5 10						[129]
		30	60					10			[137]

Phosphate-based glasses (PG) are degradable glasses that use phosphorus pentoxide (P₂O₅) as a network former, with additional elements such as sodium oxide (Na₂O) and calcium oxide (CaO) added to create a ternary system and modify the PGs properties. For instance, it was shown that increasing the amount of CaO in the glass leads to an increase in weight loss over time (see Figure 2.15) [138].

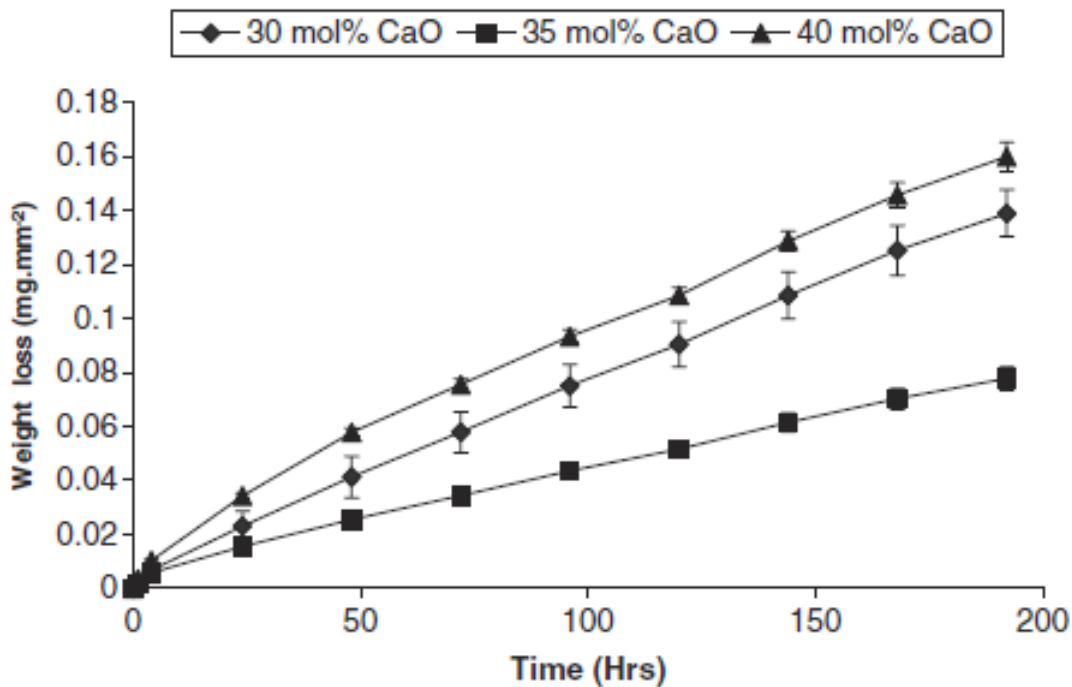


Figure 2.15: Weight loss vs time for different CaO mol% [138]

The addition of CuO within PG is also of interest; while toxic in large amounts, copper is important to biological processes, such as the synthesis and cross-linking of collagen [139]. Research has shown that the presence of copper leads to anti-microbial properties within bioglass [140]–[143], as well as fabricate anti-bacterial coatings [144], but it also promotes angiogenesis (the formation of blood vessels) [145]–[147] (see Figure 2.16) and improves cell survival rate [148].

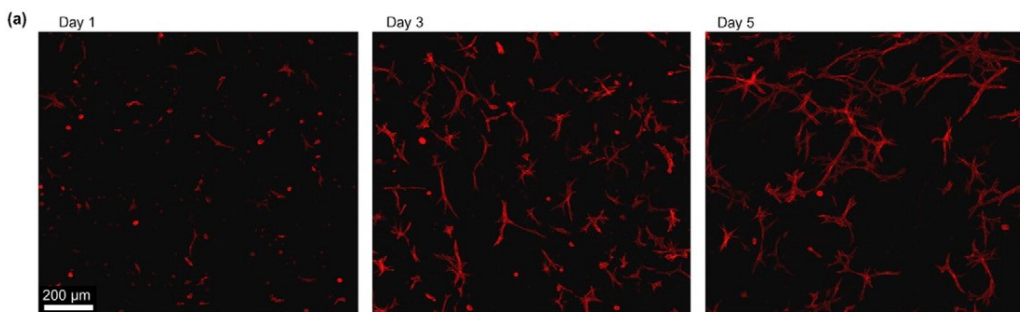


Figure 2.16: Confocal Laser Scanning Microscopy images showing cells assemble into a capillary-like network over 5 days of culture in collagen gels [147]

These ternary glasses are composed of network building blocks (tetrahedral sites) that form larger molecular units in the amorphous glass, and can further be modified by adding metal oxides, which result in a lowering of the network connectivity (see Figure 2.17) of the glasses [149], [150]. The

conversion of Q^3 to Q^2 , Q^1 and Q^0 species has the end result of stabilizing the PG through the creation of ionic bonds between the non-bridging oxygen atoms and the metal cations, which act as network cross-linkers and increase chemical stability while decreasing dissolution rates [151].

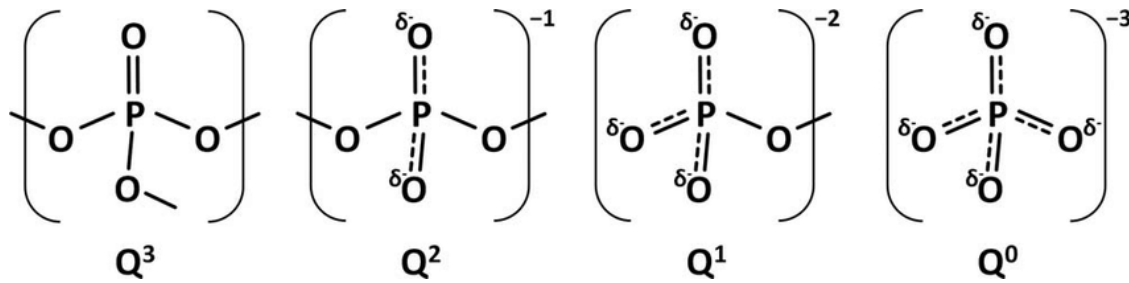


Figure 2.17: The possible tetrahedral sites that occur in phosphate glasses [150]

The release of phosphate anions from the PG as it degrades is done under the form different structures, such as Orthophosphate (PO_4^{3-}), Pyrophosphate ($P_2O_7^{4-}$), Cyclic Trimetaphosphate ($P_3O_9^{3-}$), and Tripolyphosphate ($P_3O_{10}^{5-}$) (see Figure 2.18), with the phosphate glass releasing phosphate anions at a different rate depending on the anion structure (see Figure 2.19) [138].

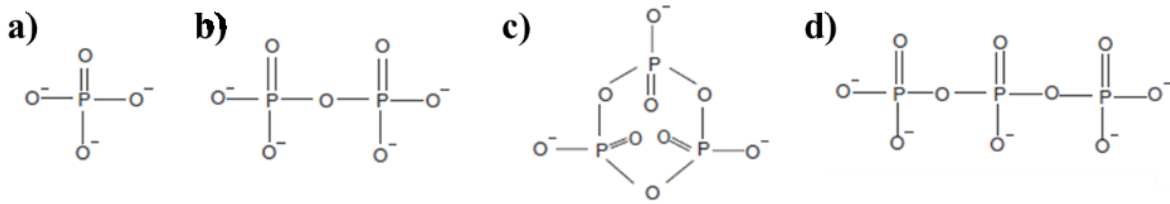


Figure 2.18: Structure of phosphate anions a) PO_4^{3-} , b) $P_2O_7^{4-}$, c) $P_3O_9^{3-}$ and d) $P_3O_{10}^{5-}$. Adapted from [138]

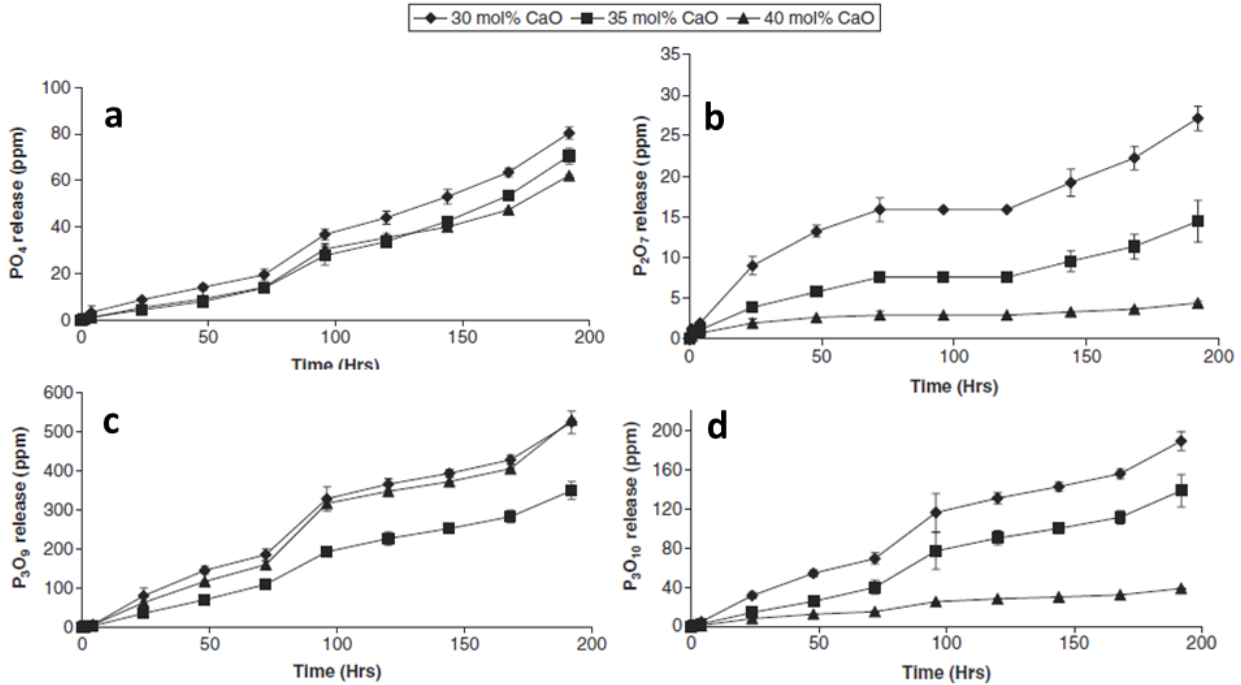


Figure 2.19: Release rate of a) PO₄³⁻, b) P₂O₇⁴⁻, c) P₃O₉³⁻ and d) P₃O₁₀⁵⁻ anions. [138]

2.7. Scaffold construction

2.7.1. Sol-gel method

Hydrogels are created from polymers held together by association bonds (covalent bonds and weaker forces such as ionic bonds, hydrogen bonds, and intermolecular hydrophobic association) arranged in a three-dimensional network that holds a large quantity of water within it without dissolving [152].

The classification of hydrogels follows several criteria (see Table 2.5), such as the source, components, method of preparation, charge, physical structure, method of crosslinking and function of the hydrogel [152].

Table 2.5: Classification of Hydrogels [152]

Classification	Contents
Source	Natural, synthetic
Component	Homopolymer, copolymer, multipolymer
Preparation method	Simultaneous polymerization, crosslink of polymer
Electric charge	Nonion, anion, cation, zwitter ion
Physical structure	Amorphous, semicrystalline, hydrogen bonded
Crosslink	Covalent bond, intermolecular force
Functions	Biodegradable, stimuli responsive, superabsorbent, etc.

The gelation of CTS is affected by several factors, specifically the relationship between pH, temperature, and the degree of deacetylation. The degree of deacetylation, as mentioned before, refers to the amount of amine functional groups present on a CTS molecule. For gelation, these are important since the protonated amine group causes electrostatic repulsion between CTS molecules; adjusting the pH reduces the charge on the CTS molecules by deprotonating the amine group, which in turn reduces the intermolecular charge between CTS chains. This allows the chains to come closer together and undergo hydrogen bonding, forming a porous network of CTS [153].

In addition to the ionic cross-linking that CTS undergoes when its charge is neutralized, anions and cations within the CTS solution affect gelation as well. Divalent polyol anions such as sulfate, oxalate, molybdate or phosphate effect the gelation of CTS due to their influence on water, allowing for the removal of a hydrating sheath surround the CTS molecule. This allows for temperature-dependent hydration or dehydration [101].

2.7.2. Electrophoretic deposition

Electrophoretic deposition (EPD) is a method for creating thick films via electrophoresis, where charged particles (either metal, ceramic, glass or polymer) migrate to an electrode driven by an electric field [154]–[158] (see Figure 2.20). Composites of organic (polymers) and inorganic (ceramics, glasses) materials can be deposited to fabricate soft composite coatings [95], [159]–[162]. These composite coatings can be tailored depending on the composition, morphology, stiffness and thickness desired [95], [157]–[159]. The end result is desirable in biomedical applications, especially in next-generation implants, as composite coatings can provide a better connection between the rigid metallic implants and vascularized bone tissue as well as provide extra protection in the form of corrosion resistance [96], [157], [158], [163]. The process is versatile, and can be easily modified to fit specific applications. The film deposited can be easily controlled as well by changing the deposition time (see Figure 2.21) or applied potential (see Figure 2.22) [95], [157], [164].

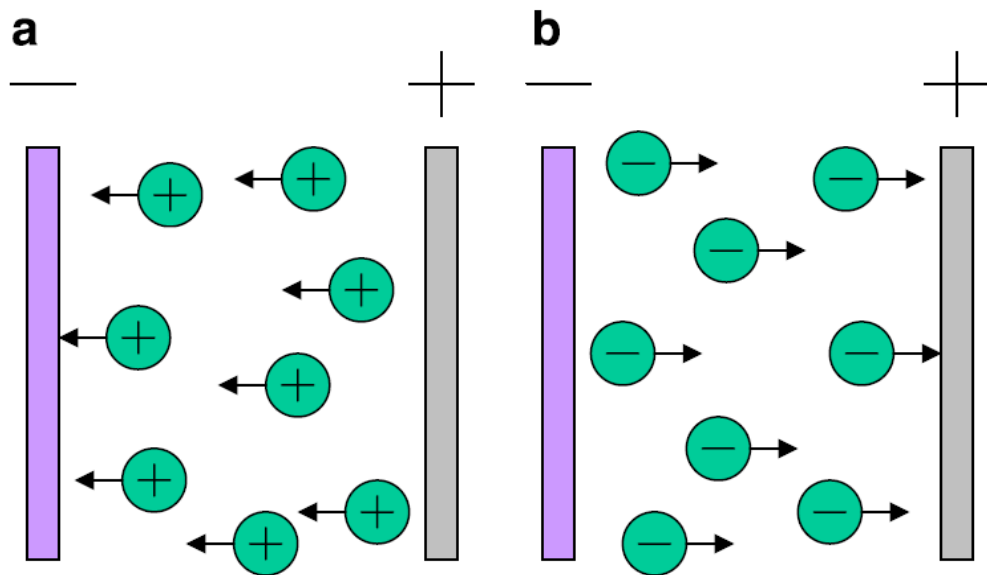


Figure 2.20: Schematic illustration of (a) cathodic and (b) anodic electrophoretic deposition process [157]

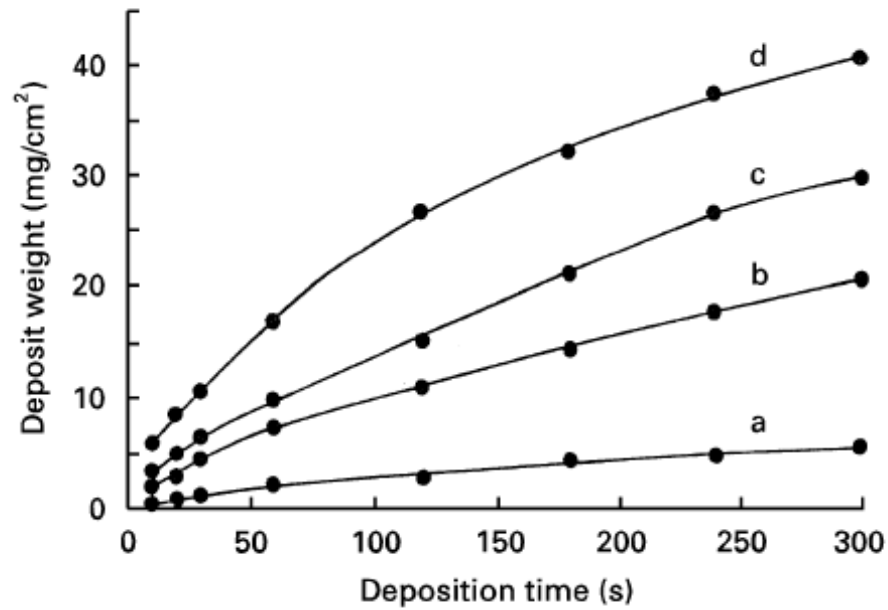


Figure 2.21: Weight of deposited HA2 versus applied voltage for different deposition durations: (a) 30 s; and (b) 120 s [164].

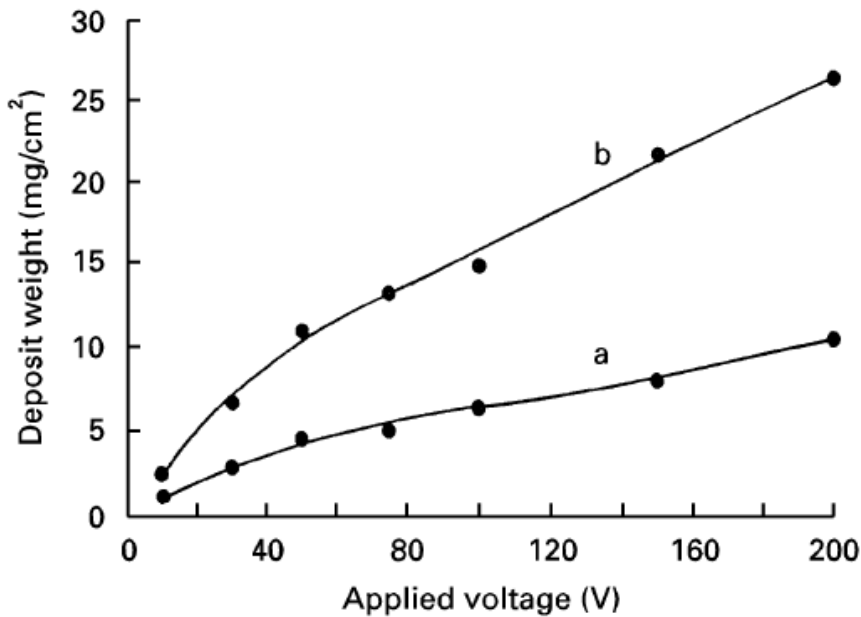
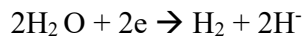
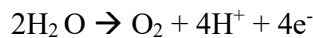


Figure 2.22: Weight of deposited HA2 versus deposition time at different applied voltages: (a) 10 V; (b) 50 V; (c) 100 V; (d) 200 V [164].

During EPD, the proposed mechanism of deposition is based on the movement of charged anionic or cationic macromolecules due to electrophoresis, which then have their charge neutralized in either the high or low pH regions, respectively, at the electrodes. These regions are created when the electrochemical decomposition of water at the electrode surfaces results in an electrogenerated acid or base, under the following reactions [158]:



The relationship between the yield of an electrophoretically deposited film and deposition parameters was first described in 1940 by H.C. Hamaker. The yield, Y (g), being proportional to the EPD of materials onto a substrate is dependent on the electrophoretic velocity of the particles, μ ($\text{cm}^2/\text{V}\cdot\text{s}$), the applied electric field, E (V/cm), the initial concentration of the solution, C_s (g/cm^3), surface area being coated, S (cm^2), and time, t (s), can be described by the following equation [155].

$$Y = \mu C_s E S t \quad (2.1)$$

Though these parameter control the deposition rate, the above equation does not take into account the decrease in concentration as materials deposit and are removed from the solution, as well as the weakening of the electric field due to the insulating properties of the coating [165]. In reality, the mass deposited eventually reaches a plateau. Later models incorporated the change in concentration [166] and drop in potential due to the coating's insulating effect [167].

2.7.2.1. Factors affecting EPD

2.7.2.1.1. Electrolyte conductivity

As a deposit grows, if it has poor conductivity, it can act as an insulating material, causing the voltage drop in the EPD cell, as can be seen Figure 2.23. The applied potential (ϕ) is consumed by a potential drop at each electrode ($\Delta\phi_1$ and $\Delta\phi_2$) and by a drop over the suspension and the deposit ($\Delta\phi_{dep}$) [167].

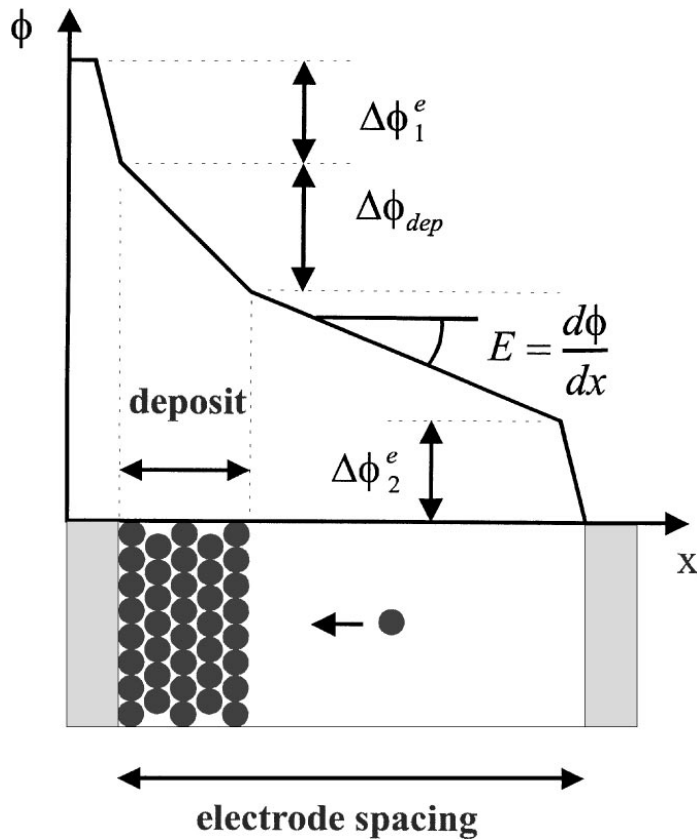


Figure 2.23: Evolution of the potential in an electrophoretic deposition cell.

An equivalent electrical circuit of showing the resistances in the suspension and deposit is shown in Figure 2.24. The potential drop in an EPD cell was described by Van der Biest and Vanderperre in a

series of four terms in series using the following [167]:

$$V_a = \Delta V_1 + IR_{dep}d_1 + IR_{sus}(d - d_1) + \Delta V_2 \quad (2.2)$$

where V_a is the applied voltage, I is the current, R_{dep} and R_{sus} are the resistances per unit length of the deposit and suspension respectively, d_1 is the thickness of the deposit, d is the distance between electrodes and ΔV_i is the potential drop at an electrode [167].

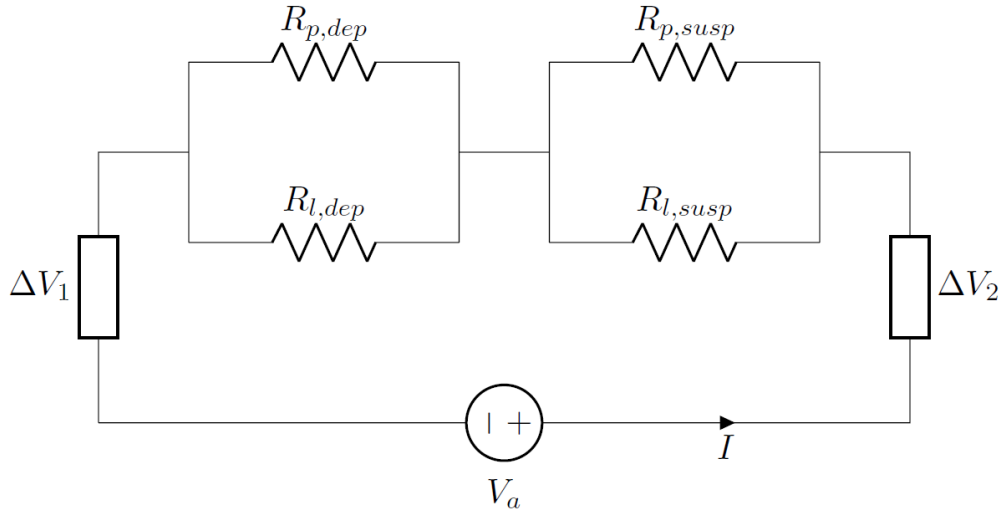


Figure 2.24: Electrical circuit of an EPD cell [165]

Both the resistance of the suspension (described by Equation 2.3) and the resistance of the coating (described by Equation 2.4) are a function of two resistances in parallel.

$$R_{sus} = \left[\frac{1}{R_{l,sus}} + \frac{1}{R_{p,sus}} \right]^{-1} \quad (2.3)$$

$$\text{where } R_{l,sus} = \rho_{l,sus} \frac{(L - d)}{A} \quad \text{and} \quad R_{p,sus} = \rho_{p,sus} \frac{(L - d)}{\mu Ac Q_{eff}}$$

$$R_{dep} = \left[\frac{1}{R_{p,dep}} + \frac{1}{R_{l,dep}} \right]^{-1} \quad (2.4)$$

$$\text{where } R_{l,dep} = \rho_{l,dep} \frac{d}{(1 - p)A} \quad \text{and} \quad R_{p,dep} = \rho_{p,dep} \frac{d}{pA}$$

The electrical resistance of the deposit, calculated using Equation 6, is also derived from applying Kirchhoff's law (see Equation 2.5) on the equivalent circuit of EPD shown in Figure 2.25 [168], [169].

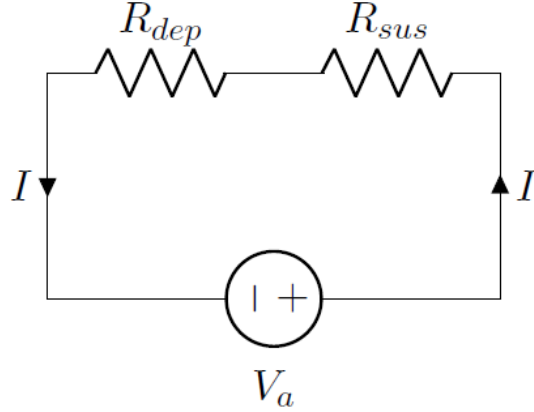


Figure 2.25: Equivalent circuit of electrophoretic deposition [168]

$$V_a = V_{sus} + V_{dep} = I(R_{sus} + R_{dep}) \quad (2.5)$$

rearranged to give the following:

$$R_{dep} = \frac{V_a}{I} - R_{sus} \quad (2.6)$$

2.7.2.1.2. Concentration of the suspension

While Hamaker's expression for the deposition yield during EPD in equation 2.5 shows that the only parameter to change is time, as time progresses the concentration changes as materials is transferred from the suspension to the deposit [165], [170]. Furthermore, the concentration can be expressed as a function of the deposited mass, as in the following [165]:

$$C = \frac{M_0 - Y}{v} \quad (2.7)$$

where M_0 is the initial mass (g), Y is the deposited mass (g), and v (cm³) is the volume of the solution.

Incorporating equation 2.7 into Hamaker's equation, and assuming the deposit is a good conductor

(thus ensuring a constant electric field) and that no sedimentation occurs, shows that the deposition yield increases with time until it reaches a plateau where $Y = M_0$, as seen in the following [165], [170].

$$Y(t) = M_0(1 - e^{-kt}) \quad (2.8)$$

where k is a constant determined by the electrophoretic mobility, surface area of the electrode, electric field, and volume of the solution, as seen in the following.

$$k = \frac{\mu SE}{v} \quad (2.9)$$

2.7.2.1.3. Conductivity of the liquid

The conductivity of the suspension, S_{sus} , is an important parameter affecting EPD. Work by Van der Biest et al. showed that the conductivity increases linearly with the concentration of powders in the solution (see Figure 2.26a) and decreases with time (see Figure 2.26b), and can be expressed as Equation 2.10 [165].

$$S_{sus} = aC + b \quad (2.10)$$

with C the concentration of powder in suspension, a the slope and b the intercept.

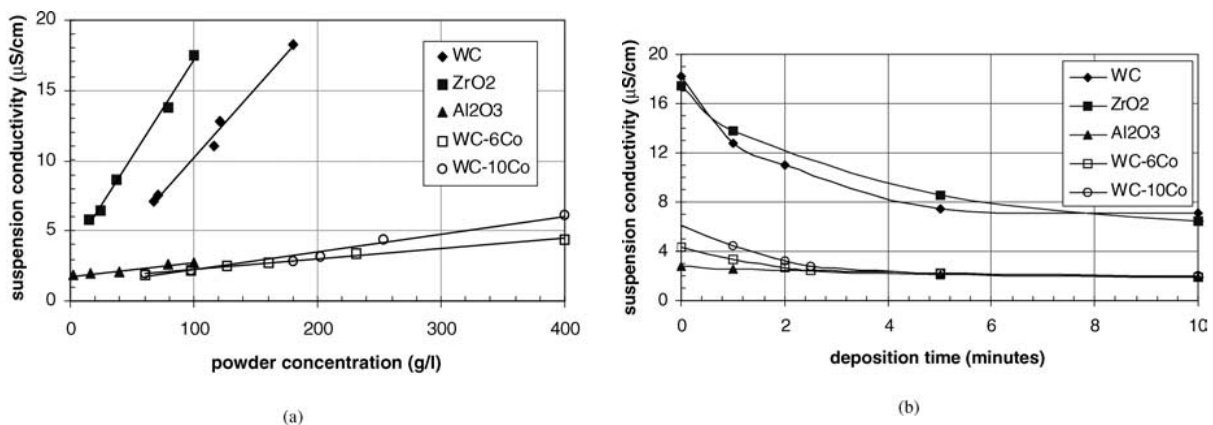


Figure 2.26: Suspension conductivity as a function of (a) remaining powder concentration in suspension during EPD and (b) deposition time for different powders in acetone/n-butylamine [165].

By incorporating equations 2.7 and 2.8 into 2.10, the conductivity of the suspension can be expressed as the following equation.

$$S_{sus} = a \frac{M_0}{v} e^{-kt} + b \quad (2.11)$$

The electric field can also be calculated from the relationship between the conductivity, σ (S/cm), the current, I (A), and the surface area do the electrode, S (cm²), using the following equation.

$$E = \frac{I}{S\sigma} \quad (2.12)$$

2.7.2.1.4. Electrophoretic mobility

The electrophoretic mobility of particles can also be calculated using the following equation [171].

$$\mu = \frac{\epsilon_0 \epsilon_r \zeta}{\eta} \quad (2.13)$$

where ϵ_0 is the vacuum permittivity ($8.854 \times 10^{-12} F/m$), ϵ_r is the relative dielectric constant of medium, ζ is the zeta potential of particles, and η is the viscosity of medium.

It is known that for mixtures of multiples components, a component-constitutive property F is the product of the molar volume M_v (mol/cm³ or mol/mL) times a function of a physical property. For the n th component of the mixture of n components, with the component-constitutive property is designated F_i and the molar volume $M_{v,i}$, the value of F is obtained the following equation [172], [173].

$$F = \sum_{i=1}^n \phi_i \times F_i \quad (2.14)$$

where ϕ_i is the mole fraction ($M_{v,i}/M_{v,total}$) and F_i the component-constitutive property for the i^{th} component.

For a binary solution of, the dielectric constant, ϵ_{sol} , and viscosity, η_{sol} , of the solution can be calculated using equations 2.15 and 2.16 [173]–[175].

$$\varepsilon_{sol} = \phi_1 \varepsilon_1 + \phi_2 \varepsilon_2 \quad (2.15)$$

$$\eta_{sol} = \phi_1 \eta_1 + \phi_2 \eta_2 \quad (2.16)$$

2.7.2.1.5. Steric stabilization

Due to their small size and high surface area, particles in colloidal suspensions have a tendency to agglomerate and sediment, resulting in a solution that has a decreased additive concentration. To prevent this agglomeration, steric (polymeric) stabilization, electrostatic stabilization, and electrosteric stabilization can be used and ensure greater colloidal stability of the suspension by increasing the repulsive force between particles (see Figure 2.27) [176].

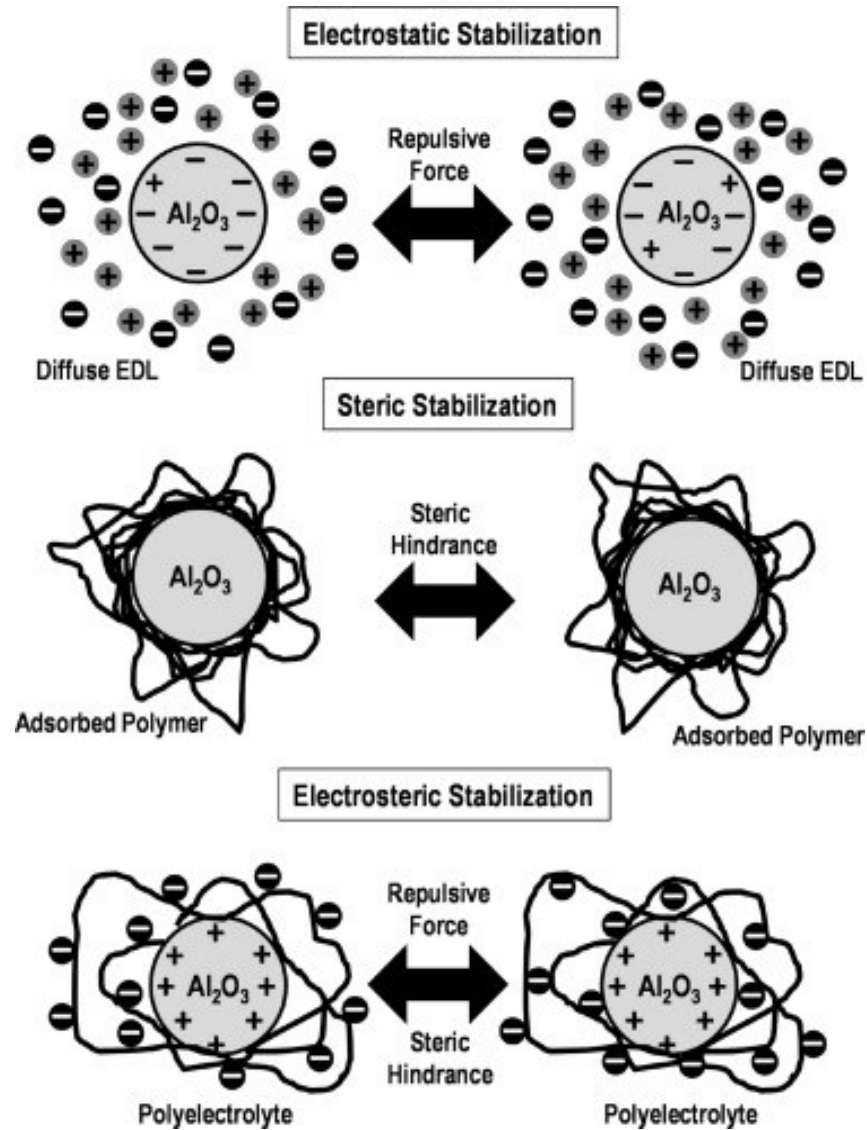


Figure 2.27: Representation of the electrostatic, steric and electrosteric stabilizing mechanisms of aqueous alumina suspension. (EDL = electric double layer) [176]

2.7.3. Bioglass fabrication

Traditionally, bioglasses were melt-derived. The inventor of the first bioglass, Larry Hench, melted precursors at 1450 °C and allowed for a homogenization time of 18-24 hours, then annealed the glass at 450 °C for 1-4 hours [119]. Melt manufacturing methods have largely followed the same process: heating at 1000-1500 °C [132], [135], [137], [177] in an electric furnace for approximately an hour, and in certain cases annealed at 400-500 °C to remove thermal stress [132], [177]. Bioglasses containing copper [130], [151], strontium [133], [178], [179], magnesium [178], vanadium [136] and zinc [179] (typically <25 mol%) were fabricated using a melt-derived technique.

Porosity can be achieved by adding fillers (e.g. sucrose [180], gelatine [181], Poly(methyl methacrylate) (PMMA) microbeads [182]), which burn out during sintering [122]. Typically, melt-derived glasses exhibit low porosities (<50% [183], [184]) and interconnected pores in the range 100-300 µm, and a compressive strength of 22 ± 1 MPa [183].

3. Research outline and organisation

3.1. Research outline

The following research outlines a plan to investigate the suitability of CuO-doped phosphate-based glasses in biomedical applications, specifically the incorporation of PGs in collagen-based scaffolds in lieu of autografts and coatings for orthopaedic implants.

The use of PGs in collagen gels was previously shown to release a multitude of ions during dissolution, including Ca^{2+} , Cu^{2+} , and various polyphosphate anions. These ions can be used in both the crosslinking of biopolymers as well as the nucleation of hydroxyapatite. The feasibility of using CuO-doped PG particles to increase the rate of nucleation of hydroxyapatite in collagen-CTS hydrogels is to be determined. Additionally, the use of these particles to increase the mechanical performance via crosslinking the polymers within the hydrogel is to be investigated.

Further experiments are designed to investigate the co-deposition of PG particles with collagen/CTS to create coatings for orthopaedic implants, including the kinetics of deposition morphology and composition of the film.

3.2. Aim and research hypothesis

The aim of this project is to determine the suitability of silk FDPs and CuO-doped phosphate glass for use in biomedical applications, specifically collagen-CTS hydrogels or orthopaedic implant coatings for bone repair or replacement. It is hypothesized that unlike conventional bioglass (e.g. Bioglass 45S5) that nucleates HA on its surface, the FDPs and water-soluble PG particles will cause the following to occur within the collagen-CTS scaffolds:

- The charged Cs will attract PO_4^{3-} and Ca^{2+} , causing saturation and leading to the nucleation of HA.
- The presence of collagen or CTS will cause the chelation of anions and cations released during dissolution, which will lead to either chemical or physical crosslinking, respectively.
- The local supersaturation of PO_4^{3-} and $\text{Ca}^{2+}/\text{Cu}^{2+}$ released infiltrate the collagen molecules and will cause the intrafibrillar nucleation of hydroxyapatite, similar to natural bone.

3.3. Research objectives

The main objective of this work is to develop and characterize collage-CTS scaffolds incorporating additives for bone tissue engineering. For this purpose, scaffolds with C_s/C_p and varying PG concentrations, as well as different concentrations of CuO, were created, examined and characterized to determine their properties and potential for bone regeneration. The incorporation of these elements allows tailoring the bioactivity and composition of the scaffold. Additionally, CuO-doped phosphate glasses in a colloidal solution of dissolved collagen/CTS are to be deposited on stainless steel substrates via EPD to form a biocompatible film and characterized. Different CuO concentration and deposition parameters are to be used in EPD of these films. Within this research, different objectives were established to meet the end goal of the project:

- Analyse the potential for HA nucleation *in vitro* using bioadditives by immersing them in SBF and characterising the result.
- Develop collagen-CTS hydrogels with C_s/C_p and CuO-doped phosphate glasses incorporated and conduct *in vitro* tests to determine the location and extent of nucleation (e.g. fully mineralized intrafibrillar nucleation vs surface/interfibrillar nucleation).
- Fabricate collage-CTS-PG films using electrophoretic deposition. Assess different deposition parameters (time, concentration, and voltage) and characterize the resulting films (morphology, adhesion, composition, uniformity) as well as deposition kinetics to determine if CuO-doped phosphate glasses are suitable for orthopaedic implant coatings.

3.4. Thesis organization

The present chapter (Chapter 1) consists of a general overview of the field of biomaterials and bone Tissue engineering (BTE). The clinical need for improved biomaterials and motivations behind this doctoral research is presented herein. The aim of this doctoral project is explained, the research hypothesis is described, and a set of objectives to achieve the goals of the project are clarified.

Chapter 2 provides background information of the fundamental engineering and biological principles of the field of biomaterials and BTE. An overview of the skeletal system, bone and its components, the mineralization of bone tissue are provided. Conventional BTE techniques (bone autografts and orthopaedic implants) are presented, along with their associated limitations. Lastly, current research in

the field of bone tissue engineering is presented, highlighting promising biomaterials and their results in BTE.

Chapter 3 contains an outline of the thesis, the research aims and objective, and the thesis organization.

Chapter 4 outlines the methodology followed. Materials and proposed system chosen are outlined. The experimental techniques used, as well as their protocols, are specified.

Chapter 5 shows the results of the characterization of the materials used to enhance HA mineralization. The silk FDPs, CuO-doped PGs and collagen/CTS biopolymers are investigated to determine the composition, chemical and electrical properties, and shape and size.

Chapter 6 examines the potential for silk fibroin-enhanced hydroxyapatite mineralization *in vitro*. Silk FDPs, both as-made and incorporated into hydrogels, were tested under physiological conditions. The resulting samples were analyzed chemically via XRD and ATR-FTIR, visually by SEM, and in terms of mass (to determine the extent of HA mineralization via weight gain).

Chapter 7 presents the results of PG immersed in SBF. The dissolution of PG and resulting particles that formed were analyzed via SEM, EDS, ATR-FTIR and in terms of mass to determine what changes occurred, both physical and chemical. The PG particles were also incorporated into DC gels and analysed *in vitro* using the same methods.

Chapter 8 shows the results of the investigation of fabricating coatings via EPD by co-depositing biopolymers (either CTS or collagen, or a combination of the two) with CuO-doped PG. The effect of copper on deposition kinetics, the ratios of polymers in the solution, and the applied voltage were all investigated to determine how they affected the resulting film, which were assessed via SEM and BSE images, in terms of composition via mass analysis and ATR-FTIR, and with ASTM standards adhesion tests.

Finally, Chapter 9 provides a general discussion of the results achieved in this thesis. The overall conclusions and perspectives are presented, as well as the potential research that may be undertaken based on this thesis.

4. Methodology

4.1. Sample preparation

4.1.1. Silk fibroin polypeptides preparation

Soluble silk fibroin-derived peptides were produced from raw *Bombyx Mori* (silkworm) silk provided by Stazione Sperimentale per la Seta (Milan, Italy). The silk sericin was degummed and the fibroins were cleaved and separated into their soluble (C_s) and non-soluble phases (C_p), using a method reported in the literature [80], [185], [186].

Silk fibroin fibers were produced through a heating cycle that removed the silk sericin. The resulting fibroin was dissolved in a concentrated aqueous solution of LiBr (Sigma) [187], [188], due to LiBr being a chaotropic salt, which disrupts the bonds in protein molecules [189], [190]. The dissolved fibroin results in both α -helical and β -folded structures [188], heated, then separated using dialysis to produce a 2% silk fibroin solution [185].

The resulting silk fibroin was diluted with a 0.1 M ammonium bicarbonate solution (NH_4CO_3 , Fisher Scientific), then enzymatically digested with α -chymotrypsin (Sigma) at an enzyme-to-substrate ratio of 1:100 to generate C_p and C_s in solution, which was incubated at 37°C for 24 hours then centrifuged to separate the supernatant (containing C_s) from the pellet (containing C_p). Both the supernatant and the pellet were freeze-dried to produce C_s and C_p [80].

4.1.2. Fabrication of CuO-doped phosphate glass

PG doped with CuO with the formulation 50P₂O₅-30CaO-(20-x)Na₂O-xCuO (x = 0, 5 and 10 mol%) [147], [151] were synthesized via a melt-derived process. Glass formed from CuO, P₂O₅, CaHPO₄, NaH₂PO₄ melted at 1350 °C [151]. The glass reagents were melted in a Pt/10%Rh crucible (XRF Scientific) to avoid contamination the glass as well as withstand high temperatures. The compositions listed in Table 4.1 were used.

Table 4.1: CuO-doped phosphate glass compositions (mol%)

Sample	P ₂ O ₅	CaO	Na ₂ O	CuO
0 mol% CuO	50	30	20	0
5 mol% CuO	50	30	15	5
10 mol% CuO	50	30	10	10

4.1.3. Preparation of simulated body fluid

Kokubo's SBF was created based on a protocol developed for analysing apatite formation [191]. Reagents were mixed in 3 L of distilled water in the following order: NaCl (Fisher Scientific) (24.105 g), NaHCO₃ (Fisher Scientific) (1.065 g), KCl (Sigma) (0.675 g), K₂HPO₄·3H₂O (0.693 g), MgCl₂·6H₂O (Fisher Scientific) (0.933 g) 1.0M HCl (117 mL), CaCl₂ (Sigma) (0.876 g), Na₂SO₄ (Sigma) (0.216 g), Tris(hydroxymethyl)aminomethane (Tris) (Fisher Scientific) (18.354 g), 1.0M HCl (Fisher Scientific) (0-15 mL). Tris and HCl were added concurrently to maintain a pH of ~7.4.

4.1.4. Plastically compressed dense collagen hydrogels

A solution of 13:1 10X Dulbecco's Modified Eagle Medium (DMEM) (Gibco) to 5N NaOH (Fisher Scientific, Sodium Hydroxide Solution 5N) was created. A 5.83 mg/mL bovine dermis (BD) collagen solution collagen solution (Devro Medical, Purified Soluble Collagen) was added at 4:1 by volume to the DMEM. The pH was adjusted to 7.4 by adding NaOH while kept at ~4 °C using an icepack or a box filled with ice. [80], [84].

To produce Dense Collagen (DC) gels, a 48-well plate (10.5 mm diameter per well) was filled with 1 mL of the above solution (DMEM, NaOH and collagen) and, similar to a previously established protocol [80], left in an incubator (Thermo Scientific, Forma Series II) at 37 °C for 30 minutes. Collagen gels were then subjected to a plastic compression method [80], [83], [84], [192] by applying 1 kPa (40 g per 350 mm²; 160 g for four gels) for five minutes to collagen gels placed between two nylon meshes and on top a steel mesh and blot paper (the latter to collect expelled water). The load was applied to expel water and retain collagen, and produce DC gels (see Figure 4.1).

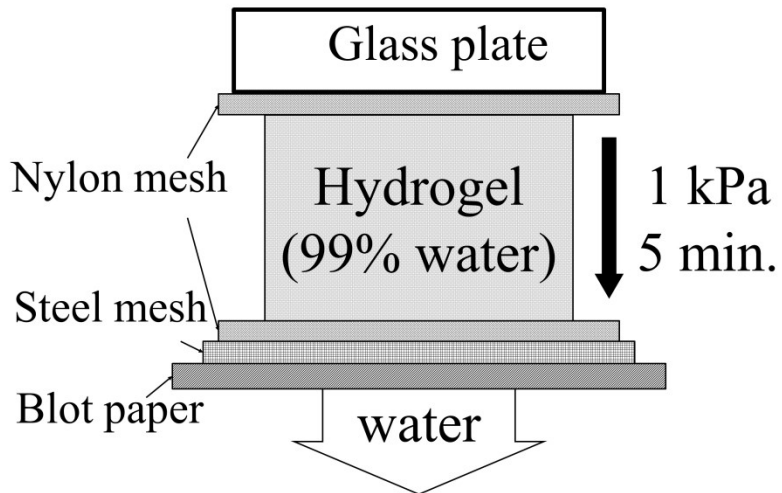


Figure 4.1: Schematic of method used for plastic compression

Hydrogels containing a FDP additive (C_s or C_p) were created following the previously outlined protocol [80]. The process for creating DC hydrogels containing C_s (DC- C_s), and C_p (DC- C_p) was identical to that outlined above, with an interim step of mixing the additive in the DMEM then ultrasonication the solution prior to adding NaOH and collagen. Collagen was added to the DMEM at 4:1, and FDPs to polymer ratios of 1:10 1:2 and 1:1 were used to determine the effect of FDPs in the biominerilization of collagen gels, with pure collagen gels used as control. After adding collagen, the solution was magnetically stirred to ensure a homogenous solution.

4.1.5. Coatings preparation

CTS with a degree of deacetylation of 75%, anhydrous ethanol and acetic acid were purchased and CTS was protonated and dissolved in a 0.6 M acetic acid solution to create a 3 mg/mL solution. A commercial 2 mg/mL acid soluble Type I collagen solution in acetic acid was used. CuO-doped phosphate glasses (0, 5 and 10 mol% CuO) with the formulation of $50P_2O_5-30CaO-(20-x)Na_2O-xCuO$ were created by melting several reagents ($CaCO_3$, $CuSO_4$, $NaH_2PO_4 \cdot H_2O$ and P_2O_5) in a 90%Pt/10%Rh crucible at 1350 °C [151]. Anhydrous ethanol was used to create a solution with CTS, collagen and PG.

PG was obtained by dry blending P_2O_5 , $CaCO_3$, NaH_2PO_4 , and $CuSO_4$ precursor powders, heating the mixture at 350 °C for moisture elimination for 30 min, and melting at 1350 °C for 3 h in the 90%Pt/10%Rh crucible. Once cooled, it was ground into fine particles with a mortar and pestle and separated by size using a 38 µm sieve.

Initial EPD experiments of CuO-doped phosphate glass were carried out by creating a solution of 17% polymer, 83% ethanol. CuO-doped phosphate glass (0, 5 and 10 mol% CuO) was added to the solution to reach a final concentration of 0.5 g/L and ultrasonicated to ensure a homogenous distribution.

CuO-doped phosphate glass (0, 5 and 10 mol% CuO) was separated using a 38 µm sieve and was added to an ethanol solution (to prevent dissolution) and ultrasonicated. The 38 µm sieve, the smallest size available, was used as larger PG particles sediment to the bottom of the flask faster than smaller ones. Collagen/CTS was then added to the solution while being magnetically stirred, then ultrasonicated, to create a 40 mL solution (see Table 4.2). The end result was a 0.5 g/L PG, 0.5 g/L polymer solution in 83% ethanol. The solution was magnetically stirred and then ultrasonicated for 15 minutes prior to deposition to ensure homogenous distribution of both the polymer and glass particles.

Table 4.2: Collagen/CTS-PG solutions used for EPD

Polymer mixture	[CTS] (g/L)	[collagen] (g/L)	[PG] (g/L)
CTS	0.50	0.00	0.5
1:2	0.33	0.17	0.5
1:1	0.25	0.25	0.5
2:1	0.17	0.33	0.5
Collagen	0.00	0.50	0.5

4.1.6. Electrophoretic deposition

Electrophoretic deposition was carried out under constant voltage at 30 V for 10 minutes in triplicate using a DC power supply (YaeTek Variable Adjustable Lab DC Bench Power Supply 0-30 V, 0-5 A) on 304 stainless steel (McMaster-Carr). Electrodes 40×20 mm² in size were used for both the anode and the cathode. The electrodes were submerged to a depth of 20 mm. Then immediately post-deposition the electrodes were removed and left to dry at room temperature. The electrodes were weighted before and after deposition to measure the amount of material deposited.

4.2. Mineralization of hydroxyapatite within additive-incorporated hydrogels

Additives (C_s, C_p and PG) were immersed in SBF (pH 7.4, 37°C) at a minimum 1:3 ratio (3 mg/mL) and placed in an incubator from 24 hours (for C_s and C_p) to a week (for PG) before being removed and analysed. Hydrogels incorporating additives were immersed in SBF using a hydrogel to SBF ratio of 1:3 (mg/mL). The solution was replaced at two or three-day intervals by fresh SBF.

DC-C_s and DC-C_p Samples were taken at days 0, 3, 7, 10 and 14, and hydrogels congaing PG samples were analysed at days 0, 1, 3 and 7. The results were compared to gels that had no additives incorporated. HA nucleation in bone occurs within the gaps of collagen fibrils [48], though for scaffolds constructed *in vitro*, a high concentration of carboxyl groups was shown to lead to HA nucleation. Charged amino acids act as nucleation sites, where calcium ions are gathered through electrostatic attraction, which then attract phosphate ions until a critical concentration is reached, leading to HA formation [49-52]. The nucleation of HA is thus expected to occur around the charged particles within the collagen scaffold.

4.3. Liquid chromatography–mass spectrometry

Liquid Chromatography–Mass Spectrometry (LCMS) is an analytical technique that combines separating the samples via liquid chromatography and analysing them in a mass spectrometer to determine the mass-to-charge ratio of ions and identify them [193].

Analysis of samples was carried to determine the amino acid composition of the silk fibroin derived polypeptides on a QTOF (Agilent). LCMS was carried out at IRIC-Université de Montréal Proteomics facilities. The results were analysed in Microsoft Excel.

4.4. Particle size analysis

Particle Size Analysis (PSA) is useful for determining the size distribution of a group of particles. PSA (Horiba LA-920) was performed on C_s and C_p to determine the size distribution. A 0101 (non-spherical) correction factor was used to account for the irregular shapes of C_s, C_p, and glass particles. Isopropanol was used to create a solution that was then ultrasonicated before analysis. A refractive index of n_D²² 1.55 (n_D²² 1.13 in isopropanol) was used to calculate the size distribution of the FDPs based on values obtained from the literature [194], [195].

We used a refractive index of 1.54 [196] to analyse the PG particles. Particles were immersed in isopropanol and measured immediately after and 15 minutes after being ultrasonicated, and analysed using a 0101 (non-spherical) correction factor.

4.5. Fourier transform infrared spectroscopy

Attenuated Total Reflectance Fourier Transform Infrared Spectroscopy (ATR FT-IR) (Perkin Elmer, Spectrum 400) was used to characterize the mineralization that occurred in the sample, as well as any changes in the chemical composition of the sample itself. ATR-FTIR can be used to determine the

extent of mineralization by measuring the change in peaks associated with phosphate relative to the amide peaks of collagen/chitosan. As the amount of organic material within the scaffold is fixed, spectra normalized to these peaks will show HA via a change in the phosphate peaks. These can be compared to control samples as a baseline to show the nucleation/growth of HA.

The bands associated with PO_4^{3-} , indicative of the presence of HA, were compared between timepoints and samples to monitor HA mineralization [80], [197]. Additionally, IR is sensitive to the substitution of PO_4^{3-} ions by CO_3^{2-} ions, and can detect the presence of small amounts of carbonate, indicating the formation of carbonated hydroxyapatite [198].

Samples were prepared for ATR-FTIR analysis by first washing in dH₂O to remove any excess SBF, then freezing in liquid nitrogen, then freeze-drying (lyophilizing) the sample until all the excess moisture had been removed. The sample was then analysed at a resolution of 2 cm⁻¹ in the IR range of 4000 to 650 cm⁻¹ at 32 scans per sample. The resulting spectra were normalized against the Amide I band found between 1800 to 1650 cm⁻¹ for comparison (Spectrum 10 software, Perkin-Elmer) [81], [84].

Samples of bone were obtained from a local butcher, and were prepared by boiling in water and then acetone at room temperature for defatting and to help remove oils and soft tissue. The bone was then grated into fine particles, a portion of which were then calcined at 1000 °C to produce natural HA [199].

4.6. X-Ray diffraction

X-Ray Diffraction (XRD) XRD can be used to pinpoint the crystal structure of HA. The pattern obtained from XRD can be compared to that of HA within the International Centre for Diffraction Data (ICDD) databases; a match to this pattern would confirm the presence of HA.

XRD (Bruker D8, Bruker-AXS Corp.) was performed on C_p and C_s fragments, CuO-doped PG as well as freeze-dried hydrogels that had been immersed in SBF and natural and calcined bone. Samples were compressed and taped onto glass slides to produce a flat, fixed surface, and XRD analysis was performed using a Cu-K_α source. XRD patterns were recorded from 3 to 104° 2 theta at 40 kV and 40 mA. Four frames of 25° were recorded for 150 seconds and then merged during data post processing. The resulting patterns were analysed (EVA 14.0.0.0, Bruker) and compared with spectra with HA peaks identified in ICDD file 00-009-0432

4.7. Scanning electron microscopy

Samples for Scanning Electron Microscopy (SEM) imaging can be used to determine how HA nucleated within the hydrogel (e.g. localized vs interfibrillar). SEM will also be used to determine the form of HA – within bone HA forms “plates” that cover collagen, while *in vitro* it typically forms a “cauliflower” crystal.

Samples were prepared by immersing the hydrogels in 30, 50, 70, 80, 90, 95 and 100% ethanol solutions to remove all the water [80], [84]. The gels were then immersed in 1,1,1,3,3-hexamethyldisilazane (HMDS) and left overnight until all the HMDS had evaporated. All samples were sputter-coated with a layer of Au/Pd then analysed by SEM (FEI Inspect F-50 FE-SEM, FEI).

Films were morphologically assessed via SEM. The samples were sputter-coated with 5 nm platinum to ground the samples and prevent charging, and analysed at a 5 kV acceleration voltage and at a working distance of 10 mm.

4.7.1. Backscattered Electrons and Electron Diffraction Spectroscopy

The prepared SEM samples were analysed using backscattered electrons (BSE) and electron diffraction spectroscopy (EDS). BSE can be used to determine the extent of mineralization across the hydrogel. BSE shows the contrast between organic/inorganic materials, and can show where HA is within the collagen/chitosan hydrogel. EDS can be used to determine elemental composition of samples, as well as create an EDS map of elements across the sample.

Samples were analysed by increasing the acceleration voltage to 20 keV. This high voltage is required to increase the contrast between the SEM hydrogel samples and the underlying phosphate glass particles. EDS was performed on the SEM samples to determine the composition of particles seen in hydrogels after seven days’ immersion in SBF. Also, determine the elemental distribution of the particles, Point analysis was used.

4.8. Quartz Crystal Microbalance

A Quartz Crystal Microbalance (QCM) can measure the mass of a deposit relative to time, giving information on the deposition kinetics of the process for different materials.

Deposition kinetics of different mixtures was investigated using an electrochemical quartz crystal

microbalance (Princeton Applied Research, QCA922). The deposited mass, Δm , was calculated using Sauerbrey's equation [200]:

$$\Delta f_M = -\frac{2f_0^2}{A\sqrt{p_q\mu_q}}\Delta m \quad (4.1)$$

where f_0 is the resonant frequency (Hz), Δf is the change in frequency (Hz), Δm is the change in mass (g), A is the active area of the crystal (cm^2), p_q is the density of quartz (2.648 g/cm^3) and μ_q is the shear module of AT-cut crystal ($2.947 \times 10^{11} \text{ g/cm}\cdot\text{s}^2$).

For a quartz crystal in a liquid, there is a damping effect described by Kanazawa and Gordon as follows [201]:

$$\Delta f_L = -f_0^{3/2} \sqrt{\frac{p_L n_L}{\pi p_q \mu_q}} \quad (4.2)$$

where n_L is the solution viscosity (1.095 cP for ethanol, 0.89 for water) and p_L is the solution density (0.8 g/cm³ for ethanol, 1 g/cm³ for water). The overall resonance of the QCM [202], Δf , is then calculated by:

$$\Delta f = \Delta f_M + \Delta f_L \quad (4.3)$$

4.9. Electrophoretic mobility and zeta potential

The zeta potential of collagen, CTS, and collagen/CTS molecules were determined using a particle electrophoresis system. Collagen and chitosan were analysed in a 0.1M solution of acetic acid at 20 °C, with a viscosity of 1.020 cP, a refractive index of 1.33 and a dielectric constant of 78. A Zeta Potential/Particle Size Analyzer (ZETA) (Brookhaven Instrument Corp., ZetaPlus / BI-PALS) was used to measure the electrophoretic mobility distributions of different particles/mixtures under a 15 V/cm electric field, from which the zeta potential distribution was calculated.

4.10. Electrical Impedance Spectroscopy

Electrical Impedance Spectroscopy (EIS) is a useful technique for monitoring the electrical impedance during electro-chemical processes, and revealing electrical properties of materials. EIS was carried out

to measure the current density of the cell during EPD, between 5-30 V for 5 minutes. The current density at each voltage was recorded using a source meter (Keithley 2400 Source Meter, Tektronix), and the resistance was calculated using Ohm's law.

4.11. Thermogravimetric Analysis

Thermogravimetric analysis (TGA) allows for quantifying the extent of organic vs inorganic materials in a sample. The amount of HA/PG can be determined by raising the temperature to cause all organic matter to burn off and be released a gas, leaving the mineral/glass component.

TGA (TA Instruments, TGA Q500) was carried out on samples that had been left to dry overnight at SATP. Samples were heated at a rate of 10 °C/minute in air until they reached 700 °C.

4.12. Statistical analysis

The data was analyzed for statistical significance using a one-way ANOVA with a statistical significance level of 0.05. Tukey and Holm-Bonferroni methods were used for comparison (Origin Pro v9.0 software, OriginLab).

5. Materials characterization

5.1. Silk Fibroin-derive polypeptides

Characterization of the starting materials (C_s and C_p) was carried out using ATR-FTIR to determine their chemical composition, which can serve as a reference (control) for future tests. While the ATR-FTIR spectra of C_p and C_s are quite similar, still there are slight differences, such as the shoulder at 1695 cm^{-1} in C_p and the amide I band at 1650 cm^{-1} for C_s . This can be attributed to C_p polypeptides being composed of the crystalline regions of silk fibroin and having a β -sheet type structure, while C_s has an α -helix type structure [118], [203]. The spectra for C_p (see Figure 5.1: A) exhibit a shoulder on the amide I band at 1695 cm^{-1} that is typically associated with a β -sheet structure of SF, as well as Amide I, II and III absorptions at 1622 , 1515 and 1230 cm^{-1} that are characteristic of SF [80], [204]. The spectra for C_s (see Figure 5.1: B) differed slightly in the amide I band at 1650 cm^{-1} that is typical of an α -helix type structure, though it still has the Amide II and III bands at 1530 - 1515 cm^{-1} and 1239 cm^{-1} , respectively [80].

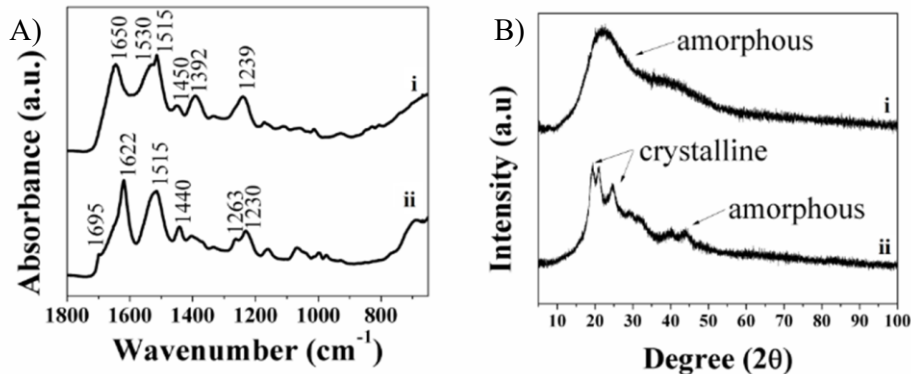


Figure 5.1: A) ATR-FTIR spectra showing secondary structures and B) XRD patterns showing amorphous/crystalline structure for as-made i) C_s and ii) C_p . Arrows in the XRD patterns indicate crystalline regions and amorphous regions

XRD patterns for C_s and C_p (see Figure 5.1B) fragments revealed a crystalline structure in C_p that is similar to XRD patterns of SF reported elsewhere [205], while C_s fragments resulted in spectra confirming their amorphous nature. SEM images of C_s and C_p also indicate that C_p has a crystalline structure, while C_s has an amorphous structure (see Figure 5.2). These results confirmed that the structure of SF is composed of both the crystalline phase of C_p and the amorphous phase of C_s .

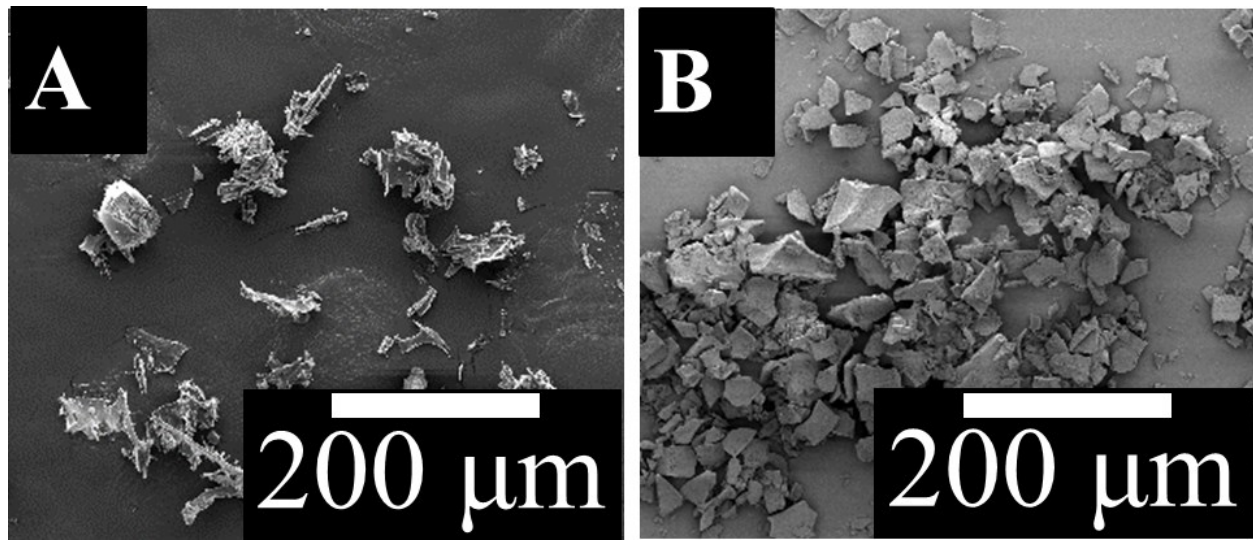


Figure 5.2: SEM images of A) C_s and B) C_p particles

The size distribution of C_p and C_s particles indicates that C_p is significantly larger than C_s (see Figure 5.3). The mean particle size of C_p is 91.02 μm , while C_s is only 22.46 μm . The difference in size can be attributed to C_p having a molecular weight 4-20 times higher than C_s [80], but is more likely due to the structure of C_p taking the shape of compacted crystals, whereas C_s is an amorphous chain [206]–[209]. The use of α -chymotrypsin to separate the two phases can more easily cleave the amide bonds between proteins revealed in the amorphous C_s chain, while not being able to affect the crystalline C_p to the same degree, resulting in larger crystalline C_p and smaller chunks of C_s [209]–[211]

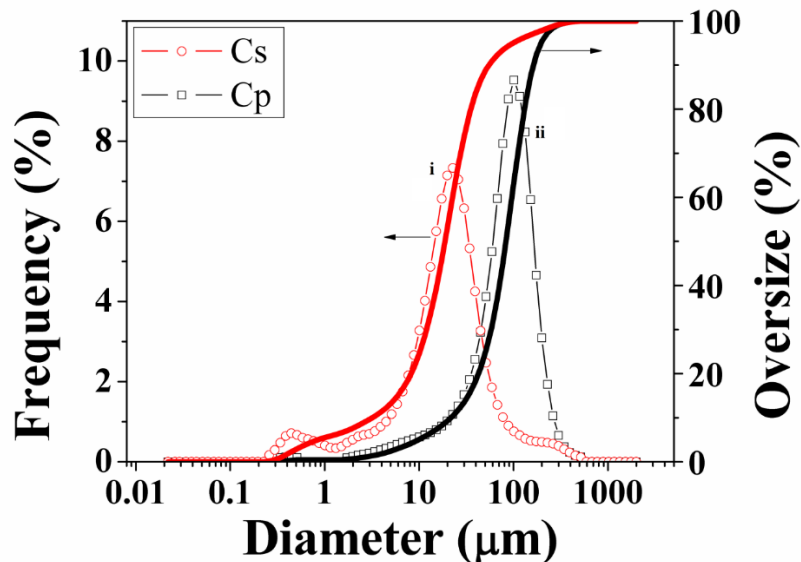


Figure 5.3: Size distribution of i) C_p and ii) C_s particles

LCMS results contrast with the previously assumed composition of the silk fibroin-derived polypeptides (see Table 5.1). LCMS showed that C_s and C_p have a similar composition to silk fibroin. The composition of C_p is similar to values found previously [118]. In contrast, C_s has a slightly more varied composition, though it has a lower concentration of sequences rich in aspartic acid and glutamic acid residues compared to similar results reported in the literature [118], [195]. The values obtained from LCMS match the structure seen previously, with the Glycine amino acids alternating with other amino acids (except for one Ala-Ala link) [212]. The NCBI database for the amino acid composition of silk fibroin polypeptides that are composed of a mixture of Heavy Chains (HC) (NCBI Reference Sequence: NP_001106733.1) and Light Chains (LC) (NCBI Reference Sequence: NP_001037488.1) shows that C_s and C_p also have a similar composition to silk fibroin, though with a lower concentration of glutamic acid (HC – 0.57%, LC – 1.91%) and aspartic acid (HC – 0.48%, LC – 6.49%).

Table 5.1. Comparison of Amino Acid Composition for Fibroin-derived Polypeptides, C_p and C_s, obtained from LCMS (Right – from literature, left – as-made)

Amino Acid	C _p (%) [195]	C _s (%) [195]	C _p (%)	C _s (%)
Alanine	32.03	24.12	29.5±1.7	27.6±2.4
Arginine	0.10	1.31	0.5±0.1	0.4±0.4
Asparagine	0.00	0.00	1.3±0.7	1.8±1.2
Aspartic acid	0.42	4.53	0.9±0.4	1.3±0.8
Cysteine	-	-	0.0±0.1	0.0±0.0
Glutamic acid	0.34	3.12	0.4±0.3	0.4±0.1
Glutamine	0	0	1.1±0.6	2.2±1.1
Glycine	49.13	36.50	43.7±2.5	40.7±3.8
Histidine	0.04	0.54	0.4±0.3	0.7±0.2
Isoleucine	0.19	1.61	1.4±0.6	1.9±0.9
Leucine	0.10	1.71	1.3±1.0	2.5±1.4
Lysine	0.12	0.95	0.2±0.1	0.4±0.2
Methionine	0.03	0.31	0.1±0.1	0.4±0.2
Phenylalanine	0.34	1.47	0.5±0.0	0.6±0.1
Proline	0.13	0.96	0.1±0.0	0.2±0.1
Serine	11.79	9.20	10.8±1.6	10.2±0.4
Threonine	0.47	1.91	1.6±0.5	1.7±0.4
Tryptophan	0.00	0.00	0.0±0.1	0.0±0.1
Tyrosine	3.66	7.55	4.5±0.8	4.7±0.7
Valine	1.11	4.21	1.6±0.5	2.4±0.5

Regarding the charge of the FDPs (see Table 5.2), tabulating the LCMS results shows that overall the FDP is composed of neutral amino acids (97.6% and 96.8% for C_p and C_s, respectively). Compared to the charge calculated from the composition of the FDPs obtained from the literature [195], where 7.6% of the amino acids are negatively charged, there is a significant difference in the charge of C_s, as only 1.5% of the amino acids within the samples examined are negatively charged. It is unlikely that the C_s fragments incorporated into the hydrogel have a high enough charge to be attracted to the collagen, which is cationic in nature [80], as was previously assumed.

Table 5.2. Comparison of charged amino acids (as percentage of total) within FDPs (Right – from literature, left – as-made)

Charge	Quantity of polypeptides			
	C _p (%) [195]	C _s (%) [195]	C _p (%)	C _s (%)
positive	0.22	2.25	1.3% ± 0.5%	1.7% ± 0.9%
negative	0.76	7.65	1.1% ± 0.5%	1.5% ± 0.8%
neutral	98.98	89.56	97.6% ± 0.9%	96.8% ± 1.7%

5.2. Collagen and CTS

5.2.1. Electrophoretic mobility and zeta potential measurements

The Zeta potential, an important parameter when analysing deposition kinetics during EPD, was determined indirectly by measuring the movement of particles in an electric field, and calculating the zeta potential using this value. Collagen, CTS, and collagen/CTS particles (see Figure 5.4) were measured. The results show that CTS has a potential of 85 ± 2 mV, whereas collagen has a much lower potential at 42 ± 3 mV. The addition of collagen to CTS is known to result in an electrochemical reaction between the two molecules, possibly forming a hydrogen bond between the CTS and collagen molecules [84], [213]. The addition of collagen into CTS results in a molecule whose zeta potential decreases linearly with collagen content, with the exception of a 1:2 collagen/CTS molecule.

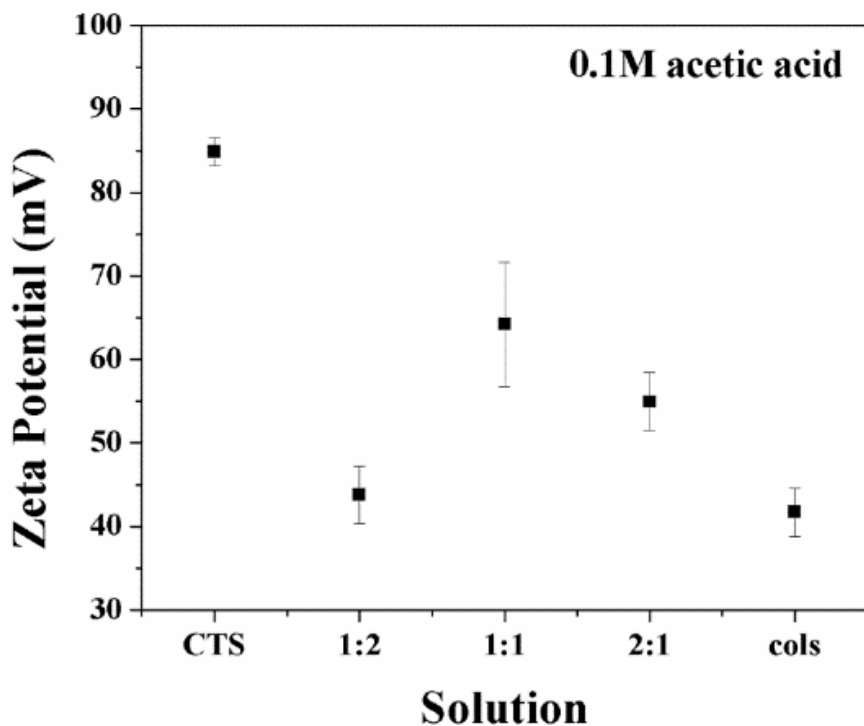


Figure 5.4: Zeta potential measurements of collagen, CTS, and collagen:CTS particles with different relative ratio of collagen and CTS in solution (SD for n=10, p<0.05)

The impact of the zeta potential of a molecule is directly proportional to the electrophoretic mobility [214], which is itself proportional to the deposition rate [154], as higher zeta potential values typically lead to higher deposition yields.

5.2.2. ATR-FTIR Spectroscopy of collagen-CTS Hydrogels

ATR-FTIR of collagen, 1:1 and 1:2 collagen-CTS and CTS hydrogels show distinct patterns depending on the composition of the hydrogel (see Figure 5.5a-d). Figure 5.5a shows that for collagen, the -NH and H-O-H stretching frequencies of collagen corresponding to amide A and B bands were located at 3310 and 2950 cm⁻¹, respectively. The -CN stretching corresponding to the amide III was located at 1240 cm⁻¹. The presence of amide I (-C=O and NH₂) and II (-NH) was confirmed by the bands at 1640 and 1550 cm⁻¹, respectively [84], [215]. With CTS, Figure 5.5d shows the bands corresponding to the glycosidic linkages of the saccharine unites of CTS were observed between 1160 and 1030 cm⁻¹ and are associated with the stretching of C-O-C bonds and C-O stretching. The band at 1510-1650 cm⁻¹ represents the amide group [216], [217], while the broad band at 1408 cm⁻¹ that are associated with the

stretching vibration of --COO^- [216]–[218]. The shift in Amide I and II bands with the addition of chitosan, which can be attributed to the formation of hydrogen bonds between the chitosan and collagen [213], [219].

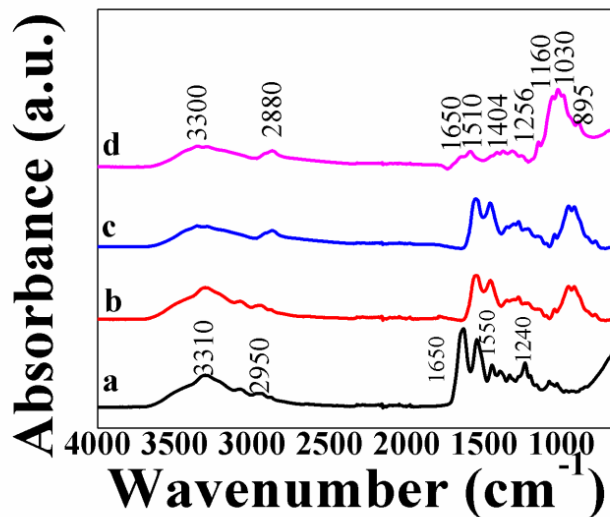


Figure 5.5: ATR-FTIR spectra for collagen a) collagen b) 1:1 collagen-CTS, c) 1:2 collagen-CTS and d) CTS

Both the 1:1 and 1:2 collagen-CTS hydrogels displayed bands corresponding to collagen and CTS, as can be seen in Figure 5.5b,c, with some slight differences due to the interaction between the two molecules. The shift in the amide A band to 3360 cm^{-1} may be attributed to the overlapping of the amide bands of collagen and the -OH of CTS. The increased absorbance bands of the glycosidic linkages and relative decrease the bands of amide I and II with increasing CTS content could also be seen.

ATR-FTIR analysis of the obtained spectra showed that the positively charged NH^{3+} groups of CTS and negatively charged COO^- groups in collagen underwent electrostatic interactions. This interaction can be seen in previous works where collagen interacted with CTS at the molecular level by forming a polyanion-polycation complex or hydrogen bonding [84].

5.3. Copper-doped phosphate glasses

5.3.1. Scanning Electron Microscopy of phosphate glasses

SEM was used to image the morphology of CuO-doped PG particles at various magnifications. Given that electron microscopy is capable of acquiring high-resolution images at extremely high magnification, SEM imaging allows visual inspection of the shapes and sizes of the PG particles.

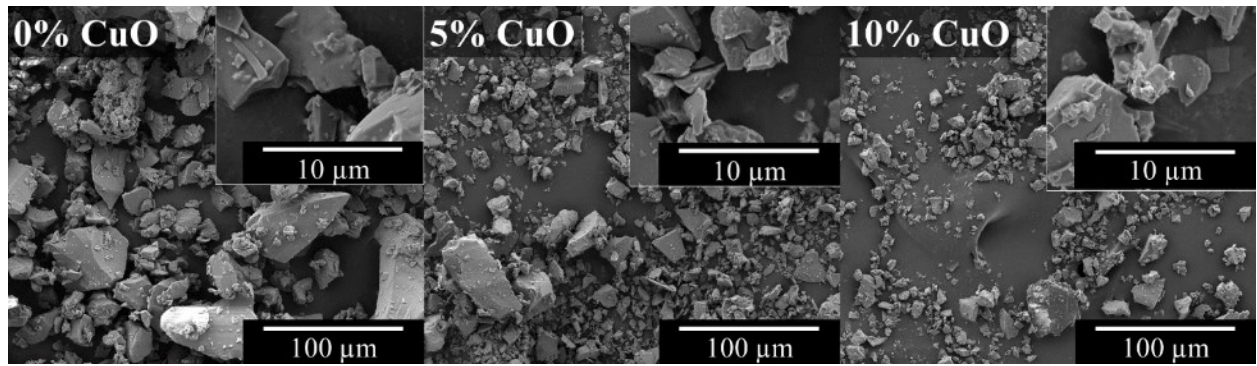


Figure 5.6: SEM images of CuO-doped phosphate glass particles with different doping of CuO: 0% (left); 5% (middle); 10% (right)

SEM images of CuO-doped PG particles (see Figure 5.6) with variable content of CuO (0, 5 and 10 mol%) were acquired. SEM images of CuO-doped PG particles show that the glass particles, which were separated using a 38 µm mesh sieve, have a non-homogenous size distribution with no dimension exceeding 12 µm on average. The addition of CuO to the PG does not appear to have had any effect on the size distribution or shape of the particles, with particles having irregular shapes common to other forms of powdered glass [220].

5.3.2. XRD of phosphate glasses

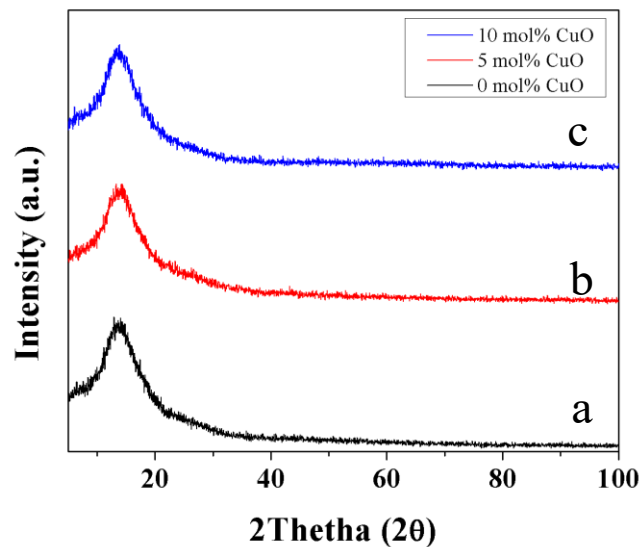


Figure 5.7: XRD patterns for a) 0 mol% b) 5 mol% and c) 10 mol% CuO-doped PG

To further characterize the CuO-doped PG particles, XRD patterns of CuO-doped PG particles with different mol% of CuO were acquired. Figure 5.7 shows the XRD patterns of CuO-doped PG with CuO

(0, 5 and 10 mol%). The diffraction patterns of the different glasses are identical, regardless of the amount of CuO (5 and 10 mol%) incorporated. There are no discrete or sharp peaks, but the continuous broad diffuse peak around $2\theta=15^\circ$ due to the scattering of X-rays, is typical of an amorphous structure, similar to reports in the literature for PG doped with metal oxides [221], [222].

5.3.3. ATR-FTIR of phosphate glasses

ATR-FTIR was used to create a distinct spectrum associated with the material being analysed. These spectra could then be compared to other materials to determine similarities or differences, and determine the chemical compositions of the samples.

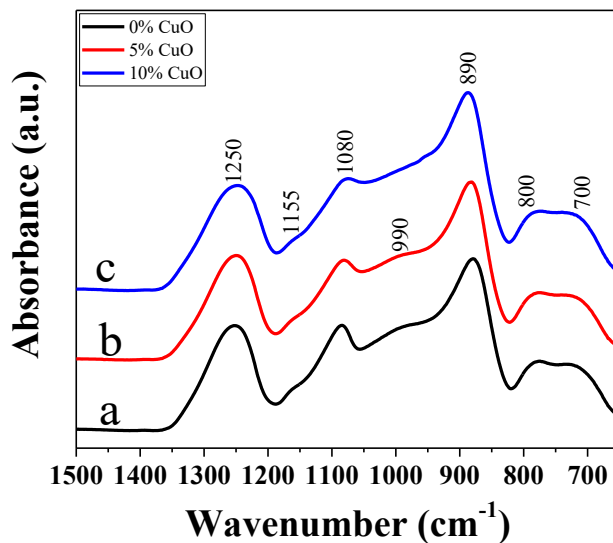


Figure 5.8: ATR-FTIR spectra for PG incorporating a) 0 mol% b) 5 mol% and c) 10 mol% CuO

ATR-FTIR absorption spectra, specifically the region related to phosphate absorption bands (see Figure 5.8), shows specific absorption bands related to the symmetric/asymmetric stretching of phosphate groups (denoted by the “sym” and “asym” subscripts, respectively). Specifically, the band at 1250 cm^{-1} correlates with the PO_2 as units in a Q^2 phosphate tetrahedral, while the shoulder at 1155 cm^{-1} correlates with the stretching of $(\text{PO}_2)_{\text{sym}}$ units. The band at 1080 cm^{-1} and the broad band at 990 cm^{-1} are associated with P-O^- bonds of a Q^1 chain. The strong band at 890 cm^{-1} is associated with $(\text{P-O-P})_{\text{asym}}$ units, while the two bands between 800 and 700 cm^{-1} are associated with $(\text{P-O-P})_{\text{sym}}$ units. CuO content could not be verified by additional bands, but it affected the intensity of P-O^- band at 1080 cm^{-1} , which showed a dampening in the band that is due to the metal oxide bonds forming between copper and oxygen [151], [223].

5.3.4. Particle Size Analysis before and after sedimentation

Particle size analysis was used to measure the size distribution of PG particles used for deposition. The results demonstrated that particles form a polydisperse suspension and that, regardless of dopant, the size distribution shifts to towards smaller diameters (see Figure 5.9A-C). Figure 5.9D shows that that smaller particles remained suspended in solution, yet gravitational forces overcame repulsive forces for larger particles [224], regardless of the dopant. The median and mean diameter of the remaining particles decreased by 2.9 – 4.5 μm and 5.2 – 6.25 μm , respectively (see Table 5.3), which is expected, since the particles were filtered using a 38 μm sieve.

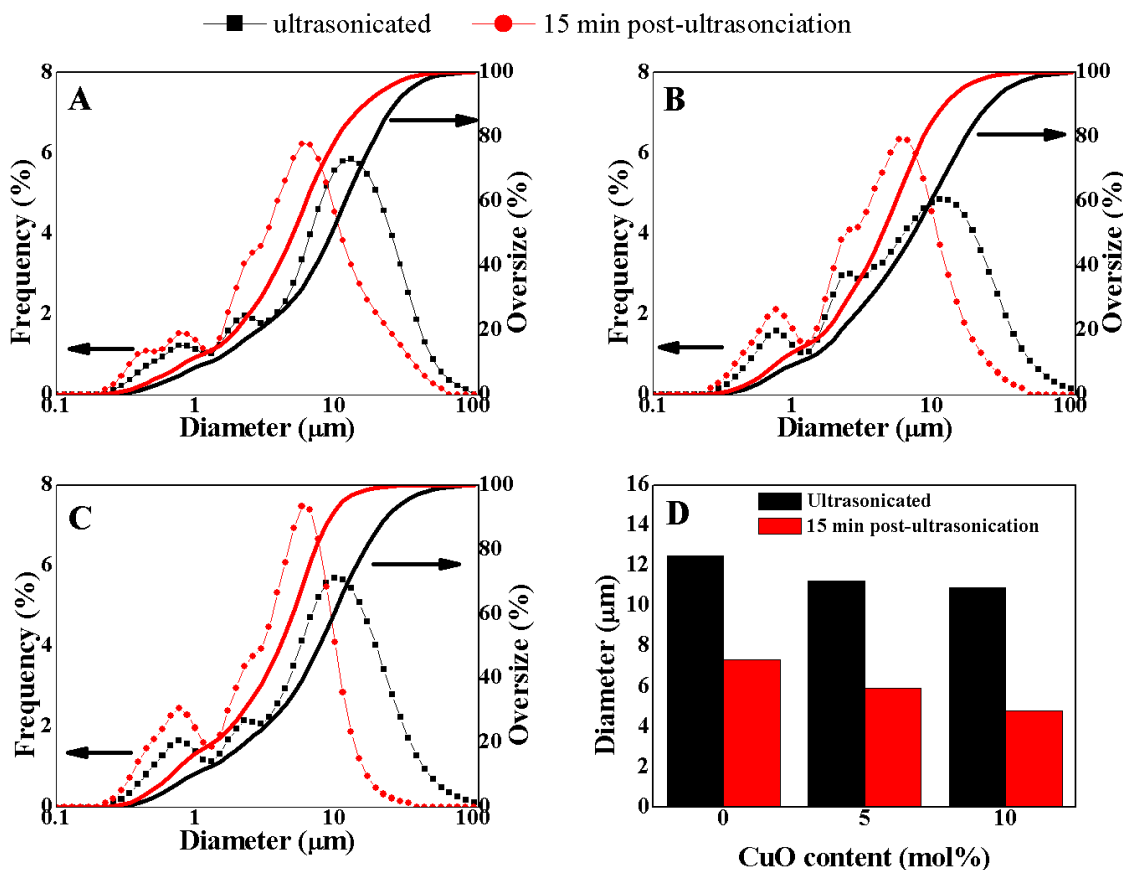


Figure 5.9: Particle size analysis of CuO-doped PG immediately after (black color line/circle) and 15 minutes after ultrasonication (red color line/circle): A) 0 mol% B) 5 mol% and C) 10 mol%; D) Variation of Diameter with CuO doping (mol%)

Table 5.3: Diameter of particles before and after sedimentation

CuO (mol%)	Ultrasonicated		Post-ultrasonication		Change	
	Median (μm)	Mean (μm)	Median (μm)	Mean (μm)	Median (μm)	Mean (μm)
0	9.52	12.50	5.05	7.32	4.47	5.18
5	7.39	11.26	4.45	5.90	2.94	5.36
10	7.81	10.92	4.09	4.77	3.72	6.15

The difference in particle size with the presence of CuO can be attributed to an increase in the strength imparted by copper atoms to the PG. Previous work has shown that CuO-doped PG glass exhibits a decrease in dissolution because the presence of CuO results in higher M-O bond strength [151]. Similarly, it can be expected that the stronger the bonds within the glass, the more brittle it is, as the lack of ductility would make it break more easily and into smaller particles.

6. Silk Fibroin-enhanced hydroxyapatite mineralization *in vitro*

6.1. XRD analysis of silk fibroin-derived polypeptides *in vitro*

Polypeptides (C_s and C_p) immersed in Kokubo's SBF at 37 °C (see Figure S.1), in order to imitate a physiological environment. The FDPs showed aggregation within a day. The HA aggregate was confirmed from XRD analysis (see Figure 6.1). While HA can exist in different forms, depending on the condition of its formation [225], the method of nucleation remains the same. It is known that HA forms an intermediary amorphous calcium phosphate, that HA crystals exhibit “polycrystalline character of the elemental particles,” and nucleation is favoured [226], which would indicate that HA forms are determined by nucleation conditions.

The resulting XRD pattern showed peaks that matched the corresponding pattern for HA (ICDD file 00-009-0432), and was also similar to XRD patterns obtained from analyzing natural bone (see Fire S.2), indicating that both polypeptides lead to the nucleation of HA at physiological conditions. Given the similar composition and charge of C_s and C_p (see Table 5.1), it is to be expected that both would nucleate HA. Previous work has shown that the presence of acid-rich proteins (specifically aspartic and glutamic acid) led to biominerization *in vitro* [227], [228] via epitactic nucleation, whereas heterogeneous nucleation occurs via the formation of critical nuclei on a surface [229]. The XRD measurements of C_s and C_p immersed in SBF results in a diffraction pattern identical to that arising from HA.

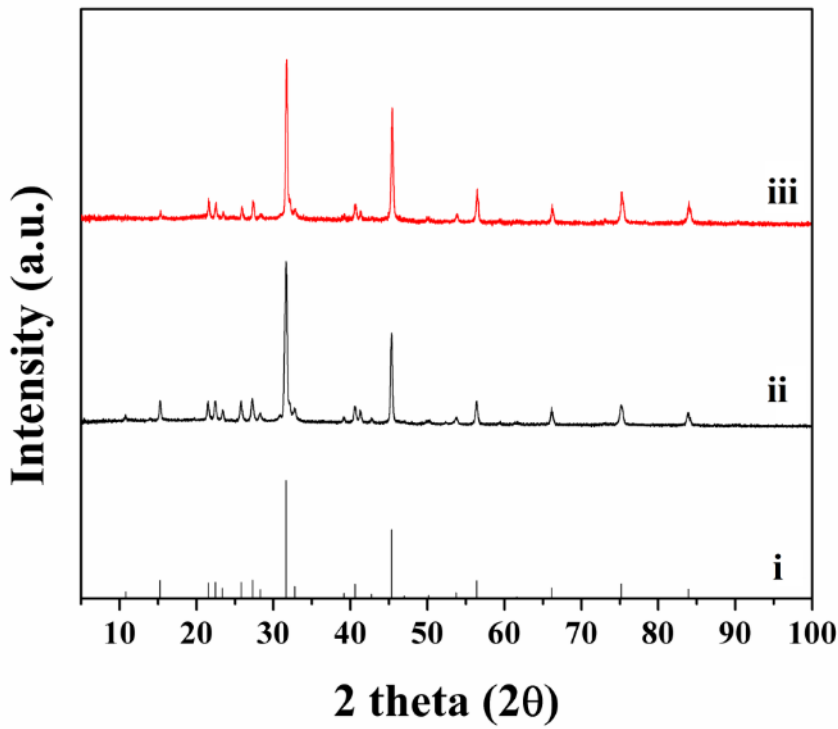


Figure 6.1: XRD patterns of i) HA (ICDD file 00-009-0432) and polypeptides ii) C_s and iii) C_p immersed in SBF

6.2. Scanning electron images of DC hydrogels post-immersion in SBF

Hydrogels incorporating C_s and C_p at a 1:10 additive to collagen ratio (by mass) were created as stated. SEM imaging was performed as described above. The results for DC, 1:10 DC-C_p and 1:10 DC-C_s gels, after seven days' immersion in Kokubo's SBF were analysed to visually determine whether HA nucleation occurred.

SEM reveals no major differences in the morphology of the as-made hydrogels, either DC, 1:10 DC-C_s or 1:10 DC-C_p (see Figure 6.2). Particles that differed were seen in the DC and 1:10 DC-C_p gels at day 7, though there were no signs of particle nucleation in the 1:10 DC-C_p gels. In the DC/1:10 DC-C_s gels, the particles were located in small clumps of 1-20 particles randomly spaced across the surface of the hydrogel. Similar results were seen in DC gels incorporating silk sericin, though particles were much more uniformly dispersed and larger [230], compared to the hydrogel surface remaining bare with silk FDPs. No evidence of C_s is observed in the hydrogels via SEM at day 7, indicating that electrostatic interactions between collagen and the hydrophilic FDP [80] do not last.

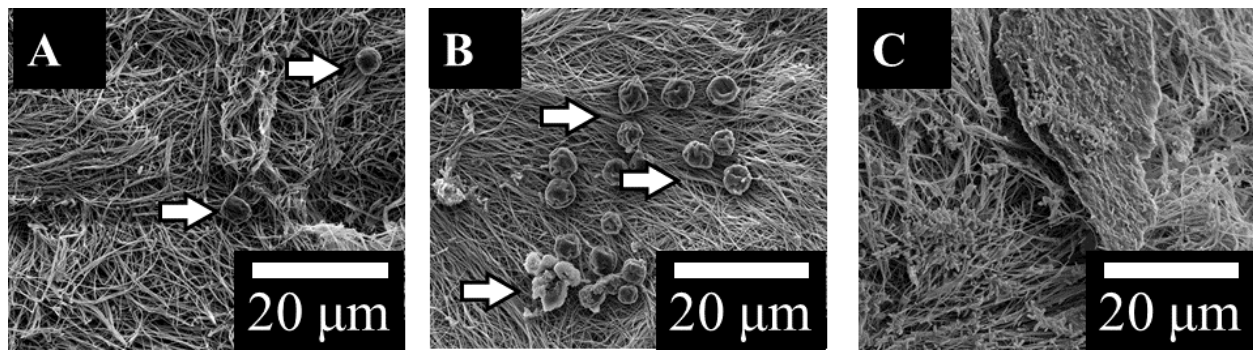


Figure 6.2: SEM of Plastically compressed A) DC, B) 1:10 DC-C_s and C) 1:10 DC-C_p hydrogels immersed in SBF for 7 days (scale bar is 10 μ m, arrows indicate particles)

6.3. ATR-FTIR and XRD analysis of DC/FDPs hydrogels

Spectroscopic and XRD analysis was conducted on DC hydrogels, both with and without additives incorporated, as described above. The resulting ATR-FTIR spectra were plotted and showed that bands indicative of the presence of HA; ν_3 PO₄³⁻ (1030 and 1080 cm⁻¹) [81], [231], [232], as well as the bands for ν_3 and ν_2 CO₃²⁻ (1450 and 1400 cm⁻¹ and 850 cm⁻¹ respectively) [81], [231] were present in all samples, post-immersion in SBF. The presence of type I collagen is confirmed from the bands at 1630, 1550 and 1240 cm⁻¹, corresponding to the amide I, II and III groups respectively [81], [233] (see Figure 6.3) present in all samples.

The spectra obtained show that there was an increase in the ν_3 PO₄³⁻ over the first 10 days compared to the initial band, indicating the occurrence of HA nucleation/growth. This was particularly apparent in DC and 1:10 DC-C_s gels (see Figure 6.3A, B), as well as in the 1:10 DC-C_p gels (see Figure 6.3:C).

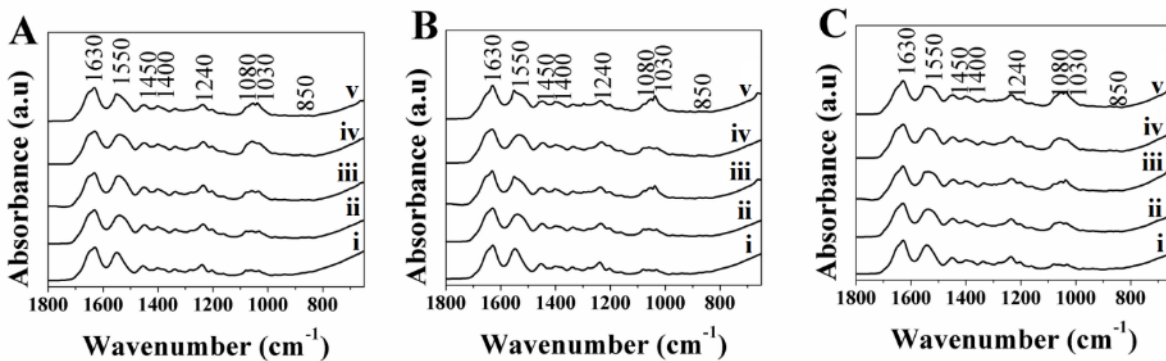


Figure 6.3: ATR-FTIR Spectra for A) DC, B) 1:10 DC-C_s and C) 1:10 DC-C_p, gels immersed in SBF at day i) 0, ii) 3, c) 7, iii) 10 and iv) 14.

The spectra indicated that all hydrogels showed a presence of phosphate and carbonate groups, suggesting that some HA nucleation occurs within the hydrogel. Comparing the value of the peaks associated with phosphate and carbonate showed the bands associated with phosphate increased with time (see Figure 6.4A), with Dc and DC-C_s showing statistical significance from day 0 to 10, and DC-C_p remaining stable. The value of the peaks associated with carbonate did not show any statistical significance with each other, save for DC at day 0 (see Figure 6.4B), indicating that phosphate absorbance within the collagen increases over time. This change can be attributed to the mineralization of non-carbonated HA, and is consistent with previous findings [81]. The hydrogels that had C_s incorporated did not show significantly higher values associated with the phosphate peak, contrary to earlier work [80], indicating that it does not serve to nucleate HA at a higher rate. The ratio of phosphate and carbonate peaks to the Amide I band remained nearly constant over time, indicating that little change takes place within the 1:10 DC-C_p or C_s gels, and was significantly lower than phosphate band in natural bone (see Figure S.3). The similarity between DC-C_s and DC-C_p can be attributed to both FDPs having similar amino acid compositions, as was shown via LCMS. While there appears to be some difference with the pure DC gels, particularly at day 10, there is significant overlap, indicating that it is collagen, and not the FPDs, that are responsible for mineralization *in vitro*. It is likely that the FDPs distributed within the hydrogel lack the acidic amino acids, particularly glutamic acid, necessary for the nucleation of HA [227], [228], [234]. Additionally, the lack of electrostatic interaction between collagen and the mainly neutral FDP is also a barrier to HA formation, as it was shown to be necessary for mineralization to occur [229], [235].

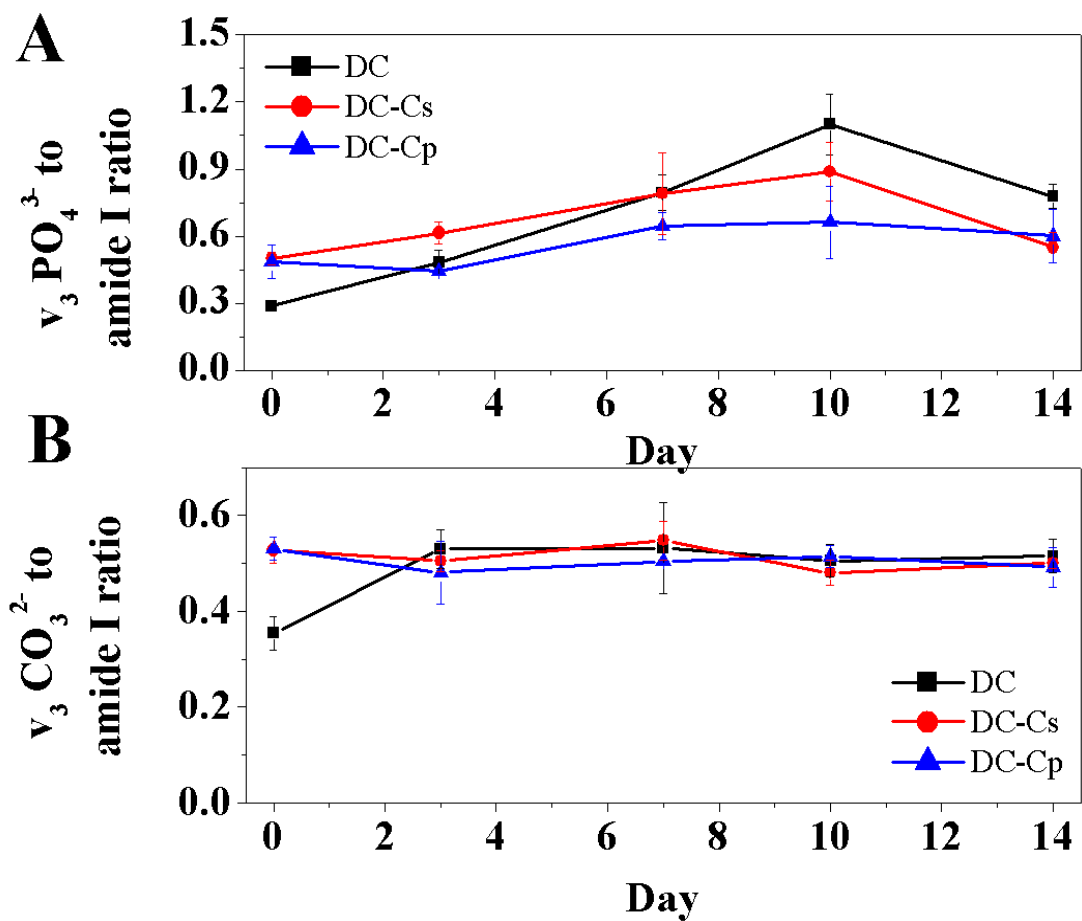


Figure 6.4: Ratio of A) v₃ PO₄³⁻ and B) v₃ CO₃²⁻ bands to amide I bands from ATR-FTIR spectra of DC gels containing no additives, C_s and C_p (at a 1:10 ratio to collagen) immersed in SBF (SD, n=4, p<0.05)

The XRD patterns for DC hydrogels immersed in SBF showed that the formation of HA occurs in all samples and increases over time, though the extent of mineralization differs based on whether it was a DC, DC-C_p or DC-C_s hydrogel (see Figure 6.5). XRD patterns for pure collagen hydrogels showed peaks at $2\theta = 33^\circ$ and 45° in all samples, which are associated with HA [236]. The latter also exhibit a peak at $2\theta = 23^\circ$ in an otherwise amorphous section of the pattern. As collagen is an amorphous material with no defined peaks, and the $2\theta = 23^\circ$ peak does not match any peaks associated with HA, the presence of this peak was attributed to the polyethylene (PE) tape used to hold the samples in place. In addition, the peak corresponds to ICDD file 00-060-1505 for PE.

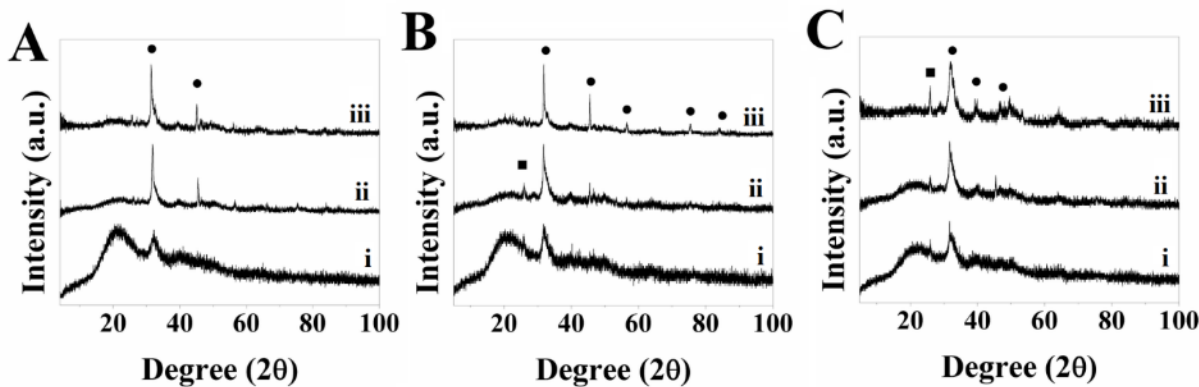


Figure 6.5. XRD pattern for A) DC, B) 1:10 DC-C_s and C) 1:10 DC-C_p hydrogels immersed in SBF at days i) 3, ii) 7, iii) 14 (• – HA corresponding to ICDD file 00-009-0432, ■ – PE corresponding to ICDD file 00-060-1505)

XRD patterns confirmed the nucleation of HA in all samples. The 1:10 DC-C_s hydrogels (see Figure 6.5B) initially showed a similar extent of mineralization as DC and 1:10 DC-C_p gels on days 3 and 7. However, the XRD patterns for DC and DC-C_s hydrogels (see Figure 6.5A, B) showed much higher HA peaks at day 14, indicating a greater extent of mineralization than DC-C_p (see Figure 6.5C) hydrogels in the long-term. In particular, the peak at $2\theta = 45^\circ$ was not as apparent as in other DC and DC-C_s hydrogels. In general, however, both 1:10 DC-C_s and DC-C_p hydrogels showed that their incorporation led to HA nucleation, which can be explained by the fact that both C_s and C_p have similar amino acid compositions, as seen by the LCMS results, and the fact that both C_s and C_p lead to the nucleation of HA, as confirmed by the XRD pattern from the particles were immersed in SBF (see Figure 6.1). The major difference between C_s and C_p is related to the high, narrow peak at $2\theta = 23^\circ$. The $2\theta = 23^\circ$ peak is present in all samples, but the intensity is much greater in the DC and DC-C_s samples. The broad peaks in the DC-C_p samples are attributed to a relatively small crystal size [237]–[239] or to the poorly crystalline nature [240], [241] of HA within the sample. The XRD results match ATR-FTIR results, which shows that FDPs do not have a significant impact on HA nucleation due to the lack of the necessary acidic amino acids [227], [228], [234] or of the electrostatic interaction between collagen and FDP [229], [235].

ATR-FTIR was also conducted on hydrogels with a higher amount of FDPs additive added (1:2 and 1:1) that were immersed in SBF for 3 and 7 days (see Figure 6.6). The resulting spectra for the different types of hydrogels, only DC-C_p showed that bands attributed to ν_3 PO₄³⁻ (1030 and 1080 cm⁻¹) [81], [231], [232], increased with time, while the bands for ν_3 and ν_2 CO₃²⁻ (1450 and 1400 cm⁻¹ and 850 cm⁻¹ respectively) [81], [231] remained relatively constant, similar to the results obtained for additives

added at a 1:10 ratio. The results obtained are contrary to the expectation that the inclusion of a greater amount of FDPs would lead to previously reported increased HA nucleation [80].

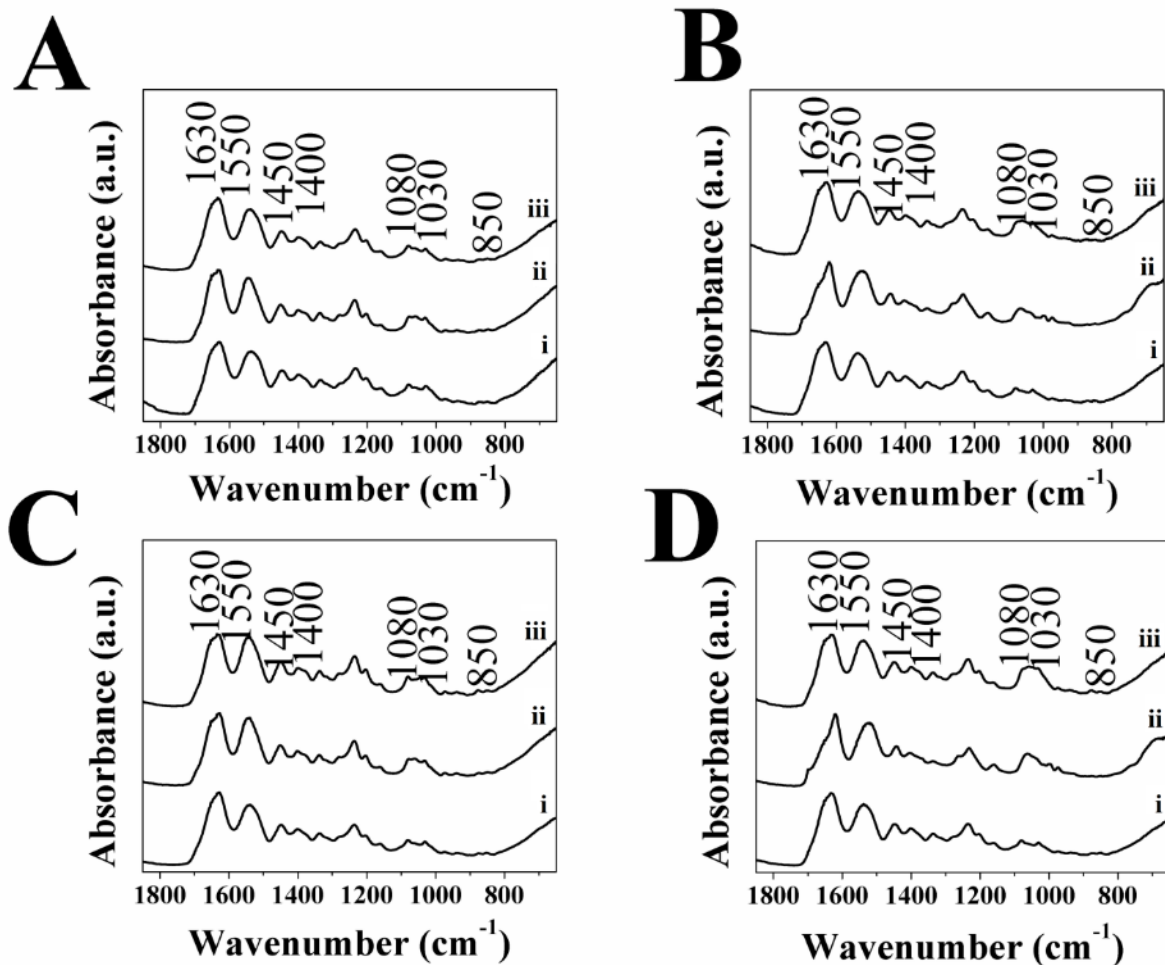


Figure 6.6: ATR-FTIR for A) 1:1 DC-Cs, B) 1:1 DC-C_p, C) 1:2 DC-Cs, and D) 1:2 DC-C_p, i) as-made and immersed in SBF for ii) 3 and iii) 7 days

6.4. Mass analysis of DC/FDPs hydrogels

The freeze-dried DC hydrogels with different ratios of C_s and C_p (1:2 and 1:1 relative to collagen) before and after immersion in SBF were weighed to determine if the addition of FDP led to a change in mass due to HA nucleation over time.

Previously [80], it was reported that DC and DC-C_s hydrogels with 1:10 C_s to collagen should result in a hydrogel that is 5 wt.% and ~60 wt.% HA, respectively, by day 7 after immersion in SBF. However,

the present results show that there is no significant difference between plastically compressed DC gels and DC gels with C_s incorporated (see Figure 6.7). Comparison of the difference in the masses of the DC, DC-C_s and DC-C_p hydrogels to the theoretical value of an as-made (day 0) gel with the same amount of additive incorporated is reported in Table 6.1. The mass analysis of the DC gels after PC matched up closely (-3.6%) with the theoretical mass of a gel of the same volume. Results demonstrated that the DC-C_s hydrogels have a significantly lower mass than their theoretical value, while the mass of the DC-C_p gels is close to its theoretical value. Furthermore, the difference of mass in the DC-C_s was similar to the amount of C_s added to the solution, and statistically, the difference in mass between the DC and DC-C_s gels is not significant. This indicates that C_s is expelled with the water inside the gel during the plastic compression of the highly hydrated hydrogel, and that the remaining scaffold is only collagen.

Table 6.1. Mass of as-made hydrogels at compared to the theoretical values

Sample	Theoretical mass (mg)	Initial mass (mg)	Difference in mass (%)	Difference in mass from control (mg)
DC (ctrl)	4.7	4.9±0.5	3.6	0.0
1:2 DC-Cs	7.0	5.1±0.5	-27.4	0.2
1:1 DC-Cs	9.4	4.2±0.5	-55.7	-0.7
1:2 DC-Cp	7.0	7.2±0.4	3.0	2.3
1:1 DC-Cp	9.4	10.3±0.7	9.7	5.4

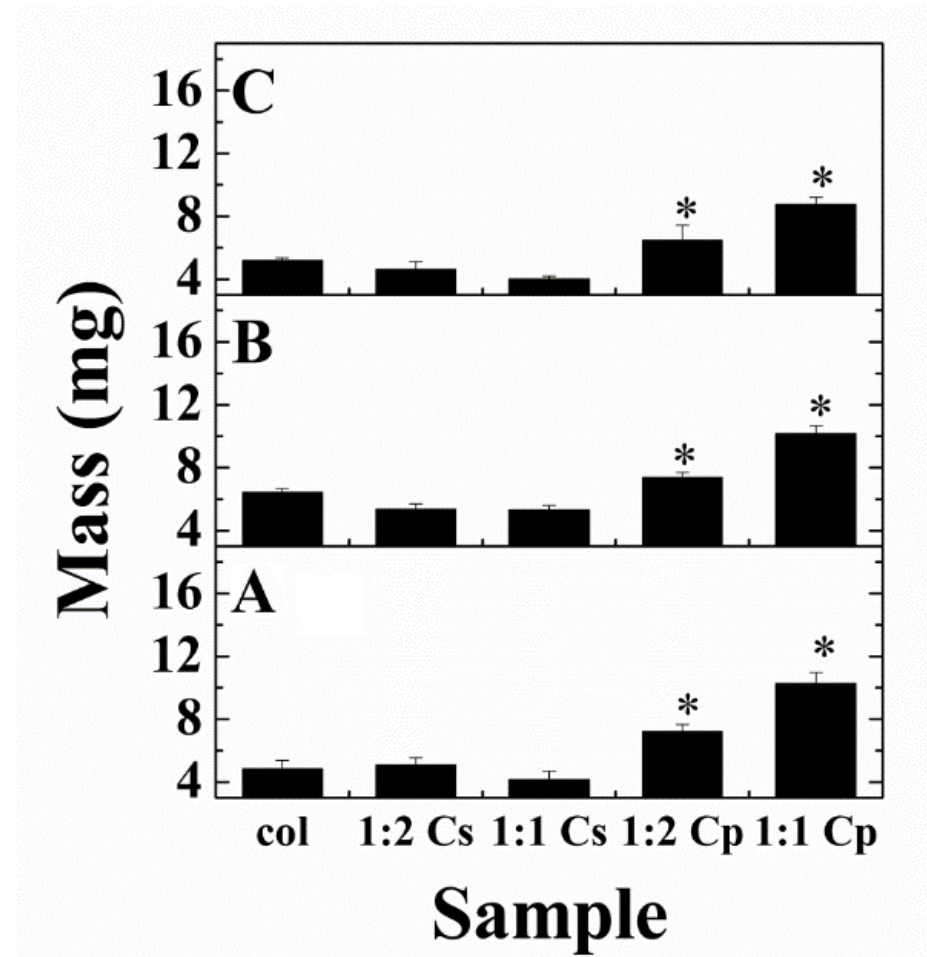


Figure 6.7: Mass of DC, DC-Cs, and DC-C_p hydrogels immersed in SBF for A) 0 (as-made), B) 3 and C) 7 days (* - statistically significant, one-way ANOVA, SD, n=4, p < 0.05)

7. Copper-doped Phosphate glass additives for hydroxyapatite mineralization

7.1. Analysis of PG and DC hydrogels in SBF

Figure 7.1A displays the mass of PG particles doped with different % CuO and immersed in SBF at one, three and five days. The decrease in mass indicate that the PG particles immersed in SBF begin to dissolve immediately.

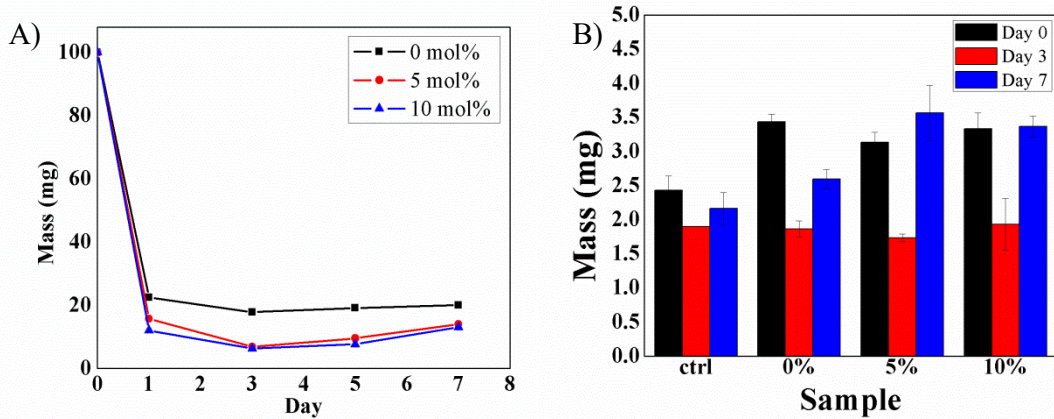


Figure 7.1: Mass of A) PG immersed in SBF for 1, 3 and 5 days and B) collagen gels with 50 wt% PG, immersed in SBF for 3 and 7 days ($n = 3$, $p < 0.05$)

In SBF, the dissolution did not achieve 100% completion. Also, increasing the amount of CuO dopant, which is known to result in slower dissolution rates due to surface erosion being prohibited by the stronger M-O bonds [242], did not occur. Of the 100 mg of PG originally added to the SBF, the mass of the particles in solution did not fall below 17.8, 6.8 or 6.3 mg for 0, 5 and 10% CuO-doped PG respectively, by day three, compared to previous experiments that showed full dissolution of phosphate glass occurs within 48 hours. This can be attributed to the formation of HA while the particles were in SBF; the mass loss was countered by the nucleation of HA particles. Mass gain appears after three days in SBF, indicating that the initial dissolution of PG is overtaken by nucleation of other materials.

Measurement of the mass of CuO-doped PG in DC hydrogels as made (day 0), and immersed in SBF for three and seven days (see Figure 7.1B), showed a significant drop in mass after the first three days, followed by an increase over the next four days (day seven). The increased mass at day seven increased with CuO content. By day seven relative to day three, hydrogels, both the control and 0% CuO, showed a small mass increase, whereas the hydrogels containing 5% and 10% CuO PG showed a significant increase in mass values, that is, their mass at day seven is now greater than at day three. The results

indicate that there is some sort of copper-collagen interaction taking place within the hydrogel that helps to increase either the nucleation or growth of particles.

XRD analysis of PG particles immersed in SBF shows a diffraction pattern consistent with an amorphous material for all samples (see Figure 7.2). The presence of copper did not affect the XRD patterns. The resulting pattern is different than the previously obtained patterns for the as-made PG (see Figure 5.7), but is similar to that seen in previous works for an ACP. In particular, it mimics the XRD pattern for ACP with a large slope at $2\theta = 10^\circ$ and a slight slope at $2\theta = 30^\circ$ [243]–[245].

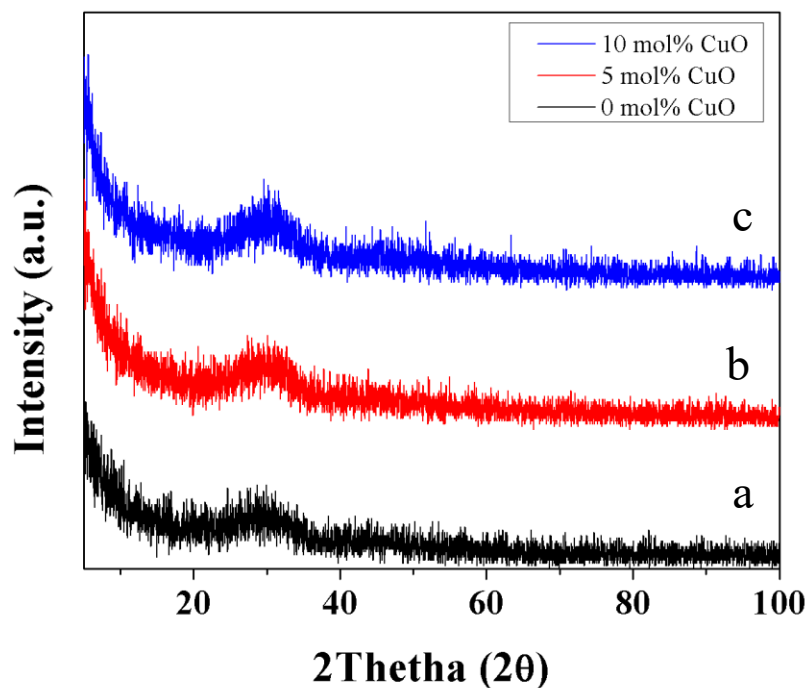


Figure 7.2: XRD for a) 0 mol% b) 5 mol% and c) 10 mol% CuO PG immersed in SBF

7.2. Scanning Electron Microscopy and Electron Diffraction Spectroscopy

SEM was also used to investigate the nucleation of HA and the morphology of hydrogels, as well as the effect of the dissolution of PG on the morphology of the collagen-CTS hydrogels. SEM-BSE was able to provide an increased depth of penetration compared to secondary electrons, and provide high-contrast images that better showed the PG particles and their distribution.

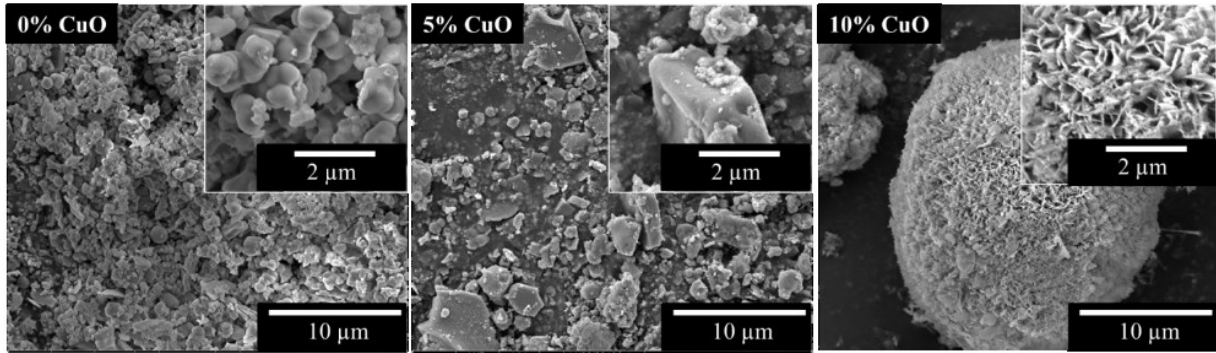


Figure 7.3: SEM images of 0, 5 and 10 mol% CuO-doped PG immersed in SBF 5 days

The SEM images of CuO-doped PGs immersed in SBF for five days are shown in Figure 7.3. Compared to the original PG particles shown in Figure 7.1, the particles are significantly smaller, and lack the typical sharp corners of glass particles. The 10% CuO-doped PG formed a “cauliflower” shape typical of HA [71]. In contrast, the 5% CuO-doped PG still showed remnants of large PG particles, while the PG with no copper showed a globular structure. Several images (see Figure 7.4) showed that dissolution differed with copper content, with 0% CuO showing relatively quick, uniform dissolution within 24 hours while particles with 5% and 10% CuO-doping dissolved more erratically, with “lines” and “pockets” dissolving first, which could be attributed to its slower dissolution rate compared to 0% and 5% CuO-doped PG [151], while “smooth” features are due to acute corners and edges being preferentially dissolved [246].

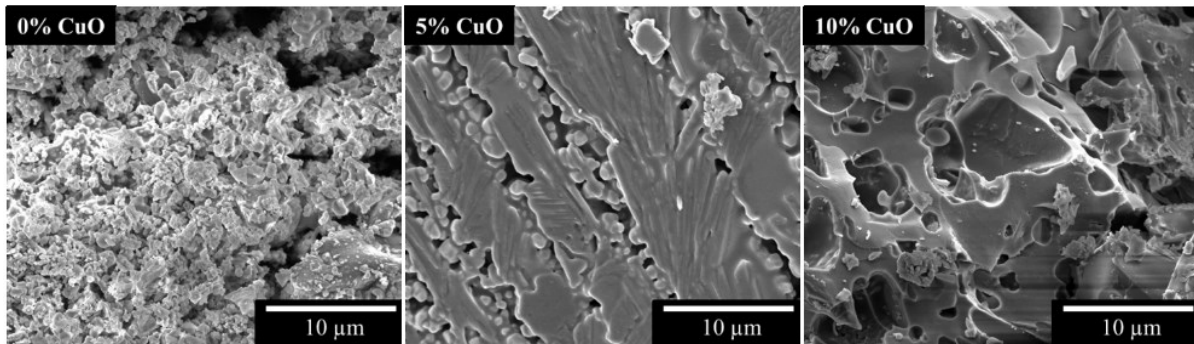


Figure 7.4: SEM images of 0, 5 and 10 mol% CuO-doped PG immersed in SBF 1 day

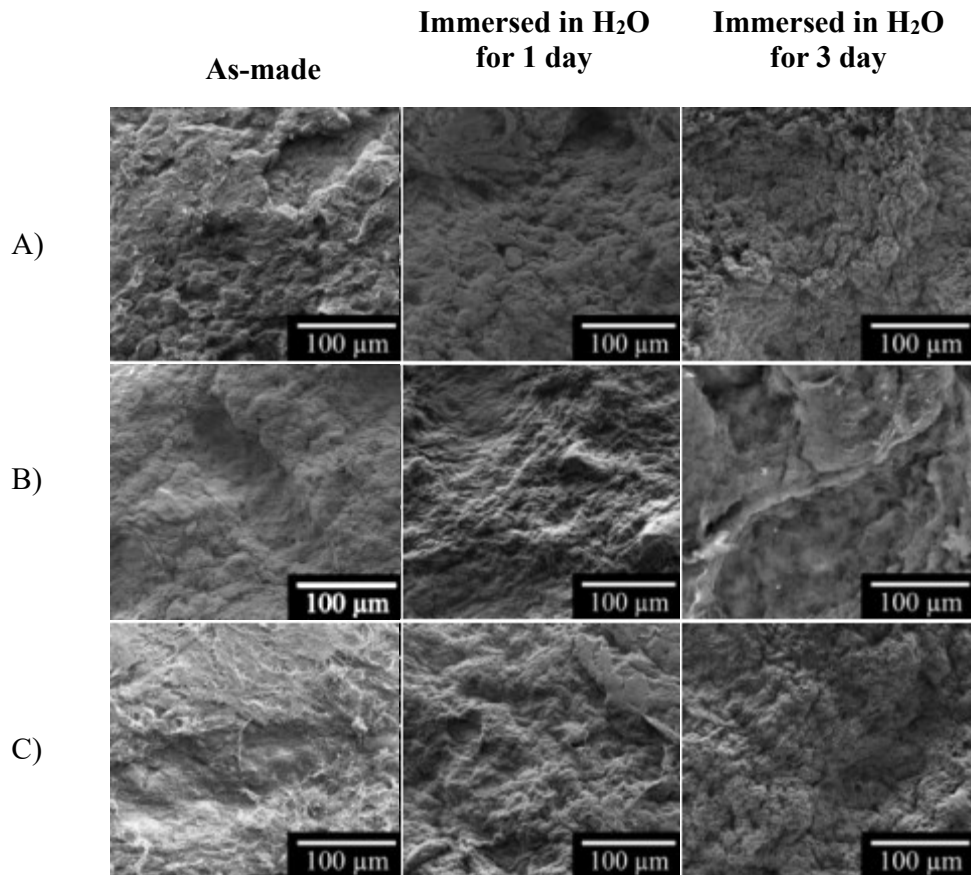


Figure 7.5: SEM of as-made hydrogels with a 1:1 collagen-CTS ratio containing 50 wt% A) 0, B) 5 and C) 10% CuO-doped PG particles, as made and immersed in H₂O for 1 and 3 days (scale bars are 100 μm)

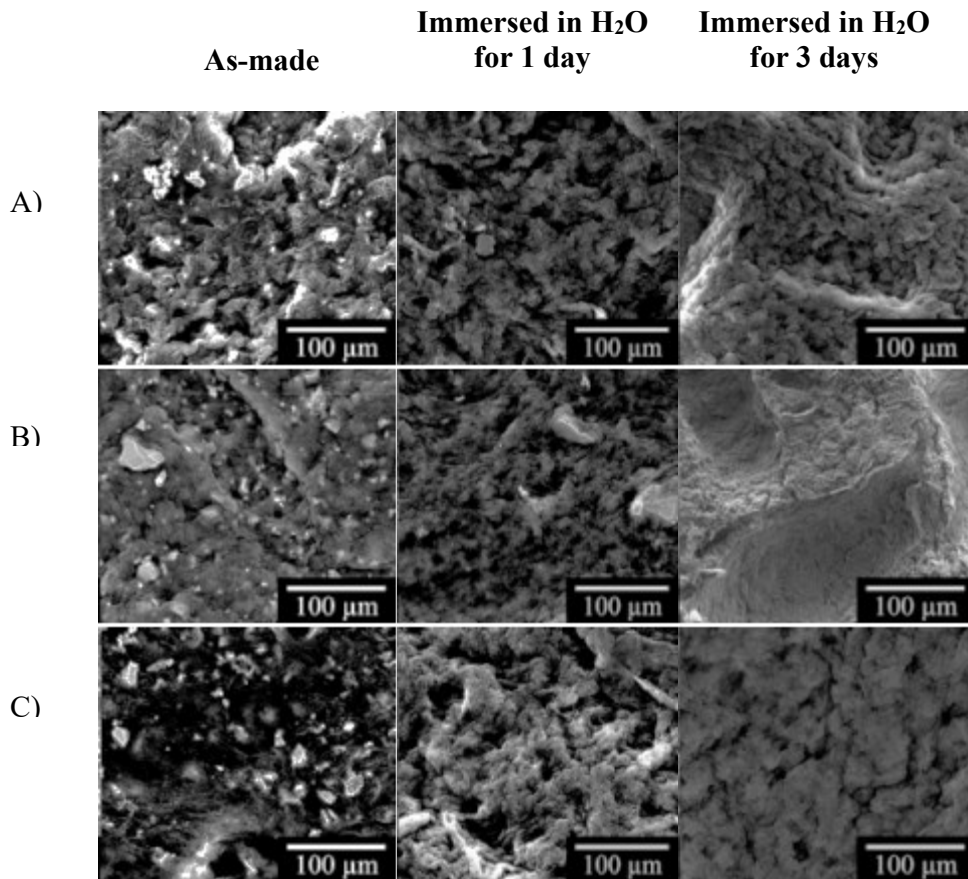


Figure 7.6: SEM-BSE of as-made hydrogels with a 1:1 collagen-CTS ratio containing 50 wt% A) 0, B) 5 and C) 10% CuO-doped PG particles, as made and immersed in H₂O for 1 and 3 days (scale bars are 100 µm)

Figure 7.5 and Figure 7.6 shows SEM images and their respective SEM-BSE images of hydrogels composed of a 1:1 ratio of collagen and CTS, with 50 wt% CuO-doped PG particles (CuO = 0, 5 and 10%), both as-made and after immersion in water. SEM images shows patterned morphology, with grooves imparted from the mesh used in the plastic compression. The morphology of the hydrogels remains consistent over time and does not vary with the type of PG incorporated. SEM-BSE show that the distribution of PG particles (seen via the brighter areas in the BSE images) is fairly uniform in all hydrogels, and the dissolution of the PG particles is nearly complete after 24 hours. After three days of immersion in DW, there are no traces of any PG particles left.

No mineral formation was observed, indicating that the molecules released during dissolution of the phosphate glass either attach to specific sites within the hydrogel or diffuse out of the hydrogel, instead of causing the nucleation of apatite. The lack of apatite formation can be explained by the lack of free phosphate molecules or calcium ions, both of which are necessary for the nucleation and growth of hydroxyapatite [247].

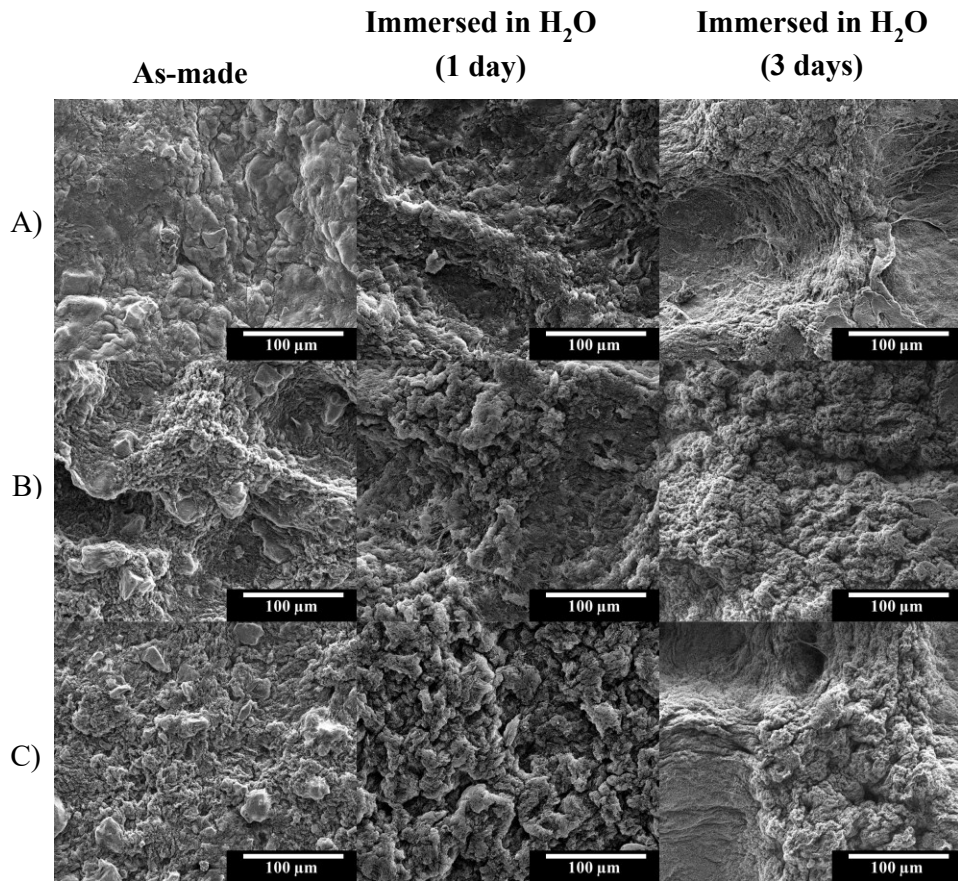


Figure 7.7: SEM of as-made hydrogels with a 1:2 collagen-CTS ratio containing 50 wt% A) 0, B) 5 and C) 10% CuO-doped PG particles, as-made and immersed in H₂O for 1 and 3 days (scale bars are 100 μm)

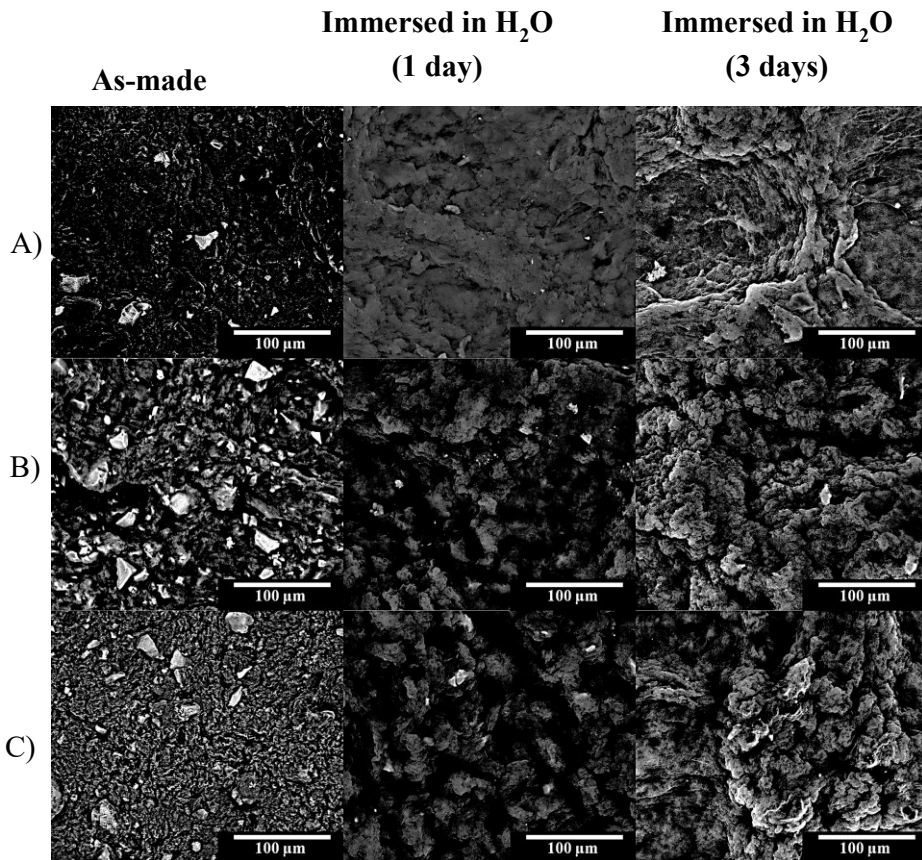


Figure 7.8: SEM-BSE of hydrogels with a 1:2 collagen-CTS ratio containing 50 wt% A) 0, B) 5 and C) 10% CuO-doped PG particles, as-made and immersed in H₂O for 1 and 3 days (scale bars are 100 μm)

Figure 7.7 and Figure 7.8 and shows SEM and their respective SEM-BSE of hydrogels composed of a 1:2 ratio of collagen and CTS, with 50 wt% due to the incorporation of CuO-doped PG particles (0, 5 and 10%). Similar to the 1:1 collagen-CTS hydrogels, these showed a good distribution of PG particles within the hydrogel as well as a similar morphology. The increase in CTS content does not appear to have had a significant effect on the structure of the hydrogel. As with the previous hydrogels, no mineral formation was observed.

7.3. Elemental Analysis of Hydrogels Over Time

EDS maps of the 1:1 collagen-CTS hydrogels (see Figure 7.9) show concentrated areas of phosphorus (in green) and carbon (purple), the former being attributed to the PG particles and the latter to the hydrogel. Calcium, copper and sodium were also measured, but cannot be seen due to low concentrations. Like with SEM-BSE, it shows a good distribution over the hydrogel. The localized spots of phosphorus begin to decrease within a day, and by day three EDS mapping shows that there is

phosphorus distributed all over the hydrogel. The images show that while PG will dissolve within the hydrogel, the phosphate will be retained as it forms chemical bonds within the hydrogel [248], [249].

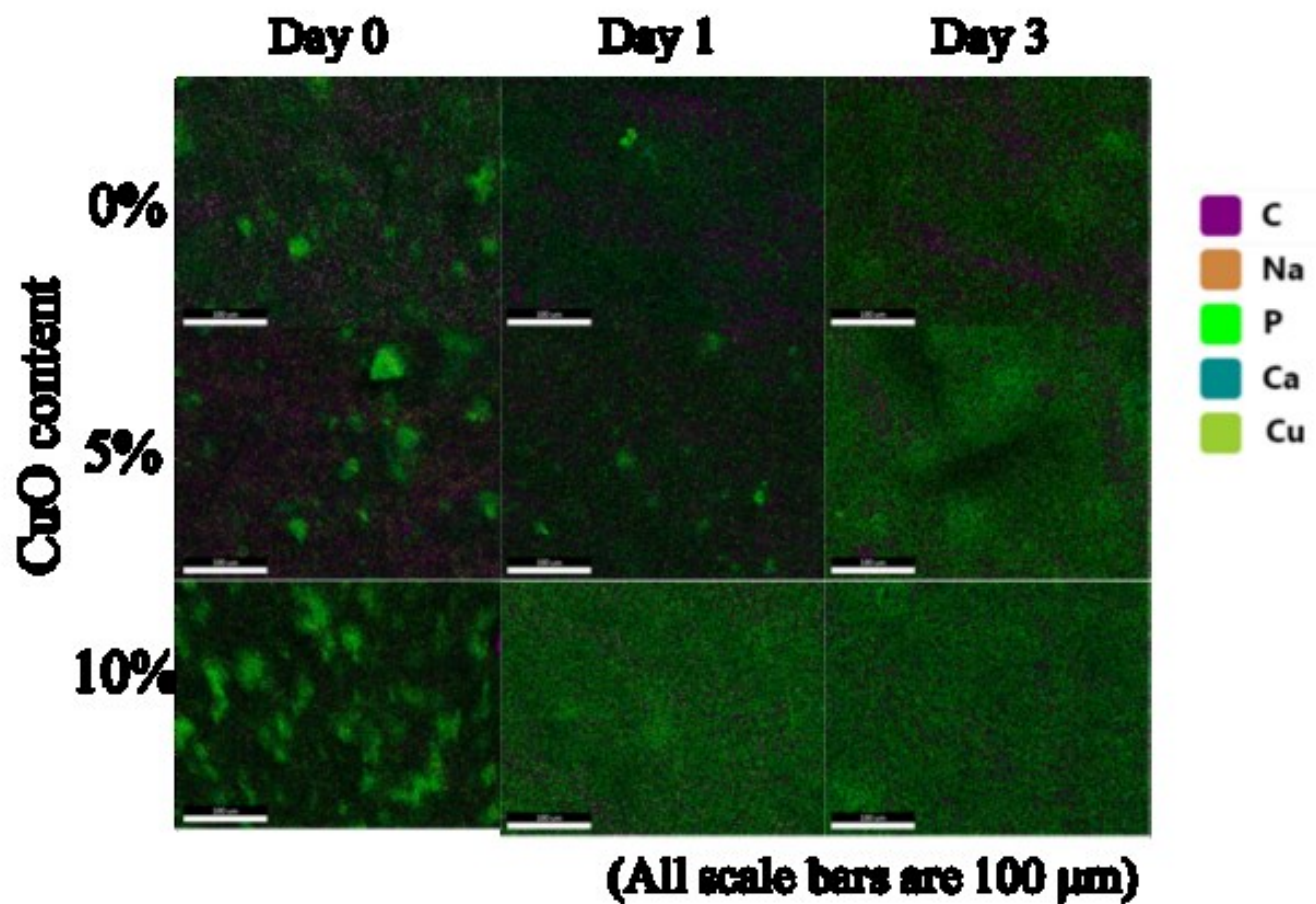


Figure 7.9: EDS of 1:1 collagen-CTS gels containing 50 wt% 0, 5 and 10 mol% CuO-doped PG particles, immersed in H_2O for 0, 1 and 3 days

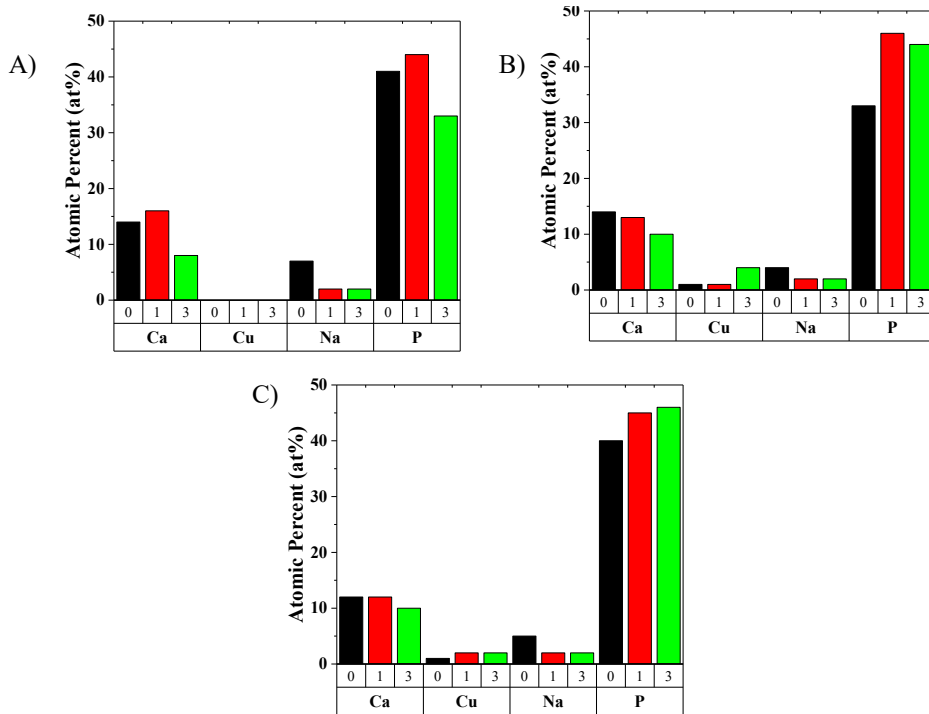


Figure 7.10: Elemental composition of 1:1 collagen-CTS gels containing 50 wt% A) 0, B) 5 and C) 10% CuO-doped PG particles, immersed in H₂O for 0, 1 and 3 days

The concentration of elements retained from PG can also be seen in Figure 7.10. In addition to the large amount of phosphorus, a high quantity of calcium was retained, as well as small amounts of sodium and trace amounts of copper. The high quantity of phosphorus can be attributed to the bonding of phosphate within the hydrogel, especially to the amide of the CTS molecules, as was seen in ATR-FTIR. The remaining calcium and copper likely forms physical crosslinks with the -OH/-COO⁻ of collagen/CTS [250]–[252], indicating that dual crosslinking is present within the hydrogel [252].

EDS maps of the 1:2 collagen-CTS hydrogels (see Figure 7.11) showed a better distribution of PG particles throughout the gel than its 1:1 collagen-CTS counterpart. However, full dissolution of the PG particles does not appear to have occurred, even by day three. The increased amount of CTS appears to play an important role in the distribution of PG particles. It is possible that the excess CTS is adsorbed onto the surface of the particle, which leads to some form of steric stabilization, though the PG particles are much larger than particles typically seen to undergo this process [253], [254].

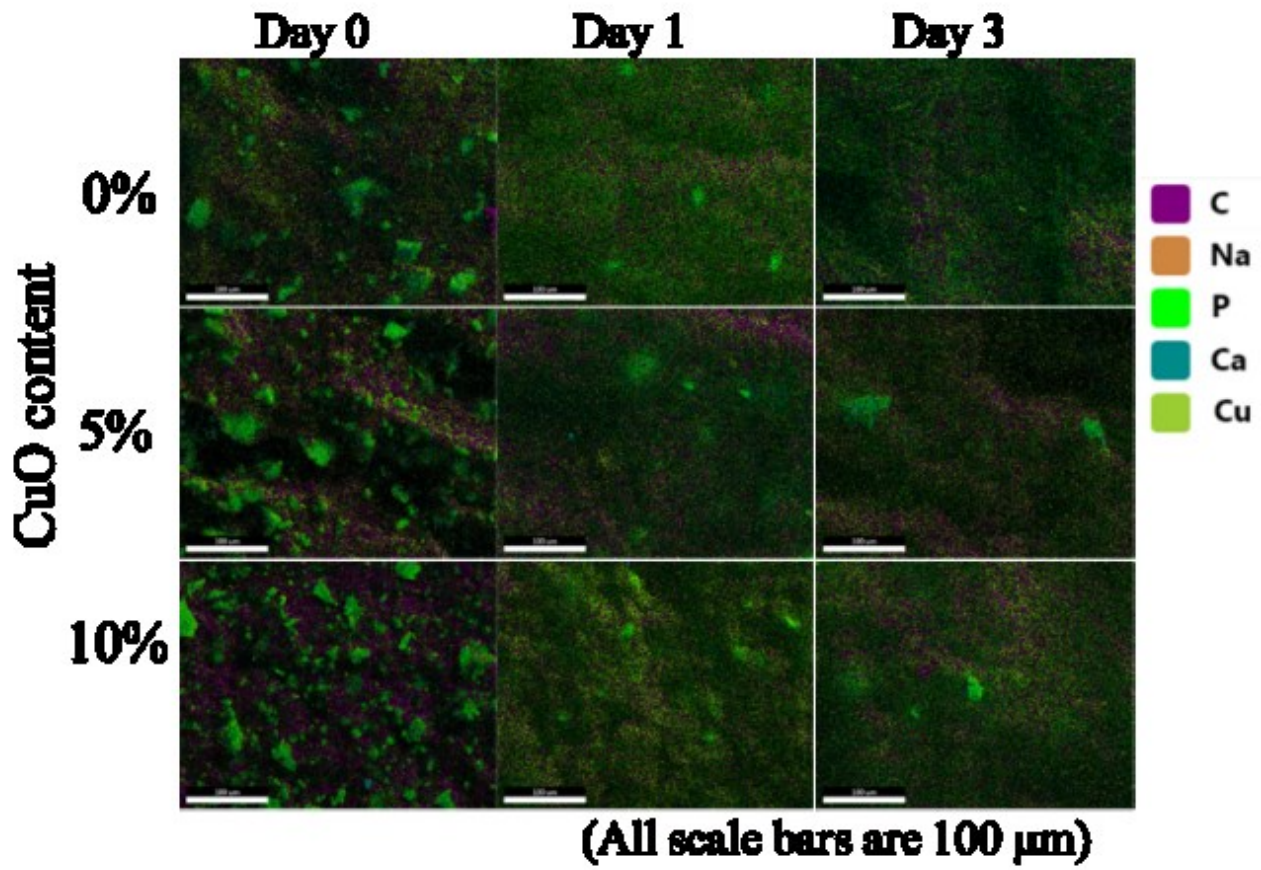


Figure 7.11: EDS of 1:2 collagen-CTS gels containing 50 wt% 0, 5 and 10 mol% CuO-doped PG particles, immersed in H₂O for 0, 1 and 3 days

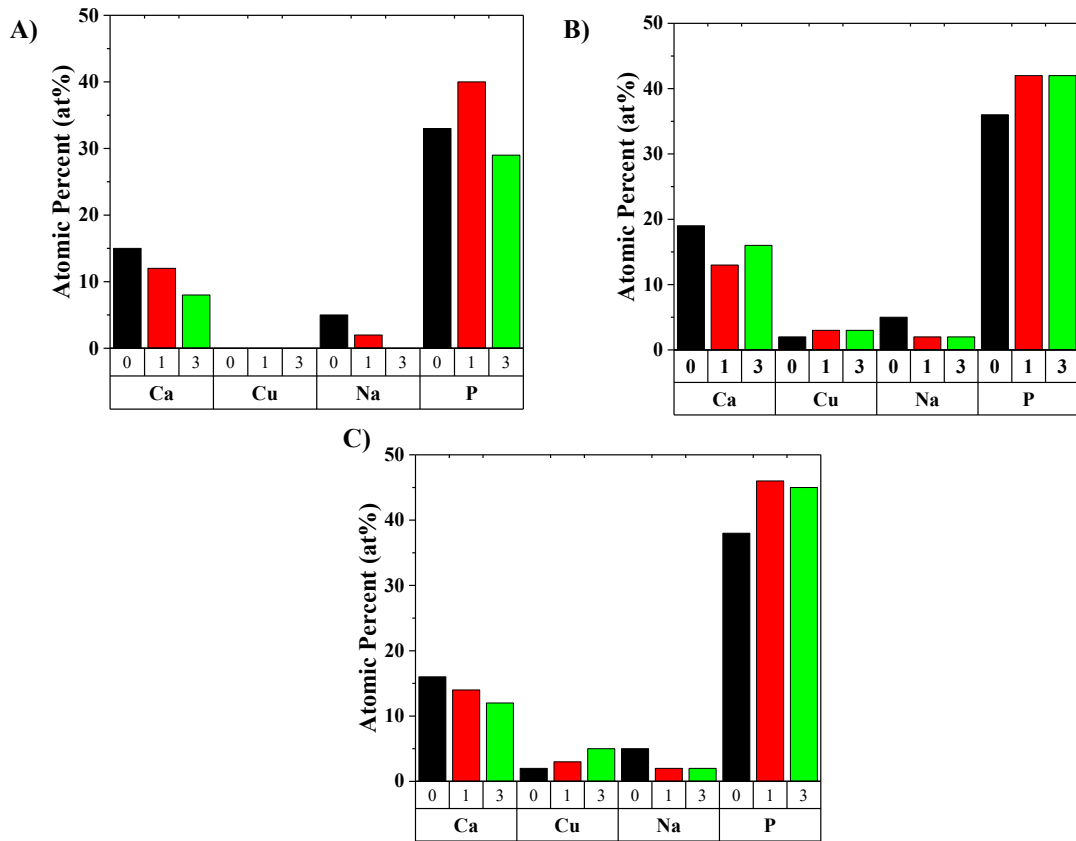


Figure 7.12: Elemental composition of 1:2 collagen-CTS gels containing 50 wt% A) 0, B) 5 and C) 10% CuO-doped PG particles, immersed in H₂O for 0, 1 and 3 days

The concentration of elements retained from PG can also be seen in Figure 7.12. Like previous samples, there is a large amount of phosphorus, a high quantity of calcium, small amounts of sodium and trace amounts of copper. The decreased presence of phosphorus, calcium and sodium also occurs in the absence of copper. The phosphorus can be attributed to the bonding of phosphate, as was seen in ATR-FTIR. The remaining calcium and copper indicates physical crosslinks occurs [250]–[252], indicating that dual crosslinking is present within the hydrogel [252]. In Figure 7.13, the SEM images of hydrogels with CuO-doped PG immersed in SBF are shown. The images of PG immersed in SBF show that small, round globules begin to grow on the dissolving PG. Remnants of PG were seen by day three. However, by day 5, both 0 and 10% CuO-doped PG have fully dissolved, leaving either small globules similar to amorphous calcium phosphate (ACP) [255], [256] or particles with the characteristic “cauliflower” shape of HA behind [71]. In contrast, the 5% CuO-doped PG still showed remnant of large PG particles.

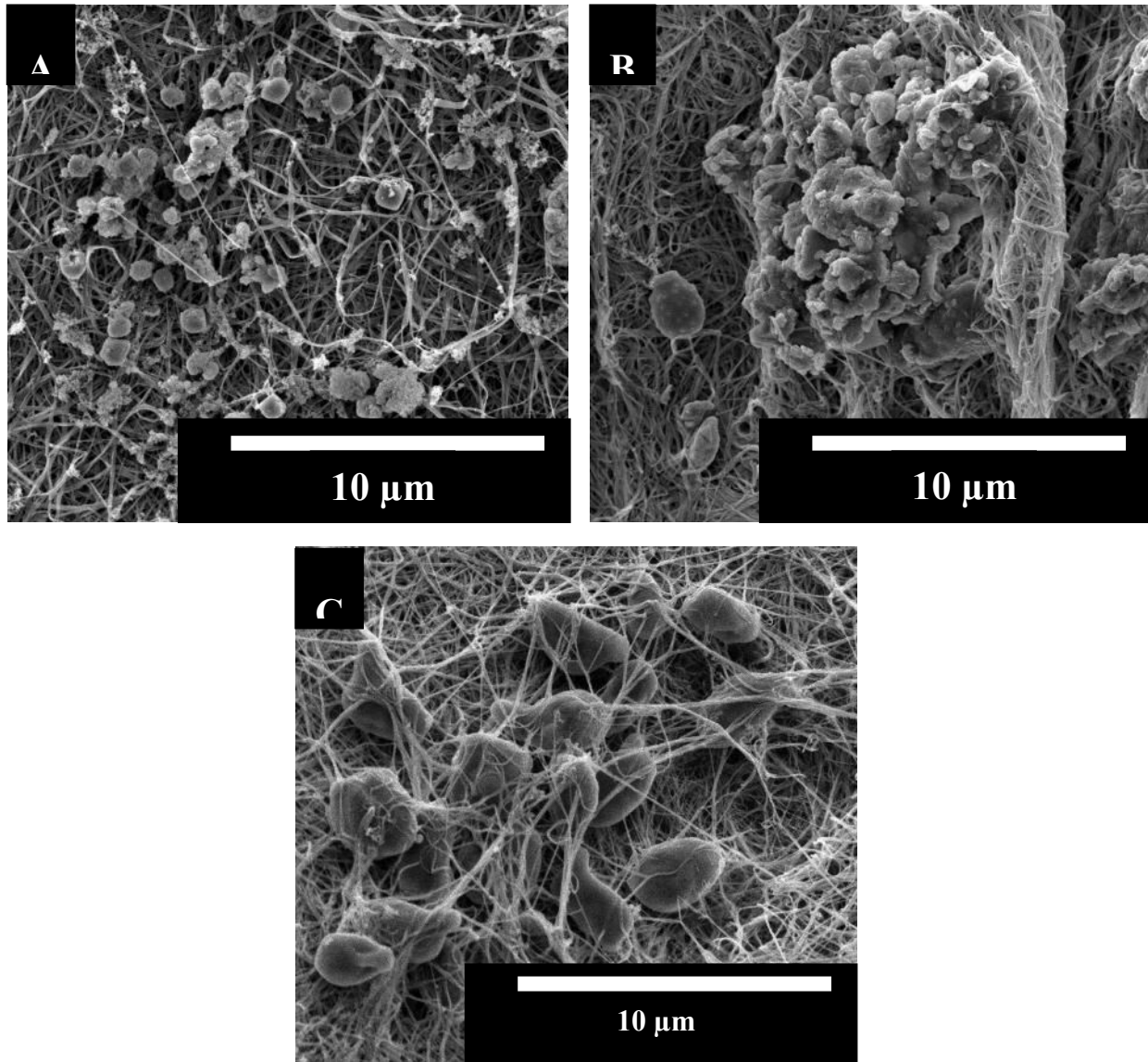


Figure 7.13: SEM images A) 0% B) 5% and C) 10% CuO-doped PG DC hydrogels immersed in SBF for 7 days

EDS point analysis of the particles (see Figure 7.14) seen in the DC hydrogels show that particles from the gels with 0 and 5% CuO-doped PG incorporated were composed of a high amount of calcium and a smaller amount of phosphorus. Particles from gels with 10% CuO-doped PG showed a much lower amount of calcium, though it has a similar amount of phosphorus. While the results support that the dissolution of PG in a DC hydrogel leads to the nucleation of calcium phosphate particles, the Ca/P ratios for 0 and 5% CuO-doped PG gels (10 and 5, respectively) were much higher than Ca/P ratio of 1.67 associated with HA [257]–[259], while the Ca/P ratio for 10% CuO-doped PG gels was 0.16.

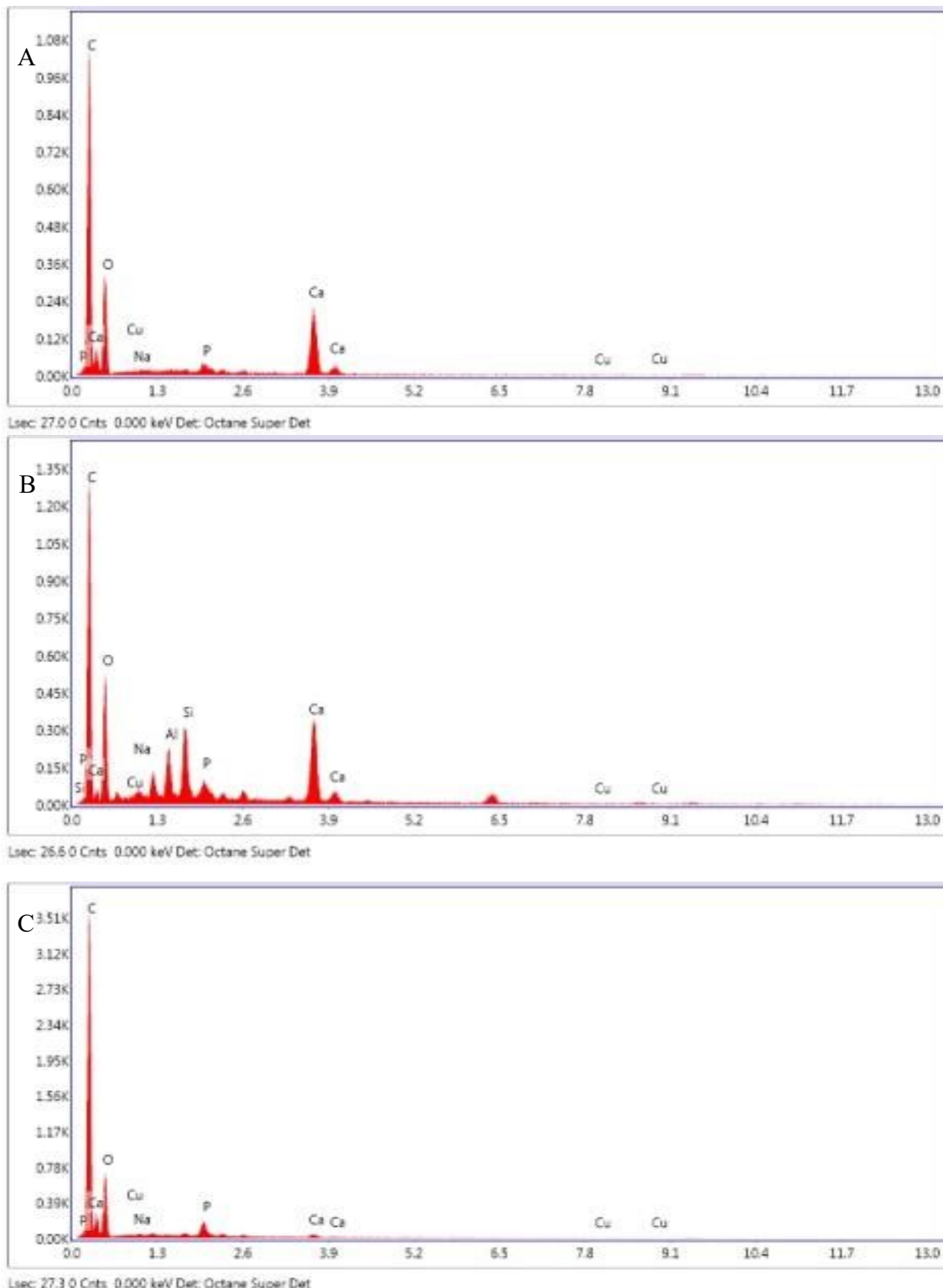


Figure 7.14: Elemental analysis of particles in collagen gels with A) 0 mol%, B) 5 mol% and C) 10 mol% CuO-doped PG immersed in SBF for 7 days

7.4. ATR-FTIR Spectroscopy copper-doped PG

The attenuated total reflectance Fourier transform infrared ATR-FTIR spectra for CuO-doped PG immersed in SBF (see Figure 7.15) shows specific absorption bands related to phosphate groups that resembles natural bone (see Figure S.3). The as-made PG show a band at $\sim 1250\text{ cm}^{-1}$ that is associated with PO_2 . The band at $\sim 1082\text{-}1087\text{ cm}^{-1}$ is associated with P-O^- bonds. The strong band at $884\text{-}910\text{ cm}^{-1}$ is associated with P-O-P bonds [151]. The CuO content could not be verified by additional bands, but it affected the intensity of the P-O^- band at $1082\text{-}1087\text{ cm}^{-1}$, which showed a weakened peak that is due to the metal oxide bonds forming between copper and oxygen [242]. The spectra at day 5 is similar to that obtained from mature bone, with a strong PO_4^{3-} band at $1000\text{-}1150\text{ cm}^{-1}$ [260], [261]. The strong band at 910 cm^{-1} is attributed to a core of PG that did not fully dissolve but was instead coated by the new particle, similar to bioglass coated HA [262].

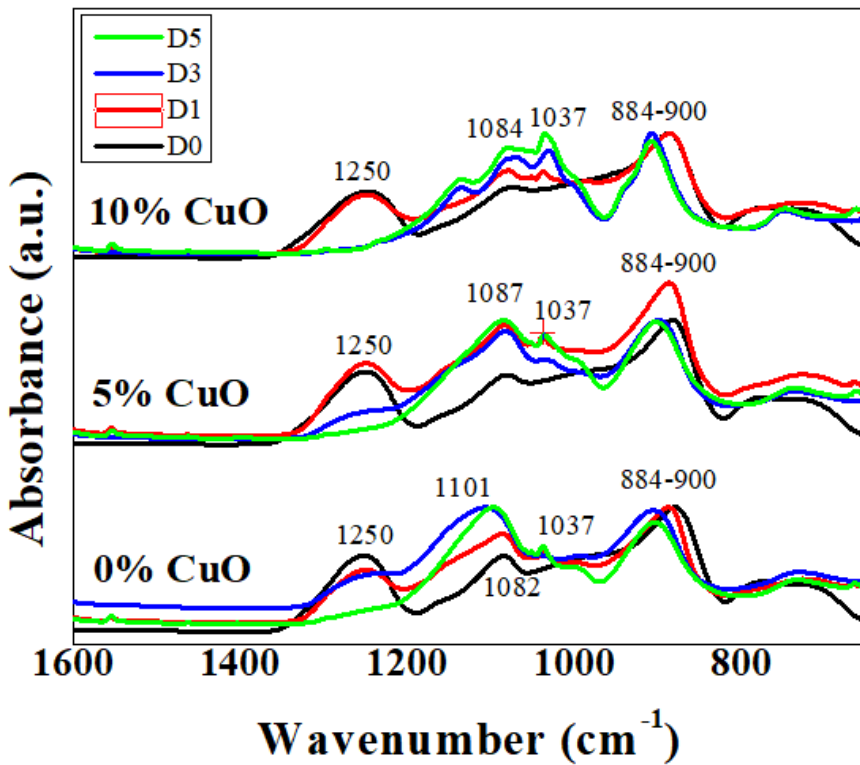


Figure 7.15: ATR-FTIR for 0%, 5% and 10% CuO-doped PG, as-made (D0) and immersed in SBF 1, 3 and 5 days (D1, D3 and D5, respectively)

ATR-FTIR of 1:1 blended collagen-CTS gels showed the characteristic spectra associated with collagen and CTS (see Figure 7.16), particularly the amide I and II bands at 1650 cm^{-1} and 1550 cm^{-1} , respectively [84], [215]. The large, broad band at 3320 and 2866 cm^{-1} is associated with the overlap of

the amide A and B groups of collagen and the -OH of CTS. The band at 1400 cm^{-1} is associated with the -CO group of CTS, while the large band at 1250 cm^{-1} is due to the overlap of the -CN group of collagen and CTS. The large band at 1075 is associated with the overlap of the glycosidic linkages of CTS and the presence of PO_4^{3-} , and the band at 880 cm^{-1} with the C-O of CTS [84], [216], [263]. The growth of the band at 1075 cm^{-1} is indicative of an increase presence of PO_4^{3-} as time progresses (see Figure 7.16C), which would indicate that dissolved phosphate anions are retained within the collagen-CTS matrix.

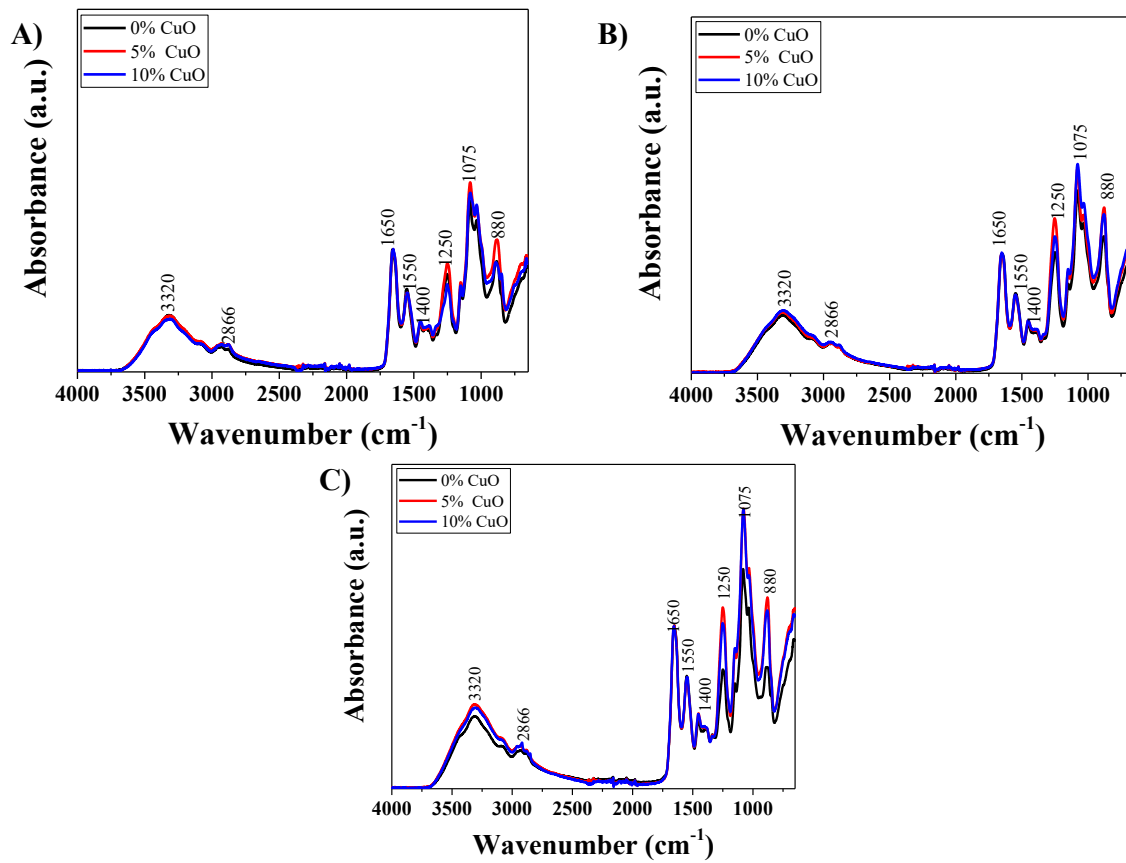


Figure 7.16: Hydrogels with a 1:1 collagen-CTS ratio containing 50 wt% CuO-doped PG particles (0, 5 and 10 mol%), immersed in H_2O for A) 0, B) 1 and C) 3 days

Hydrogels made up of a collagen-CTS ratio of 1:2 showed a similar spectrum (see Figure 7.17) to that of the 1:1 collagen-CTS hydrogel, with the characteristic bands associated with collagen and CTS present, as seen previously. The growth of the band at 1075 cm^{-1} is indicative of an increased presence of PO_4^{3-} as time progresses, though at day 1 there is a difference in the absorbance, along with the band at 330 cm^{-1} with increasing CuO content of the PG particles (see Figure 7.17B), which would indicate that either dissolution is slowed down or that the excess of CTS interacts with the Cu^{2+} ions, forming a

physical bond. Given that the 3300 cm^{-1} is associated with the -OH of CTS, it is likely that physical bonds are forming, which FTIR shows via a decrease in absorbance of the bands. By day three, this difference is gone, and all hydrogel show identical spectra (see Figure 7.17C), possibly indicating that the polyphosphates present have fully bonded to the CTS and overcome the effects due to copper.

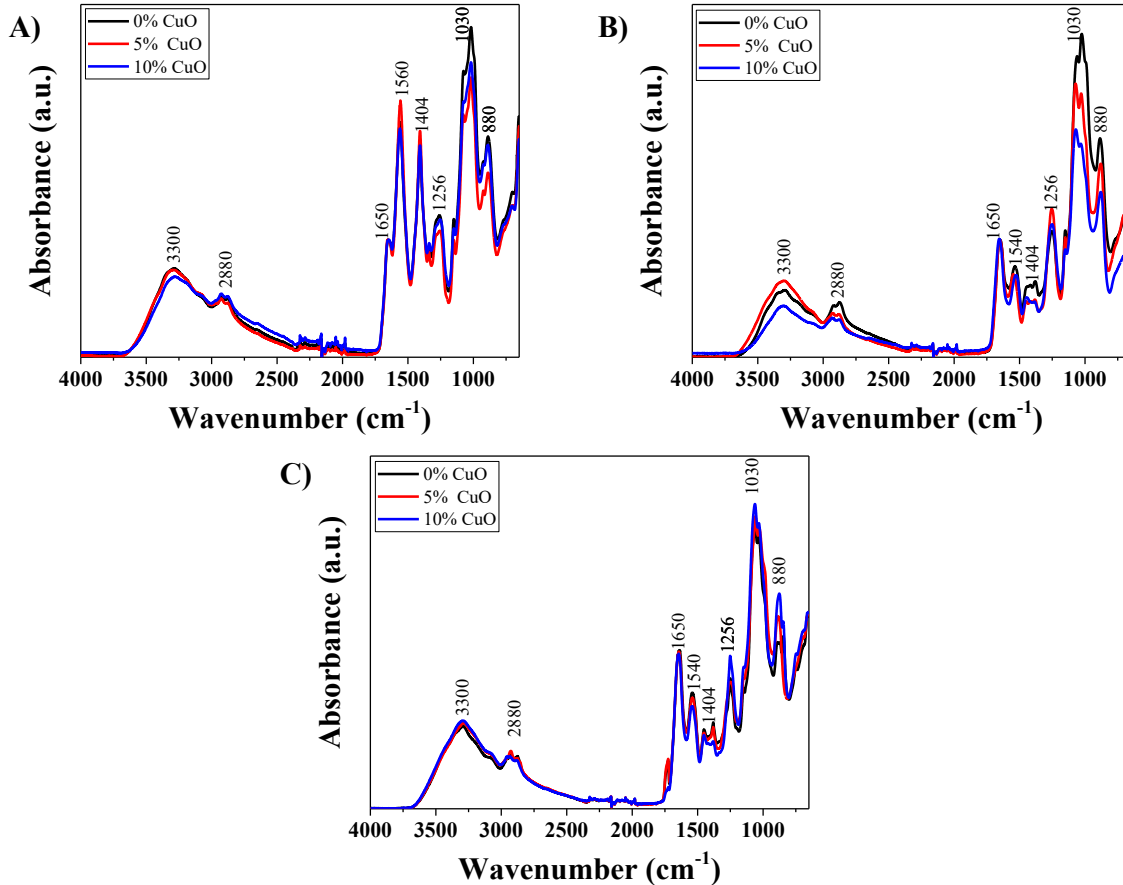


Figure 7.17: Hydrogels with a 1:2 collagen-CTS ratio containing 50 wt% CuO-doped PG particles (0, 5 and 10 mol%), immersed in H_2O for A) 0, B) 1 and C) 3 days

The ATR-FTIR spectra for CuO-PG DC hydrogels immersed in simulated body fluid (SBF) are shown in Figure 7.18. Here, the collagen gels showed the characteristic spectra associated with collagen and CTS, particularly the amide I and II bands at 1640 cm^{-1} and 1550 cm^{-1} , respectively [84], [215]. The band at $1030 - 1070\text{ cm}^{-1}$ is indicative of the presence of PO_4^{3-} [264]–[266]. Also, for samples A and B, the spectra for as-made and after 3-days immersion in SBF are almost the same. The same is seen for samples C and D. By day seven, the growth of the band at $1030 - 1070\text{ cm}^{-1}$ for gels with 5 and 10% CuO-doped PG incorporated is higher compared to that of DC and DC gels with 0% CuO-doped PG incorporated. These results indicate that copper helps retain phosphate. There is also a slight

increase in the peak at 880 cm^{-1} , which is associated with carbonate. The spectra indicate that the nucleation of hydroxyapatite (HA) in DC and DC gels with 0% CuO-doped PG occurs, while nucleation of amorphous calcium phosphate (ACP) is greater in the presence of copper.

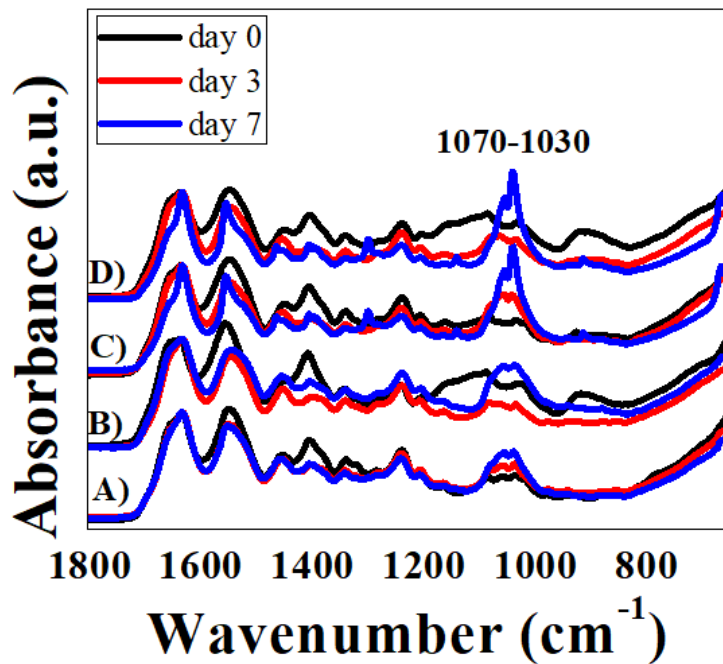


Figure 7.18: ATR-FTIR for A) DC and B) 0% C) 5% and D) 10% CuO-PG DC hydrogels a) as-made (black) and 3 (red) and 7 days (blue) immersed in SBF

8. Electrophoretic deposition of composited glass-polymers coatings

8.1. Electrical characterizations of co-polymer films

EIS measurements of collagen/CTS films were used to determine the resistance of films formed from different ratios of collagen and CTS. It is known that the electric field decreases with film growth, and films with higher resistivity, barring other factors, result in lower deposition rates [167]. The results show that increasing the ratio of collagen to CTS resulted in lower current densities across all voltages (see Figure 8.1A-E) when analysed in a three-electrode cell (see Figure 8.1G).

With an increasing concentration of collagen in the film, the current density measured across the film decreases proportionally (see Figure 8.1F). Similar work shows that collagen has a lower conductivity than CTS [159]. A possible explanation lies in the structure of collagen compared to CTS; both collagen and CTS are polycationic in nature, but the former is composed of many different amino acids, and has a mix of positive and negative charges [44]–[46]. As such, collagen also expresses polyanionic traits [67]–[69], which results in a decrease in conductivity. The presence of CTS results in the protonated side groups dominating in the film, and cations become the dominant charge [159].

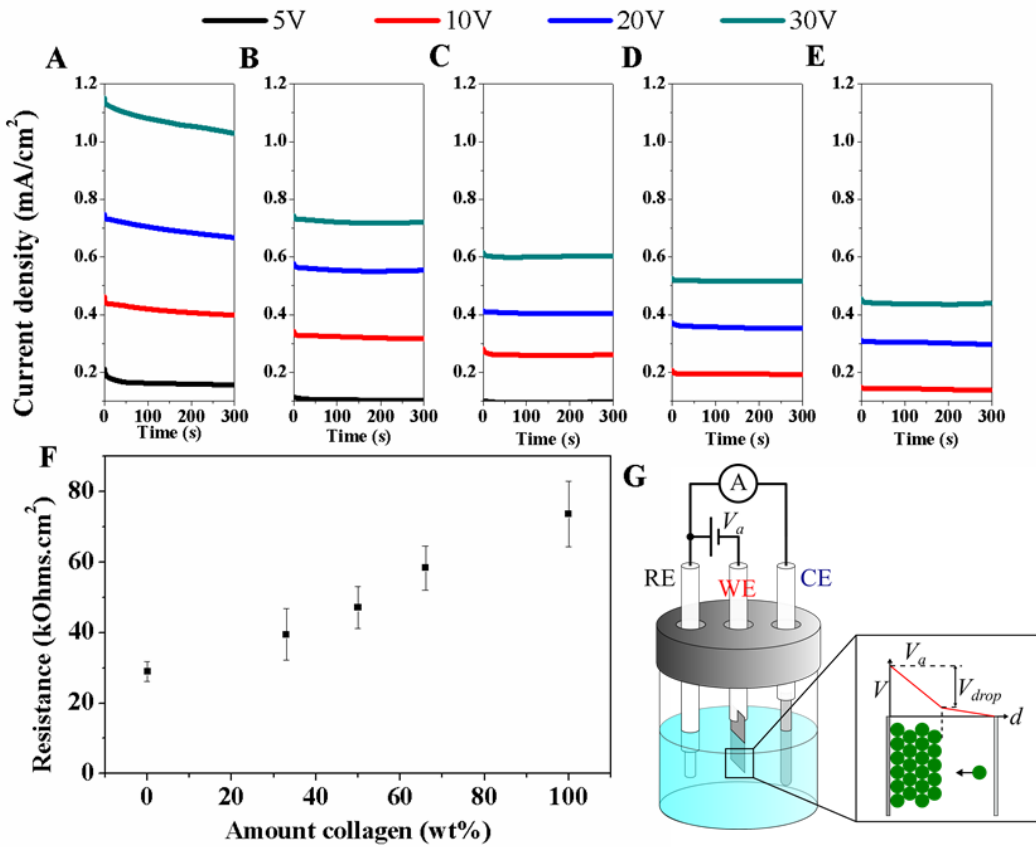
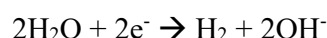


Figure 8.1: EIS measurements of Current produced at 5-30V for EPD of collagen/CTS solutions containing collagen: A) 0 wt.%; B) 33 wt.%; C) 50 wt.%; D) 66 wt.%; E) 100 wt.% F) shows the calculated resistance of films for various collagen (wt.%) contents G) Schematic of EPD cell (SD for $n=4$, $p<0.05$)

8.2. Structural characterizations of EPD deposited CuO-doped PG film

EPD of CTS, collagen/CTS and collagen resulted in uniform films, with the exception of pure collagen, which showed multiple instances of bubble formation and resulted in an uneven film. Cracking and spalling (flaking of the coatings) were also observed when PG was incorporated, as well as poor adhesion to the electrode's surface (see Figure 8.2). The formation of bubbles is due to the generation of hydrogen gas at the cathode [273]–[275], and can be attributed to collagen acting as an insulator (low conductivity, $\sim 10^{-13} \text{ S/cm}$ [276]), as was shown by the EIS measurements displayed in Figure 8.1. The low conductivity leads to the evolution of hydrogen gas at the cathode/film interface according to the following reaction [273], [274]:



CTS and collagen/CTS films did not show hydrogen gas evolution at the cathode, likely due to CTS having a higher electrical conductivity (30 S/cm [277]) compared to collagen [159].

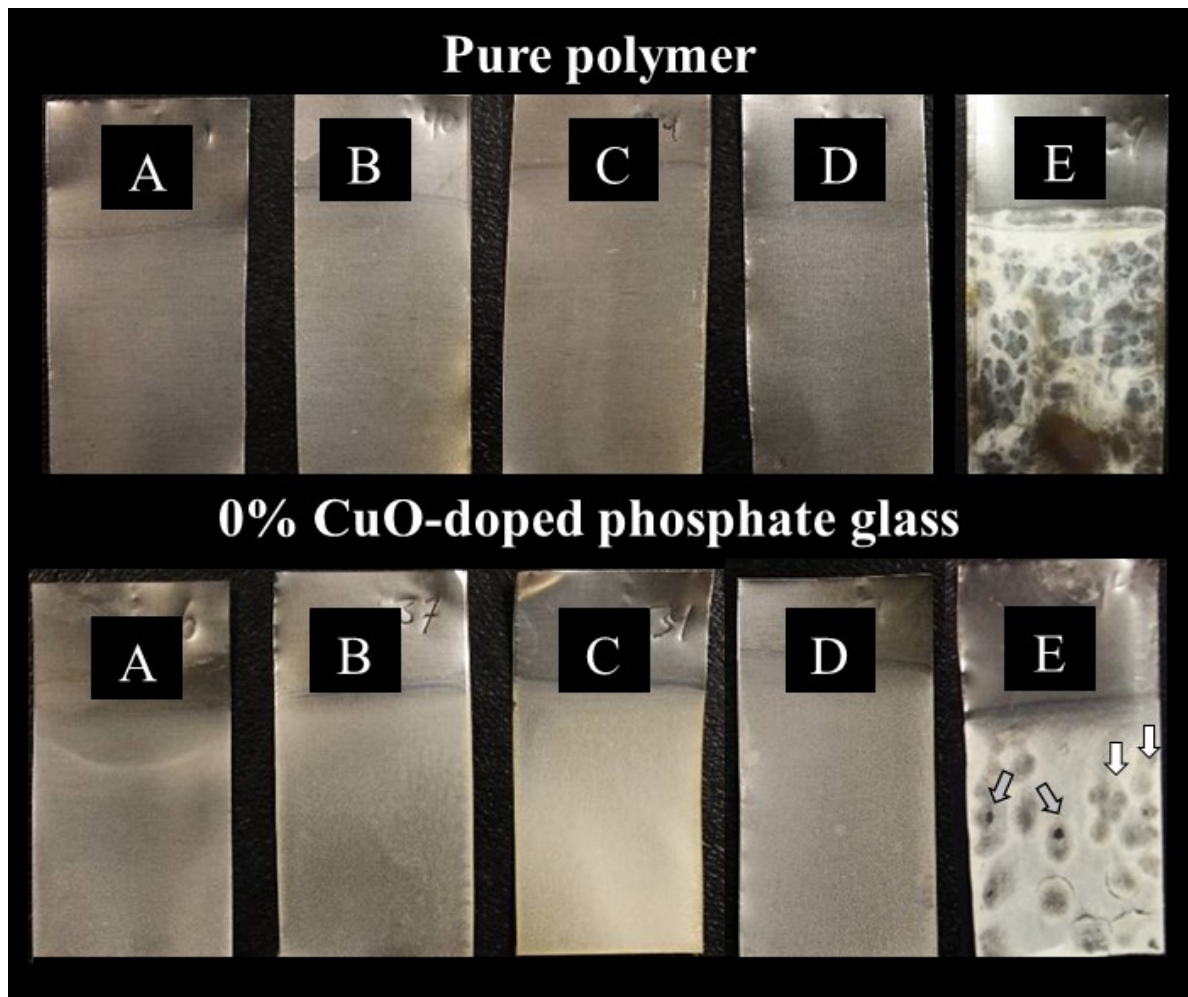


Figure 8.2: Images for EPD of A) 0.5 g/L CTS B) 0.33 g/L CTS, 0.17 g/L collagen, C) 0.25 g/L CTS, 0.25 g/L collagen, E) 0.17 g/L CTS, 0.33 g/L collagen and F) 0.5 g/L collagen films co-deposited with 0.5 g/L 0% CuO-doped phosphate glass (arrows: white = bubbles, grey = spalling, black = crack)

Electron microscopy allows to image morphology in-depth, and can be used to determine whether PG particles deposit uniformly, and if the polymers have good film-forming properties. Deposition of 0, 5 and 10 mol% of CuO-doped PG showed that the glasses deposited anodically (see Figure 8.3a-c), indicating that PG has a negative charge at neutral pH, similar to silica [278], [279], 45S5 Bioglass [280], and calcium phosphate particles [281]. Deposition of 0 mol% CuO-doped PG particles was achieved evenly across the electrode, though clumping of PG particles started to occur with increasing copper content (see Figure 8.3d-f). The results indicate that the addition of copper raises the surface charge of PG particles closer to the isoelectric point (IEP) such that flocculation occurs due to lack of

repulsive forces [224]. Similar results were reported with other Cu-doped materials, where increasing copper content raised the surface charge of the particle [282], [283].

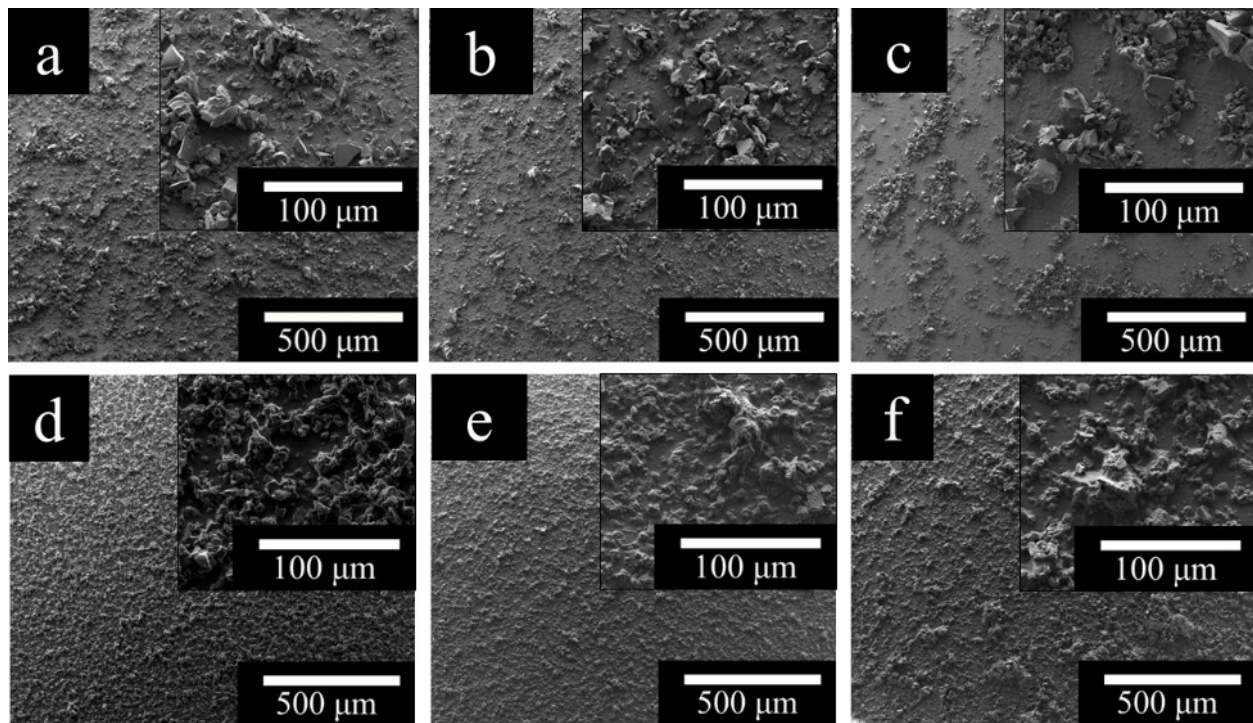


Figure 8.3: SEM images of EPD of 1 g/L (a) 0% (b) 5% and (c) 10% CuO-doped PG and 0.5 g/L CTS co-deposited with 0.5 g/L (d) 0% (e) 5% and (f) 10% CuO-doped PG. Inset of each figure shows the high resolution SEM images of the corresponding samples.

SEM images of co-deposited CTS-PG films are shown in Figure 5 (d)-(f). The deposition of the negatively charged PG is achieved when alongside a cationic polymer (see Figure 8.3d-f). While previously only deposited anodically, the results indicate that CTS is attracted to and adsorbs onto the PG which it carries to the cathode where it forms an insoluble deposit [95]. However, both SEM images and EDS (see Figure 8.4 for corresponding EDS images) mapping show that PG particles still aggregate and form an uneven film with increasing copper content, likely due to bridging flocculation [157]. The results indicate that PG doped with CuO is unsuitable for fabricating coatings via EPD due to the non-uniformity of the resulting film.

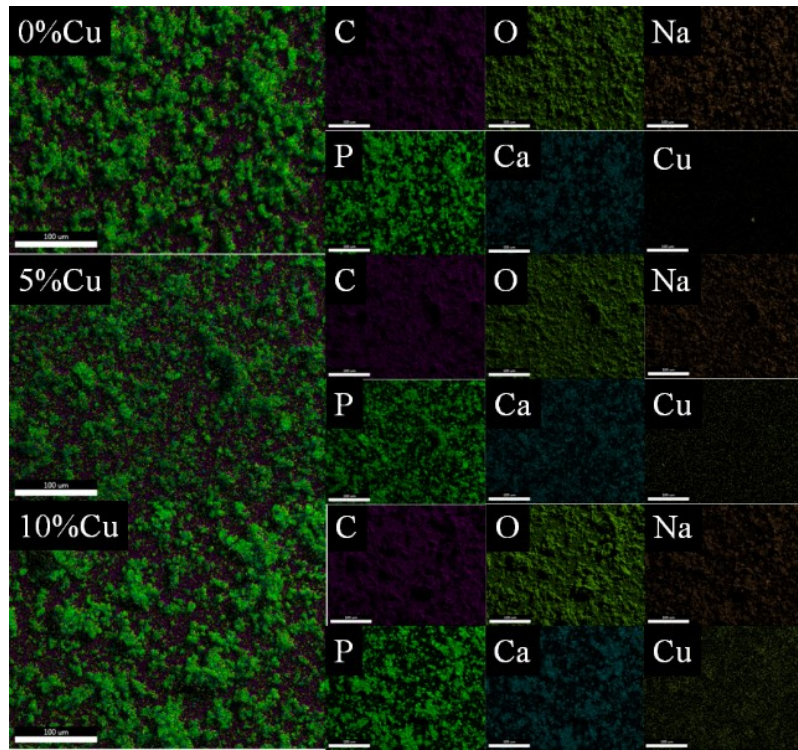


Figure 8.4: EDS map of CTS-PG films of 0, 5 and 10% CuO-doped PG (scale bars are 100 μm)

SEM images show that increasing the amount of collagen present in solution leads to more PG particles as well as larger particles being deposited, but increasing amounts of copper lead to a decreased deposition yield (see Figure 8.5). Previous work showed that collagen adsorbs onto oxide particles in solution at low pH [284]. Furthermore, tropocollagen (collagen molecules) have a length of 300 nm [60], whereas CTS has a length of \sim 50 nm [285]. The collagen present in the solution adsorbed onto the PG particles more than CTS, and the longer chain length of collagen likely result in an increased electrostatic double layer, increasing the repulsive force between particles and resulting in steric stabilization and to greater colloidal stability [286]–[288].

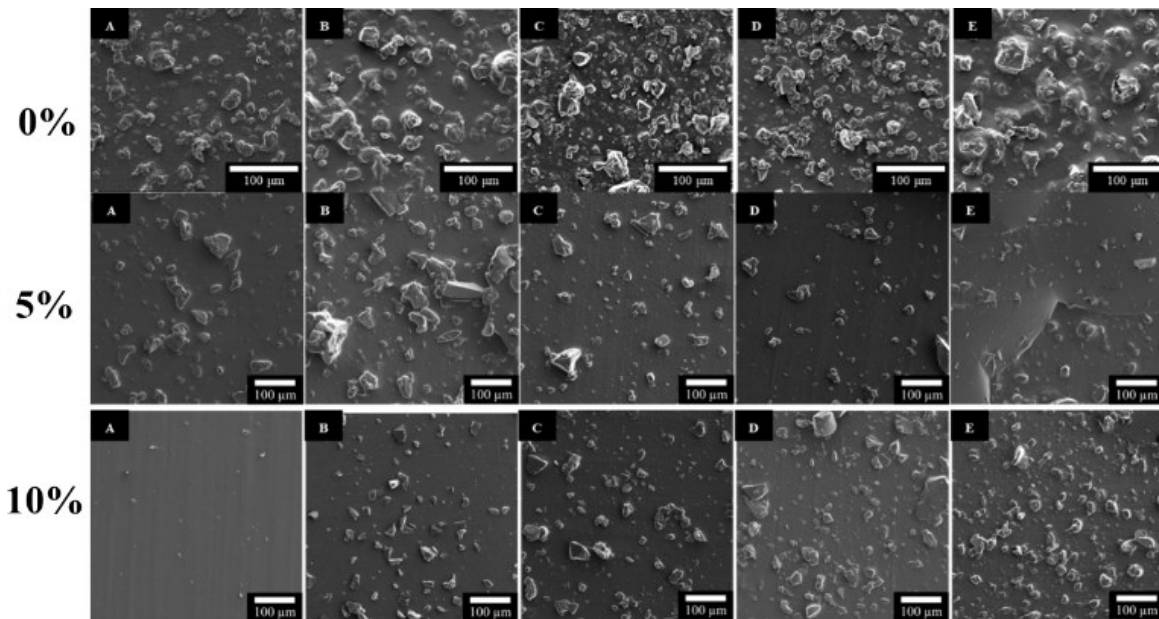


Figure 8.5: SEM images for EPD of A) 0.5 g/L CTS B) 0.33 g/L CTS, 0.17 g/L collagen and C) 0.25 CTS, 0.25 g/L collagen, D) 0.17 g/L col. 0.33 g/L CTS, E) 0.5 g/L collagen co-deposited with 0.5 g/L 0, 5 and 10 mol% CuO-doped phosphate glass

8.3. Adhesion tests of co-polymer films

Adhesion tests are useful for determining whether coatings are useable under conditions where they may otherwise peel or flake off. Adhesion tests (see Figure 8.6) show that the inclusion of collagen has a negative effect on the bonding of the single layer film to the substrate. Of all the films deposited, the single layer collagen film had the weakest adhesion. However, multilayer films fabricated using a single layer of collagen, with an additional layer of collagen, CTS, or a blended layer (BL) consisting of different collagen/CTS ratios deposited, showed that when subjected to the adhesion test, the underlying layer of collagen acted as a binder between the outer film and the substrate, significantly improving adhesion (see Table 8.1).

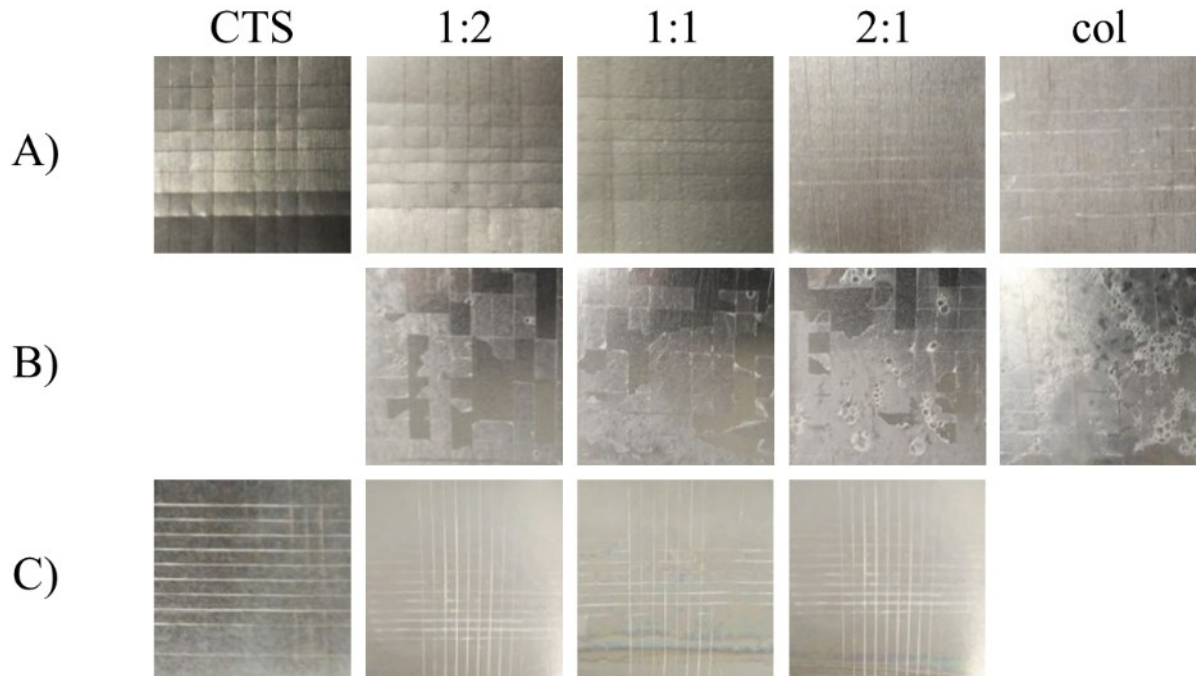


Figure 8.6: Adhesion test carried out to ASTM D3359 protocol for A) blended polymer layer, B) pure CTS layer+blended polymer layer and c) pure col layer+blended polymer layer (Note: pure col film was completely removed).

Table 8.1: Adhesion rating of EPD collagen/CTS and multilayer collagen/CTS films to SS substrate according to ASTM D3359 standards (0B – lowest, 5B – highest)

Film	Blended layer	Pure CTS+BL	Pure col+BL
Col	0B	5B	
2:1	5B	3B	5B
1:1	5B	3B	5B
1:2	5B	1B	5B
CTS	5B		5B

8.4. Chemical characterization of EPD deposited CuO-doped PG films

We acquired ATR-FTIR spectra to investigate the chemical composition of the coatings. The spectra obtained show that collagen, CTS and collagen/CTS coatings all have distinct spectra determined by the composition of their solution during deposition (see Figure 8.7). In particular, the Amide I and II bands of collagen at 1640 and 1550 cm⁻¹, respectively, were confirmed [84], [215]. The presence of CTS is confirmed by the band between 1160 and 1030 cm⁻¹, denoting the glycosidic linkages of the saccharine units of CTS [216], [217] (Figure 8.7A). The bands of collagen and CTS are more pronounced, depending on the concentration. Increased amounts of collagen led to higher deposition

yields of phosphate glass, as confirmed by the increase in the phosphate band at 1050 cm^{-1} (see Figure 8.7B-D) which indicates the presence of PO_4^{3-} [289], [290]. Conversely, increasing the CTS content of the solution shows a decrease in the phosphate band, indicating that the presence of collagen improves the stability of the colloidal suspension.

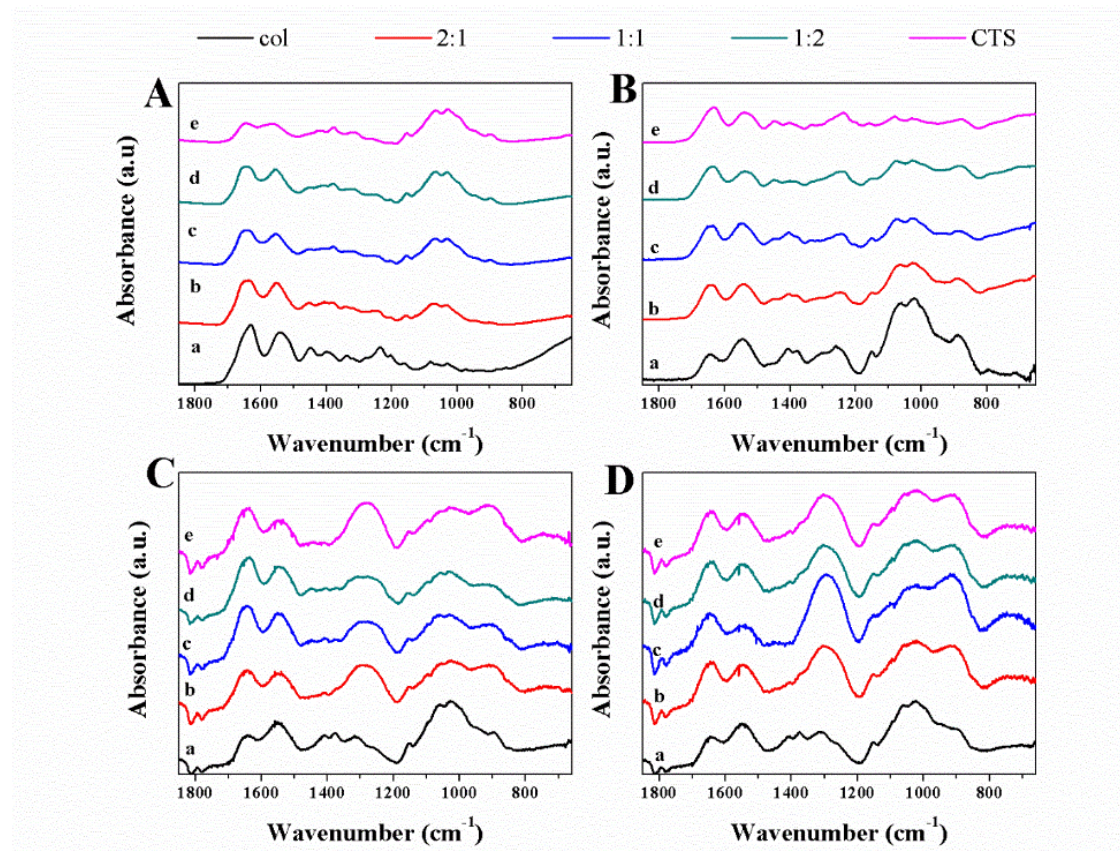


Figure 8.7: ATR-FTIR spectra of collagen, CTS and collagen/CTS films incorporating A) no PG and B) 0% c) 5% and D) 10% CuO-doped PG in (a) 0.5 g/L collagen, (b) 0.17 g/L CTS, 0.33 g/L collagen (c) 0.25 g/L CTS, 0.25 g/L collagen, (e) 0.33 g/L CTS, 0.17 g/L collagen and (e) 0.5 g/L CTS solutions

8.5. Deposition yield of EPD composite films

Measuring the deposition yield for different concentrations of collagen and CTS shows that increasing the collagen to CTS ratio has little effect on the final mass of the pure polymer film deposited. However, when co-deposited with PG, increasing the collagen concentration is accompanied by an increase in the deposition yield of the films (see Figure 8.8), similarly to what is inferred from SEM images and FTIR spectra. The results indicate that collagen is strongly adsorbed onto the particle surface [286] compared to CTS.

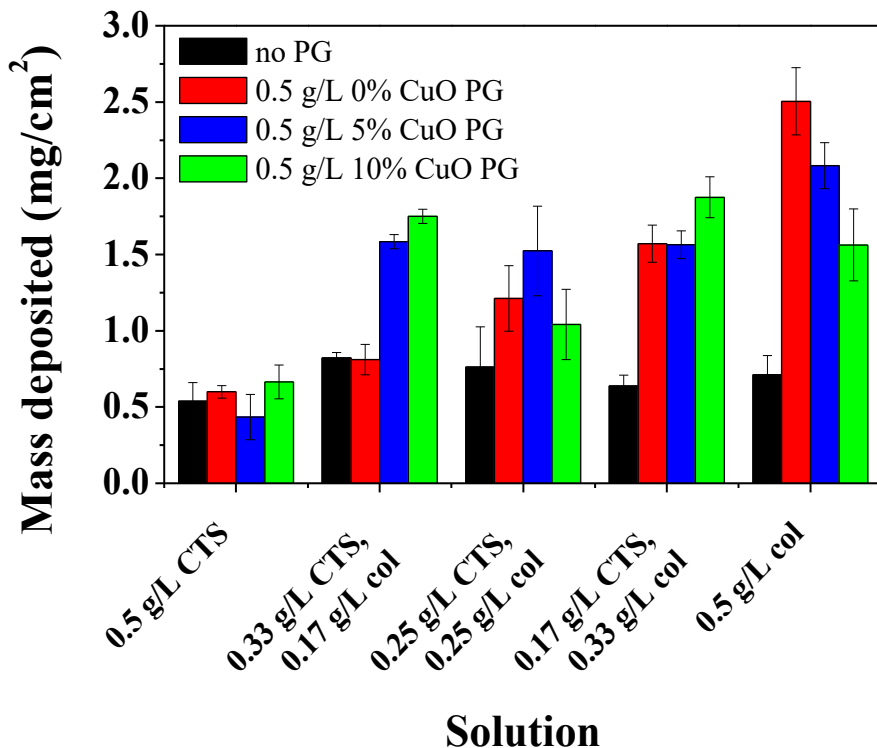


Figure 8.8: Mass deposited for EPD of collagen, collagen/CTS and CTS solutions compared to polymer co-deposited with PG ($n=3$, $p < 0.05$).

Thermogravimetric analysis (TGA) is a useful tool to determine the composition of composite materials, and the analysis of the deposits via TGA (see Figure 8.9) show that the addition of collagen greatly increases the amount of PG material within the deposit. Weight loss decreases when collagen is added, indicating that there is a larger amount of PG particles within the films. The results show that the mass of PG particles deposited increases from 5-15 wt% with only CTS to 62-68 wt% with collagen.

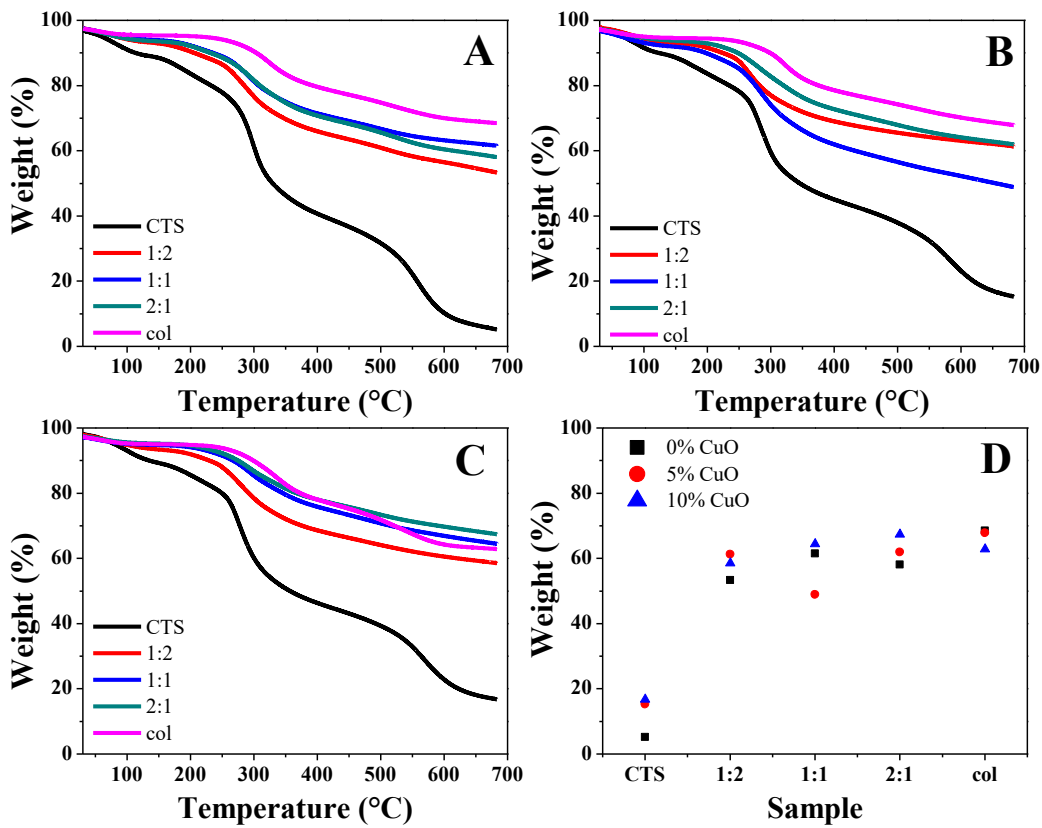


Figure 8.9: TGA for films fabricated by EPD of collagen, collagen/CTS and CTS solutions co-deposited with CuO-doped PG: (a) 0 mol%; (b) 5 mol%; (c) 10 mol% and (d) their weight percent.

Deposition yields were further analysed via QCM, which measures the deposition yield vs time on a vibrating quartz crystal. The results showed behaviour typical of constant voltage EPD, where the deposition rate decreases asymptotically with time. This behaviour is observed in both the EPD of CTS-PG and collagen-PG (see Figure 8.10). Collagen-PG exhibits a higher deposition rate, which can be attributed to a higher affinity to adsorb to the PG in solution. A linear increase accompanied by a gradual plateau is typical of constant voltage deposition where the concentration of the polymer/glass in solution decreases with time [291], [292]. Furthermore, the electric field necessary for electrophoresis also decreases due to the deposited film's resistivity, leading to a decrease in particle velocity towards the electrode [291].

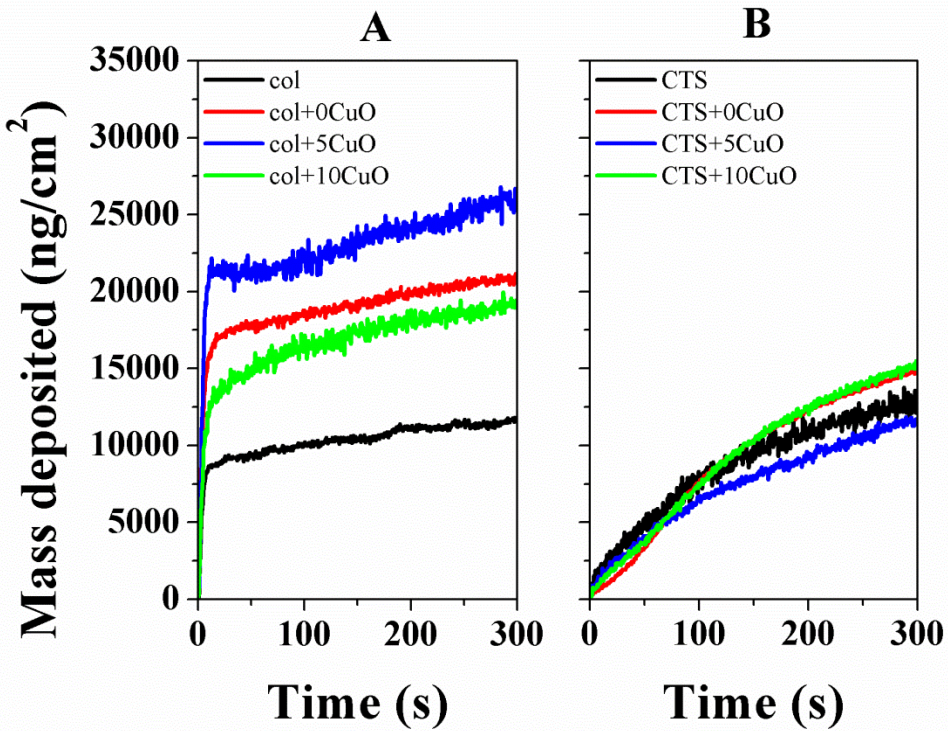


Figure 8.10: QCM measurements of mass deposited vs time for the EPD in A) collagen and B) CTS co-deposited with phosphate glass.

The resulting higher deposition yields are not consistent with the EIS results (see Figure 8.1) and zeta potential (see Figure 5.4) measurements. However, this does not take into account that the structure of collagen is markedly different from that of CTS: collagen forms long chains, attached end to end [293], [294] vs. sheets that attach along their sidechains for CTS [295], [296].

Since the zeta potential of CTS is much higher than that of collagen (see Figure 5.4), the presence of collagen most likely interacted with the PG and led to steric stabilization. Collagen is structurally a long chain molecule with a dipole [297], [298], while CTS is instead made up of sheets whose charge is distributed across the surface [299]. This can potentially explain the increased stabilization effect of collagen, as the long dipole chains lead to a larger steric layer [300] when they adsorb on the PG particle, while the CTS sheets wrap around the particle. Without stabilization of the colloidal suspension, the particles will sediment rapidly [301], resulting in a solution that has a decreased PG concentration.

9. Conclusions and future perspectives

9.1. Conclusions

This work examined various bioactive additives in different systems that could be used as potential replacements for traditional materials used in bone surgeries. The silk FDPs in plastically compressed collagen hydrogels were developed as scaffolds for bone tissue engineering that could replace autografts which require invasive patient surgery.

Results *in vitro* show that immersing FDPs in SBF led to the nucleation of HA, yet incorporating these same FDPs within a DC hydrogel does not contribute to mineralizing the collagen. Characterization of the polypeptides using LCMS showed the presence of glutamic acid (which is important for promoting HA nucleation) was present in a lower quantity than expected, though this may be attributed to the different experimental equipment used to quantify the amino acid composition or its processing.

The results indicate that it is less suitable for promoting biomineratization than was initially thought. Furthermore, mass analysis of DC hydrogels containing C_s over time indicated that the C_s fragments are immediately expelled during plastic compression. Chemical analysis showed that silk FDPs incorporated into a collagen hydrogel show little difference compared to a pure collagen hydrogel for promoting the nucleation of HA, and thus cannot serve as a replacement for NCPs in bone tissue engineering without first refining the method of linking the polypeptide to the collagen fibril.

The use of CuO-doped PG showed significantly more promise than that of FDPs. While not necessarily leading to the nucleation of HA, *in vitro* analysis showed that PG, under physiological conditions, led to the nucleation of ACP. Mass analysis and ATR-FTIR analysis of CuO-doped PG immersed in SBF showed that PG with higher copper content had an increased presence of phosphate peaks, indicating that the presence of copper is necessary for the nucleation of ACP. Furthermore, the SEM and EDS results showed that hydrogels containing PG immersed in SBF had ACP incorporated into the structure, as well as a higher amount of calcium and phosphate than the control groups, both indicative of a larger amount of mineralization.

These results indicate that PG can be used in biomaterials implants to help accelerate mineralization and healing.

Composites of PG, collagen and CTS were successfully deposited on stainless steel substrates via EPD.

The PG particles were deposited anodically and showed flocculation as CuO content increased, while both collagen and CTS deposited cathodically. The role of copper in EPD was also determined: particles with 5% and 10 mol% CuO-doped PG resulted in non-uniform films while 0 mol% was more uniform.

The pure polymer films showed little difference in deposition yield as the collagen/CTS ratio was varied. However, the addition of CuO-doped PG, which was successfully co-deposited cathodically with collagen and CTS, showed significant differences in the mass deposited as the collagen/CTS ratio was varied. The presence of collagen led to increased stability of the colloidal suspension due to steric stabilization, and increasing the amount of collagen also resulted in a linear increase in the deposition of PG, as well as larger particles being deposited, indicating that coatings can be tailored by adjusting the ratio of collagen to CTS. A drawback of using collagen, however, was the generation of hydrogen gas at the cathode, which resulted in non-uniform films and a loss of adhesion to the substrate, as well as cracking and spalling of the film.

The results indicate it is possible to fabricate tailored coatings of collagen, CTS and PG via EPD, and show promise for using PG as coating materials for orthopaedic implants.

9.2. Future perspectives

Much work is still needed to determine the suitability for CuO-doped PG to replace traditional bioglasses in biomedical applications. While the results obtained in this work are promising, the human body's reaction to these glasses still remains largely unknown. Furthermore, copper was known to have a toxic effect when exposed to cells in large quantities. While the amount used in the CuO-doped PG is minuscule compared to the amount necessary to do actual harm to the body, it is still an aspect of CuO-doped PG that requires investigating. Further work should focus on *in vivo* assays to determine a) cellular response to PG (in terms of cell proliferation and differentiation) and b) toxicity of CuO-doped PG, as Cu²⁺ ions are released during dissolution.

While more research is needed, our results obtained are promising in that they point to a method of increasing mineralization of the hydrogel, indicating that the period needed for healing and rehabilitation of patients who undergo surgery to repair bone tissue (which can take several weeks to several months) can be decreased substantially with a collagen-CTS-PG system. Furthermore, because the hydrogel network resembles the native ECM of bone tissue, it would also aid in the proliferation of bone cells. Finally, the potential to replace the need for autografts, requiring extra, invasive surgery, improves the quality of life of patients.

References

- [1] P. Ducheyne and Q. Qiu, "Bioactive ceramics: the effect of surface reactivity on bone formation and bone cell function," *Biomaterials*, vol. 20, no. 23–24, pp. 2287–2303, Dec. 1999, doi: 10.1016/S0142-9612(99)00181-7.
- [2] M. Navarro, A. Michiardi, O. Castaño, and J. A. Planell, "Biomaterials in orthopaedics," *J. R. Soc. Interface*, vol. 5, no. 27, pp. 1137–1158, Oct. 2008, doi: 10.1098/rsif.2008.0151.
- [3] G. Duque and B. R. Troen, "Understanding the mechanisms of senile osteoporosis: new facts for a major geriatric syndrome," *J. Am. Geriatr. Soc.*, vol. 56, no. 5, pp. 935–941, May 2008, doi: 10.1111/j.1532-5415.2008.01764.x.
- [4] O. Demontiero, C. Vidal, and G. Duque, "Aging and bone loss: new insights for the clinician," *Ther. Adv. Musculoskelet. Dis.*, vol. 4, no. 2, pp. 61–76, Apr. 2012, doi: 10.1177/1759720X11430858.
- [5] S. L. Hui, C. W. Slemenda, and C. C. Johnston, "Age and bone mass as predictors of fracture in a prospective study.," *J. Clin. Invest.*, vol. 81, no. 6, pp. 1804–1809, Jun. 1988, doi: 10.1172/JCI113523.
- [6] Statistics Canada, "Census in Brief: A portrait of the population aged 85 and older in 2016 in Canada," *Statistics Canada*, May 03, 2017. <https://www12.statcan.gc.ca/census-recensement/2016/as-sa/98-200-x/2016004/98-200-x2016004-eng.cfm> (accessed Oct. 29, 2018).
- [7] G. R. Mundy, "Bone resorption and turnover in health and disease.," *Bone*, vol. 8 Suppl 1, pp. S9-16, 1987.
- [8] Statistics Canada, "2001 Census of Population," Statistics Canada, Ottawa, Statistics Canada Catalogue no. 95F0486XCB2001001, 2001. Accessed: Oct. 29, 2018. [Online]. Available: <https://www12.statcan.gc.ca/english/census01/products/standard/profiles/Rp-eng.cfm?LANG=E&APATH=3&DETAIL=1&DIM=0&FL=A&FREE=0&GC=0&GID=0&GK=0&GRP=1&PID=56136&PRID=0&PTYPE=55430,53293,55440,55496,71090&S=0&SHOWALL=0&SUB=0&Temporal=2001&THEME=57&VID=0&VNAMEE=&VNAMEF=>
- [9] Statistics Canada, "2006 Census of Population," Statistics Canada, Ottawa, Statistics Canada Catalogue no. 97-551-XCB2006006, 2006. Accessed: Oct. 29, 2018. [Online]. Available: <https://www12.statcan.gc.ca/census-recensement/2006/dp-pd/tbt/Rp-eng.cfm?LANG=E&APATH=3&DETAIL=0&DIM=0&FL=A&FREE=0&GC=0&GID=0&GK=0&GRP=1&PID=88981&PRID=0&PTYPE=88971,97154&S=0&SHOWALL=0&SUB=0&Temporal=2006&THEME=66&VID=0&VNAMEE=&VNAMEF=>
- [10] Statistics Canada, "2011 Census of Population," Statistics Canada, Ottawa, Statistics Canada Catalogue no. 98-311-XCB2011018, 2011. Accessed: Oct. 29, 2018. [Online]. Available: <https://www12.statcan.gc.ca/census-recensement/2011/dp-pd/tbt/Rp-eng.cfm?LANG=E&APATH=3&DETAIL=0&DIM=0&FL=A&FREE=0&GC=0&GID=0&GK=0&GRP=1&PID=101998&PRID=10&PTYPE=101955&S=0&SHOWALL=0&SUB=0&Temporal=2011&THEME=88&VID=0&VNAMEE=&VNAMEF=>

- [11] Statistics Canada, “2016 Census of Population,” Statistics Canada, Ottawa, Statistics Canada Catalogue no. 98-400-X2016001, 2016. Accessed: Oct. 29, 2018. [Online]. Available: <https://www12.statcan.gc.ca/census-recensement/2016/dp-pd/dt-td/Rp-eng.cfm?LANG=E&APATH=3&DETAIL=0&DIM=0&FL=A&FREE=0&GC=0&GID=0&GK=0&GRP=1&PID=109523&PRID=10&PTYPE=109445&S=0&SHOWALL=0&SUB=0&Temporal=2016&THEME=115&VID=0&VNAMEE=&VNAMEF=>
- [12] Statistics Canada, “Population Projections for Canada (2013 to 2063), Provinces and Territories (2013 to 2038),” Statistics Canada, Ottawa, Statistics Canada Catalogue no. 91-520-X, May 2015. Accessed: Oct. 29, 2018. [Online]. Available: <https://www150.statcan.gc.ca/n1/pub/91-520-x/91-520-x2014001-eng.htm>
- [13] Bone and Joint Decade, “Key facts and figures | The Bone and Joint Decade,” *The Bone and Joint Decade*, 2013. http://bjdonline.org/?page_id=1574 (accessed Nov. 12, 2013).
- [14] W. D. Leslie *et al.*, “Population-based Canadian hip fracture rates with international comparisons,” *Osteoporos. Int.*, vol. 21, no. 8, pp. 1317–1322, Aug. 2010, doi: 10.1007/s00198-009-1080-1.
- [15] E. A. Papadimitropoulos, P. C. Coyte, R. G. Josse, and C. E. Greenwood, “Current and projected rates of hip fracture in Canada,” *CMAJ Can. Med. Assoc. J.*, vol. 157, no. 10, pp. 1357–1363, Nov. 1997.
- [16] M. E. Wiktorowicz, R. Goeree, A. Papaioannou, J. D. Adachi, and E. Papadimitropoulos, “Economic implications of hip fracture: health service use, institutional care and cost in Canada,” *Osteoporos. Int.*, vol. 12, no. 4, pp. 271–278, 2001, doi: 10.1007/s001980170116.
- [17] J. G. Betts *et al.*, *Anatomy and Physiology*, 1st ed. Houston, Texas, U.S: OpenStax, 2013.
- [18] D. R. Carter, “Mechanical loading histories and cortical bone remodeling,” *Calcif. Tissue Int.*, vol. 36, no. 1, pp. S19–S24, Mar. 1984, doi: 10.1007/BF02406129.
- [19] M. A. Meyers, P.-Y. Chen, A. Y.-M. Lin, and Y. Seki, “Biological materials: Structure and mechanical properties,” *Prog. Mater. Sci.*, vol. 53, no. 1, pp. 1–206, Jan. 2008, doi: 10.1016/j.pmatsci.2007.05.002.
- [20] R. L. Jilka, “Biology of the basic multicellular unit and the pathophysiology of osteoporosis,” *Med. Pediatr. Oncol.*, vol. 41, no. 3, pp. 182–185, Sep. 2003, doi: 10.1002/mpo.10334.
- [21] C. Gentili and R. Cancedda, “Cartilage and bone extracellular matrix,” *Curr. Pharm. Des.*, vol. 15, no. 12, pp. 1334–1348, 2009.
- [22] J. Engel and H. P. Bächinger, “Structure, Stability and Folding of the Collagen Triple Helix,” in *Collagen: Primer in Structure, Processing and Assembly*, J. Brinckmann, H. Notbohm, and P. K. Müller, Eds. Berlin, Heidelberg: Springer Berlin Heidelberg, 2005, pp. 7–33. doi: 10.1007/b103818.
- [23] M. E. Nimni, “Collagen: Its structure and function in normal and pathological connective tissues,” *Semin. Arthritis Rheum.*, vol. 4, no. 2, pp. 95–150, 1974, doi: 10.1016/0049-0172(74)90001-8.

- [24] N. Goonoo, A. Bhaw-Luximon, and D. Jhurry, “In vitro and in vivo cytocompatibility of electrospun nanofiber scaffolds for tissue engineering applications,” *RSC Adv.*, vol. 4, pp. 31618–31642, Jul. 2014, doi: 10.1039/C4RA05218H.
- [25] A. Jorio, *Bioengineering Applications of Carbon Nanostructures*, 1st ed. New York City, NY: Springer International Publishing, 2016. doi: 10.1007/978-3-319-25907-9.
- [26] S. N. Deshmukh, A. M. Dive, R. Moharil, and P. Munde, “Enigmatic insight into collagen,” *J. Oral Maxillofac. Pathol. JOMFP*, vol. 20, no. 2, pp. 276–283, 2016, doi: 10.4103/0973-029X.185932.
- [27] S. Ricard-Blum, “The Collagen Family,” *Cold Spring Harb. Perspect. Biol.*, vol. 3, no. 1, p. a004978, Jan. 2011, doi: 10.1101/cshperspect.a004978.
- [28] H. Lodish, A. Berk, S. L. Zipursky, P. Matsudaira, D. Baltimore, and J. Darnell, *Molecular Cell Biology*, 4th ed. W. H. Freeman, 2000.
- [29] G. R. Mundy and T. J. Martin, Eds., *Physiology and Pharmacology of Bone*. Berlin Heidelberg: Springer-Verlag, 1993. doi: 10.1007/978-3-642-77991-6.
- [30] J. Sodek, B. Ganss, and M. D. McKee, “Osteopontin,” *Crit. Rev. Oral Biol. Med.*, vol. 11, no. 3, pp. 279–303, Jul. 2000, doi: 10.1177/10454411000110030101.
- [31] D. T. Denhardt and X. Guo, “Osteopontin: a protein with diverse functions,” *FASEB J.*, vol. 7, no. 15, pp. 1475–1482, 1993, doi: <https://doi.org/10.1096/fasebj.7.15.8262332>.
- [32] J. D. Termine, H. K. Kleinman, S. W. Whitson, K. M. Conn, M. L. McGarvey, and G. R. Martin, “Osteonectin, a bone-specific protein linking mineral to collagen,” *Cell*, vol. 26, no. 1, Part 1, pp. 99–105, Oct. 1981, doi: 10.1016/0092-8674(81)90037-4.
- [33] R. D. Cummings and J. M. Pierce, Eds., *Handbook of Glycomics*, 1 edition. Amsterdam: Academic Press, 2009.
- [34] T. E. Hardingham and A. J. Fosang, “Proteoglycans: many forms and many functions,” *FASEB J.*, vol. 6, no. 3, pp. 861–870, Feb. 1992.
- [35] E. Ruoslahti, “Structure and Biology of Proteoglycans,” *Annu. Rev. Cell Biol.*, vol. 4, no. 1, pp. 229–255, 1988, doi: 10.1146/annurev.cb.04.110188.001305.
- [36] P. Fratzl and R. Weinkamer, “Nature’s hierarchical materials,” *Prog. Mater. Sci.*, vol. 52, no. 8, pp. 1263–1334, Nov. 2007, doi: 10.1016/j.pmatsci.2007.06.001.
- [37] A. Kumari, *Sweet Biochemistry: Remembering Structures, Cycles, and Pathways by Mnemonics*, 1 edition. London, United Kingdom: Academic Press, 2017.
- [38] J. P. Bilezikian, Ed., *Primer on the Metabolic Bone Diseases and Disorders of Mineral Metabolism*. John Wiley & Sons, 2018.
- [39] S. Raynaud, E. Champion, D. Bernache-Assollant, and J.-P. Laval, “Determination of Calcium/Phosphorus Atomic Ratio of Calcium Phosphate Apatites Using X-ray Diffractometry,”

J. Am. Ceram. Soc., vol. 84, no. 2, pp. 359–66, Feb. 2001, doi: 10.1111/j.1151-2916.2001.tb00663.x.

- [40] R. Singh, C. Y. Tan, M. Abd Shukor, I. Sopyan, and W. Teng, “The influence of Ca/P ratio on the properties of hydroxyapatite bioceramics,” *Proc SPIE*, vol. 6423, Oct. 2007, doi: 10.1117/12.779890.
- [41] C. Y. Tan, S. Ramesh, Y. C. Teh, Y. M. Tan, and B. K. Yap, “The Effects of Calcium-to-Phosphorus Ratio on the Densification and Mechanical Properties of Hydroxyapatite Ceramic,” *Int. J. Appl. Ceram. Technol.*, vol. 12, no. 1, pp. 223–227, May 2014, doi: 10.1111/ijac.12249.
- [42] B. Clarke, “Normal Bone Anatomy and Physiology,” *Clin. J. Am. Soc. Nephrol.*, vol. 3, no. Supplement 3, pp. S131–S139, Nov. 2008, doi: 10.2215/CJN.04151206.
- [43] AZoM, “Hydroxyapatite - Properties and Applications,” *AZoM - The A to Z of Materials*, 2013. <http://www.azom.com/article.aspx?ArticleID=107> (accessed Apr. 03, 2014).
- [44] E. F. Morgan, D. N. Yetkinler, B. R. Constantz, and R. H. Dauskardt, “Mechanical properties of carbonated apatite bone mineral substitute: strength, fracture and fatigue behaviour,” *J. Mater. Sci. Mater. Med.*, vol. 8, no. 9, pp. 559–570, Sep. 1997, doi: 10.1023/A:1018550831834.
- [45] B. Wopenka and J. D. Pasteris, “A mineralogical perspective on the apatite in bone,” *Mater. Sci. Eng. C*, vol. 25, no. 2, pp. 131–143, Apr. 2005, doi: 10.1016/j.msec.2005.01.008.
- [46] N. A. Sims and J. H. Gooi, “Bone remodeling: Multiple cellular interactions required for coupling of bone formation and resorption,” *Semin. Cell Dev. Biol.*, vol. 19, no. 5, pp. 444–451, Oct. 2008, doi: 10.1016/j.semcdb.2008.07.016.
- [47] H. M. Frost, “Wolff’s Law and bone’s structural adaptations to mechanical usage: an overview for clinicians,” *Angle Orthod.*, vol. 64, no. 3, pp. 175–188, 1994, doi: 10.1043/0003-3219(1994)064<0175:WLABSA>2.0.CO;2.
- [48] K. D. Cashman and F. Ginty, “BONE,” in *Encyclopedia of Food Sciences and Nutrition (Second Edition)*, B. Caballero, Ed. Oxford: Academic Press, 2003, pp. 557–565. doi: 10.1016/B0-12-227055-X/00111-5.
- [49] G. K. Hunter, C. L. Kyle, and H. A. Goldberg, “Modulation of crystal formation by bone phosphoproteins: structural specificity of the osteopontin-mediated inhibition of hydroxyapatite formation.,” *Biochem. J.*, vol. 300, no. Pt 3, pp. 723–728, Jun. 1994.
- [50] H. A. Goldberg, K. J. Warner, M. C. Li, and G. K. Hunter, “Binding of bone sialoprotein, osteopontin and synthetic polypeptides to hydroxyapatite,” *Connect. Tissue Res.*, vol. 42, no. 1, pp. 25–37, 2001.
- [51] G. K. Hunter, P. V. Hauschka, A. R. Poole, L. C. Rosenberg, and H. A. Goldberg, “Nucleation and inhibition of hydroxyapatite formation by mineralized tissue proteins.,” *Biochem. J.*, vol. 317, no. Pt 1, pp. 59–64, Jul. 1996.
- [52] L. C. Palmer, C. J. Newcomb, S. R. Kaltz, E. D. Spoerke, and S. I. Stupp, “Biomimetic Systems for Hydroxyapatite Mineralization Inspired By Bone and Enamel,” *Chem. Rev.*, vol. 108, no. 11,

pp. 4754–4783, Nov. 2008, doi: 10.1021/cr8004422.

- [53] S. H. Rhee and J. Tanaka, “Hydroxyapatite formation on cellulose cloth induced by citric acid,” *J. Mater. Sci. Mater. Med.*, vol. 11, no. 7, pp. 449–452, Jul. 2000.
- [54] J. Song, V. Malathong, and C. R. Bertozzi, “Mineralization of synthetic polymer scaffolds: a bottom-up approach for the development of artificial bone,” *J. Am. Chem. Soc.*, vol. 127, no. 10, pp. 3366–3372, Mar. 2005, doi: 10.1021/ja043776z.
- [55] M. M. Stevens, “Biomaterials for bone tissue engineering,” *Mater. Today*, vol. 11, no. 5, pp. 18–25, May 2008, doi: 10.1016/S1369-7021(08)70086-5.
- [56] M. Swetha, K. Sahithi, A. Moorthi, N. Srinivasan, K. Ramasamy, and N. Selvamurugan, “Biocomposites containing natural polymers and hydroxyapatite for bone tissue engineering,” *Int. J. Biol. Macromol.*, vol. 47, no. 1, pp. 1–4, Jul. 2010, doi: 10.1016/j.ijbiomac.2010.03.015.
- [57] S. Weiner and H. D. Wagner, “The Material Bone: Structure-Mechanical Function Relations,” *Annu. Rev. Mater. Sci.*, vol. 28, no. 1, pp. 271–298, 1998, doi: 10.1146/annurev.matsci.28.1.271.
- [58] W. J. Landis, M. J. Song, A. Leith, L. McEwen, and B. F. McEwen, “Mineral and Organic Matrix Interaction in Normally Calcifying Tendon Visualized in Three Dimensions by High-Voltage Electron Microscopic Tomography and Graphic Image Reconstruction,” *J. Struct. Biol.*, vol. 110, no. 1, pp. 39–54, Jan. 1993, doi: 10.1006/jsbi.1993.1003.
- [59] S. Weiner and W. Traub, “Bone structure: from angstroms to microns.,” *FASEB J.*, vol. 6, no. 3, pp. 879–885, Feb. 1992.
- [60] M. J. Buehler, “Nature designs tough collagen: Explaining the nanostructure of collagen fibrils,” *Proc. Natl. Acad. Sci.*, vol. 103, no. 33, pp. 12285–12290, Aug. 2006, doi: 10.1073/pnas.0603216103.
- [61] C. V. M. Rodrigues *et al.*, “Characterization of a bovine collagen-hydroxyapatite composite scaffold for bone tissue engineering.,” *Biomaterials*, vol. 24, no. 27, pp. 4987–4997, 2004, doi: 10.1016/S0142-9612(03)00410-1.
- [62] C. G. Finkemeier, “Bone-Grafting and Bone-Graft Substitutes,” *J. Bone Jt. Surg.*, vol. 84, no. 3, pp. 454–464, Mar. 2002.
- [63] J. R. Lieberman and G. E. Friedlaender, *Bone regeneration and repair: biology and clinical applications*. Totowa, NJ: Humana Press, 2005.
- [64] C. J. Damien and J. R. Parsons, “Bone graft and bone graft substitutes: A review of current technology and applications,” *J. Appl. Biomater.*, vol. 2, no. 3, pp. 187–208, 1991, doi: 10.1002/jab.770020307.
- [65] A. S. Greenwald, S. D. Boden, V. M. Goldberg, Y. Khan, C. T. Laurencin, and R. N. Rosier, “Bone-Graft Substitutes: Facts, Fictions, and Applications,” *J. Bone Jt. Surg.*, vol. 83, no. 2 suppl 2, pp. S98-103, Nov. 2001, doi: 10.2106/00004623-200100022-00007.
- [66] K. J. L. Burg, S. Porter, and J. F. Kellam, “Biomaterial developments for bone tissue engineering,”

Biomaterials, vol. 21, no. 23, pp. 2347–2359, Dec. 2000, doi: 10.1016/S0142-9612(00)00102-2.

- [67] M. Wagner-Ecker, P. Voltz, M. Egermann, and W. Richter, “The collagen component of biological bone graft substitutes promotes ectopic bone formation by human mesenchymal stem cells,” *Acta Biomater.*, vol. 9, no. 7, pp. 7298–7307, Jul. 2013, doi: 10.1016/j.actbio.2013.03.037.
- [68] S. B. Goodman, Z. Yao, M. Keeney, and F. Yang, “The future of biologic coatings for orthopaedic implants,” *Biomaterials*, vol. 34, no. 13, pp. 3174–3183, Apr. 2013, doi: 10.1016/j.biomaterials.2013.01.074.
- [69] K. Katti, D. Verma, and D. Katti, “4 - Materials for joint replacement,” in *Joint Replacement Technology*, P. A. Revell, Ed. Woodhead Publishing, 2008, pp. 81–104. doi: 10.1533/9781845694807.1.81.
- [70] K. Markatos, G. Tsoucalas, and M. Sgantzos, “Hallmarks in the history of orthopaedic implants for trauma and joint replacement,” *Acta Medico-Hist. Adriat. AMHA*, vol. 14, no. 1, pp. 161–176, Aug. 2016.
- [71] K. Rezwan, Q. Z. Chen, J. J. Blaker, and A. R. Boccaccini, “Biodegradable and bioactive porous polymer/inorganic composite scaffolds for bone tissue engineering,” *Biomaterials*, vol. 27, no. 18, pp. 3413–3431, Jun. 2006, doi: 10.1016/j.biomaterials.2006.01.039.
- [72] D. C. Greenspan, “Bioactive ceramic implant materials,” *Curr. Opin. Solid State Mater. Sci.*, vol. 4, no. 4, pp. 389–393, Aug. 1999, doi: 10.1016/S1359-0286(99)00021-2.
- [73] R. A. Martin *et al.*, “Characterizing the hierarchical structures of bioactive sol–gel silicate glass and hybrid scaffolds for bone regeneration,” *Phil Trans R Soc A*, vol. 370, no. 1963, pp. 1422–1443, Mar. 2012, doi: 10.1098/rsta.2011.0308.
- [74] J. R. Porter, T. T. Ruckh, and K. C. Popat, “Bone tissue engineering: A review in bone biomimetics and drug delivery strategies,” *Biotechnol. Prog.*, vol. 25, no. 6, pp. 1539–1560, 2009, doi: 10.1002/btpr.246.
- [75] V. Ottani, D. Martini, M. Franchi, A. Ruggeri, and M. Raspanti, “Hierarchical structures in fibrillar collagens,” *Micron*, vol. 33, no. 7–8, pp. 587–596, 2002, doi: 10.1016/S0968-4328(02)00033-1.
- [76] W. Friess, “Collagen – biomaterial for drug delivery,” *Eur. J. Pharm. Biopharm.*, vol. 45, no. 2, pp. 113–136, Mar. 1998, doi: 10.1016/S0939-6411(98)00017-4.
- [77] K. Gelse, E. Pöschl, and T. Aigner, “Collagens—structure, function, and biosynthesis,” *Adv. Drug Deliv. Rev.*, vol. 55, no. 12, pp. 1531–1546, Nov. 2003, doi: 10.1016/j.addr.2003.08.002.
- [78] S. F. Badylak, D. O. Freytes, and T. W. Gilbert, “Extracellular matrix as a biological scaffold material: Structure and function,” *Acta Biomater.*, vol. 5, no. 1, pp. 1–13, Jan. 2009, doi: 10.1016/j.actbio.2008.09.013.
- [79] R. Hartwell *et al.*, “A novel hydrogel-collagen composite improves functionality of an injectable extracellular matrix,” *Acta Biomater.*, vol. 7, no. 8, pp. 3060–3069, Aug. 2011, doi:

10.1016/j.actbio.2011.04.024.

- [80] B. Marelli, C. E. Ghezzi, A. Alessandrino, J. E. Barralet, G. Freddi, and S. N. Nazhat, “Silk fibroin derived polypeptide-induced biominerization of collagen,” *Biomaterials*, vol. 33, no. 1, pp. 102–108, Jan. 2012, doi: 10.1016/j.biomaterials.2011.09.039.
- [81] S. Roessler, R. Born, D. Scharnweber, H. Worch, A. Sewing, and M. Dard, “Biomimetic coatings functionalized with adhesion peptides for dental implants,” *J. Mater. Sci. Mater. Med.*, vol. 12, no. 10–12, pp. 871–877, 2001, doi: 10.1023/a:1012807621414.
- [82] F. Chicatun, C. E. Pedraza, N. Muja, C. E. Ghezzi, M. D. McKee, and S. N. Nazhat, “Effect of Chitosan Incorporation and Scaffold Geometry on Chondrocyte Function in Dense Collagen Type I Hydrogels,” *Tissue Eng. Part A*, vol. 19, no. 23–24, pp. 2553–2564, Aug. 2013, doi: 10.1089/ten.tea.2013.0114.
- [83] R. A. Brown, M. Wiseman, C.-B. Chuo, U. Cheema, and S. N. Nazhat, “Ultrarapid Engineering of Biomimetic Materials and Tissues: Fabrication of Nano- and Microstructures by Plastic Compression,” *Adv. Funct. Mater.*, vol. 15, no. 11, pp. 1762–1770, 2005, doi: 10.1002/adfm.200500042.
- [84] F. Chicatun *et al.*, “Osteoid-mimicking dense collagen/chitosan hybrid gels,” *Biomacromolecules*, vol. 12, no. 8, pp. 2946–2956, Aug. 2011, doi: 10.1021/bm200528z.
- [85] E. A. A. Neel, U. Cheema, J. C. Knowles, R. A. Brown, and S. N. Nazhat, “Use of multiple unconfined compression for control of collagen gel scaffold density and mechanical properties,” *Soft Matter*, vol. 2, no. 11, pp. 986–992, Oct. 2006, doi: 10.1039/B609784G.
- [86] B. R. Coyac *et al.*, “Mineralization of Dense Collagen Hydrogel Scaffolds by Human Pulp Cells,” *J. Dent. Res.*, vol. 92, no. 7, pp. 648–654, Jul. 2013, doi: 10.1177/0022034513488599.
- [87] S. Mima, M. Miya, R. Iwamoto, and S. Yoshikawa, “Highly deacetylated chitosan and its properties,” *J. Appl. Polym. Sci.*, vol. 28, no. 6, pp. 1909–1917, Jun. 1983, doi: 10.1002/app.1983.070280607.
- [88] I. Aranaz *et al.*, “Functional Characterization of Chitin and Chitosan,” *Curr. Chem. Biol.*, vol. 3, no. 2, pp. 203–230, May 2009, doi: 10.2174/187231309788166415.
- [89] D. Filion and M. D. Buschmann, “Chitosan-glycerol-phosphate (GP) gels release freely diffusible GP and possess titratable fixed charge,” *Carbohydr. Polym.*, vol. 98, no. 1, pp. 813–819, Oct. 2013, doi: 10.1016/j.carbpol.2013.06.055.
- [90] F. Croisier and C. Jérôme, “Chitosan-based biomaterials for tissue engineering,” *Eur. Polym. J.*, vol. 49, no. 4, pp. 780–792, Apr. 2013, doi: 10.1016/j.eurpolymj.2012.12.009.
- [91] L. J. del Valle, A. Díaz, and J. Puiggallí, “Hydrogels for Biomedical Applications: Cellulose, Chitosan, and Protein/Peptide Derivatives,” *Gels*, vol. 3, no. 3, p. 27, Jul. 2017, doi: 10.3390/gels3030027.
- [92] M. J. Moura, H. Faneca, M. P. Lima, M. H. Gil, and M. M. Figueiredo, “In Situ Forming Chitosan Hydrogels Prepared via Ionic/Covalent Co-Cross-Linking,” *Biomacromolecules*, vol. 12, no. 9,

pp. 3275–3284, Sep. 2011, doi: 10.1021/bm200731x.

- [93] J. Zan, H. Chen, G. Jiang, Y. Lin, and F. Ding, “Preparation and properties of crosslinked chitosan thermosensitive hydrogel for injectable drug delivery systems,” *J. Appl. Polym. Sci.*, vol. 101, no. 3, pp. 1892–1898, 2006, doi: <https://doi.org/10.1002/app.23613>.
- [94] X. Z. Shu and K. J. Zhu, “The influence of multivalent phosphate structure on the properties of ionically cross-linked chitosan films for controlled drug release,” *Eur. J. Pharm. Biopharm. Off. J. Arbeitsgemeinschaft Pharm. Verfahrenstechnik EV*, vol. 54, no. 2, pp. 235–243, Sep. 2002, doi: 10.1016/s0939-6411(02)00052-8.
- [95] I. Deen, X. Pang, and I. Zhitomirsky, “Electrophoretic deposition of composite chitosan–halloysite nanotube–hydroxyapatite films,” *Colloids Surf. A*, vol. 410, pp. 38–44, Jun. 2012, doi: 10.1016/j.colsurfa.2012.06.011.
- [96] N. S. Raddaha, L. Cordero-Arias, S. Cabanas-Polo, S. Virtanen, J. A. Roether, and A. R. Boccaccini, “Electrophoretic Deposition of Chitosan/h-BN and Chitosan/h-BN/TiO₂ Composite Coatings on Stainless Steel (316L) Substrates,” *Materials*, vol. 7, no. 3, pp. 1814–1829, Mar. 2014, doi: 10.3390/ma7031814.
- [97] M. Miola, E. Verné, F. E. Ciraldo, L. Cordero-Arias, and A. R. Boccaccini, “Electrophoretic Deposition of Chitosan/45S5 Bioactive Glass Composite Coatings Doped with Zn and Sr,” *Front. Bioeng. Biotechnol.*, vol. 3, 2015, doi: 10.3389/fbioe.2015.00159.
- [98] J. P. Martínez, M. P. Falomir, and D. Gozalbo, “Chitin: A Structural Biopolysaccharide with Multiple Applications,” in *eLS*, John Wiley & Sons, Ltd, 2014. Accessed: Jan. 26, 2016. [Online]. Available: <http://onlinelibrary.wiley.com/doi/10.1002/9780470015902.a0000694.pub3/abstract>
- [99] C. Ungureanu *et al.*, “Improving Natural Biopolymeric Membranes Based on Chitosan and Collagen for Biomedical Applications Introducing Silver,” *J. Braz. Chem. Soc.*, vol. 26, no. 3, pp. 458–465, Mar. 2015, doi: 10.5935/0103-5053.20150298.
- [100] L. L. Fernandes, C. X. Resende, D. S. Tavares, G. A. Soares, L. O. Castro, and J. M. Granjeiro, “Cytocompatibility of chitosan and collagen-chitosan scaffolds for tissue engineering,” *Polímeros*, vol. 21, no. 1, pp. 1–6, Feb. 2011, doi: 10.1590/S0104-14282011005000008.
- [101] A. Chenite *et al.*, “Novel injectable neutral solutions of chitosan form biodegradable gels in situ,” *Biomaterials*, vol. 21, no. 21, pp. 2155–2161, Nov. 2000.
- [102] M. Rinaudo, G. Pavlov, and J. Desbrières, “Influence of acetic acid concentration on the solubilization of chitosan,” *Polymer*, no. 25, pp. 7029–7032, 1999, doi: 10.1016/S0032-3861(99)00056-7.
- [103] I. A. Sogias, V. V. Khutoryanskiy, and A. C. Williams, “Exploring the Factors Affecting the Solubility of Chitosan in Water,” *Macromol. Chem. Phys.*, vol. 211, no. 4, pp. 426–433, 2010, doi: 10.1002/macp.200900385.
- [104] T. Kiang, J. Wen, H. W. Lim, and K. W. Leong, “The effect of the degree of chitosan deacetylation on the efficiency of gene transfection,” *Biomaterials*, vol. 25, no. 22, pp. 5293–5301, Oct. 2004, doi: 10.1016/j.biomaterials.2003.12.036.

- [105] N. Bhattacharai, J. Gunn, and M. Zhang, “Chitosan-based hydrogels for controlled, localized drug delivery,” *Adv. Drug Deliv. Rev.*, vol. 62, no. 1, pp. 83–99, Jan. 2010, doi: 10.1016/j.addr.2009.07.019.
- [106] W. Tan, R. Krishnaraj, and T. A. Desai, “Evaluation of Nanostructured Composite Collagen–Chitosan Matrices for Tissue Engineering,” *Tissue Eng.*, vol. 7, no. 2, pp. 203–210, Apr. 2001, doi: 10.1089/107632701300062831.
- [107] Y. Zhang *et al.*, “Novel chitosan/collagen scaffold containing transforming growth factor- β 1 DNA for periodontal tissue engineering,” *Biochem. Biophys. Res. Commun.*, vol. 344, no. 1, pp. 362–369, May 2006, doi: 10.1016/j.bbrc.2006.03.106.
- [108] L. Ma *et al.*, “Collagen/chitosan porous scaffolds with improved biostability for skin tissue engineering,” *Biomaterials*, vol. 24, no. 26, pp. 4833–4841, Nov. 2003, doi: 10.1016/S0142-9612(03)00374-0.
- [109] S. H. Kim, Y. S. Nam, T. S. Lee, and W. H. Park, “Silk Fibroin Nanofiber. Electrospinning, Properties, and Structure,” *Polym. J.*, vol. 35, no. 2, Art. no. 2, Feb. 2003, doi: 10.1295/polymj.35.185.
- [110] E. Servoli, D. Maniglio, A. Motta, R. Predazzer, and C. Migliaresi, “Surface properties of silk fibroin films and their interaction with fibroblasts,” *Macromol. Biosci.*, vol. 5, no. 12, pp. 1175–1183, Dec. 2005, doi: 10.1002/mabi.200500137.
- [111] C. Guo, J. Zhang, X. Wang, A. T. Nguyen, X. Y. Liu, and D. L. Kaplan, “Comparative Study of Strain-Dependent Structural Changes of Silkworm Silks: Insight into the Structural Origin of Strain-Stiffening,” *Small*, vol. 13, no. 47, p. 1702266, 2017, doi: <https://doi.org/10.1002/smll.201702266>.
- [112] S. C. Kundu *et al.*, “Invited review nonmulberry silk biopolymers,” *Biopolymers*, vol. 97, no. 6, pp. 455–467, Jun. 2012, doi: 10.1002/bip.22024.
- [113] S. Ling, Z. Qin, C. Li, W. Huang, D. L. Kaplan, and M. J. Buehler, “Polymorphic regenerated silk fibers assembled through bioinspired spinning,” *Nat. Commun.*, vol. 8, no. 1, Art. no. 1, Nov. 2017, doi: 10.1038/s41467-017-00613-5.
- [114] W. Qiu, A. Patil, F. Hu, and X. Y. Liu, “Hierarchical Structure of Silk Materials Versus Mechanical Performance and Mesoscopic Engineering Principles,” *Small*, vol. 15, no. 51, p. 1903948, 2019, doi: <https://doi.org/10.1002/smll.201903948>.
- [115] S. Keten and M. J. Buehler, “Nanostructure and molecular mechanics of spider dragline silk protein assemblies,” *J. R. Soc. Interface*, vol. 7, no. 53, pp. 1709–1721, Dec. 2010, doi: 10.1098/rsif.2010.0149.
- [116] N. Du, X. Y. Liu, J. Narayanan, L. Li, M. L. M. Lim, and D. Li, “Design of Superior Spider Silk: From Nanostructure to Mechanical Properties,” *Biophys. J.*, vol. 91, no. 12, pp. 4528–4535, Dec. 2006, doi: 10.1529/biophysj.106.089144.
- [117] C. Guo, C. Li, X. Mu, and D. L. Kaplan, “Engineering silk materials: From natural spinning to artificial processing,” *Appl. Phys. Rev.*, vol. 7, no. 1, p. 011313, Feb. 2020, doi:

10.1063/1.5091442.

- [118] G. Freddi, S. Faragò, and T. Maifreni, “HPLC fractionation of Cs peptides of *Bombyx mori* silk fibroin,” *Séricologia*, vol. 29, no. 3, pp. 307–326, 1989.
- [119] L. L. Hench, R. J. Splinter, W. C. Allen, and T. K. Greenlee, “Bonding mechanisms at the interface of ceramic prosthetic materials,” *J. Biomed. Mater. Res.*, vol. 5, no. 6, pp. 117–141, Nov. 1971, doi: 10.1002/jbm.820050611.
- [120] J. R. Jones, D. S. Brauer, L. Hupa, and D. C. Greenspan, “Bioglass and Bioactive Glasses and Their Impact on Healthcare,” *Int. J. Appl. Glass Sci.*, vol. 7, no. 4, pp. 423–434, 2016, doi: 10.1111/ijag.12252.
- [121] V. Krishnan and T. Lakshmi, “Bioglass: A novel biocompatible innovation,” *J. Adv. Pharm. Technol. Res.*, vol. 4, no. 2, pp. 78–83, 2013, doi: 10.4103/2231-4040.111523.
- [122] J. R. Jones and L. L. Hench, “Regeneration of trabecular bone using porous ceramics,” *Curr. Opin. Solid State Mater. Sci.*, vol. 7, no. 4, pp. 301–307, Aug. 2003, doi: 10.1016/j.cossms.2003.09.012.
- [123] M. N. Rahaman *et al.*, “Bioactive glass in tissue engineering,” *Acta Biomater.*, vol. 7, no. 6, pp. 2355–2373, Jun. 2011, doi: 10.1016/j.actbio.2011.03.016.
- [124] T. Tian *et al.*, “Micro-Nano Bioactive Glass Particles Incorporated Porous Scaffold for Promoting Osteogenesis and Angiogenesis in vitro,” *Front. Chem.*, vol. 7, p. 186, 2019, doi: 10.3389/fchem.2019.00186.
- [125] J. A. Killion *et al.*, “Hydrogel/bioactive glass composites for bone regeneration applications: Synthesis and characterisation,” *Mater. Sci. Eng. C*, vol. 33, no. 7, pp. 4203–4212, Oct. 2013, doi: 10.1016/j.msec.2013.06.013.
- [126] Q. Z. Chen, I. D. Thompson, and A. R. Boccaccini, “45S5 Bioglass®-derived glass–ceramic scaffolds for bone tissue engineering,” *Biomaterials*, vol. 27, no. 11, pp. 2414–2425, Apr. 2006, doi: 10.1016/j.biomaterials.2005.11.025.
- [127] E. A. A. Neel, D. M. Pickup, S. P. Valappil, R. J. Newport, and J. C. Knowles, “Bioactive functional materials: a perspective on phosphate-based glasses,” *J. Mater. Chem.*, vol. 19, no. 6, pp. 690–701, Jan. 2009, doi: 10.1039/B810675D.
- [128] K. C. Newlands, M. Foss, T. Matchei, J. Skibsted, and D. E. Macphee, “Early stage dissolution characteristics of aluminosilicate glasses with blast furnace slag- and fly-ash-like compositions,” *J. Am. Ceram. Soc.*, vol. 100, no. 5, pp. 1941–1955, 2017, doi: <https://doi.org/10.1111/jace.14716>.
- [129] E. A. A. Neel, I. Ahmed, J. Pratten, S. N. Nazhat, and J. C. Knowles, “Characterisation of antibacterial copper releasing degradable phosphate glass fibres,” *Biomaterials*, vol. 26, no. 15, pp. 2247–2254, May 2005, doi: 10.1016/j.biomaterials.2004.07.024.
- [130] N. Aboulfotoh, Y. Elbashar, M. Ibrahim, and M. Elokr, “Characterization of copper doped phosphate glasses for optical applications,” *Ceram. Int.*, vol. 40, no. 7, Part B, pp. 10395–10399,

Aug. 2014, doi: 10.1016/j.ceramint.2014.02.125.

- [131] N. Ranga *et al.*, “Enhanced antimicrobial properties of bioactive glass using strontium and silver oxide nanocomposites,” *J. Asian Ceram. Soc.*, vol. 7, no. 1, pp. 75–81, Jan. 2019, doi: 10.1080/21870764.2018.1564477.
- [132] Y. C. Fredholm, N. Karpukhina, D. S. Brauer, J. R. Jones, R. V. Law, and R. G. Hill, “Influence of strontium for calcium substitution in bioactive glasses on degradation, ion release and apatite formation,” *J. R. Soc. Interface*, vol. 9, no. 70, pp. 880–889, May 2012, doi: 10.1098/rsif.2011.0387.
- [133] K. Fujikura, N. Karpukhina, T. Kasuga, D. S. Brauer, R. G. Hill, and R. V. Law, “Influence of strontium substitution on structure and crystallisation of Bioglass® 45S5,” *J. Mater. Chem.*, vol. 22, no. 15, pp. 7395–7402, Mar. 2012, doi: 10.1039/C2JM14674F.
- [134] J. Lopes, C. Bertran, and I. O. Mazali, “Bioactivity of $\text{Na}_2\text{O}\cdot\text{CaO}\cdot\text{SiO}_2\cdot\text{P}_2\text{O}_5\cdot\text{Nb}_2\text{O}_5$ -based glasses: in vitro evaluation,” *Front. Bioeng. Biotechnol.*, vol. 4, Jan. 2016, doi: 10.3389/conf.FBIOE.2016.01.00614.
- [135] R. K. Singh, A. Srinivasan, and G. P. Kothiyal, “Evaluation of $\text{CaO}-\text{SiO}_2-\text{P}_2\text{O}_5-\text{Na}_2\text{O}-\text{Fe}_2\text{O}_3$ bioglass-ceramics for hyperthermia application,” *J. Mater. Sci. Mater. Med.*, vol. 20, no. 1, p. 147, Jun. 2008, doi: 10.1007/s10856-008-3497-z.
- [136] N. Laorodphan, P. Pooddee, P. Kidkhunthod, P. Kunthadee, W. Tapala, and R. Puntharod, “Boron and pentavalent vanadium local environments in binary vanadium borate glasses,” *J. Non-Cryst. Solids*, vol. 453, pp. 118–124, Dec. 2016, doi: 10.1016/j.jnoncrysol.2016.10.005.
- [137] A. S. P. Altmann, F. M. Collares, G. de S. Balbinot, V. C. B. Leitune, A. S. Takimi, and S. M. W. Samuel, “Niobium pentoxide phosphate invert glass as a mineralizing agent in an experimental orthodontic adhesive,” *Angle Orthod.*, vol. 87, no. 5, pp. 759–765, Jul. 2017, doi: 10.2319/122417-140.1.
- [138] I. Ahmed, M. P. Lewis, S. N. Nazhat, and J. C. Knowles, “Quantification of Anion and Cation Release from a Range of Ternary Phosphate-based Glasses with Fixed 45 mol% P_2O_5 ,” *J. Biomater. Appl.*, vol. 20, no. 1, pp. 65–80, 2005, doi: 10.1177/0885328205049396.
- [139] W. S. Chou, J. E. Savage, and B. L. O’Dell, “Role of Copper in Biosynthesis of Intramolecular Cross-links in Chick Tendon Collagen,” *J. Biol. Chem.*, vol. 244, no. 21, pp. 5785–5789, Nov. 1969.
- [140] T. E. Paterson *et al.*, “Multifunctional Copper-Containing Mesoporous Glass Nanoparticles as Antibacterial and Proangiogenic Agents for Chronic Wounds,” *Front. Bioeng. Biotechnol.*, vol. 8, 2020, doi: 10.3389/fbioe.2020.00246.
- [141] T. M. Gross *et al.*, “Copper-containing glass ceramic with high antimicrobial efficacy,” *Nat. Commun.*, vol. 10, no. 1, Art. no. 1, Apr. 2019, doi: 10.1038/s41467-019-09946-9.
- [142] M. Miola and E. Verné, “Bioactive and Antibacterial Glass Powders Doped with Copper by Ion-Exchange in Aqueous Solutions,” *Materials*, vol. 9, no. 6, Art. no. 6, Jun. 2016, doi: 10.3390/ma9060405.

- [143] H. Wang *et al.*, “Evaluation of borate bioactive glass scaffolds as a controlled delivery system for copper ions in stimulating osteogenesis and angiogenesis in bone healing,” *J. Mater. Chem. B*, vol. 2, no. 48, pp. 8547–8557, Nov. 2014, doi: 10.1039/C4TB01355G.
- [144] R. Ghosh, O. Swart, S. Westgate, B. L. Miller, and M. Z. Yates, “Antibacterial Copper–Hydroxyapatite Composite Coatings via Electrochemical Synthesis,” *Langmuir*, vol. 35, no. 17, pp. 5957–5966, Apr. 2019, doi: 10.1021/acs.langmuir.9b00919.
- [145] Z. Lin *et al.*, “Improved osteogenesis and angiogenesis of a novel copper ions doped calcium phosphate cement,” *Mater. Sci. Eng. C*, vol. 114, p. 111032, Sep. 2020, doi: 10.1016/j.msec.2020.111032.
- [146] L. B. Romero-Sánchez, M. Marí-Beffa, P. Carrillo, M. Á. Medina, and A. Díaz-Cuenca, “Copper-containing mesoporous bioactive glass promotes angiogenesis in an in vivo zebrafish model,” *Acta Biomater.*, vol. 68, pp. 272–285, Mar. 2018, doi: 10.1016/j.actbio.2017.12.032.
- [147] C. Stähli, M. James-Bhasin, and S. N. Nazhat, “Three-dimensional endothelial cell morphogenesis under controlled ion release from copper-doped phosphate glass,” *J. Controlled Release*, vol. 200, pp. 222–232, Feb. 2015, doi: 10.1016/j.jconrel.2015.01.002.
- [148] C. Stähli, N. Muja, and S. N. Nazhat, “Controlled copper ion release from phosphate-based glasses improves human umbilical vein endothelial cell survival in a reduced nutrient environment,” *Tissue Eng. Part A*, vol. 19, no. 3–4, pp. 548–557, Feb. 2013, doi: 10.1089/ten.tea.2012.0223.
- [149] R. Lakshmikantha, R. R. R. Anavekar, and N. Ayachit, “Characterization and structural studies of vanadium doped lithium–barium–phosphate glasses,” *Can. J. Phys.*, vol. 90, pp. 235–239, Feb. 2012, doi: 10.1139/p2012-011.
- [150] C. Hermansen, J. Mauro, and Y. Yue, “A model for phosphate glass topology considering the modifying ion sub-network,” *J. Chem. Phys.*, vol. 140, no. 15, p. 154501, Apr. 2014, doi: 10.1063/1.4870764.
- [151] C. Stähli, M. Shah Mohammadi, K. E. Waters, and S. N. Nazhat, “Characterization of aqueous interactions of copper-doped phosphate-based glasses by vapour sorption,” *Acta Biomater.*, vol. 10, no. 7, pp. 3317–3326, Jul. 2014, doi: 10.1016/j.actbio.2014.03.015.
- [152] S. Dumitriu, *Polymeric Biomaterials, Revised and Expanded*. CRC Press, 2001.
- [153] M. B. A Chenite, “Rheological characterization of thermogelling chitosan/glycerophosphate solutions,” *Carbohydr. Polym.*, vol. 46, no. 1, pp. 39–47, 2001, doi: 10.1016/S0144-8617(00)00281-2.
- [154] H. C. Hamaker, “The London—van der Waals attraction between spherical particles,” *Physica*, vol. 4, no. 10, pp. 1058–1072, Oct. 1937, doi: 10.1016/S0031-8914(37)80203-7.
- [155] H. C. Hamaker, “Formation of a deposit by electrophoresis,” *Trans. Faraday Soc.*, vol. 35, p. 279, 1940, doi: 10.1039/tf9403500279.
- [156] C. Mendoza, Z. González, Y. Castro, E. Gordo, and B. Ferrari, “Improvement of TiN

nanoparticles EPD inducing steric stabilization in non-aqueous suspensions," *J. Eur. Ceram. Soc.*, vol. 36, no. 2, pp. 307–317, Jan. 2016, doi: 10.1016/j.jeurceramsoc.2015.06.023.

- [157] L. Besra and M. Liu, "A review on fundamentals and applications of electrophoretic deposition (EPD)," *Prog. Mater. Sci.*, vol. 52, no. 1, pp. 1–61, Jan. 2007, doi: 10.1016/j.pmatsci.2006.07.001.
- [158] A. R. Boccaccini, S. Keim, R. Ma, Y. Li, and I. Zhitomirsky, "Electrophoretic deposition of biomaterials," *J. R. Soc. Interface*, vol. 7, no. Suppl 5, pp. S581–S613, Oct. 2010, doi: 10.1098/rsif.2010.0156.focus.
- [159] C. G. A. Lima, R. S. de Oliveira, S. D. Figueiró, C. F. Wehmann, J. C. Góes, and A. S. B. Sombra, "DC conductivity and dielectric permittivity of collagen–chitosan films," *Mater. Chem. Phys.*, vol. 99, no. 2–3, pp. 284–288, Oct. 2006, doi: 10.1016/j.matchemphys.2005.10.027.
- [160] X. Pang and I. Zhitomirsky, "Electrodeposition of hydroxyapatite–silver–chitosan nanocomposite coatings," *Surf. Coat. Technol.*, vol. 202, no. 16, pp. 3815–3821, May 2008, doi: 10.1016/j.surfcoat.2008.01.022.
- [161] X. Pang and I. Zhitomirsky, "Electrodeposition of composite hydroxyapatite–chitosan films," *Mater. Chem. Phys.*, vol. 94, no. 2–3, pp. 245–251, Dec. 2005, doi: 10.1016/j.matchemphys.2005.04.040.
- [162] Y. Wang, X. Pang, and I. Zhitomirsky, "Electrophoretic deposition of chiral polymers and composites," *Colloids Surf. B Biointerfaces*, vol. 87, no. 2, pp. 505–509, Oct. 2011, doi: 10.1016/j.colsurfb.2011.05.043.
- [163] S. Zivanovic, J. Li, P. M. Davidson, and K. Kit, "Physical, Mechanical, and Antibacterial Properties of Chitosan/PEO Blend Films," *Biomacromolecules*, vol. 8, no. 5, pp. 1505–1510, May 2007, doi: 10.1021/bm061140p.
- [164] I. Zhitomirsky and L. Gal-Or, "Electrophoretic deposition of hydroxyapatite," *J. Mater. Sci. Mater. Med.*, vol. 8, no. 4, pp. 213–219, 1997, doi: 10.1023/A:1018587623231.
- [165] O. Van der Biest, S. Put, G. Anné, and J. Vleugels, "Electrophoretic deposition for coatings and free standing objects," *J. Mater. Sci.*, vol. 39, no. 3, pp. 779–785, Feb. 2004, doi: 10.1023/B:JMSC.0000012905.62256.39.
- [166] P. Sarkar and P. S. Nicholson, "Electrophoretic Deposition (EPD): Mechanisms, Kinetics, and Application to Ceramics," *J. Am. Ceram. Soc.*, vol. 79, no. 8, pp. 1987–2002, Aug. 1996, doi: 10.1111/j.1151-2916.1996.tb08929.x.
- [167] O. O. Van der Biest and L. J. Vandeperre, "Electrophoretic deposition of materials," *Annu. Rev. Mater. Sci.*, vol. 29, no. 1, pp. 327–352, 1999, doi: 10.1146/annurev.matsci.29.1.327.
- [168] M. Farrokhi-Rad and M. Ghorbani, "Electrophoretic Deposition of Titania Nanoparticles in Different Alcohols: Kinetics of Deposition," *J. Am. Ceram. Soc.*, vol. 94, no. 8, pp. 2354–2361, Aug. 2011, doi: 10.1111/j.1551-2916.2011.04401.x.
- [169] L. Stappers, L. Zhang, O. Van der Biest, and J. Fransaer, "The Effect of Electrolyte Conductivity

on Electrophoretic Deposition,” *J. Colloid Interface Sci.*, vol. 328, pp. 436–46, Nov. 2008, doi: 10.1016/j.jcis.2008.09.022.

- [170] B. Ferrari and R. Moreno, “EPD kinetics: A review,” *J. Eur. Ceram. Soc.*, vol. 30, no. 5, pp. 1069–1078, Mar. 2010, doi: 10.1016/j.jeurceramsoc.2009.08.022.
- [171] K. Makino and H. Ohshima, “Electrophoretic Mobility of a Colloidal Particle with Constant Surface Charge Density,” *Langmuir*, vol. 26, no. 23, pp. 18016–18019, Dec. 2010, doi: 10.1021/la1035745.
- [172] C. P. Smyth, E. W. Engel, and E. B. Wilson, “THE DIELECTRIC POLARIZATION OF LIQUIDS. IV. THE DEPENDENCE OF MOLAR REFRACTION UPON CONCENTRATION IN MIXTURES,” *J. Am. Chem. Soc.*, vol. 51, no. 6, pp. 1736–1744, Jun. 1929, doi: 10.1021/ja01381a015.
- [173] F. W. Lima, “On the Viscosity of Binary Liquid Mixtures,” *J. Phys. Chem.*, vol. 56, no. 9, pp. 1052–1054, Sep. 1952, doi: 10.1021/j150501a006.
- [174] M. J. Lee, S. M. Hwang, and Y. C. Kuo, “Densities and viscosities of binary solutions containing butylamine, benzylamine, and water,” *J. Chem. Eng. Data*, vol. 38, no. 4, pp. 577–579, Oct. 1993, doi: 10.1021/je00012a026.
- [175] O. Bintou and O. Savadogo, “Electrophoretic Deposition of Alumina and Nickel Oxide Particles,” *J. Sci. Res. Rep.*, vol. 2, pp. 190–205, Mar. 2013, doi: 10.9734/JSRR/2013/2559.
- [176] J. D. Megiatto, B. M. Cerrutti, and E. Frollini, “Sodium lignosulfonate as a renewable stabilizing agent for aqueous alumina suspensions,” *Int. J. Biol. Macromol.*, vol. 82, pp. 927–932, Jan. 2016, doi: 10.1016/j.ijbiomac.2015.11.004.
- [177] M. R. Majhi, R. Pyare, and S. P. Singh, “Preparation and Characterization of CaF₂ Doped Bioglass Ceramics,” *J. Biomim. Biomater. Tissue Eng.*, vol. 11, pp. 45–66, Oct. 2011, doi: 10.4028/www.scientific.net/JBBTE.11.45.
- [178] D. Sriranganathan, N. Kanwal, K. A. Hing, and R. G. Hill, “Strontium substituted bioactive glasses for tissue engineered scaffolds: the importance of octacalcium phosphate,” *J. Mater. Sci. Mater. Med.*, vol. 27, 2016, doi: 10.1007/s10856-015-5653-6.
- [179] A. Haider, A. Waseem, N. Karpukhina, and S. Mohsin, “Strontium- and Zinc-Containing Bioactive Glass and Alginate Scaffolds,” *Bioeng. Basel Switz.*, vol. 7, no. 1, p. 10, Mar. 2020, doi: 10.3390/bioengineering7010010.
- [180] J. C. T. Andrade, J. A. Camilli, E. Y. Kawachi, and C. A. Bertran, “Behavior of dense and porous hydroxyapatite implants and tissue response in rat femoral defects,” *J. Biomed. Mater. Res.*, vol. 62, no. 1, pp. 30–36, Oct. 2002, doi: 10.1002/jbm.10242.
- [181] V. S. Komlev and S. M. Barinov, “Porous hydroxyapatite ceramics of bi-modal pore size distribution,” *J. Mater. Sci. Mater. Med.*, vol. 13, no. 3, pp. 295–299, Mar. 2002, doi: 10.1023/A:1014015002331.
- [182] B. Flautre, M. Descamps, C. Delecourt, M. C. Blary, and P. Hardouin, “Porous HA ceramic for

bone replacement: role of the pores and interconnections - experimental study in the rabbit," *J. Mater. Sci. Mater. Med.*, vol. 12, no. 8, pp. 679–682, Aug. 2001, doi: 10.1023/a:1011256107282.

- [183] Q. Fu, M. N. Rahaman, B. S. Bal, W. Huang, and D. E. Day, "Preparation and bioactive characteristics of a porous 13-93 glass, and fabrication into the articulating surface of a proximal tibia," *J. Biomed. Mater. Res. A*, vol. 82, no. 1, pp. 222–229, Jul. 2007, doi: 10.1002/jbm.a.31156.
- [184] P. Sarkisov, N. Mikhailenko, E. Stroganova, N. Buchilin, and S. Baskov, "Porosity and solubility of bioactive calcium-phosphate glass ceramic materials for bone endoprosthesis replacement," *Glass Ceram.*, vol. 69, no. 5–6, pp. 173–177, Sep. 2012, doi: 10.1007/s10717-012-9439-8.
- [185] D. N. Rockwood, R. C. Preda, T. Yücel, X. Wang, M. L. Lovett, and D. L. Kaplan, "Materials fabrication from *Bombyx mori* silk fibroin," *Nat. Protoc.*, vol. 6, no. 10, pp. 1612–1631, Sep. 2011, doi: 10.1038/nprot.2011.379.
- [186] H. Zahn, W. Schade, and K. Ziegler, "Fractionation of the chymotryptic precipitate of *Bombyx mori* silk fibroin," *Biochem. J.*, vol. 104, no. 3, pp. 1019–1026, Sep. 1967.
- [187] Y. Qi *et al.*, "A Review of Structure Construction of Silk Fibroin Biomaterials from Single Structures to Multi-Level Structures," *Int. J. Mol. Sci.*, vol. 18, no. 3, p. E237, Mar. 2017, doi: 10.3390/ijms18030237.
- [188] E. S. Sashina, A. M. Bochek, N. P. Novoselov, and D. A. Kirichenko, "Structure and solubility of natural silk fibroin," *Russ. J. Appl. Chem.*, vol. 79, no. 6, pp. 869–876, Jun. 2006, doi: 10.1134/S1070427206060012.
- [189] G. Salvi, P. De Los Rios, and M. Vendruscolo, "Effective interactions between chaotropic agents and proteins," *Proteins*, vol. 61, no. 3, pp. 492–499, Nov. 2005, doi: 10.1002/prot.20626.
- [190] W. H. Sawyer and J. Puckridge, "The dissociation of proteins by chaotropic salts," *J. Biol. Chem.*, vol. 248, no. 24, pp. 8429–8433, Dec. 1973.
- [191] T. Kokubo and H. Takadama, "How useful is SBF in predicting in vivo bone bioactivity?," *Biomaterials*, vol. 27, no. 15, pp. 2907–2915, May 2006, doi: 10.1016/j.biomaterials.2006.01.017.
- [192] M. Bitar, V. Salih, R. A. Brown, and S. N. Nazhat, "Effect of multiple unconfined compression on cellular dense collagen scaffolds for bone tissue engineering," *J. Mater. Sci. Mater. Med.*, vol. 18, no. 2, pp. 237–244, Feb. 2007, doi: 10.1007/s10856-006-0685-1.
- [193] Y. V. Karpievitch, A. D. Polpitiya, G. A. Anderson, R. D. Smith, and A. R. Dabney, "Liquid Chromatography Mass Spectrometry-Based Proteomics: Biological and Technological Aspects," *Ann. Appl. Stat.*, vol. 4, no. 4, pp. 1797–1823, 2010, doi: 10.1214/10-AOAS341.
- [194] S. T. Parker *et al.*, "Biocompatible Silk Printed Optical Waveguides," *Adv. Mater.*, vol. 21, no. 23, pp. 2411–2415, Jun. 2009, doi: 10.1002/adma.200801580.
- [195] G. Freddi, Y. Gotoh, T. Mori, I. Tsutsui, and M. Tsukada, "Chemical structure and physical properties of *antheraea assama* silk," *J. Appl. Polym. Sci.*, vol. 52, no. 6, pp. 775–781, May 1994, doi: 10.1002/app.1994.070520608.

- [196] S. Jiang *et al.*, “Er³⁺-doped phosphate glasses for fiber amplifiers with high gain per unit length,” *J. Non-Cryst. Solids*, vol. 263–264, pp. 364–368, Mar. 2000, doi: 10.1016/S0022-3093(99)00646-8.
- [197] Z. Gou and J. Chang, “Synthesis and in vitro bioactivity of dicalcium silicate powders,” *J. Eur. Ceram. Soc.*, vol. 24, no. 1, pp. 93–99, Jan. 2004, doi: 10.1016/S0955-2219(03)00320-0.
- [198] A. Stoch, W. Jastrzbski, A. Brożek, B. Trybalska, M. Cichocińska, and E. Szarawara, “FTIR monitoring of the growth of the carbonate containing apatite layers from simulated and natural body fluids,” *J. Mol. Struct.*, vol. 511–512, pp. 287–294, Nov. 1999, doi: 10.1016/S0022-2860(99)00170-2.
- [199] W. Khoo, F. M. Nor, H. Ardhyananta, and D. Kurniawan, “Preparation of Natural Hydroxyapatite from Bovine Femur Bones Using Calcination at Various Temperatures,” *Procedia Manuf.*, vol. 2, pp. 196–201, Dec. 2015, doi: 10.1016/j.promfg.2015.07.034.
- [200] G. Sauerbrey, “Verwendung von Schwingquarzen zur Wägung dünner Schichten und zur Mikrowägung,” *Z. Für Phys.*, vol. 155, no. 2, pp. 206–222, Apr. 1959, doi: 10.1007/BF01337937.
- [201] K. Keiji. Kanazawa and J. G. Gordon, “Frequency of a quartz microbalance in contact with liquid,” *Anal. Chem.*, vol. 57, no. 8, pp. 1770–1771, Jul. 1985, doi: 10.1021/ac00285a062.
- [202] A. Alassi, M. Benamar, and D. Brett, “Quartz Crystal Microbalance Electronic Interfacing Systems: A Review,” *Sensors*, vol. 17, no. 12, p. 2799, Dec. 2017, doi: 10.3390/s17122799.
- [203] C. P. Brown, F. Rosei, E. Traversa, and S. Licoccia, “Spider silk as a load bearing biomaterial: tailoring mechanical properties via structural modifications,” *Nanoscale*, vol. 3, no. 3, pp. 870–876, Mar. 2011, doi: 10.1039/C0NR00752H.
- [204] Z. Cao, X. Chen, J. Yao, L. Huang, and Z. Shao, “The preparation of regenerated silk fibroin microspheres,” *Soft Matter*, vol. 3, no. 7, p. 910, 2007, doi: 10.1039/b703139d.
- [205] H. Zhang *et al.*, “Preparation and characterization of silk fibroin as a biomaterial with potential for drug delivery,” *J. Transl. Med.*, vol. 10, no. 1, p. 117, Jun. 2012, doi: 10.1186/1479-5876-10-117.
- [206] X. Liu and K.-Q. Zhang, “Silk Fiber — Molecular Formation Mechanism, Structure- Property Relationship and Advanced Applications,” in *Oligomerization of Chemical and Biological Compounds*, 1st ed., C. Lesieur, Ed. Rijeka: IntechOpen, 2014, pp. 69–102. doi: 10.5772/57611.
- [207] Y. Huang, K. Bailey, S. Wang, and X. Feng, “Silk fibroin films for potential applications in controlled release,” *React. Funct. Polym.*, vol. 116, pp. 57–68, Jul. 2017, doi: 10.1016/j.reactfunctpolym.2017.05.007.
- [208] A. Morin, M. Pahlevan, and P. Alam, “Silk Biocomposites: Structure and Chemistry,” in *Handbook of Composites from Renewable Materials*, V. K. Thakur, M. K. Thakur, and M. R. Kessler, Eds. 2017, pp. 189–220. doi: 10.1002/9781119441632.ch8.
- [209] J. O. Warwicker, “The crystal structure of silk fibroin,” *Acta Crystallogr.*, vol. 7, no. 8–9, pp. 565–573, 1954, doi: 10.1107/S0365110X54001867.

- [210] S. K. Samal, M. Dash, F. Chiellini, D. L. Kaplan, and E. Chiellini, “Silk microgels formed by proteolytic enzyme activity,” *Acta Biomater.*, vol. 9, no. 9, pp. 8192–8199, Sep. 2013, doi: 10.1016/j.actbio.2013.05.027.
- [211] T. Wongpinyochit, B. F. Johnston, and F. P. Seib, “Degradation Behavior of Silk Nanoparticles—Enzyme Responsiveness,” *ACS Biomater. Sci. Eng.*, vol. 4, no. 3, pp. 942–951, Mar. 2018, doi: 10.1021/acsbiomaterials.7b01021.
- [212] B. Lotz and F. Colonna Cesari, “The chemical structure and the crystalline structures of Bombyx mori silk fibroin,” *Biochimie*, vol. 61, no. 2, pp. 205–214, Apr. 1979, doi: 10.1016/S0300-9084(79)80067-X.
- [213] X. Wang, G. Wang, L. Liu, and D. Zhang, “The mechanism of a chitosan-collagen composite film used as biomaterial support for MC3T3-E1 cell differentiation,” *Sci. Rep.*, vol. 6, p. 39322, Dec. 2016, doi: 10.1038/srep39322.
- [214] H. Ohshima, “Electrophoretic mobility of soft particles,” *Colloids Surf. Physicochem. Eng. Asp.*, vol. 103, no. 3, pp. 249–255, Oct. 1995, doi: 10.1016/0927-7757(95)03293-M.
- [215] B. Marelli, C. E. Ghezzi, M. James-Bhasin, and S. N. Nazhat, “Fabrication of injectable, cellular, anisotropic collagen tissue equivalents with modular fibrillar densities,” *Biomaterials*, vol. 37, pp. 183–193, Jan. 2015, doi: 10.1016/j.biomaterials.2014.10.019.
- [216] H. S. Mansur, A. A. P. Mansur, E. Curti, and M. V. De Almeida, “Functionalized-chitosan/quantum dot nano-hybrids for nanomedicine applications: towards biolabeling and biosorbing phosphate metabolites,” *J. Mater. Chem. B*, vol. 1, no. 12, p. 1696, 2013, doi: 10.1039/c3tb00498h.
- [217] G. Sailakshmi, T. Mitra, and A. Gnanamani, “Engineering of chitosan and collagen macromolecules using sebacic acid for clinical applications,” *Prog. Biomater.*, vol. 2, no. 1, p. 11, Apr. 2013, doi: 10.1186/2194-0517-2-11.
- [218] E. A. El-Hefian, M. M. Nasef, A. H. Yahaya, and R. A. Khan, “Preparation and Characterization of Chitosan/Agar Blends: Rheological and Thermal Studies,” *J. Chil. Chem. Soc.*, vol. 55, no. 1, pp. 130–136, 2010, doi: 10.4067/S0717-97072010000100031.
- [219] X. Lü, H. Zhang, Y. Huang, and Y. Zhang, “A proteomics study to explore the role of adsorbed serum proteins for PC12 cell adhesion and growth on chitosan and collagen/chitosan surfaces,” *Regen. Biomater.*, vol. 5, no. 5, pp. 1–13, Jul. 2018, doi: 10.1093/rb/rby017.
- [220] L. L. Hench and J. R. Jones, “Bioactive Glasses: Frontiers and Challenges,” *Front. Bioeng. Biotechnol.*, vol. 3, p. 194, 2015, doi: 10.3389/fbioe.2015.00194.
- [221] K. A. Matori, M. I. Sayyed, H. A. A. Sidek, M. H. M. Zaid, and V. P. Singh, “Comprehensive study on physical, elastic and shielding properties of lead zinc phosphate glasses,” *J. Non-Cryst. Solids*, vol. 457, pp. 97–103, Feb. 2017, doi: 10.1016/j.jnoncrysol.2016.11.029.
- [222] Shwetha M and E. Bheemaiah, “Influence of europium (Eu^{3+}) ions on the optical properties of lithium zinc phosphate glasses,” *IOP Conf. Ser. Mater. Sci. Eng.*, vol. 310, p. 012033, Feb. 2018, doi: 10.1088/1757-899X/310/1/012033.

- [223] M. A. Karakassides, A. Saranti, and I. Koutselas, “Preparation and structural study of binary phosphate glasses with high calcium and/or magnesium content,” *J. Non-Cryst. Solids*, vol. 347, no. 1, pp. 69–79, Nov. 2004, doi: 10.1016/j.jnoncrysol.2004.08.111.
- [224] R. M. McDonogh, C. J. D. Fell, and A. G. Fane, “Surface charge and permeability in the ultrafiltration of non-flocculating colloids,” *J. Membr. Sci.*, vol. 21, no. 3, pp. 285–294, Dec. 1984, doi: 10.1016/S0376-7388(00)80219-7.
- [225] C. Chen, Z. Huang, W. Yuan, J. Li, X. Cheng, and R. Chi, “Pressure effecting on morphology of hydroxyapatite crystals in homogeneous system,” *CrystEngComm*, vol. 13, no. 5, pp. 1632–1637, Feb. 2011, doi: 10.1039/C0CE00090F.
- [226] R. Rodríguez-Clemente, A. López-Macipe, J. Gómez-Morales, J. Torrent-Burgués, and V. M. Castaño, “Hydroxyapatite precipitation: A case of nucleation-aggregation-agglomeration-growth mechanism,” *J. Eur. Ceram. Soc.*, vol. 18, no. 9, pp. 1351–1356, Jan. 1998, doi: 10.1016/S0955-2219(98)00064-8.
- [227] L. Addadi and S. Weiner, “Interactions between acidic proteins and crystals: stereochemical requirements in biomineralization.,” *Proc. Natl. Acad. Sci.*, vol. 82, no. 12, pp. 4110–4114, Jun. 1985.
- [228] A. Veis and A. Perry, “The Phosphoprotein of the Dentin Matrix*,” *Biochemistry*, vol. 6, no. 8, pp. 2409–2416, Aug. 1967, doi: 10.1021/bi00860a017.
- [229] G. S. Baht, G. K. Hunter, and H. A. Goldberg, “Bone sialoprotein–collagen interaction promotes hydroxyapatite nucleation,” *Matrix Biol.*, vol. 27, no. 7, pp. 600–608, Sep. 2008, doi: 10.1016/j.matbio.2008.06.004.
- [230] G. Griffanti, W. Jiang, and S. N. Nazhat, “Bioinspired mineralization of a functionalized injectable dense collagen hydrogel through silk sericin incorporation,” *Biomater. Sci.*, vol. 7, no. 3, pp. 1064–1077, Feb. 2019, doi: 10.1039/C8BM01060A.
- [231] A. Ślösarczyk, C. Paluszkiewicz, M. Gawlicki, and Z. Paszkiewicz, “The FTIR spectroscopy and QXRD studies of calcium phosphate based materials produced from the powder precursors with different CaP ratios,” *Ceram. Int.*, vol. 23, no. 4, pp. 297–304, 1997, doi: 10.1016/S0272-8842(96)00016-8.
- [232] A. Rapacz-Kmita, C. Paluszkiewicz, A. Ślösarczyk, and Z. Paszkiewicz, “FTIR and XRD investigations on the thermal stability of hydroxyapatite during hot pressing and pressureless sintering processes,” *J. Mol. Struct.*, vol. 744–747, pp. 653–656, Jun. 2005, doi: 10.1016/j.molstruc.2004.11.070.
- [233] T. Nagai, N. Suzuki, Y. Tanoue, and N. Kai, “Collagen from Tendon of Yezo Sika Deer (*Cervus nippon yesoensis*) as By-Product,” *Food Nutr. Sci.*, vol. 03, no. 01, pp. 72–79, 2012, doi: 10.4236/fns.2012.31012.
- [234] Y. Yang, Q. Cui, and N. Sahai, “How Does Bone Sialoprotein Promote the Nucleation of Hydroxyapatite? A Molecular Dynamics Study Using Model Peptides of Different Conformations,” *Langmuir*, vol. 26, no. 12, pp. 9848–9859, Jun. 2010, doi: 10.1021/la100192z.

- [235] G. He and A. George, “Dentin matrix protein 1 immobilized on type I collagen fibrils facilitates apatite deposition in vitro,” *J. Biol. Chem.*, vol. 279, no. 12, pp. 11649–11656, Mar. 2004, doi: 10.1074/jbc.M309296200.
- [236] M. Prokopowicz, J. Zegliński, A. Gandhi, W. Sawicki, and S. A. M. Tofail, “Bioactive silica-based drug delivery systems containing doxorubicin hydrochloride: In vitro studies,” *Colloids Surf. B Biointerfaces*, vol. 93, pp. 249–59, May 2012, doi: 10.1016/j.colsurfb.2012.01.020.
- [237] C. J. Wilcock, P. Gentile, P. Hatton, and C. Miller, “Rapid Mix Preparation of Bioinspired Nanoscale Hydroxyapatite for Biomedical Applications,” *J. Vis. Exp.*, vol. 2017, no. 120, p. 55343, Sep. 2016, doi: 10.3791/55343.
- [238] E. O. López, A. Mello, M. Farina, A. M. Rossi, and A. L. Rossi, “Nanoscale analysis of calcium phosphate films obtained by RF magnetron sputtering during the initial stages of deposition,” *Surf. Coat. Technol.*, vol. 279, pp. 16–24, Oct. 2015, doi: 10.1016/j.surfcoat.2015.08.021.
- [239] K. Venkateswarlu, A. Chandra Bose, and N. Rameshbabu, “X-ray peak broadening studies of nanocrystalline hydroxyapatite by Williamson–Hall analysis,” *Phys. B Condens. Matter*, vol. 405, no. 20, pp. 4256–4261, Oct. 2010, doi: 10.1016/j.physb.2010.07.020.
- [240] M. D. Calasans-Maia *et al.*, “Cytocompatibility and biocompatibility of nanostructured carbonated hydroxyapatite spheres for bone repair,” *J. Appl. Oral Sci.*, vol. 23, pp. 599–608, Dec. 2015, doi: 10.1590/1678-775720150122.
- [241] E. Lam, Q. Gu, P. J. Swedlund, S. Marchesseau, and Y. Hemar, “X-ray diffraction investigation of amorphous calcium phosphate and hydroxyapatite under ultra-high hydrostatic pressure,” *Int. J. Miner. Metall. Mater.*, vol. 22, no. 11, pp. 1225–1231, Nov. 2015, doi: 10.1007/s12613-015-1189-5.
- [242] C. Staehli, “Dose-dependent effects of copper ion-releasing phosphate- and silicate-based glasses on endothelial cell growth and morphogenesis «in vitro»,” McGill University, Montreal, QC, 2014. Accessed: Apr. 06, 2016. [Online]. Available: http://digitool.library.mcgill.ca/R/?func=dbin-jump-full&object_id=127109&local_base=GEN01-MCG02
- [243] X. Wang, H. C. Schröder, and W. Müller, “Amorphous polyphosphate, a smart bioinspired nano-/bio-material for bone and cartilage regeneration: Towards a new paradigm in tissue engineering,” *J. Mater. Chem. B*, vol. 6, pp. 2385–2412, Apr. 2018, doi: 10.1039/C8TB00241J.
- [244] Y. Yang, G. Wang, G. Zhu, X. Xu, H. Pan, and R. Tang, “The effect of amorphous calcium phosphate on protein protection against thermal denaturation,” *Chem Commun*, vol. 51, pp. 8705–8707, Apr. 2015, doi: 10.1039/C5CC01420D.
- [245] J. R. O’Donnell, D. Škrtić, and J. Antonucci, “Amorphous Calcium Phosphate Composites with Improved Mechanical Properties,” *J. Bioact. Compat. Polym.*, vol. 21, no. 3, pp. 169–184, 2006, doi: 10.1177/0883911506064476.
- [246] K. Yuan *et al.*, “Mapping Three-dimensional Dissolution Rates of Calcite Microcrystals: Effects of Surface Curvature and Dissolved Metal Ions,” *ACS Earth Space Chem.*, vol. 3, no. 5, pp. 833–843, May 2019, doi: 10.1021/acsearthspacechem.9b00003.

- [247] A. Takeuchi *et al.*, “Heterogeneous nucleation of hydroxyapatite on protein: structural effect of silk sericin,” *J. R. Soc. Interface*, vol. 2, no. 4, pp. 373–378, Sep. 2005, doi: 10.1098/rsif.2005.0052.
- [248] A. Chenite *et al.*, “Novel injectable neutral solutions of chitosan form biodegradable gels in situ,” *Biomaterials*, vol. 21, no. 21, pp. 2155–2161, Nov. 2000.
- [249] G. O. Kim, N. Kim, D. Y. Kim, J. S. Kwon, and B.-H. Min, “An electrostatically crosslinked chitosan hydrogel as a drug carrier,” *Molecules*, vol. 17, no. 12, pp. 13704–13711, Nov. 2012, doi: 10.3390/molecules171213704.
- [250] M. Bruchet and A. Melman, “Fabrication of patterned calcium cross-linked alginate hydrogel films and coatings through reductive cation exchange,” *Carbohydr. Polym.*, vol. 131, pp. 57–64, Oct. 2015, doi: 10.1016/j.carbpol.2015.05.021.
- [251] S. Yang, J. Wang, H. Tan, F. Zeng, and C. Liu, “Mechanically robust PEGDA–MSNs-OH nanocomposite hydrogel with hierarchical meso-macroporous structure for tissue engineering,” *Soft Matter*, vol. 8, no. 34, pp. 8981–8989, 2012, doi: 10.1039/c2sm25123j.
- [252] Q. Xing, K. Yates, C. Vogt, Z. Qian, M. C. Frost, and F. Zhao, “Increasing Mechanical Strength of Gelatin Hydrogels by Divalent Metal Ion Removal,” *Sci. Rep.*, vol. 4, p. 4706, Apr. 2014, doi: 10.1038/srep04706.
- [253] I. S. Tyukova, A. P. Safronov, A. P. Kotel’nikova, and D. Y. Agalakova, “Electrostatic and steric mechanisms of iron oxide nanoparticle sol stabilization by chitosan,” *Polym. Sci. Ser. A*, vol. 56, no. 4, pp. 498–504, Jul. 2014, doi: 10.1134/S0965545X14040178.
- [254] A. R. Maity and N. R. Jana, “Chitosan–Cholesterol-Based Cellular Delivery of Anionic Nanoparticles,” *J. Phys. Chem. C*, vol. 115, no. 1, pp. 137–144, Jan. 2011, doi: 10.1021/jp108828c.
- [255] D. Rohanová, A. Roberto Boccaccini, D. Horkavcová, P. Bozděchová, P. Bezdička, and M. Častorálová, “Is non-buffered DMEM solution a suitable medium for in vitro bioactivity tests?,” *J. Mater. Chem. B*, vol. 2, no. 31, pp. 5068–5076, 2014, doi: 10.1039/C4TB00187G.
- [256] D. Rabadjieva *et al.*, “Biomimetic Modifications of Calcium Orthophosphates,” in *On Biomimetics*, 1st ed., Rijeka, Croatia: InTech, 2011. doi: 10.5772/19054.
- [257] N. Y. Mostafa, “Characterization, thermal stability and sintering of hydroxyapatite powders prepared by different routes,” *Mater. Chem. Phys.*, vol. 94, no. 2–3, pp. 333–341, Dec. 2005, doi: 10.1016/j.matchemphys.2005.05.011.
- [258] S. Joschek, B. Nies, R. Krotz, and A. Göpferich, “Chemical and physicochemical characterization of porous hydroxyapatite ceramics made of natural bone,” *Biomaterials*, vol. 21, no. 16, pp. 1645–1658, Aug. 2000, doi: 10.1016/S0142-9612(00)00036-3.
- [259] E. Sada, H. Kumazawa, and Y. Murakami, “Hydrothermal synthesis of crystalline hydroxyapatite ultrafine particles,” *Chem. Eng. Commun.*, vol. 103, no. 1, pp. 57–64, Apr. 1991, doi: 10.1080/00986449108910862.

- [260] J. Mahamid, A. Sharir, L. Addadi, and S. Weiner, “Amorphous calcium phosphate is a major component of the forming fin bones of zebrafish: Indications for an amorphous precursor phase,” *Proc. Natl. Acad. Sci.*, vol. 105, no. 35, pp. 12748–12753, Sep. 2008, doi: 10.1073/pnas.0803354105.
- [261] H. H. Malluche, D. S. Porter, and D. Pienkowski, “Evaluating bone quality in patients with chronic kidney disease,” *Nat. Rev. Nephrol.*, vol. 9, no. 11, pp. 671–680, Nov. 2013, doi: 10.1038/nrneph.2013.198.
- [262] G. Sandeep, H. K. Varma, T. V. Kumary, S. S. Babu, and A. John, “Characterization of Novel Bioactive Glass Coated Hydroxyapatite Granules in Correlation with in vitro and in vivo Studies,” *Trends Biomater. Artif. Organs*, vol. 19, no. 2, pp. 99–107, 2006.
- [263] R. Kumar, K. H. Prakash, P. Cheang, L. Gower, and K. A. Khor, “Chitosan-mediated crystallization and assembly of hydroxyapatite nanoparticles into hybrid nanostructured films,” *J. R. Soc. Interface*, vol. 5, no. 21, pp. 427–439, Apr. 2008, doi: 10.1098/rsif.2007.1141.
- [264] A. Roguska, M. Pisarek, M. Andrzejczuk, M. Dolata, M. Lewandowska, and M. Janik-Czachor, “Characterization of a calcium phosphate–TiO₂ nanotube composite layer for biomedical applications,” *Mater. Sci. Eng. C*, vol. 31, no. 5, pp. 906–914, Jul. 2011, doi: 10.1016/j.msec.2011.02.009.
- [265] B. Bermúdez-Reyes, M. E. Contreras-García, J. L. Almaral-Sánchez, I. Espitia-Cabrera, and F. J. Espinoza-Beltrán, “Chemical anchorage of Hydroxyapatite on 316LSS using a ZrO₂ interlayer for orthopedic prosthesis applications,” *Superf. Vacío*, vol. 25, no. 3, pp. 150–156, Sep. 2012.
- [266] E. Garskaite, K.-A. Gross, S.-W. Yang, T. C.-K. Yang, J.-C. Yang, and A. Kareiva, “Effect of processing conditions on the crystallinity and structure of carbonated calcium hydroxyapatite (CHAp),” *CrystEngComm*, vol. 16, no. 19, pp. 3950–3959, 2014, doi: 10.1039/C4CE00119B.
- [267] J. A. Fallas, J. Dong, Y. J. Tao, and J. D. Hartgerink, “Structural Insights into Charge Pair Interactions in Triple Helical Collagen-like Proteins,” *J. Biol. Chem.*, vol. 287, no. 11, pp. 8039–8047, Mar. 2012, doi: 10.1074/jbc.M111.296574.
- [268] M. D. Shoulders and R. T. Raines, “COLLAGEN STRUCTURE AND STABILITY,” *Annu. Rev. Biochem.*, vol. 78, pp. 929–958, 2009, doi: 10.1146/annurev.biochem.77.032207.120833.
- [269] H. Lodish, A. Berk, S. L. Zipursky, P. Matsudaira, D. Baltimore, and J. Darnell, “Collagen: The Fibrous Proteins of the Matrix,” *Mol. Cell Biol. 4th Ed.*, 2000, Accessed: May 12, 2019. [Online]. Available: <https://www.ncbi.nlm.nih.gov/books/NBK21582/>
- [270] M. R. Bet, G. Goissis, and C. A. Lacerda, “Characterization of polyanionic collagen prepared by selective hydrolysis of asparagine and glutamine carboxyamide side chains,” *Biomacromolecules*, vol. 2, no. 4, pp. 1074–1079, 2001.
- [271] M. R. Bet, G. Goissis, S. Vargas, and H. S. Selistre-de-Araujo, “Cell adhesion and cytotoxicity studies over polyanionic collagen surfaces with variable negative charge and wettability,” *Biomaterials*, vol. 24, no. 1, pp. 131–137, Jan. 2003.
- [272] L. B. Rocha, R. L. Adam, N. J. Leite, K. Metze, and M. A. Rossi, “Biomineralization of

polyanionic collagen-elastin matrices during cavarial bone repair," *J. Biomed. Mater. Res. A*, vol. 79, no. 2, pp. 237–245, Nov. 2006, doi: 10.1002/jbm.a.30782.

- [273] A. R. Boccaccini, S. Keim, R. Ma, Y. Li, and I. Zhitomirsky, "Electrophoretic deposition of biomaterials," *J. R. Soc. Interface*, vol. 7, no. Suppl 5, pp. S581–S613, Oct. 2010, doi: 10.1098/rsif.2010.0156.focus.
- [274] S. Seuss, M. Lehmann, and A. R. Boccaccini, "Alternating current electrophoretic deposition of antibacterial bioactive glass-chitosan composite coatings," *Int. J. Mol. Sci.*, vol. 15, no. 7, pp. 12231–12242, Jul. 2014, doi: 10.3390/ijms150712231.
- [275] O. Sakurada, K. Suzuki, T. Miura, and M. Hashiba, "Bubble-free electrophoretic deposition of aqueous zirconia suspensions with hydroquinone," *J. Mater. Sci.*, vol. 39, no. 5, pp. 1845–1847, Mar. 2004, doi: 10.1023/B:JMSC.0000016200.89677.57.
- [276] M. A. Piza, C. J. L. Constantino, E. C. Venancio, and L. H. C. Mattoso, "Interaction mechanism of poly (o-ethoxyaniline) and collagen blends," *Polymer*, vol. 44, no. 19, pp. 5663–5670, Sep. 2003, doi: 10.1016/S0032-3861(03)00612-8.
- [277] A. M. Martins, G. Eng, S. G. Caridade, J. F. Mano, R. L. Reis, and G. Vunjak-Novakovic, "Electrically Conductive Chitosan/Carbon Scaffolds for Cardiac Tissue Engineering," *Biomacromolecules*, vol. 15, no. 2, pp. 635–643, Feb. 2014, doi: 10.1021/bm401679q.
- [278] H. I. Alkhammash, N. Li, R. Berthier, and M. R. R. de Planque, "Native silica nanoparticles are powerful membrane disruptors," *Phys. Chem. Chem. Phys.*, vol. 17, no. 24, pp. 15547–15560, Jun. 2015, doi: 10.1039/C4CP05882H.
- [279] Â. L. Andrade, J. M. F. Ferreira, and R. Z. Domingues, "Zeta potential measurement in bioactive collagen," *Mater. Res.*, vol. 7, no. 4, pp. 631–634, Dec. 2004, doi: 10.1590/S1516-14392004000400018.
- [280] S. Eqtesadi, A. Motealleh, P. Miranda, A. Lemos, A. Rebelo, and J. M. F. Ferreira, "A simple recipe for direct writing complex 45S5 Bioglass® 3D scaffolds," *Mater. Lett.*, vol. 93, pp. 68–71, Feb. 2013, doi: 10.1016/j.matlet.2012.11.043.
- [281] U. Gbureck, J. Probst, and R. Thull, "Surface properties of calcium phosphate particles for self setting bone cements," *Biomol. Eng.*, vol. 19, no. 2–6, pp. 51–55, Aug. 2002.
- [282] T. Wang *et al.*, "Cu doped Fe₃O₄ magnetic adsorbent for arsenic: synthesis, property, and sorption application," *RSC Adv.*, vol. 5, no. 62, pp. 50011–50018, Jun. 2015, doi: 10.1039/C5RA03951G.
- [283] Z. Qi, H. Lan, T. P. Joshi, R. Liu, H. Liu, and J. Qu, "Enhanced oxidative and adsorptive capability towards antimony by copper-doping into magnetite magnetic particles," *RSC Adv.*, vol. 6, no. 71, pp. 66990–67001, Jul. 2016, doi: 10.1039/C6RA13412B.
- [284] Y.-M. Zhou, Y. Shan, Y.-Q. Sun, and H.-X. Ju, "Adsorption of collagen to indium oxide nanoparticles and infrared emissivity study thereon," *Mater. Res. Bull.*, vol. 43, no. 8–9, pp. 2105–2112, Sep. 2008, doi: 10.1016/j.materresbull.2007.09.007.

- [285] S. Morariu, C.-E. Brunchi, and M. Bercea, “The Behavior of Chitosan in Solvents with Different Ionic Strengths,” *Ind. Eng. Chem. Res.*, vol. 51, no. 39, pp. 12959–12966, Oct. 2012, doi: 10.1021/ie301309g.
- [286] E. B. Zhulina, O. V. Borisov, and V. A. Priamitsyn, “Theory of steric stabilization of colloid dispersions by grafted polymers,” *J. Colloid Interface Sci.*, vol. 137, no. 2, pp. 495–511, Jul. 1990, doi: 10.1016/0021-9797(90)90423-L.
- [287] A. Tulpar, R. D. Tilton, and J. Y. Walz, “Synergistic Effects of Polymers and Surfactants on Depletion Forces,” *Langmuir*, vol. 23, no. 8, pp. 4351–4357, Apr. 2007, doi: 10.1021/la063191d.
- [288] Z. Yu, F. Yang, S. Dai, and R. Qiao, “Structure and Dynamics of Polymeric Canopies in Nanoscale Ionic Materials: An Electrical Double Layer Perspective,” *Sci. Rep.*, vol. 8, no. 1, Art. no. 1, Mar. 2018, doi: 10.1038/s41598-018-23493-1.
- [289] A. Attia, Q. Wang, X. Huang, and Y. Yang, “Titanium phosphates as positive electrode in lithium-ion batteries: Composition, phase purity and electrochemical performance,” *J. Solid State Electrochem.*, vol. 16, pp. 1461–1471, Apr. 2011, doi: 10.1007/s10008-011-1543-0.
- [290] D. Luna-Zaragoza, E. Romero Guzman, and R. Reyes, “Surface and Physicochemical Characterization of Phosphates Vivianite, $\text{Fe}_2(\text{PO}_4)_3$ and Hydroxyapatite, $\text{Ca}_5(\text{PO}_4)_3\text{OH}$,” *J. Miner. Mater. Charact. Eng.*, vol. 08, pp. 591–609, Jan. 2009, doi: 10.4236/jmmce.2009.88052.
- [291] P. Sarkar, D. De, and H. Rho, “Synthesis and microstructural manipulation of ceramics by electrophoretic deposition,” *J. Mater. Sci.*, vol. 39, no. 3, pp. 819–823, Feb. 2004, doi: 10.1023/B:JMSC.0000012909.46419.0e.
- [292] X. Pang, T. Casagrande, and I. Zhitomirsky, “Electrophoretic deposition of hydroxyapatite- CaSiO_3 -chitosan composite coatings,” *J. Colloid Interface Sci.*, vol. 330, no. 2, pp. 323–329, Feb. 2009, doi: 10.1016/j.jcis.2008.10.070.
- [293] B. Brodsky and J. A. M. Ramshaw, “The collagen triple-helix structure,” *Matrix Biol.*, vol. 15, no. 8, pp. 545–554, Mar. 1997, doi: 10.1016/S0945-053X(97)90030-5.
- [294] A. V. Persikov, J. A. M. Ramshaw, A. Kirkpatrick, and B. Brodsky, “Amino Acid Propensities for the Collagen Triple-Helix,” *Biochemistry*, vol. 39, no. 48, pp. 14960–14967, Dec. 2000, doi: 10.1021/bi001560d.
- [295] V. I. Pedroni, P. C. Schulz, M. E. Gschaider, and N. Andreucetti, “Chitosan structure in aqueous solution,” *Colloid Polym. Sci.*, vol. 282, no. 1, pp. 100–102, Dec. 2003, doi: 10.1007/s00396-003-0965-3.
- [296] S. Yasmeen, M. Kabiraz, B. Saha, M. Qadir, M. Gafur, and S. Masum, “Chromium (VI) Ions Removal from Tannery Effluent using Chitosan-Microcrystalline Cellulose Composite as Adsorbent,” *Int. Res. J. Pure Appl. Chem.*, vol. 10, pp. 1–14, Jan. 2016, doi: 10.9734/IRJPAC/2016/23315.
- [297] D. Fan, A. Takawale, J. Lee, and Z. Kassiri, “Cardiac fibroblasts, fibrosis and extracellular matrix remodeling in heart disease,” *Fibrogenesis Tissue Repair*, vol. 5, no. 1, p. 15, Sep. 2012, doi: 10.1186/1755-1536-5-15.

- [298] R. Improta, R. Berisio, and L. Vitagliano, “Contribution of dipole–dipole interactions to the stability of the collagen triple helix,” *Protein Sci.*, vol. 17, no. 5, pp. 955–961, 2008, doi: 10.1110/ps.073301908.
- [299] C. Pillai, W. Paul, and C. P. Sharma, “Chitin and Chitosan Polymers: Chemistry, Solubility and Fiber Formation,” *Prog. Polym. Sci.*, pp. 641–678, Jul. 2009, doi: 10.1016/j.progpolymsci.2009.04.001.
- [300] L. Qiao and M. T. Swihart, “Solution-phase synthesis of transition metal oxide nanocrystals: Morphologies, formulae, and mechanisms,” *Adv. Colloid Interface Sci.*, vol. 244, pp. 199–266, Jun. 2017, doi: 10.1016/j.cis.2016.01.005.
- [301] H. Nyin Yow and S. Biggs, “Probing the stability of sterically stabilized polystyrene particles by centrifugal sedimentation,” *Soft Matter*, vol. 9, no. 42, pp. 10031–10041, 2013, doi: 10.1039/C3SM51534F.
- [302] Statistique Canada, “Recensement en bref : Un portrait de la population âgée de 85 ans et plus en 2016 au Canada, année de recensement 2016,” May 03, 2016. <https://www12.statcan.gc.ca/census-recensement/2016/as-sa/98-200-x/2016004/98-200-x2016004-fra.cfm> (accessed Aug. 12, 2021).
- [303] Thermo Fisher Scientific, “14025 - HBSS, calcium, magnesium, no phenol red,” *Thermo Fisher Scientific*, 2016. <http://www.thermofisher.com/ca/en/home/technical-resources/media-formulation.153.html> (accessed Sep. 14, 2016).
- [304] Q. Liu, S. Huang, J. P. Matinlinna, Z. Chen, and H. Pan, “Insight into Biological Apatite: Physiochemical Properties and Preparation Approaches,” *BioMed Res. Int.*, vol. 2013, 2013, doi: 10.1155/2013/929748.
- [305] S. Pramanik, H. A. S. M., B. Pingguan-Murphy, and N. A. Abu Osman, “Morphological Change of Heat Treated Bovine Bone: A Comparative Study,” *Materials*, vol. 6, pp. 65–75, Jan. 2013, doi: 10.3390/Ma6010065.
- [306] W. Querido, A. L. Rossi, A. P. C. Campos, A. M. Rossi, and M. Farina, “Does crystallinity of extracted bone mineral increase over storage time?,” *Mater. Res.*, vol. 16, no. 5, pp. 970–974, Oct. 2013, doi: 10.1590/S1516-14392013005000096.
- [307] J. Akindoyo, H. Beg, S. Ghazali, E. Akindoyo, and N. Jeyaratnam, “Synthesis of Hydroxyapatite through Ultrasound and Calcination Techniques,” *IOP Conf. Ser. Mater. Sci. Eng.*, vol. 203, p. 012003, May 2017, doi: 10.1088/1757-899X/203/1/012003.
- [308] N. Bano, S. S. Jikan, H. Basri, S. Adzila, and D. M. Zago, “XRD and FTIR study of A&B type carbonated hydroxyapatite extracted from bovine bone,” *AIP Conf. Proc.*, vol. 2068, no. 1, p. 020100, Feb. 2019, doi: 10.1063/1.5089399.

Appendix I: Sommaire récapitulatif

Échafaudages de biopolymère avec additifs pour la réparation des os

Introduction

Les maladies musculo-squelettiques (ex. l'ostéoporose) sont un problème fréquent qui affecte la santé et la qualité de vie de nombreuses personnes à mesure qu'elles vieillissent. Ces dernières années, de plus en plus de personnes souffrent de maladies osseuses [1] telles que fractures osseuses, ostéoporose, scoliose et autres problèmes musculo-squelettiques [2] en raison d'une population de plus en plus âgée souffrant de perte de masse osseuse liée à l'âge, qui conduit à des incidences plus élevées de fracture osseuse [3], [4] (voir Figure A.1). Souvent, cela nécessite une chirurgie invasive pour corriger, ce qui peut entraîner un traumatisme résiduel chez le patient et affecter sa qualité de vie.

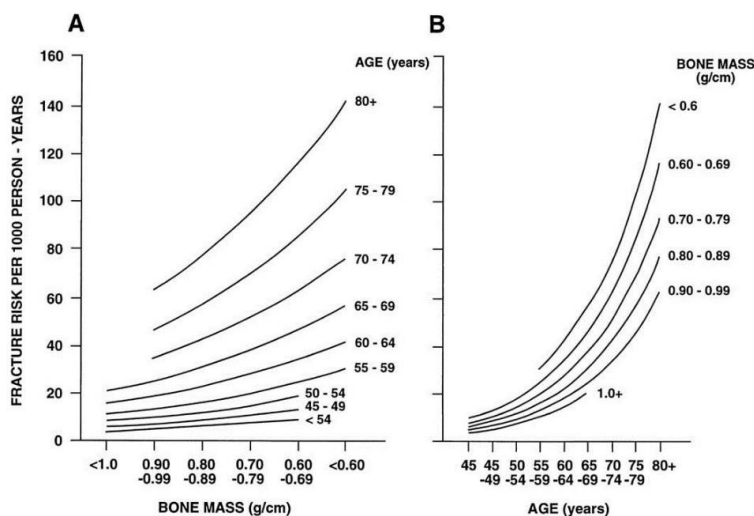


Figure A.1: Estimation de l'incidence des fractures en fonction A) de la masse osseuse et B) de l'âge [5].

En 2017, Statistique Canada a publié un *Recensement en bref* fondé sur les données du recensement de 2016. Ils ont constaté que si l'espérance de vie au Canada est d'environ 80 et 84 ans parmi les hommes et les femmes, respectivement, de plus en plus de canadiens et canadiennes vivent au-delà de 85 ans [6]. Le rapport indiquait que:

Compte tenu du vieillissement de la population au Canada, il est important d'en apprendre davantage sur nos aînés, particulièrement en raison de leurs besoins accrus en matière de soins de santé et d'autres services. Les personnes âgées de 85 ans et plus contribuent de nombreuses façons à la société, par exemple en transmettant leur sagesse,

en servant de modèles à suivre et en favorisant les relations familiales intergénérationnelles. Parallèlement, une part importante de la population âgée de 85 ans et plus doit composer avec des limitations d'activités et présente des besoins particuliers sur le plan des soins de santé et des soins communautaires, du logement, de la sécurité du revenu et du transport [302].

Avec le vieillissement croissant de la population, qui est susceptible de subir une perte osseuse [3], [4], les maladies osseuses, telles que l'ostéoporose, vont entraîner une augmentation des interventions chirurgicales pour remplacer les os endommagés, qu'il s'agisse de simples fractures, de greffes osseuses ou de prothèses de hanche et d'articulation. Par conséquent, la perte osseuse excessive est un problème de santé publique majeure chez les personnes âgées [7]. Une analyse de la population du Canada basée sur les recensements antérieurs (2001-2016) [8]–[11] (voir Figure A.2) montre que la population du Canada est de plus en plus âgée, les projections actuelles indiquant que la population âgée (personnes de 80 ans ou plus) continuera d'augmenter dans les années à venir [12] (voir Figure A.3).

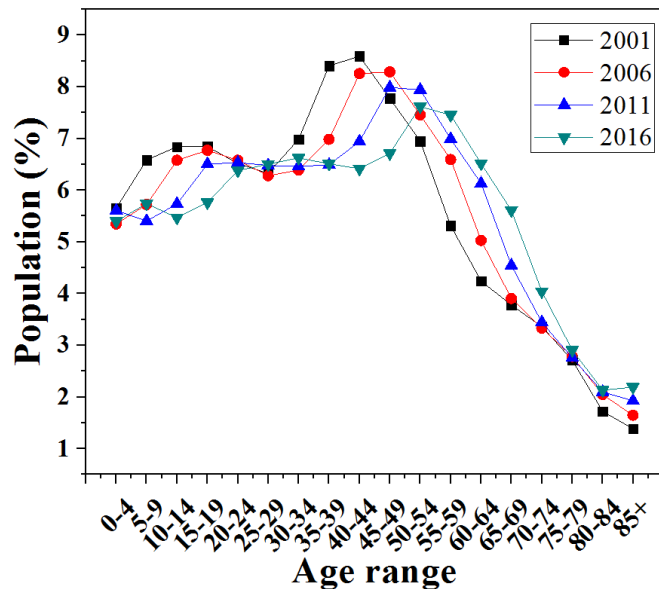


Figure A.2: Population du Canada par group d'âge, 2001-2016 [8]–[11].

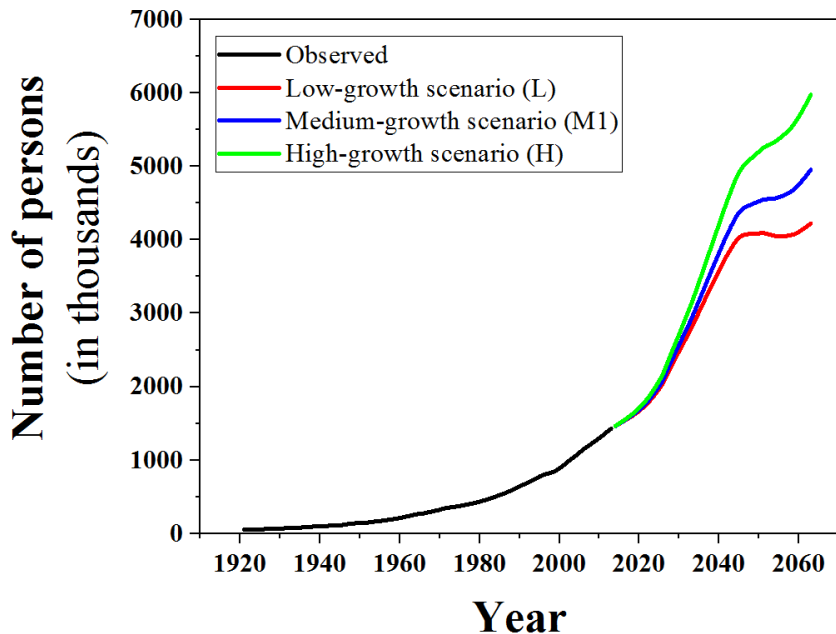


Figure A.3: Nombre de personnes âgées de 80 ans et plus, observé (1923 à 2013) et projeté (2023 à 2063) selon les scénarios de croissance faible (L), de croissance moyenne (M1) et de croissance forte (H) [12].

L'invalidité liée aux troubles musculo-squelettiques est estimé d'avoir augmenté en moyenne de 45 % entre 1990 et 2010, contre 33 % pour l'ensemble des autres maladies [13]. Donc, une solution plus robuste que la chirurgie traditionnelle est nécessaire. Par exemple, au Canada, une étude en 2005 a révélé que 30,000 fractures de la hanche se produisent chaque année [14]; d'ici 2041, ce chiffre atteindrait 88,124 cas [15]. Cette augmentation a également des effets économiques: le coût annuel associé aux fractures de la hanche, présentement 650 millions de dollars, devrait passer à 2,4 milliards de dollars en 2041 [16]. Des dispositifs biodégradables, temporaires ou permanents sont nécessaires pour traiter les maladies musculo-squelettiques, dont la fréquence augmente [2]. Des solutions, soit en termes de nouvelles techniques ou de nouveaux matériaux, sont nécessaires pour répondre à la demande croissante de traitement des difficultés musculo-squelettiques, et pour contenir l'augmentation des coûts qui en résulte et pour améliorer la qualité de vie des patients.

Informations générales

L'os (ou le tissu osseux) est un tissu conjonctif dur et dense qui constitue la majorité du système squelettique. Le système squelettique, essentiellement le cadre du corps, est une composite organique/inorganique qui fournit l'appui et la protection aux organes internes contre les forces extérieures [17], [18]. En tant que tel, il remplit les fonctions critiques suivantes pour le corps [17]:

- Soutient le corps.
- Facilite le mouvement en servant de sites pour la fixation des muscles et en agissant (mécaniquement) comme des leviers et des points d'appui.
- Protège les organes internes (ex. le cerveau, le cœur, les poumons, etc.) en les recouvrant ou en les entourant.
- Produit des cellules sanguines dans la moelle osseuse.
- Stocke les minéraux (ex. les ions de calcium) dans le tissu osseux, qui peuvent être libérés pour maintenir des niveaux physiologiques normaux.

Pour remplir ces fonctions, il est essentiel que le squelette ne fracture pas ou ne tombe pas en défaillance lorsqu'il est exposé aux forces répétées au cours des activités quotidiennes - les charges cycliques peuvent entraîner une fatigue dans les os, causant des dommages microscopiques qui s'accumulent [18]. À des fins structurelles, c'est l'interaction entre la phase inorganique (minérale) et la phase organique au niveau nanoéchelle ou microéchelle qui confère les propriétés inhérentes au système. La phase inorganique assure la rigidité ou la force, tandis que la phase organique est responsable de la ductilité. La combinaison des deux assure une absorption d'énergie avant d'empêcher la rupture [19].

L'os peut être divisé en deux catégories: la matrice extracellulaire (MEC), dans laquelle se trouvent les composants organiques (le tissu ostéoïde) et inorganiques (HA) de l'os, et l'unité multicellulaire de base (UMB); les cellules responsables pour la dissolution et la reconstruction des tissus osseux endommagé, afin de maintenir l'intégrité de la structure osseuse [20] (voir Figure A.4). La MEC peut être subdivisée dans un réseau de protéines et d'hydrates de carbone qui fournit un appui structurel et biologique aux cellules. Le tissu ostéoïde de la MEC est composé de quatre éléments principaux [21] :

- le collagène
- protéines non-collagéniques (PCN)
- hyaluronane
- protéoglycanes

Parmi ces composants, le collagène est particulièrement important dans la structure ostéoïde de la MEC

elle-même.

Composants de l'os		
MEC	UMB	
Tissus ostéoides (fibrilles de collagène liée)	Hydroxyapatite (minéral osseuse)	ostéoblastes ostéoclastes ostéocytes

Figure A.4: Les composants organiques, inorganiques, et cellulaire de l'os [21]

Plan et organisation de la recherche

Aperçu de la recherche

La recherche suivante présente un plan visant à étudier l'aptitude des verres à base de phosphate (VP) dopé avec CuO dans les applications biomédicales, en particulier l'incorporation des verres dans des échafaudages à base de collagène et dans les revêtements pour les implants orthopédiques.

Il a été démontré précédemment que l'utilisation des verres de phosphate dans les gels de collagène libère une multitude d'ions pendant la dissolution, y compris Ca^{2+} , Cu^{2+} , et divers anions polyphosphates. Ces ions peuvent être utilisés pour la réticulation des biopolymères et pour la nucléation de l'hydroxyapatite. La faisabilité de l'utilisation de particules de VP dopés avec CuO pour augmenter le taux de nucléation de l'hydroxyapatite dans les hydrogels de collagène-CTS est déterminée. De plus, l'utilisation de ces particules pour augmenter la performance mécanique via la réticulation des polymères dans l'hydrogel sera étudiée.

D'autres expériences sont conçues pour étudier le co-dépôt de particules de VP avec du collagène/CTS afin de créer des revêtements pour les implants orthopédiques, y compris la cinétique de la formation du dépôt, la morphologie et la composition du film.

But et hypothèse de recherche

Le but de ce projet est de déterminer l'aptitude des VPs dopé avec CuO pour être utilisé dans des

applications biomédicales, en particulier les hydrogels de collagène-CTS et les revêtements d'implants orthopédiques pour la réparation ou le remplacement des os. L'hypothèse est que, contrairement au bioglass conventionnel (ex. Bioglass 45S5) qui nucléise le HA sur sa surface, les particules de VP solubles dans l'eau provoqueront à l'intérieur des échafaudages de collagène-CTS :

- La présence de collagène ou de CTS provoque la chélation des anions et des cations libérés lors de la dissolution, ce qui entraîne une réticulation chimique ou physique, respectivement.
- La sursaturation locale de PO_4^{3-} et de $\text{Ca}^{2+}/\text{Cu}^{2+}$ libérés infiltrent les molécules de collagène et provoquent la nucléation intrafibrillaire d'hydroxyapatite, similaire à celle de l'os naturel.

Objectifs de la recherche

L'objectif principal de ce travail est de développer et de caractériser des échafaudages de collage-CTS incorporant du VP pour l'ingénierie du tissu osseux. Dans ce but, des échafaudages avec des concentrations variables de VP, ainsi que différentes concentrations de CuO, ont été fabriqués, examinés et caractérisés afin de déterminer leurs propriétés et leur potentiel pour la régénération osseuse. L'incorporation de ces éléments a permis de personnaliser la bioactivité et la composition ainsi que les propriétés mécaniques de l'échafaudage. De plus, des VPs dopés avec CuO dans une solution colloïdale de collagène/CTS seront déposés sur des substrats en acier inoxydable par déposition électrophorétique (DEP) pour former un film biocompatible, et caractérisés. Différentes concentrations de CuO et différents paramètres de dépôt seront utilisés pour la DEP de ces films. Dans le cadre de cette recherche, deux objectifs différents ont été établis pour atteindre le but final du projet :

- Développer des hydrogels de collagène-CTS avec des bioadditifs (soit des PDF, soit des verres de phosphate dopés au CuO) incorporés et mener des tests *in vitro* pour déterminer l'emplacement et l'étendue de la nucléation (ex. nucléation intrafibrillaire entièrement minéralisée vs nucléation de surface/interfibrillaire).
- Fabriquer des films de collage-CTS-VP en utilisant le DEP. Évaluer différents paramètres de dépôt (temps, concentration et tension) et caractériser les films obtenus (morphologie, adhésion, composition, uniformité) ainsi que la cinétique de déposition pour déterminer si les VPs dopés avec CuO conviennent aux exigences des revêtements d'implants orthopédiques.

Les résultats et les discussions

Caractérisation des matériaux

La caractérisation des matériaux a été effectuée à l'aide de l'ATR-FTIR afin de déterminer leur composition chimique, qui peut servir comme référence (contrôle) pour les tests futurs. Bien que les spectres ATR-FTIR de C_p et de C_s soient assez similaires, il existe tout de même de légères différences, comme l'épaulement à 1695 cm⁻¹ dans C_p et la bande de l'amide I à 1650 cm⁻¹ pour C_s. Cela est attribué au fait que les polypeptides C_p sont composés des régions cristallines de la fibroïne de soie et ont une structure de type β-feuille, alors que C_s a une structure de type α-hélice [118], [203]. Les spectres de C_p (voir Figure A.4A) présentent un épaulement sur la bande de l'amide I à 1695 cm⁻¹ qui est typiquement associée à une structure β-feuille de SF [80], [204], ainsi que des absorptions d'amide I, II et III à 1622, 1515 et 1230 cm⁻¹, respectivement, qui sont caractéristiques de SF [80], [204]. Les spectres du C_s diffèrent légèrement au niveau de la bande amide I à 1650 cm⁻¹ qui est typique d'une structure de type α-hélice, bien qu'il présente toujours les bandes amide II et III à 1530-1515 cm⁻¹ et 1239 cm⁻¹, respectivement [80].

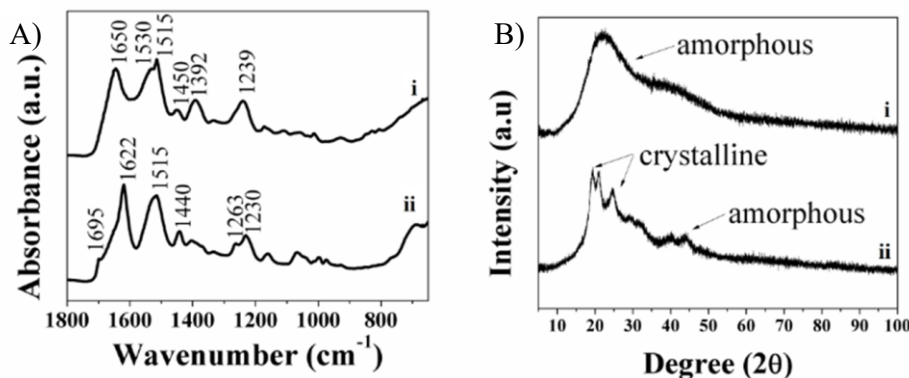


Figure A.4: A) Spectres ATR-FTIR montrant les structures secondaires et B) diagrammes XRD montrant la structure amorphe/cristalline pour i) C_s et ii) C_p tels que fabriqués. Les flèches dans les diagrammes XRD indiquent les régions cristallines et les régions amorphes.

Les images XRD des fragments de C_s et de C_p solubilisés (voir Figure A.4B) ont révélé une structure cristalline dans le C_p, similaire aux spectres XRD de SF rapportés ailleurs [205], tandis que les fragments de C_s ont donné des spectres confirmant leur nature amorphe.

Les résultats de la LCMS contrastent avec la composition précédemment déterminé des polypeptides dérivés de la fibroïne de la soie. Le LCMS a montré que C_s et C_p ont une composition similaire à celle

de la fibroïne de soie. La composition de C_p est similaire aux valeurs trouvées précédemment [118]. En revanche, la composition de C_s est légèrement plus variée, bien qu'elle présente une concentration plus faible de séquences riches en résidus d'acide aspartique et d'acide glutamique par rapport aux résultats similaires rapportés dans la littérature [118], [195]. Les valeurs obtenues par LCMS correspondent à la structure observée précédemment, avec les acides aminés de la Glycine alternant avec d'autres acides aminés (à l'exception d'une liaison Ala-Ala) [212].

En ce qui concerne la charge des PDF (voir Table A.1), la tabulation des résultats LCMS montre que, dans l'ensemble, le PDF est composé d'acides aminés neutres (97,6% et 96,8% pour C_p et C_s, respectivement). Comparé à la charge calculée à partir de la composition des PRD obtenue dans la littérature [195], où 7,6% des acides aminés sont chargés négativement, il y a une différence significative dans la charge de C_s, puisque seulement 1,5% des acides aminés dans les échantillons examinés sont chargés négativement. Il est donc peu probable que les fragments de C_s incorporés dans l'hydrogel soient attirés par le collagène, qui est de nature cationique [80], comme cela a été supposé précédemment.

Table A.1: Comparaison des acides aminés chargés (en pourcentage du total) dans (droite - de la littérature, gauche - du laboratoire)

Charge	Quantités de polypeptides			
	C _p (%) [195]	C _s (%) [195]	C _p (%)	C _s (%)
positive	0.22	2.25	1.3% ± 0.5%	1.7% ± 0.9%
négative	0.76	7.65	1.1% ± 0.5%	1.5% ± 0.8%
neutre	98.98	89.56	97.6% ± 0.9%	96.8% ± 1.7%

Pour caractériser davantage les particules de VP dopés au CuO, des diagrammes de XRD de particules de VP dopés au CuO avec différents % molaires de CuO ont été obtenu. La Figure A.5 montre les diagrammes de diffraction XRD de VP dopés au CuO avec CuO (0, 5 et 10 mol%). Les diagrammes de diffraction des différents verres sont identiques, quelle que soit la quantité de CuO (5 et 10 mol%) incorporée. Il n'y a pas de pics discrets ou nets, mais le large pic diffus continu autour de 2θ=15° dû à la diffusion des rayons X, est typique d'une structure amorphe, similaire aux rapports de la littérature pour le VP dopés avec des oxydes métalliques [221], [222].

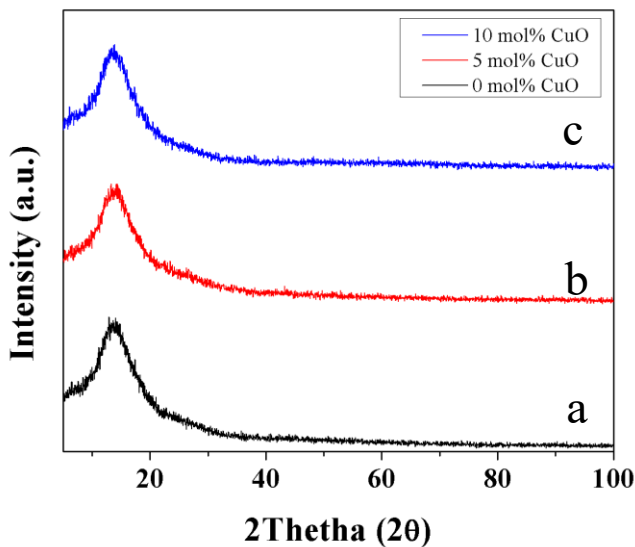


Figure A.5: Schémas XRD pour VP dopés avec a) 0 mol% b) 5 mol% et c) 10 mol% CuO

Minéralisation de l'hydroxyapatite renforcée par la fibroïne de soie in vitro

Des analyses spectroscopiques et XRD ont été menées sur les hydrogels DC, avec et sans additifs incorporés, comme décrit ci-dessus. Les spectres ATR-FTIR résultants ont montré les bandes indiquant la présence de HA ; ν_3 PO_4^{3-} (1030 et 1080 cm^{-1}) [81], [231], [232], ainsi que les bandes pour ν_3 et ν_2 CO_3^{2-} (1450 et 1400 cm^{-1} et 850 cm^{-1} respectivement) [81], [231] étaient présentes dans tous les échantillons, après immersion dans le FCS. La présence de collagène de type I est confirmée par les bandes à 1630 , 1550 et 1240 cm^{-1} , correspondant aux groupes amides I, II et III respectivement [81], [233] présents dans tous les échantillons.

Les spectres obtenus montrent qu'il y a eu une augmentation de la bande ν_3 PO_4^{3-} au cours des 10 premiers jours par rapport à la bande initiale, indiquant l'apparition de la nucléation/croissance de HA. Ceci était particulièrement apparent dans les gels DC et 1:10 DC-C_s, ainsi que dans les gels 1:10 DC-C_p.

Les spectres indiquent que tous les hydrogels présentent des groupes phosphate et carbonate, ce qui suggère que la nucléation de HA se produit dans l'hydrogel, malgré l'absence de PDF. La comparaison de la valeur des pics associés au phosphate et au carbonate a montré que les bandes associées au phosphate augmentaient avec le temps (voir Figure A.6A), celles associées au carbonate ne le faisaient pas (voir Figure A.6B), ce qui indique que l'absorbance du phosphate dans le collagène augmente avec le temps. Ce changement peut être attribué à la minéralisation de HA non-carbonaté, et est cohérent

avec les résultats précédents [81]. Les hydrogels dans lesquels C_s a été incorporé n'ont pas montré de valeurs significativement plus élevées associées au pic de phosphate, contrairement à des travaux antérieurs [80], ce qui indique qu'il ne sert pas à nucléer HA à un taux plus élevé. Le rapport entre les pics de phosphate et de carbonate et la bande de l'amide I est resté presque constant au fil du temps, ce qui indique que peu de changements ont lieu dans les gels 1:10 DC-C_p ou C_s. Il est probable que les PDF distribués dans l'hydrogel ne possèdent pas la quantité d'acides aminés acides, en particulier l'acide glutamique, nécessaires à la nucléation de HA [227], [228], [234]. De plus, l'absence d'interaction électrostatique entre le collagène et les PDF principalement neutres est également une barrière à la formation de HA, car il a été démontré qu'elle était nécessaire à la minéralisation [229], [235].

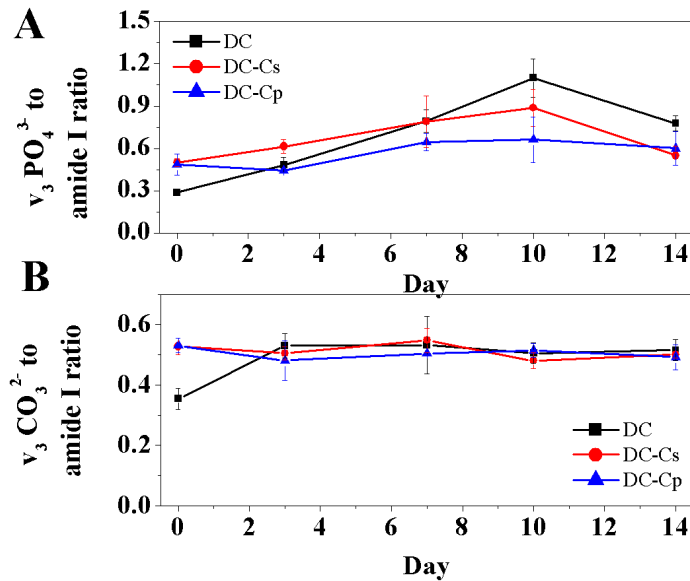


Figure A.6: Rapport entre les bandes A) v3 PO₄³⁻ et B) v3 CO₃²⁻ et les bandes de l'amide I des spectres ATR-FTIR des gels de DC avec aucun additif, C_s et C_p (dans un rapport de 1:10 avec le collagène) immersés dans le FCS (SD, n=4, p<0,05).

La masse des hydrogels de DC lyophilisés avec différents ratios de C_s et de C_p (1:2 et 1:1 par rapport au collagène) avant et après immersion dans le FCS a été mesurée pour déterminer si l'ajout de PDF entraînait un changement de masse dû à la nucléation de HA au fil du temps.

Précédemment [80], il a été rapporté que les hydrogels de DC et de DC-C_s (avec 1:10 de C_s par rapport au collagène) devraient donner un hydrogel contenant 5 wt% et ~60 wt% de HA, respectivement, après sept jours d'immersion dans le FCS. Cependant, les résultats actuels montrent qu'il n'y a pas de différence significative entre les gels de DC et les gels de DC-C_s. La comparaison de la différence des

masses des hydrogels DC, DC-C_s et DC-C_p à la valeur théorique d'un gel tel que fabriqué (sans immersion) avec la même quantité d'additif incorporé est présentée dans le Table A.2. L'analyse de la masse des gels DC après PC correspondait étroitement (3,6 % de différence) à la masse théorique d'un gel de même volume. Les résultats ont montré que les hydrogels DC-C_s ont une masse significativement inférieure à leur valeur théorique, tandis que la masse des gels DC-C_p est proche de sa valeur théorique. De plus, la différence de masse des DC-C_s était similaire à la quantité de C_s ajoutée à la solution, et statistiquement, la différence de masse entre les gels DC et DC-C_s n'est pas significative. Cela indique que le C_s est expulsé avec l'eau à l'intérieur du gel pendant la compression plastique de l'hydrogel hautement hydraté, et que l'échafaudage restant n'est que du collagène.

Table A.2: Masse des hydrogels tels que fabriqués comparé aux valeurs théoriques.

Échantillon	Masse théorétique (mg)	Masse initial (mg)	Différence de masse (%)	Différence de masse du contrôle (mg)
DC (ctrl)	4.7	4.9±0.5	3.6	0.0
1:2 DC-C _s	7.0	5.1±0.5	-27.4	0.2
1:1 DC-C _s	9.4	4.2±0.5	-55.7	-0.7
1:2 DC-C _p	7.0	7.2±0.4	3.0	2.3
1:1 DC-C _p	9.4	10.3±0.7	9.7	5.4

Minéralisation de l'hydroxyapatite utilisant les verres de phosphates dopés avec CuO

La Figure A.7A montre la masse des particules de VP dopés avec différents mol% de CuO et immergées dans FCS à un, trois et cinq jours. La décroissance de la masse indique que les particules de VP immergées dans FCS commencent à se dissoudre immédiatement.

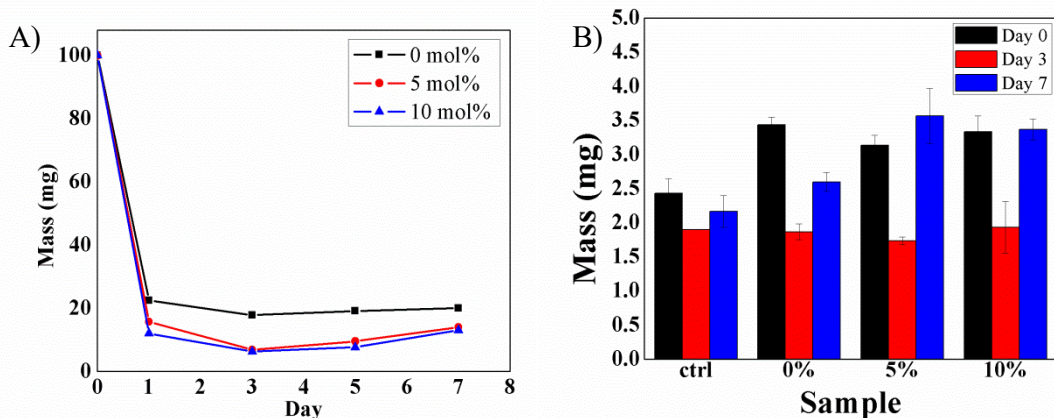


Figure A.7: Masse de A) VP immergé dans FCS pendant 1, 3 et 5 jours et B) gels de collagène avec 50 wt% de VP, immergés dans FCS pendant 3 et 7 jours (n = 3, p < 0,05)

Dans le FCS, la dissolution n'a pas achevé 100 %. De même, l'augmentation de la quantité de dopant CuO, qui est connue pour entraîner des taux de dissolution plus lents en raison de l'érosion de surface interdite par les liaisons M-O plus fortes [242], ne s'est pas produite. Du 100 mg de VP initialement ajoutés au FCS, la masse des particules en solution n'est pas tombée en dessous de 17,8, 6,8 ou 6,3 mg pour les VP dopés avec CuO à 0, 5 et 10 mol%, respectivement, au troisième jour, alors que des expériences précédentes ont montré que la dissolution complète du verre phosphaté se produit en 48 heures. Ceci peut être attribué à la formation de HA pendant que les particules étaient dans le FCS ; la perte de masse a été contrebalancée par la nucléation des particules de HA. Un gain de masse apparaît après trois jours dans FCS, ce qui indique que la dissolution initiale de VP est dépassée par la nucléation d'autres matériaux.

La masse des hydrogels DC incorporant les VP dopés avec CuO immergés dans le FCS pendant trois et sept jours (voir Figure A.7B), a montré une baisse significative de la masse après les trois premiers jours, suivie d'une augmentation au cours des quatre jours suivants (jour sept). L'augmentation de la masse au septième jour a augmenté avec la quantité de CuO. Au septième jour, le contrôle et l'échantillon avec 0 mol% CuO ont montré une petite augmentation de masse, alors que les hydrogels contenant 5% et 10% CuO VP ont montré une augmentation significative des valeurs de masse, c'est-à-dire que leur masse au septième jour est maintenant plus grande qu'au troisième jour. Ces résultats indiquent qu'il existe une sorte d'interaction cuivre-collagène au sein de l'hydrogel qui contribue à augmenter la nucléation ou la croissance des particules.

L'analyse par XRD des particules de VP immergées dans le FCS montre un schéma de diffraction correspondant à un matériau amorphe pour tous les échantillons (voir Figure A.8). La présence de cuivre n'a pas affecté les résultats. Le schéma résultant est différent des schémas obtenus précédemment pour le VP tel qu'il est fabriqué (voir Figure A.8), mais il est similaire à celui observé dans les travaux précédents pour les phosphate de calcium amorphe (ACP). En particulier, il imite le modèle XRD pour l'ACP avec une grande pente à $2\theta = 10^\circ$ et une légère pente à $2\theta = 30^\circ$ [243]–[245].

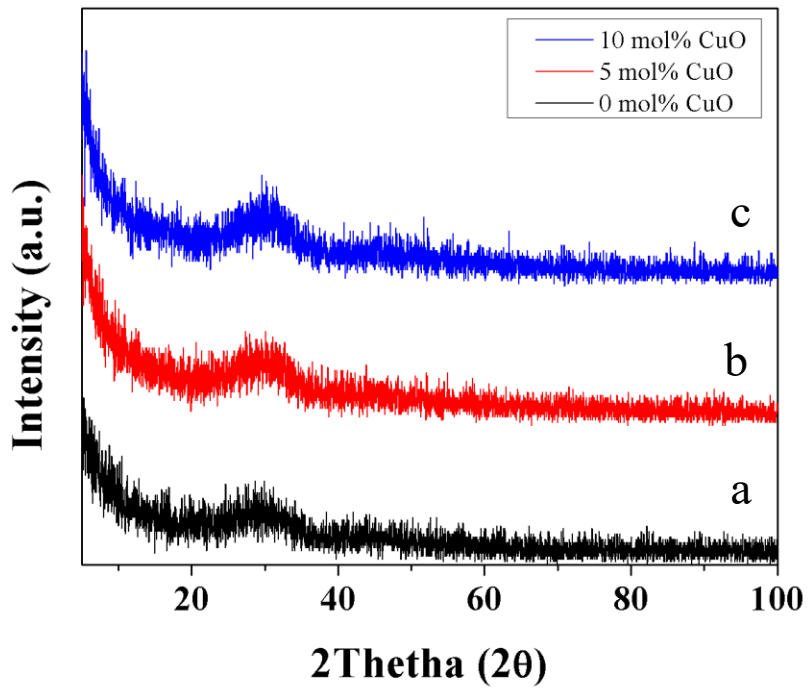


Figure A.8: XRD pour VP dopés avec a) 0 mol% b) 5 mol% et c) 10 mol% CuO immerge dans le FCS

L’analyse EDS des hydrogels 1:1 collagène-CTS montre que la concentration des éléments retenus de VP peut également être observée dans la Figure A.9. En plus de la grande quantité de phosphore, une grande quantité de calcium a été retenue, ainsi que de petites quantités de sodium et des traces de cuivre. La quantité élevée de phosphore peut être attribuée à la liaison du phosphate dans l’hydrogel, en particulier à l’amide des molécules de CTS, comme l’a montré l’ATR-FTIR. Le calcium et le cuivre restants forment probablement des réticulations physiques avec les -OH/-COO⁻ du collagène/CTS [250]–[252], indiquant que la double réticulation est présente dans l’hydrogel [252]. Le phosphate est retenu car il forme des liaisons chimiques dans l’hydrogel [248], [249].

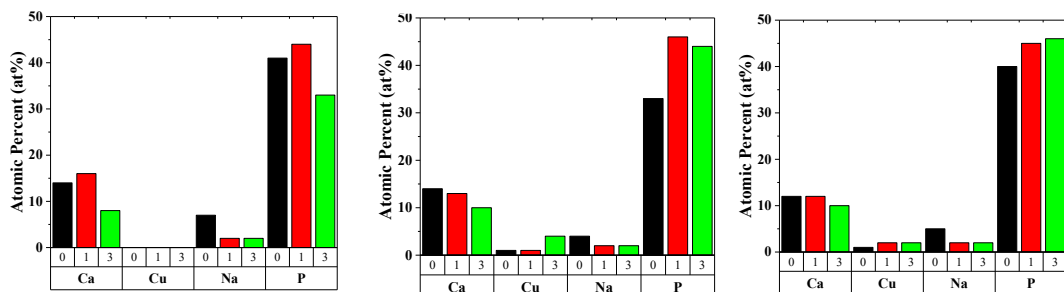


Figure A.9: Composition élémentaire de gels de 1:1 collagène-CTS contenant 50 wt% A) 0, B) 5 et C) 10 % VP dopés avec CuO, immergées dans H₂O pendant 0, 1 et 3 jours.

L'analyse EDS des hydrogels 1:2 collagène-CTS montre que la concentration des éléments retenus de VP est visible dans la Figure A.10. Comme les échantillons précédents, on trouve une grande quantité de phosphore, une grande quantité de calcium, de petites quantités de sodium et des traces de cuivre. La présence réduite de phosphore, de calcium et de sodium se produit également dans l'absence de cuivre. Le phosphore peut être attribué à la liaison du phosphate avec le collagène/CTS. Le calcium et le cuivre restants indiquent que des réticulations physiques se produisent [250]–[252], indiquant qu'une double réticulation est présente dans l'hydrogel [252].

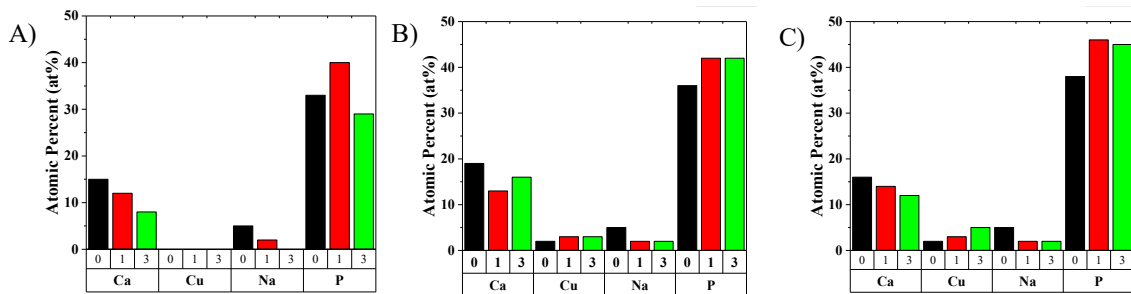


Figure A.10: Composition élémentaire de gels de 1:2 collagène-CTS contenant 50 wt% A) 0, B) 5 et C) 10 % VP dopés avec CuO, immergées dans H₂O pendant 0, 1 et 3 jours.

Les spectres ATR-FTIR des hydrogels avec VP immersés dans le FCS sont présentés dans la Figure A.11. Ici, les gels de collagène ont montré les spectres caractéristiques associés au collagène et au CTS, en particulier les bandes d'amide I et II à 1640 cm⁻¹ et 1550 cm⁻¹, respectivement [84], [215]. La bande à 1030 - 1070 cm⁻¹ est indicative de la présence de PO₄³⁻ [264]–[266]. De même, pour les échantillons A et B, les spectres pour les échantillons tels que fabriqués et après 3 jours d'immersion dans FCS sont presque identiques. Ceci est aussi observé pour les échantillons de 5 et 10 mol% CuO. Au septième jour, la croissance de la bande à 1030 - 1070 cm⁻¹ pour les gels avec VP avec 5 et 10 mol% de CuO incorporé est plus élevée comparée à celle des gels DC et DC avec 0 mol% de CuO. Ces résultats indiquent que le cuivre contribue à la rétention du phosphate. On observe également une légère augmentation du pic à 880 cm⁻¹, qui est associé au carbonate. Les spectres indiquent que la nucléation de HA dans les gels DC avec VP sans CuO se produit, tandis que la nucléation du phosphate de calcium amorphe est plus importante en présence de cuivre.

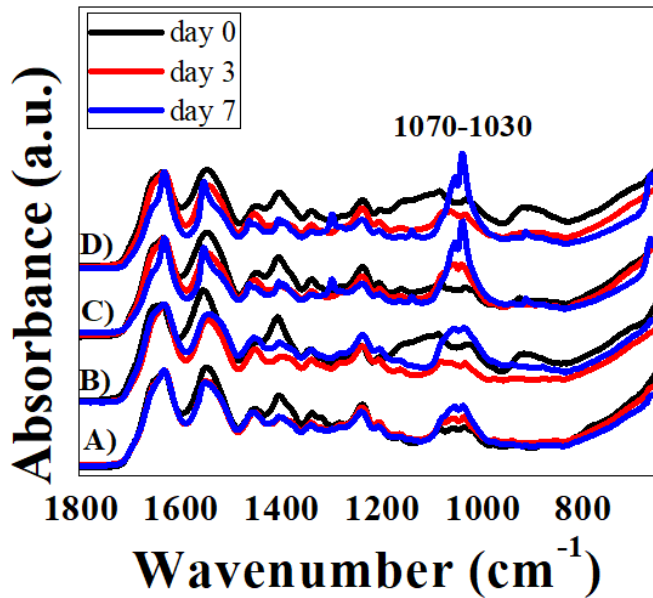
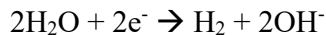


Figure A.11: ATR-FTIR pour A) DC et VP dopes avec B) 0 mol% C) 5 mol% and D) 10 mol% CuO dans DC gels tel que fabriqués (noir) et immergé dans FCS pour 3 (rouge) et 7 jours (bleu)

Dépôt électrophorétique de composites verre-polymères

L'EPD du CTS, du collagène/CTS et du collagène a donné lieu à des films uniformes, à l'exception du collagène pur, qui a montré de multiples cas de formation de bulles et a donné lieu à un film inégal. Des fissures et l'écaillage des revêtements ont également été observées lors de l'incorporation de VP, ainsi qu'une mauvaise adhésion à la surface de l'électrode. La formation de bulles est due à la génération d'hydrogène gazeux à la cathode [273]–[275], et peut être attribuée au collagène (avec un faible conductivité, $\sim 10^{-13}$ S/cm [276]) agissant comme un isolant. La faible conductivité conduit à l'évolution de l'hydrogène gazeux à l'interface cathode/film selon [273], [274]:



Les films CTS et collagène/CTS n'ont pas montré la formation d'hydrogène gazeux à la cathode, probablement en raison de la conductivité électrique plus élevée du CTS (30 S/cm [277]) par rapport au collagène [159].

La mesure de la masse des revêtements pour différentes concentrations de collagène et de CTS montre que l'augmentation du rapport collagène/CTS a peu d'effet sur la masse finale du film de polymère pur déposé. Cependant, lorsqu'il est co-déposé avec VP, l'augmentation de la concentration de collagène est accompagnée d'une augmentation de déposition des films (voir Figure A.12). Les résultats indiquent

que le collagène est fortement adsorbé sur la surface des particules [286] par rapport au CTS.

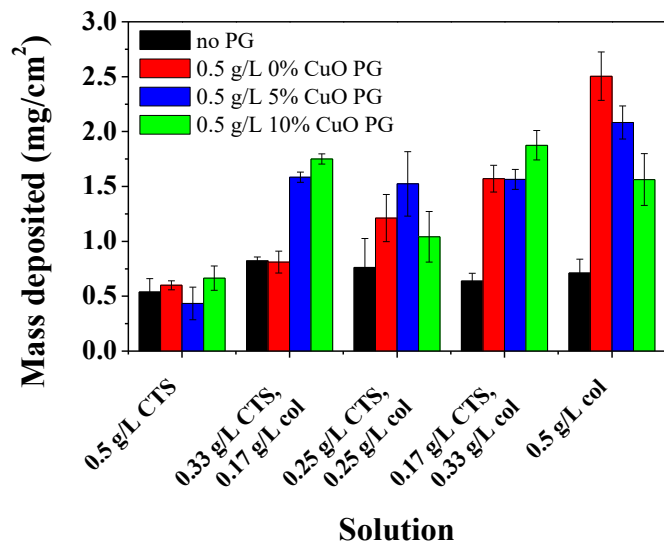


Figure A.12: Masse déposée par PED pour des solutions de collagène, de collagène/CTS et de CTS par rapport au polymère co-déposé avec VP ($n=3$, $p<0.05$)

L'analyse thermogravimétrique (TGA) est un outil utile pour déterminer la composition des matériaux composites. L'analyse des dépôts par TGA (voir Figure A.13) montre que l'ajout de collagène augmente considérablement la quantité de VP dans le dépôt. La perte de poids diminue lorsque le collagène est ajouté, ce qui indique qu'il y a une plus grande quantité de particules de VP dans les films. Les résultats montrent que la masse des particules de VP déposées passe de 5-15% en poids avec le CTS seul à 62-68% en poids avec le collagène.

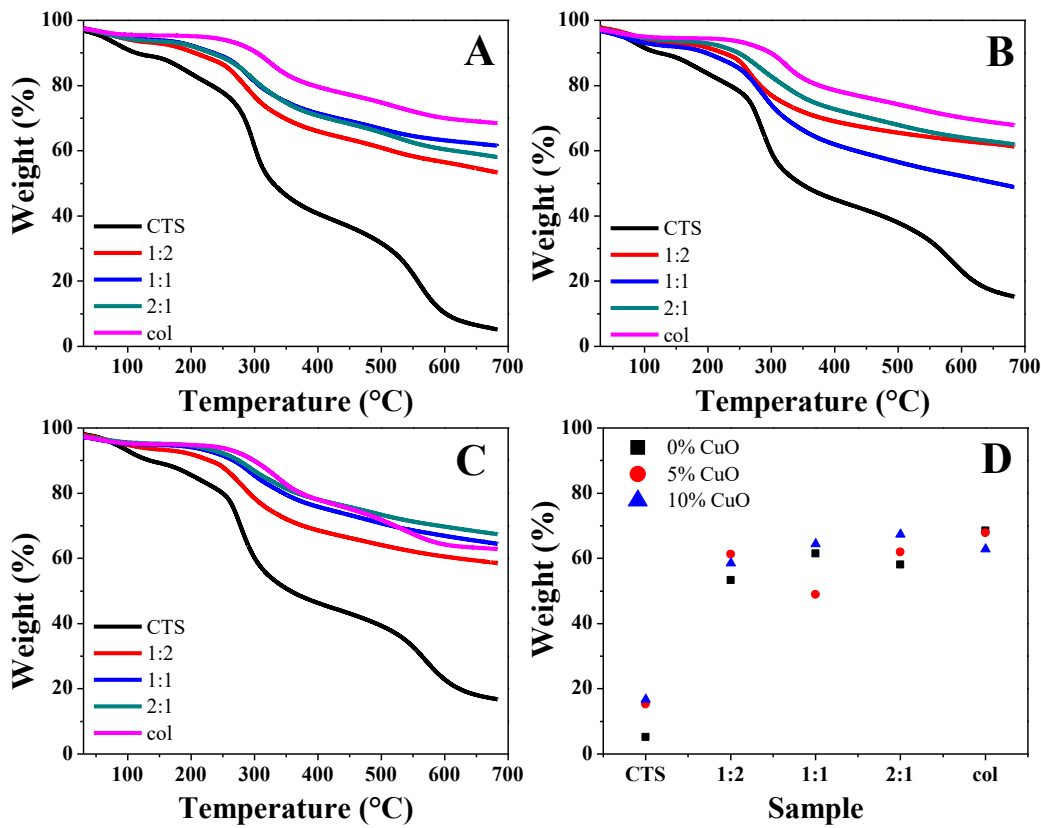


Figure A.13: TGA pour les films fabriqués par EPD de solutions de collagène, de collagène/CTS et de CTS co-déposées avec du VP dopés avec A) 0 mol% ; B) 5 mol% ; V) 10 mol% CuO, et D) leur pourcentage en poids

Les cinétiques de déposition ont été analysées par QCM, qui mesure la masse de dépôt en fonction du temps sur un cristal de quartz vibrant. Les résultats ont montré que le taux de dépôt diminue de façon asymptotique avec le temps, qui est typique de l'EPD à tension constante. Ce comportement est observé dans l'EPD des VP avec du CTS et du collagène (voir Figure A.14). Le collagène-VP présente un taux de déposition plus élevé, ce qui peut être attribué à une plus grande affinité d'adsorption sur le VP en solution. Une augmentation linéaire accompagnée d'un plateau graduel est typique du dépôt à tension constante où la concentration du polymère/verre en solution diminue avec le temps [291], [292]. De plus, le champ électrique nécessaire à l'électrophorèse diminue également en raison de la résistivité du film déposé, ce qui entraîne une diminution de l'attraction et la vitesse des particules vers l'électrode [291].

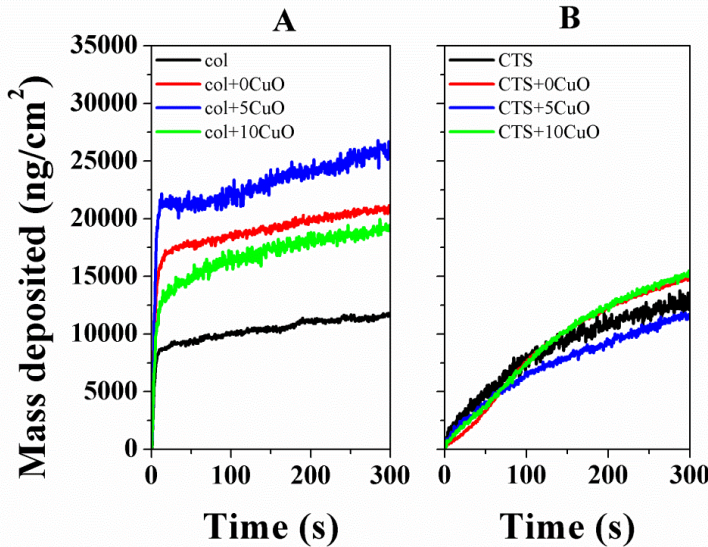


Figure A.14: Mesures QCM de la masse déposée en fonction du temps pour le DEP de A) collagène et B) CTS co-déposés avec VP sans CuO

Conclusions et perspectives futures

Ce travail a examiné divers additifs bioactifs dans différents systèmes qui pourraient être utilisés comme remplacements potentiels des matériaux traditionnels utilisés dans les chirurgies osseuses. Les additifs de soie dans des hydrogels de collagène compressés ont été développés comme échafaudages pour l'ingénierie du tissu osseux qui pourraient remplacer les autogreffes qui nécessitent une chirurgie invasive pour le patient.

Les résultats in vitro montrent que l'immersion des PDF dans le FCS conduit à la nucléation de HA, mais que l'incorporation de ces mêmes PDF dans un hydrogel ne contribue pas à minéraliser le collagène. La caractérisation des polypeptides par LCMS a montré que l'acide glutamique (qui est important pour favoriser la nucléation de HA) était présent en quantité inférieure à celle attendue, bien que cela puisse être attribué aux différentes techniques expérimentales utilisées pour quantifier la composition en acides aminés ou à son traitement.

Les résultats indiquent qu'il est moins apte à promouvoir la biominéralisation que ce que l'on pensait initialement. En outre, l'analyse de masse des hydrogels de DC contenant du C_s au fil du temps a indiqué que les fragments de C_s sont immédiatement expulsés lors de la compression plastique. L'analyse chimique a montré que les PDF incorporés dans un hydrogel de collagène présentent peu de différence par rapport à un hydrogel de collagène pur pour favoriser la nucléation de HA, et ne peuvent donc pas servir de substitut aux PCN dans l'ingénierie du tissu osseux sans avoir amélioré la méthode de liaison

du polypeptide à la fibrille de collagène.

L'utilisation de VP dopés avec CuO a montré beaucoup plus prometteuse que les PDF. Bien qu'ils ne conduisaient pas nécessairement à la nucléation de HA, l'analyse in vitro a montré que le VP, dans des conditions physiologiques, conduisait à la nucléation de l'ACP. L'analyse de masse et l'analyse ATR-FTIR du VP dopés avec CuO immergé dans le FCS ont montré que les VP plus élevée en cuivre présentaient une présence accrue de phosphate, ce qui indique que la présence de cuivre est nécessaire à la nucléation de l'ACP. De plus, les résultats du SEM et de l'EDS ont montré que les hydrogels contenant du VP immergé dans le FCS avaient des ACP incorporés dans la structure, ainsi qu'une quantité plus élevée de calcium et de phosphate que les groupes de contrôle, ce qui indique une plus grande minéralisation.

Ces résultats indiquent que les VPs peuvent être utilisés dans les implants de biomatériaux pour aider à accélérer la minéralisation et la guérison des os.

Des composites de VP, collagène et CTS ont été déposés avec succès sur des substrats en acier inoxydable par DEP. Les particules de VP ont été déposées de manière anodique et ont montré une flocculation lorsque la quantité de CuO augmentait, tandis que le collagène et le CTS se sont déposés de manière cathodique. Le rôle du cuivre dans le PED a également été déterminé : les particules de VP dopés à 5 % et 10 % molaires de CuO ont donné lieu à des couches non-uniformes, tandis que les particules à 0 % molaire étaient plus uniformes.

Les films de polymère pur ont montré peu de différence dans le rendement du dépôt lorsque la concentration de collagène et CTS variait. Cependant, l'ajout de VP dopés avec CuO, qui a été co-déposé cathodiquement avec le collagène et le CTS, a montré des différences significatives dans la masse déposée lorsque la concentration de collagène et CTS variait. La présence de collagène a conduit à une stabilité de la suspension colloïdale en raison de la stabilisation stérique, et l'augmentation de la quantité de collagène a également entraîné une augmentation linéaire du dépôt de VP, ainsi que le dépôt de plus grosses particules, ce qui indique que les revêtements peuvent être adaptés en ajustant le rapport collagène/CTS. Un inconvénient de l'utilisation du collagène, cependant, était la génération d'hydrogène gazeux à la cathode, ce qui a entraîné des films non-uniformes et une perte d'adhérence au substrat, ainsi que la fissuration et l'écaillage du film.

Les résultats indiquent qu'il est possible de fabriquer des revêtements de collagène, de CTS et de VP par DEP, et le VP est un biomatériau prometteur pour les revêtements d'implants orthopédiques.

Perspectives futures

De nombreux travaux sont encore nécessaires pour déterminer si les VPs dopé avec CuO peuvent remplacer les verres biologiques traditionnels dans les applications biomédicales. Tandis que les résultats obtenus dans ce travail sont prometteurs, la réaction du corps humain reste encore largement inconnue. De plus, le cuivre est connu pour avoir un effet毒ique lorsqu'il est exposé aux cellules en grande quantité. Bien que la quantité utilisée dans les VPs dopé avec CuO soit minuscule par rapport à la quantité nécessaire pour endommager le corps humain, il s'agit néanmoins d'un aspect du VP dopés avec CuO qui doit être étudié. Les travaux futurs devraient se concentrer sur des essais *in vivo* pour déterminer a) la réponse cellulaire au VP (en termes de prolifération et de différenciation cellulaires) et b) la toxicité des VP dopés avec CuO, étant donné que des ions Cu²⁺ sont libérés pendant sa dissolution.

Bien que des recherches supplémentaires soient nécessaires, les résultats que nous avons obtenus sont prometteurs, comme ils indiquent une méthode permettant d'augmenter la minéralisation d'un hydrogel, ce qui indique que la période nécessaire à la guérison et à la réhabilitation des patients qui subissent une intervention chirurgicale pour réparer le tissu osseux (qui peut prendre plusieurs semaines à plusieurs mois) peut être considérablement réduite avec un système collagène-CTS-VP. En outre, comme le réseau d'hydrogel ressemble à la MEC native du tissu osseux, il favoriserait également la prolifération des cellules osseuses. Enfin, la possibilité de remplacer les autogreffes, qui nécessitent une chirurgie supplémentaire et invasive, est certaine d'améliorer la qualité de vie des patients.

Appendix II: Supporting figures

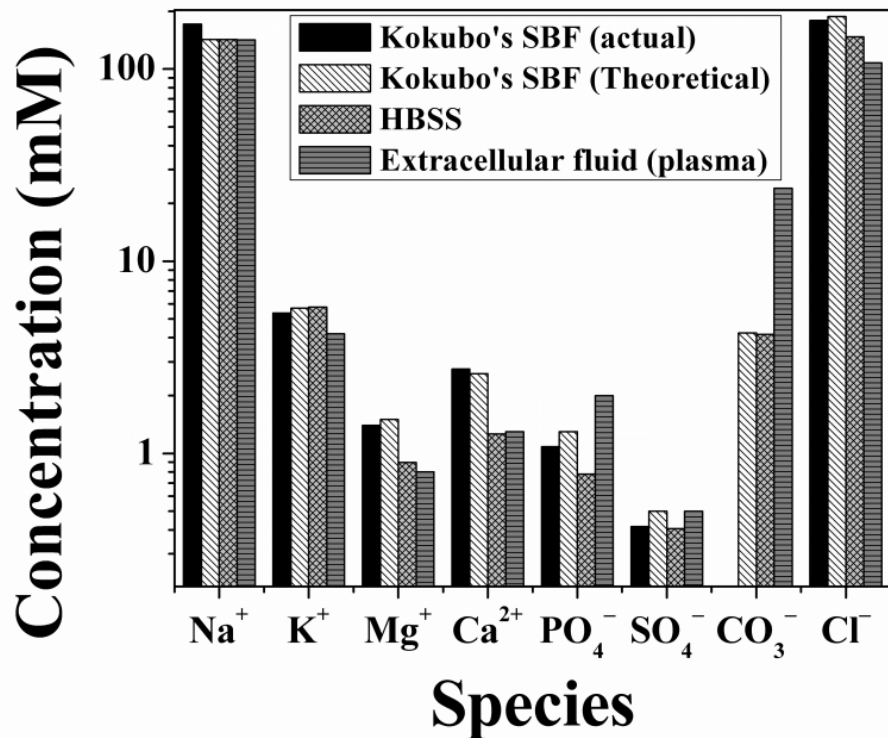


Figure S.1: Analysis of Kokubo's SBF via IC compared to theoretical values for Kokubo's SBF and HBSS, as well ECF (plasma)

Figure S.3 shows the analysis of Kokubo's SBF via Ion Chromatography (IC). The IC results show that the composition is nearly identical to the calculated theoretical values, as well as the composition of commercial SBF (Hank's Balance Salt Solution, HBSS) [303]. In addition, it is also similar to the composition of ECF [191], with the exception of the amount carbonate, which is taken to be much lower than that of ECF given the theoretical value.

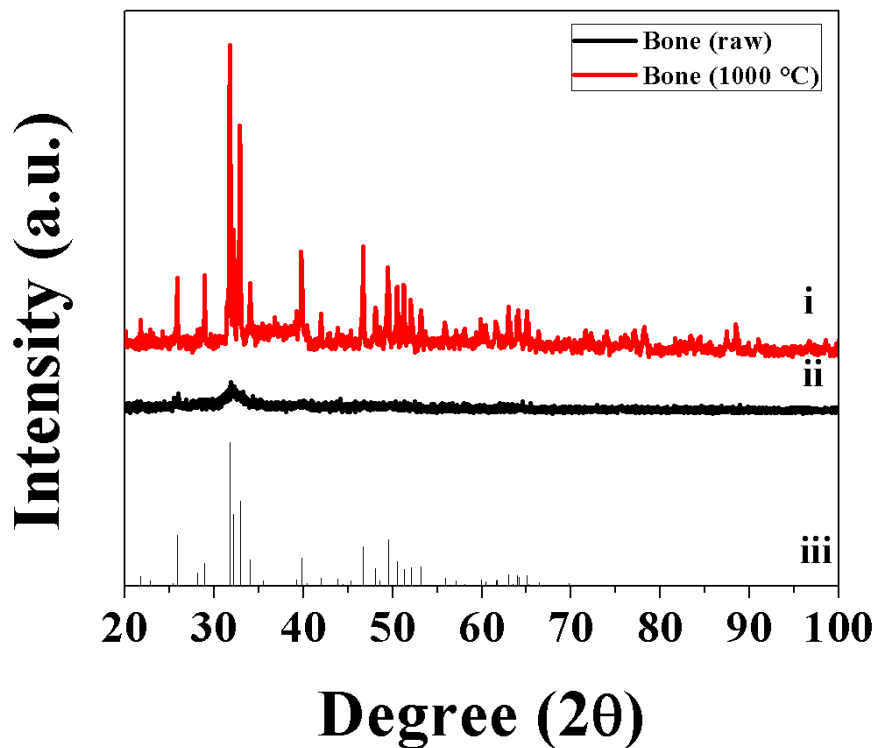


Figure S.2: XRD spectra for bone (bovine) i) as-received and ii) after heat treatment. iii) ICDD file 00-046-0905

Figures S.2 shows XRD analysis of the samples of bone match that seen in literature [304], [305]. Heat treatment reveals the band pattern of bone and calcined bone, with the peaks of the latter matching that of calcium-deficient hydroxyapatite (CDHA) (ICDD file 00-046-0905).

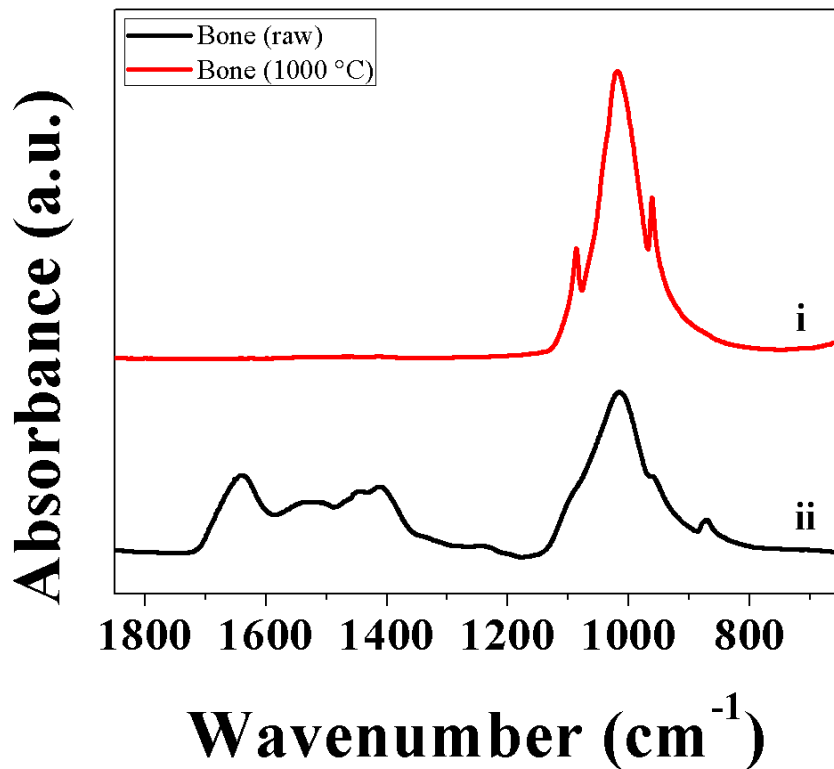


Figure S.3: ATR-FTIR spectra for bone (bovine) i) as-received and ii) after heat treatment

Figures S.1 shows ATR FT-IR of bovine bone has the characteristic peaks of collagen from the bands amide I, II and II groups at 1630, 1550 and 1240 cm^{-1} [81], [233], while the presence of HA is seen in the large phosphate band at 1030 and 1080 cm^{-1} [81], [231], [232]. The results are supported by those seen in literature [306]–[308] of FT-IR conducted on bone and bone samples that have had collagen removed.